COMPREHENSIVE FULL-DEPTH CONDITION ASSESSMENT OF REINFORCED CONCRETE BRIDGE DECKS USING GROUND PENETRATING RADAR

By

FATEMEH SEDIGH IMANI

A Dissertation submitted to the

School of Graduate Studies

Rutgers, The State University of New Jersey

in partial fulfillment of the requirements

for the degree of

Doctor of Philosophy

Graduate Program in Civil and Environmental Engineering

written under the direction of

Nenad Gucunski

and approved by:

_____

_____

_____

_____

New Brunswick, New Jersey

May 2019

ABSTRACT OF THE DISSERTATION

COMPREHENSIVE FULL-DEPTH CONDITION ASSESSMENT OF REINFORCED CONCRETE BRIDGE DECKS USING GROUND PENETRATING RADAR

by Fatemeh S. Imani

Dissertation Director:

Dr. Nenad Gucunski

The traditional practice for condition evaluation of concrete bridge decks using GPR is limited to evaluating the upper section above the top reinforcement mat. As such, it does not provide any useful information about the condition of concrete below. In an attempt to expand the GPR evaluation zone beyond the top rebar, this research focuses on the development of a machine learning algorithm for the full depth condition assessment. Two learning algorithms were developed: (i) an algorithm based on numerical data, which was then applied to the experimental data from a GPR survey of a validation slab, and (ii) an algorithm based on a dataset comprised entirely of experimental data, which was later validated using a bridge and validation slab GPR survey data.

For the first algorithm, a database was developed through a series of two-dimensional numerical simulations of GPR surveys of slabs with variable influential or characteristic

parameters. The slab was divided into three separate yet interconnected longitudinal layers. The quality of concrete was characterized by two electromagnetic properties – permittivity and conductivity, which were varied for each layer. Using the electromagnetic properties as characteristic parameters, six concrete conditions from good to critical were simulated. A machine learning technique, called gradient boosting, was used to predict the layers' condition.

Gradient boosting was also used to analyze a dataset compiled through GPR surveys of four concrete bridge decks to predict the deck condition. Two independent prediction modules were developed: *Module 1* to predict the condition above the top rebars, and *Module 2* to predict the condition of concrete between the top and bottom rebars. A laboratory validation test slab and a fifth concrete highway bridge deck were surveyed using the same GPR system, and the data were used to validate the learning algorithm. The implementation of the proposed method in the validation phase showed that using machine learning and a vast library of GPR data, it is possible to avoid the arbitrary 90^{th} percentile depth correction for new bridges without compromising the ability to assess the deck condition accurately. It was additionally demonstrated that it is possible for GPR to assess the condition of the deck beyond the top reinforcing mat.

To develop a more effective learning algorithm based on numerical simulations, it is recommended that a more extensive dataset is generated. It is also imperative to calibrate the numerical data with experimental data through laboratory testing in which the electromagnetic properties of concrete can be controlled at various depths.

Acknowledgment

There are many people who helped me get to this point, both in my academic and personal life. Among those who contributed to my education at Rutgers, I would like to start by giving huge thanks to Dr. Nenad Gucusnki, my advisor and mentor for the past several years. His intelligence, expertise, wit, and encouraging personality were the driving force behind each step of this journey. It has been a privilege to work under his supervision.

I would not have been able to complete this work were it not for the support of my friends and colleagues at CAIT. Specifically, I would like to acknowledge Dr. Maher for creating a warm, friendly research environment for students and researchers to thrive. I am grateful for my friend, Shahin Saadati, for his guidance and for sharing his wealth of knowledge of machine learning in addition to graciously mentoring me over the past eighteen months. Daniel Cortes helped me improve my coding skills and assisted me with the technical challenges associated with my project. I also appreciate Kien Dinh for his support and advice throughout this process.

I would also like to express special gratitude to my friends, the people with whom I shared hours of conversations on topics other than NDE and bridge decks. In particular, I would like to thank Julia Conrath for all her kind support and encouragement over the years, and for consistently reminding me how to keep things in perspective. I will always appreciate Eugene Raymundo for his friendship and support.

Last but certainly not least, I am eternally grateful for my dear family. Not a day goes by that I am not thankful for my mother for sacrificing it all for her children. My father will always have a special place in my heart, and with each life lesson, I am reminded of how

he always wanted the best for me. And Amir, I wouldn't have been where I am today if it weren't for you. Many thanks to you and Sepideh for your unconditional love and support. This one is for you!

Table of Contents

List of Figures

Nomenclature

Abbreviations

1D	One Dimensional
2D	Two-Dimensional
3D	Three dimensional
ABC	Absorbing Boundary Condition
ACI	American Concrete Institute
ANDERS	Automated Nondestructive Evaluation and Rehabilitation System
ASCE	American Society of Civil Engineers
ASR	Alkali-Silica Reaction
BMS	Bridge Management System
CAIT	Center for Advanced Infrastructure and Transportation
CMP	Common Midpoint
CSE	Copper Sulfate Electrode
CWT	Continuous Wavelet Transform
DFT	Discrete Fourier Transform
DOT	Department of Transportation
DPC	Dry Point Contact
DWT	Discrete Wavelet Transform
EM	Electromagnetic
ER	Electrical Resistivity
FDFD	Finite-Difference Frequency-Domain
FDTD	Finite-Difference Time-Domain
FEM	Finite Element
FFT	Fast Fourier Transform
FHWA	Federal Highway Administration
GB	Gradient Boosting
GPR	Ground Penetrating Radar
GUI	Graphical User Interface
HCP	Half-Cell Potential
HFSS	High-Frequency Structure Simulator
IE	Impact Echo

(IRT)	Infrared Thermography
LTBP	Long Term Bridge Performance
ML	Machine Learning
MoM	Method of Moments
MPO	Metropolitan Planning Organization
NBI	National Bridge Inventory
NDE	Nondestructive Evaluation
NIST	National Institute of Standard and Technology
NIST-TIP	National Institute of Standards and Technology-Technology Innovation Program
ns	NanoSecond
ODE	Ordinary Differential Equation
PDE	Partial Differential Equation
PEC	Perfect Electric Conductor
PML	Perfectly Matched Layer
PSPA	Portable Seismic Pavement Analyzer
PT	Post-Tensioned
RAF	Royal Air Force
RC	Reinforced Concrete
RF	Radio Frequency
RILEM	Réunion Internationale des Laboratoires et Experts des Matériaux, systèmes de construction et ouvrages French for: The International Union of Laboratories and Experts in Construction Materials, Systems and Structures
SHRP 2	The Second Strategic Highway Research Program
STFT	Short-Time Fourier Transform
TWTT	Two-Way Travel Time
UPV	Ultrasonic Pulse Velocity
USDOT	The U.S. Department of Transportation
USW	Ultrasonic Surface Waves
WWII	World War II

Chapter 1. Introduction

1.1 Introduction

Communities are dependent on transportation systems for their economic development and growth. The quality of employment, education, healthcare, and life, in general, is intertwined with the quality of transportation. In the long term, highways are the most essential mode of transportation that elevate communities through increased mobility. In the short term, investment in highways helps the local economy through construction-related activities.

A 2011 research by the Rand Corporation found that investment in highway infrastructure can boost the economy through improving productivity and output. The same report showed that in addition to quantity, the quality and condition of the highway system is a significant factor in improving economic activities (1).

Availability and condition of bridges are vital to the greater highway system because of both their impact on mobility, and the fact that bridge failures, similar to the collapse of I-35 bridge in Minneapolis, or the Genoa bridge in Italy, could lead to loss of life and significant economic ramifications.

In 1988, ASCE began publishing periodic report cards on condition of the nation's infrastructure. These report cards grade the US infrastructure in 16 categories including roads and bridges. In the latest infrastructure report card published in 2017, the nation's infrastructure was given a D^{+}. The same document reports that among over 614,000 bridges in the country, one in every 11 bridges is structurally deficient. Figure 1-1 illustrates the percentage of all and structurally deficient bridges by material type.

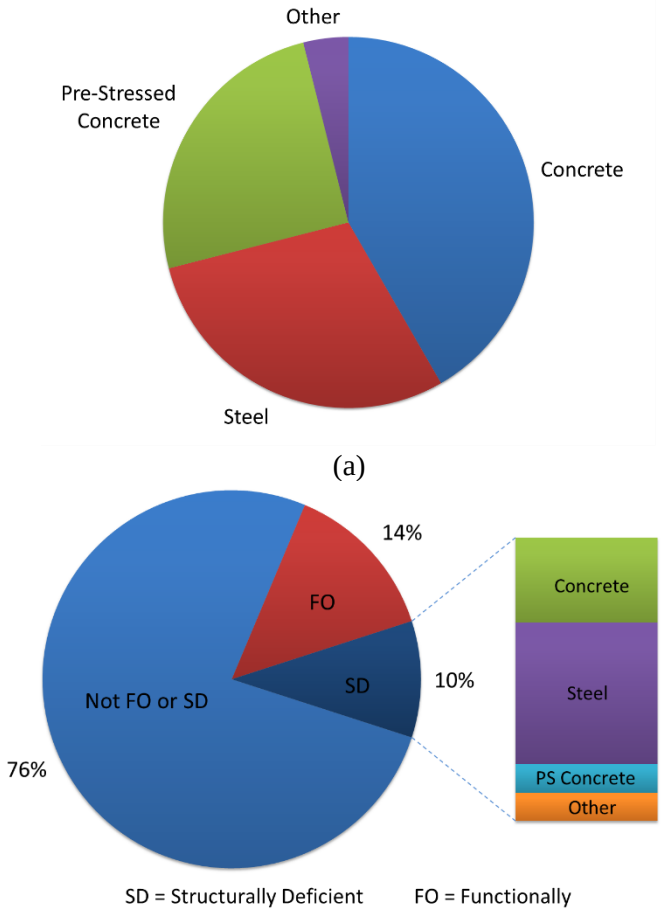

Figure 1-1. (a) All bridges by material type; (b) Structurally deficient bridges by material type (based on 2015 NBI data).

The bridges in the U.S. highway system are aging faster than we can renew them. A significant number of bridges have reached or passed the service life they were designed

for. The average age of the U.S. bridges is 43 years, with nearly 39% of bridges over the age of 50 (2). ASCE gave a C^+ grade to the U.S. bridges in 2017, which was a slight improvement from the C grade in 2009. In addition to the nationwide scores, the report card also delineates the infrastructure grades state by state. In New Jersey, for example, about 9% or 577 bridges are structurally deficient. The average age of NJ bridges is 51 years, eight years more than the national average of 43 years. The issue demands more attention considering the fact that most bridges were designed for a service life of 50 years (2).

According to the Federal Highway Administration (FHWA), as of December 2017, roughly 22 million m^2 of the total 370 million m^2 of bridge deck area in the United States are structurally deficient, with another 21 million m^2 in poor condition. That puts more than 11% of the total area of the nation bridges in dire need of rehabilitation (3). In 2013, the American Society of Civil Engineers (ASCE) estimated that an annual investment of $20.25 billion is needed to improve the current condition of the nation's bridges by 2028. The scale of this amount of needed funding becomes more significant in view of the fact that the current level of annual spending is $12.8 billion (2). The 2015 USDOT's report to Congress estimated a backlog of $123.1 billion for bridge rehabilitation (4). The most substantial portion of this expenditure is needed for assessing and upgrading the condition of bridge decks since given their exposure they deteriorate faster than other bridge components.

The significance of the condition of the U.S. bridges was made clear in President Obama's 2013 State of the Union Address when he referred to the nearly 70,000 structurally deficient bridges across the country as one of the most urgent repair needs that require

immediate attention. The condition of more than 2,700 bridges and more than 42,000 miles of roadways was improved throughout the country thanks to the nearly $28 billion of the 2009 stimulus plan (American Recovery and Reinvestment Act) dedicated by the USDOT to the highway program (5).

Considering the significance of bridges in the greater highway system, the proper management, preservation maintenance, and rehabilitation of bridges are critically important. Inspection and health monitoring are essential elements of bridge management needed for appropriate planning and scoping of maintenance and rehabilitation activities. This is particularly true for bridge decks, which deteriorate faster than other bridge elements, and which inspection and rehabilitation disrupt mobility.

Accurate and rapid condition monitoring enables bridge owners and authorities to manage bridges more efficiently through an informed allocation of funds and proper maintenance and rehabilitation planning while minimizing disruption to mobility. Nondestructive evaluation (NDE) methods and ground penetrating radar (GPR) in particular are best suited for such evaluations. GPR allows for large swathes of the deck to be scanned in a short period of time and with high accuracy, and provide an objective assessment of the deck condition. Proper implementation of rapid, nondestructive techniques for the accurate evaluation of the deck condition is imperative for: (1) detecting the deterioration during its early stages and mitigating it by application of proper remedies, (2) reducing the traffic interruption, while adhering to *get in-get out-stay out* motto.

Despite all the advantages of GPR over the traditional methods of bridge deck condition assessment and detection of localized damages, it is not yet widely accepted as an essential tool for condition evaluation in the bridge management systems (BMS) by the Departments

of Transportation (DOTs) around the country. The limited use of GPR in health monitoring of bridges can be attributed to the high level of expertise required to analyze and effectively interpret the GPR data. The current practice of assessing bridge deck condition using GPR involves evaluating the electromagnetic wave attenuation propagating through the deck. This approach does not provide a full-depth assessment of bridge decks and is only limited to the top portion of the deck above the top reinforcing bars. Therefore, further research is needed to understand the alteration of electromagnetic waves in the scattering response and signal attenuation in a given bridge deck for accurate interpretation of GPR data.

1.2 Problem Statement

Efficient management of bridges, proper maintenance, preservation and rehabilitation, and timely rebuilding has emerged today into a challenging call for public mobility and safety to which federal, state and local agencies must respond. Of all the bridge elements, bridge decks demand special attention as they deteriorate faster than the other bridge components. Besides, bridge deck inspections require traffic interruptions which are costly and impact mobility.

The traditional approach for condition assessment of bridge decks that is narrowed to the visual survey, often in conjunction with chain dragging and hammer sounding, provides limited insight into incipient degradation trends and even some types of medium-coarse and coarse discontinuities. The existence of overlays, such as asphalt or polyester overlays, causes the aforementioned sounding methods to be even less informative. The concept of basing bridge management decisions on the information provided by visual survey and traditional sounding only needs to be revisited due to its apparent limitations. This points

squarely to the need for a means of obtaining an objective, accurate assessment of the bridge deck inventory.

The global trend for obtaining reliable, comprehensive information about the condition of reinforced concrete decks in the least mobility-impacting manner is the use of nondestructive evaluation techniques. When equally reliable information can be obtained using NDE methods, invasive sampling may be abandoned, or used only for validation.

Various NDE techniques are used for the condition assessment of bridge decks, including ground penetrating radar (GPR), impact echo (IE), ultrasonic surface waves (USW), shear wave tomography, half-cell potential (HCP), electrical resistivity (ER), infrared thermography (IRT) and chain drag/hammer sounding. These techniques address different conditions, impacting service life and functional performance of bridge decks. Some examples are the existence of discontinuities (voids, delaminations, and cracks), electrochemical potential of reinforcing steel and ongoing or anticipated corrosion, and protective properties of concrete towards reinforcing steel, degradation and reduction of the modulus of elasticity caused by alternate freezing and thawing, and others. To obtain a comprehensive and reliable condition assessment, an adequately selected battery of nondestructive evaluation methods needs to be used, combined with a minimum sufficient destructive testing to establish ground truth information.

Given the GPR's potential for collecting data at the traffic speed, using GPR for condition assessment of bridge decks will reduce the impact of the survey on mobility and reduce associated costs. Despite all the advantages of GPR over the traditional methods of bridge deck inspection, it is not yet widely accepted by DOTs and MPOs (Metropolitan Planning Organizations) as an essential tool in bridge management. The current practice of assessing

bridge deck condition using GPR involves evaluating the electromagnetic wave attenuation at the top reinforcement level. This method does not provide a full depth assessment of the deck and is limited only to the portion of the deck above the top reinforcement level, without giving any useful information about the condition of concrete below (6; 7; 8; 9; 10; 11) (Figure 1-2). In an attempt to assess the full depth of a concrete bridge deck, this study examines a machine learning algorithm as an alternative to the traditional GPR data analysis.

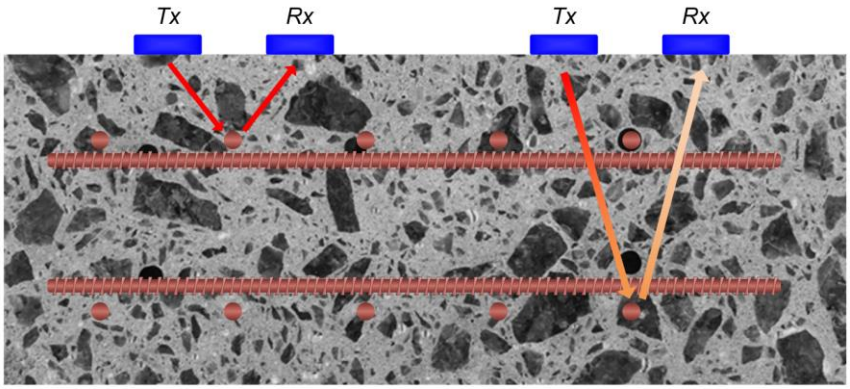

Figure 1-2. The objective is to achieve a full-depth assessment of the deck using GPR.

1.3 Research Objectives and Scope

The main impediments in the broader use of GPR in the bridge management system and the current limitations for assessing the full depth of a bridge deck using GPR were discussed earlier. This research was conducted to tackle those problems. Accordingly, the following objectives were established:

- Developing a new data processing approach to enable expanding the depth of GPR evaluation beyond the top rebar level,

- Developing a new post-processing method to allow an objective assessment of bridge decks at the network level without the need for the 90th percentile depth correction for every new bridge,
- Converting the dB-based condition maps into ratings, which are a more intuitive way of presentation,
- Using the time-frequency analysis as a complementary approach to the traditional time domain GPR data analysis.

The primary objective of this study was to develop a new GPR data analysis method to expand the depth of evaluation from the top portion above the rebars only to the full depth of a bridge deck. The goal was to develop a post-processing technique with low computational costs, which could enable the operator to draw conclusions as to the condition of the deck below the top reinforcing bars.

A secondary objective of this research was a comprehensive investigation of GPR application in condition assessment of bridge decks, and specifically to further the DOTs' and other bridge owners' confidence in this technique. The results will facilitate the implementation of GPR as a complementary tool in long term health monitoring of bridge decks as a part of routine maintenance and repair programs.

Since experimental studies are expensive, time-consuming, and labor-intensive, numerical simulations were used as a precursor to the experimental work. Computational simulations help researchers optimize a machine or technique in a cost-effective and timely fashion because the ground truth information is controlled and known. Among different methods of computational electromagnetics, finite-difference time-domain (FDTD) and finite

element method (FEM) were used. The results were further post-processed and after conditioning were used as input features of a machine learning algorithm. The feasibility of a full depth condition evaluation using GPR was first examined using these numerical simulations. A learning algorithm was developed using a dataset generated by a parametric study based on two-dimensional finite-difference time-domain (FDTD) simulations. This method was then adopted for analyzing the data from actual bridge deck surveys and a laboratory validation slab. In the process, a new data analysis model was developed using machine learning to improve the traditional GPR analysis for the top layer of the deck. Using the reflection from the bottom rebars, the same methodology was modified and adopted for the condition assessment of a deck below the top reinforcing bars. The same learning algorithm was used for analyzing a test slab fabricated in the laboratory with known defects.

1.4 Organization of the Dissertation

Following the introduction, Chapter 2 begins with a brief review of common deterioration mechanisms in concrete bridge decks followed by a concise summary of the most promising NDE techniques for condition assessment of bridge decks. In Chapter 3, the basic principles of a GPR system and the parameters impacting electromagnetic wave propagation are discussed. Next, the current dominant practice for evaluation of concrete bridge decks using GPR is explained in detail. The chapter concludes by introducing time-frequency analysis as an alternative to the traditional time domain analysis of GPR data. Chapter 4 provides a brief review of the most prominent computational electromagnetic methods. Finite Element Method (FEM), Finite-Difference Time-Domain (FDTD), and Method of Moments (MoM) are discussed. The preliminary finite element simulation

results are presented in Chapter 5. The FEM results are post-processed using STFT. The results of the parametric study using FDTD are presented in Chapter 6. Chapter 7 starts by reviewing the relevant machine learning methodologies. Next, two learning algorithms were developed using gradient boosting: (i) an algorithm based on the results of the numerical simulations, and (ii) an algorithm based on a dataset generated by actual GPR surveys of four bridge decks. The former was then used to evaluate a validation slab made in the laboratory, and the latter was validated by assessing both the validation slab and another bridge deck. Finally, the findings and conclusions are presented and discussed in Chapter 8.

Chapter 2. Background

2.1 Introduction

GPR is used in a wide variety of applications in the evaluation of transportation infrastructure. For example, in mapping bridge decks identifying areas with high propensity for corrosion and corrosion-induced delaminations, locating PT cables in girders and distinguishing them from reinforcing bars, determining thickness of the element and reinforcement layout, etc. (12; 9; 13; 14) Despite GPR's many capabilities, it has limitations when it comes to identifying several deterioration types, such as vertical cracks or deterioration caused by freeze-thaw cycles. A comprehensive condition assessment of a bridge deck requires complementary use of multiple NDE techniques, together with gathering a reasonable amount of ground truth information combined with some laboratory testing. This chapter continues with a review of common deterioration mechanisms in concrete bridge decks followed by a review of various NDE methods used for condition assessment of such deteriorations. The chapter concludes with a brief discussion on GPR. The electromagnetic principles governing GPR and different ways of post-processing GPR data are discussed in detail in the next chapter.

2.2 Common Deterioration Types of Concrete Bridge Deck

Bridge decks carry increasing traffic loads and are exposed to environmental impacts: direct heating by the sun, snow and rain, alternate freezing-thawing often in the presence of deicing chemicals, acidic rains, etc. Global warming has worsened environmental impacts on concrete in various geographical areas. Natural disasters, such as Super Strom Sandy and Hurricane Harvey, continue to damage highway transportation infrastructure. As a result of Super Storm Sandy, more than 500 miles of roads were severely damaged (15). A bridge along the Highway 96 in Houston collapsed during Hurricane Harvey (16). Given the high average age of the U.S. bridges, many of them were not initially designed to withstand the current traffic loads and environmental impacts.

Deterioration of the deck is the most common reason for classifying a bridge as structurally deficient (Figure 2-1) (17). Delamination, corrosion, vertical cracks, expansion caused by the alkali-silica reaction, scaling due to freeze-thaw cycles, creep, and fatigue are some deterioration mechanisms affecting concrete bridge decks. Quite often, these deterioration mechanisms are interconnected with one giving rise to another. The second Strategic Research Highway Program (SHRP 2) concluded that among all the different deterioration phenomena occurring in concrete bridge decks, four deterioration mechanisms are of the highest importance to bridge engineers: reinforcement corrosion, deck delamination, vertical cracking, and concrete degradation (14). Each of the aforementioned defects is explained in the following section.

Figure 2-1. Deck deterioration.

2.2.1 Reinforcement Corrosion

In 1993, the Strategic Highway Research Program (SHRP) reported that roughly 40% of the expenditure on repair/retrofit of highway bridges was ascribed to reinforcing steel corrosion (18).

In its intended state, concrete is an ideal environment to protect embedded steel reinforcement given its alkalinity. In the absence of moisture and chloride ions, the iron oxides, Fe_3O_4 and Fe_2O_3, or their hydroxides form a protective layer around the reinforcement steel called a *passive film* (19). However, given the porous nature of concrete, (i) penetration of CO_2 causes carbonation and neutralization of paste thus reducing its protective properties, and (ii) intrusion of solutions of chloride ions from deicing salts and ambient when reaching the steel reinforcement, damage the passive film and trigger corrosion. Since the corrosion products occupy a larger volume than the original steel, they create internal stresses in concrete inducing cracking, delamination, spalling which combined with the loss of reinforcing steel cross-section, result in an eventual reduction of structural capacity (Figure 2-2).

Figure 2-2. Extensive cracks caused by the corrosion of reinforcing steel.

In cold climates, such as northeast of the United States, the chloride ions are present because of the deicing salts. In an arid climate, corrosion could still be an issue due to the high concentration of chloride salts in the soil. In coastal areas, chlorides may exist in soil, which is especially prevalent in splash zones. Acidic rains and sea spray may be another source of chloride ions.

The process of metal corrosion in concrete is described in ACI 222 R (19) and is schematically shown in Figure 2-3.

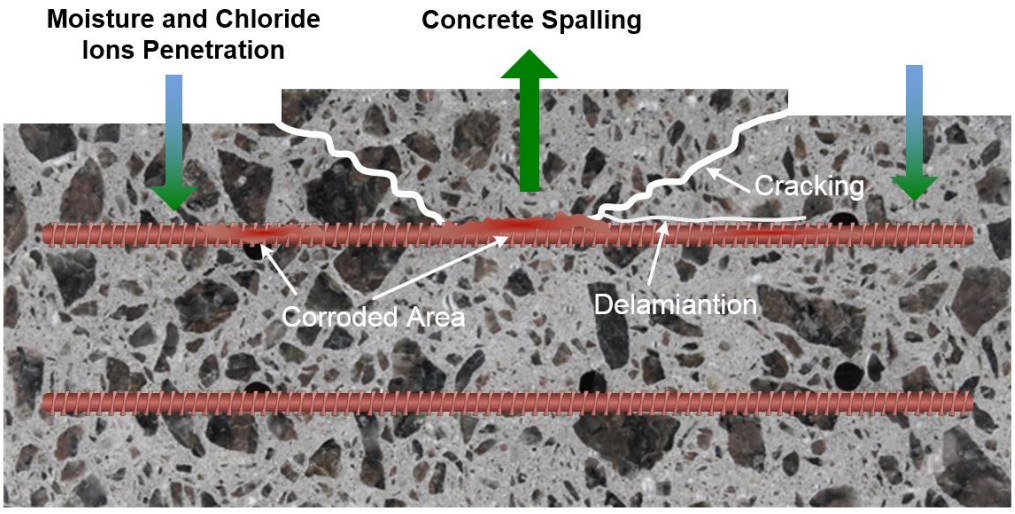

Figure 2-3. Corrosion Process.

2.2.2 Delamination

American Concrete Institute's ACI 116R report points to corrosion of reinforcing steel as the primary cause of delamination (20). As the corrosion products take up a larger volume than the original steel, they create internal stresses inside the concrete at the reinforcement level. These internal stresses result in delamination and debonding. Figure 2-4 depicts delamination caused by corrosion of reinforcing steel and formation of growing clusters of halite (NaCl). Delamination may also occur due to repeated loading. Other mechanisms causing delamination are horizontal cold joints and subsidence of a portion of placement while concrete is still plastic.

The NDE techniques that have demonstrated the optimal potential for delamination detection are impact echo, ultrasonic tomography, infrared thermography, and under specific circumstances, ground penetrating radar. As mentioned earlier, chain dragging and hammer sounding have been the most common inspection techniques used by state DOTs and other bridge owners for the detection of delamination in concrete bridge decks.

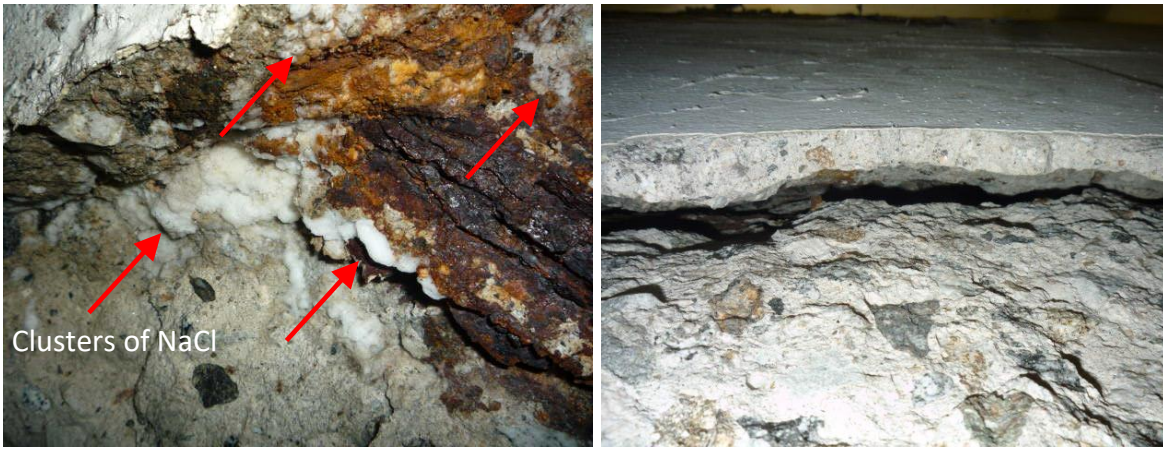

Figure 2-4. Delamination caused by corrosion.

Often, delamination is not visible on the surface and, therefore, may suddenly turn into spalls with little to no prior warning. This points squarely to the importance of preventive condition evaluation. Examples of delamination in cores extracted from a highway bridge deck are provided in Figure 2-5.

Figure 2-5. Delamination in cores extracted from a bridge deck in Virginia.

2.2.3 Vertical Cracks

Different mechanisms may create vertically oriented cracks in concrete. These cracks may occur at an early age in plastic concrete, or later on, in hardened concrete (21). The most common mechanisms causing vertical cracks in bridge decks are summarized below.

(a) Early-age cracks in plastic concrete are typically caused by:

- Plastic shrinkage as a result of moisture evaporation and absorption of water by dry aggregates; and
- Plastic settlement as a result of subsidence of fresh concrete over reinforcing steel or load transfer devices.

(b) Cracks in hardened concrete may result from several mechanisms, among them:

- Restrained volume changes of concrete (triggered by moisture content reduction and temperature changes) causing stresses exceeding the tensile strength of concrete – this type of cracks, especially in the transverse direction, predominantly develops during the first seven days, however, continues growing at a lower magnitude in later ages as well. This is the most commonly observed type of crack in reinforced concrete decks;
- Structural movements resulting in shear strains and stresses exceeding concrete capacity;
- Over and under-stressing of post-tensioned steel cables;
- Design and detailing of decks; and
- Deleterious processes in concrete.

2.2.4 Concrete Degradation

Various physical and chemical mechanisms may cause degradation of concrete structural and functional performance; among them are corrosion, alkali-silica reaction, alternate freezing and thawing, alternate wetting and drying, and others.

Investigation of concrete condition often times requires an evaluation of concrete at microscopic levels through petrographic examination and electronic scanning microscopy, etc. Figure 2-6 depicts ASR and plastic shrinkage cracking.

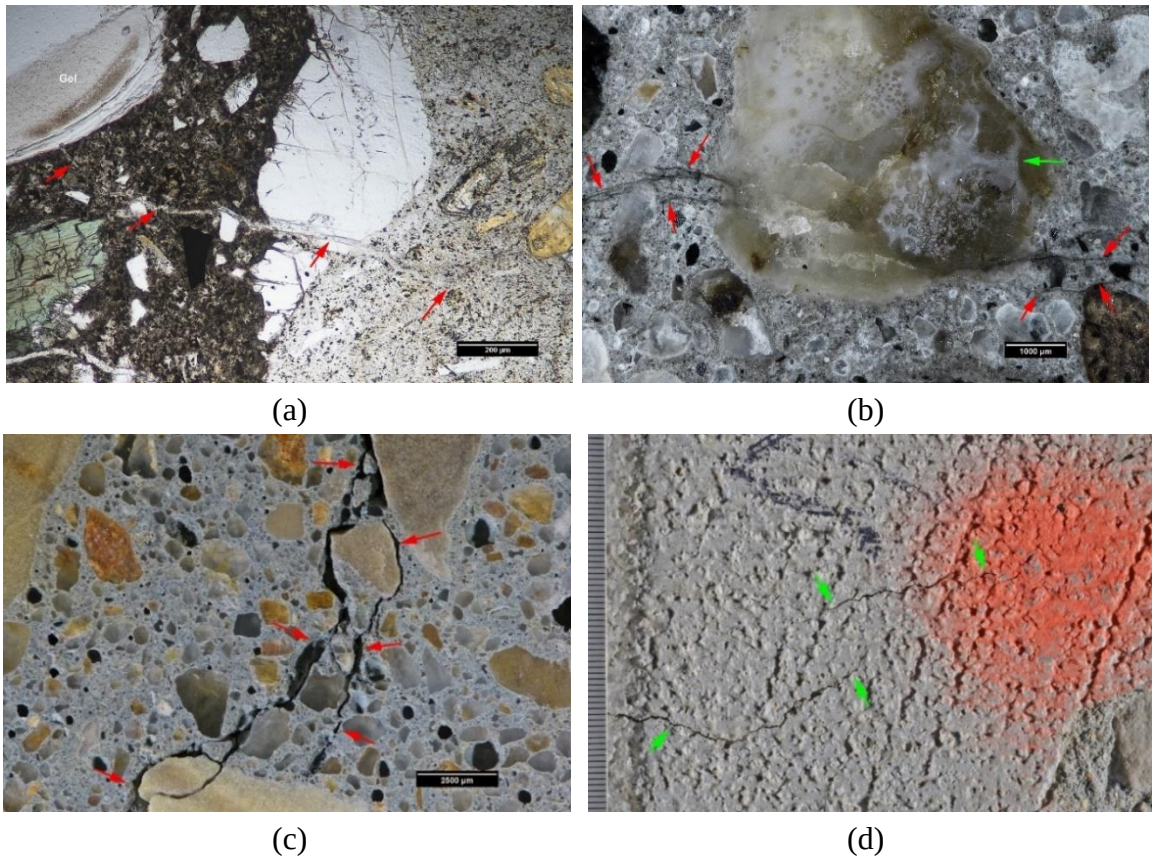

(a) (b)

(c) (d)

Figure 2-6. (a, b) ASR, (c, d) plastic shrinkage cracking. (Photos courtesy of Dr. David Rothstein, DRP)

2.3 NDE Methods for Bridge Deck Inspection

The most promising and most commonly used NDE technologies for condition assessment of bridge decks are reviewed in this section and compared with GPR.

2.3.1 Impact Echo (IE)

Impact echo is a commonly used NDE method to evaluate concrete and reinforced concrete elements for discontinuities and delamination. Impact echo is used to determine the depth and extent of flaws, such as porous areas, coarse horizontal cracks, delamination, and coarse voids, and to determine the thickness of an element. This technique is based on stress wave propagation. During an IE test, the surface of the deck is impacted using an

impactor to generate stress waves. The frequency of the generated wave is dependent on the characteristics of the impactor. As a rule of thumb, smaller impactors generate higher frequency waves, providing a higher near surface resolution and lower penetration depth. When stress waves propagating in a solid medium reach an interface with a different material, a portion of the incident wave is transmitted through the second medium, and another part is reflected back to the surface. The amplitude of the reflected wave is a function of the acoustic impedance gradient between the two media. The signal is then analyzed in the frequency domain using fast Fourier transform (FFT). The peak frequency in the response spectrum, also known as return frequency, gives the depth of the reflector, which could be possible delamination or an external boundary, using:

$$d = \beta \frac{V_p}{f} \tag{2-1}$$

where V_p is P-wave velocity, β is the shape factor and f is the return frequency (22).

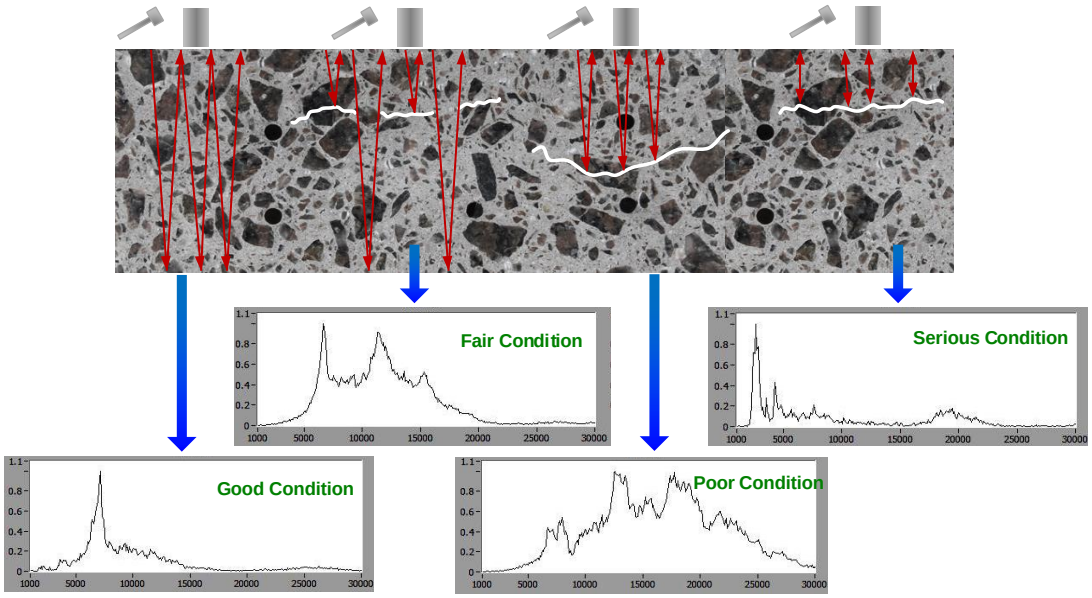

Figure 2-7. Impact echo evaluation of various degrees of deterioration.

Impact echo testing is performed in accordance with the ASTM C1383-15 “Standard Test Method for Measuring the P-Wave Speed and the Thickness of Concrete Plates Using the Impact-Echo Method” (23).

If the delamination is corrosion-induced and fully developed, impact echo and GPR condition maps correlate well. However, if the delaminations are caused by repetitive loading and fatigue, GPR will not be able to detect them as the electromagnetic properties of concrete are not affected by physical loading (24). By the same token, at early stages of corrosion-induced delamination, the attenuation maps and impact echo maps do not necessarily correlate, as it takes longer for delamination to fully develop and alter the response spectrum.

2.3.2 Ultrasonic Tomography / Ultrasonic Pulse Echo

When assessing a bridge deck, the deck is often accessible for testing only from one side. Therefore, the use of test methods, such as ultrasonic pulse velocity (UPV) which requires access to both sides of the element is not practical. This problem can be resolved using an array of dry point contact (DPC) shear wave transducers (25). Shear wave tomography can be used for thickness measurement, detection of delamination and voids in the slab, detection of voids in grouted ducts for post-tensioned tendons, etc.

One of the best-known tomographers is MIRA. The device has up to 12 channels, each consisting of four DPC transducers. For a given scan (shot), each channel acts as a transmitter, while the other eleven channels act as receivers. Therefore, one shot consists of 264 A-scans. The A-scans are then used in real time to create a 2D image of the cross-

section. During post-processing, a three-dimensional representation of the element can be reconstructed should the survey be performed on a fine enough grid.

Schematics, testing, and maps related to ultrasonic tomography are presented in Figure 2-8 through Figure 2-10.

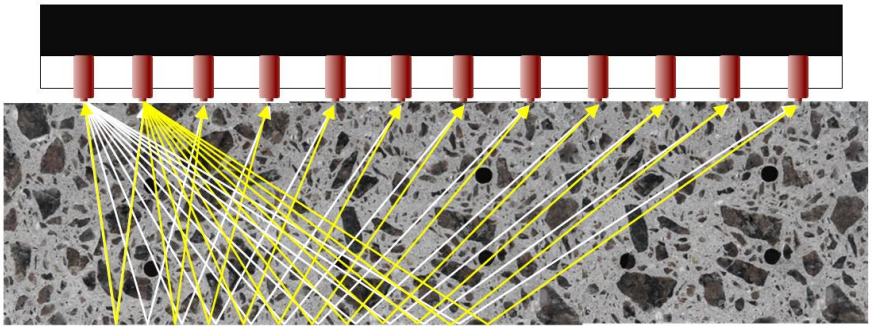

Figure 2-8. Shear wave tomography schematic.

Figure 2-9. Shear wave tomography application.

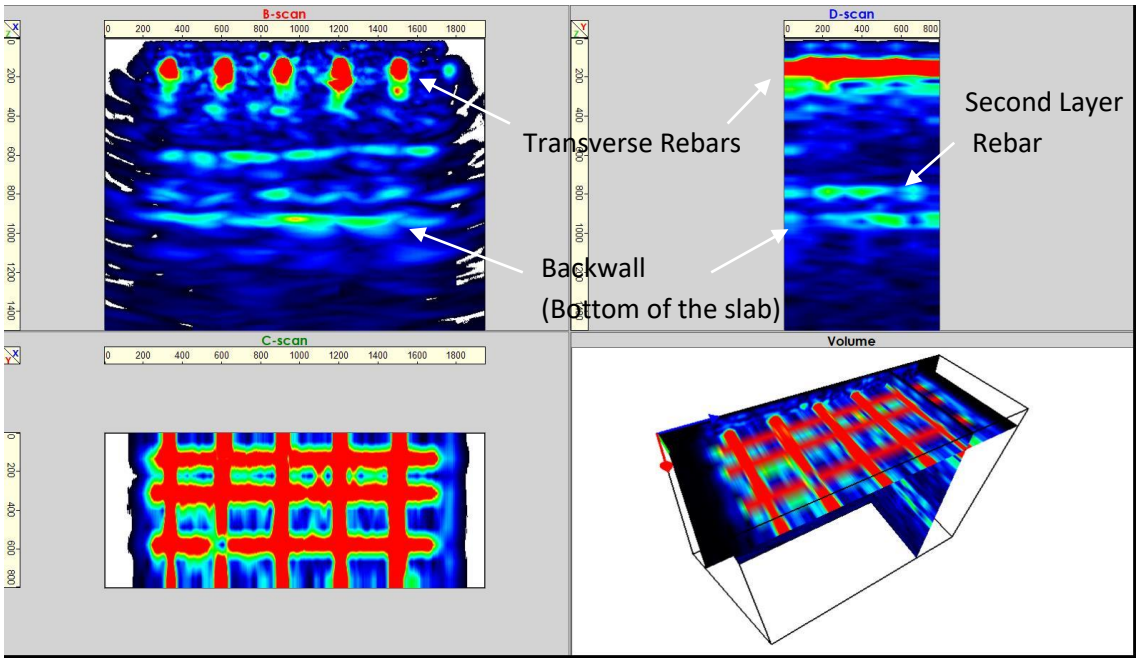

Figure 2-10. Shear wave tomography maps.

Much like impact echo, the areas with fully developed corrosion-induced delamination can be detected by both shear wave tomography and GPR. Otherwise, the deteriorated regions identified by the two methods may not necessarily correlate.

2.3.3 Electrical Surface Resistivity

Electrical resistivity (ER) measurements provide insight into whether reinforcing steel in concrete is susceptible to corrosion. The decrease in surface electrical resistivity of concrete is known to be consistent with the degrading of protective properties of concrete toward reinforcing steel, which increases the potential for corrosion. With the increase of permeability and volume of interconnected pores, saturation of concrete subject to water intrusion increases, and its electrical resistivity decreases accordingly. The presence of dissolved Cl^- increases electrical conductivity as well.

One of the most commonly utilized tools for resistivity measurements is the four-point Wenner probe devised by Frank Wenner at NIST (Bureau of Standards at the time). The Wenner probe has four equally spaced electrodes (Figure 2-11). An alternating current is applied to the two outer electrodes, and the voltage is measured between the two inner probes. Using the applied current and measured voltage, the resistivity is then calculated as follows:

$$\rho = \frac{2\pi dV}{I} \tag{2-2}$$

where ρ is resistivity in Ω.m, d is electrode separation in m, V is voltage in V, and I is current in A.

The inverse of the electrical resistivity is the electrical conductivity σ [S/m], which is one of the material properties affecting the electromagnetic wave propagation.

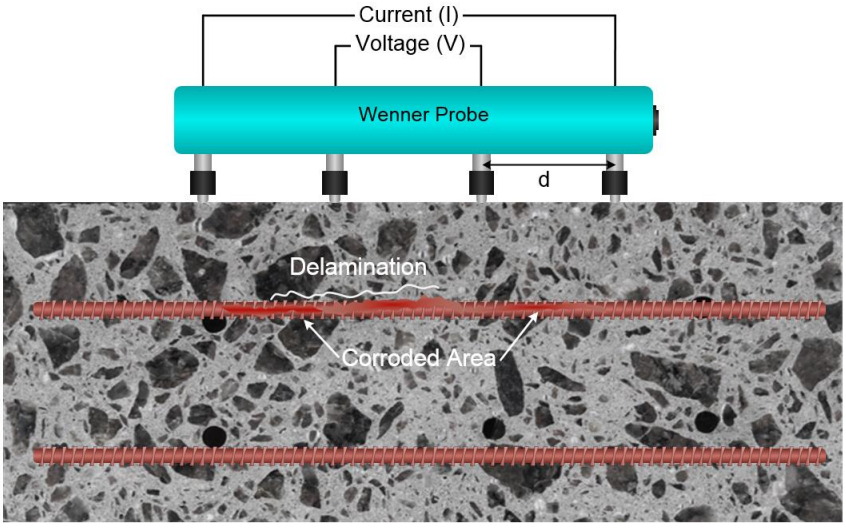

Figure 2-11. Electrical resistivity measurement.

It is generally accepted in the literature that resistivity values less than 10 kΩ.cm are indicative of anticipated high corrosion rates. The relationship between the electrical resistivity and the corrosion rate per ACI 222R-01 is provided in Table 2-1 (19).

Table 2-1
The relationship between concrete surface resistivity and corrosion rates (ACI 222R-01)

Resistivity [kΩ×cm]	**Corrosion Rate**
< 5	Very high
5 – 10	High
10 – 20	Moderate – low
> 20	low

Currently, there is no ASTM standard specifically for testing electrical surface resistivity of reinforced concrete elements. ASTM G57 is the standard test method for measuring electrical resistivity of soil using a four-electrode Wenner probe, *"Standard Test Method for Field Measurement of Soil Resistivity Using the Wenner Four-Electrode Method"* (26). In the absence of an ASTM standard procedure, the test is performed per the guidelines of ACI 228.2R-13, *"Report on Nondestructive Test Methods for Evaluation of Concrete in Structures"* (25). Electrical resistivity testing on a slab is shown in Figure 2-12.

Contour maps based on electrical resistivity do not contain information about whether the reinforcing steel is actively corroding (27). Half-cell potential measurements can shed light on the likelihood of corrosion activity.

The deteriorated areas as detected by GPR attenuation and surface resistivity are both characterized by the corrosive environment. However, the GPR attenuation is a function of corrosiveness within the bulk of concrete in which the EM waves travel, while the Wenner probe measures the resistivity above the top rebar.

Figure 2-12. Electrical Resistivity measurements using a Wenner probe.

2.3.4 Half-Cell Potential (HCP)

In its recommendations on strategies for developing repair procedures for reinforced concrete structures damaged by corrosion, RILEM (French acronym for The International Union of Laboratories and Experts in Construction Materials, Systems and Structures) submits that the engineers need to first have a thorough understanding of (a) causation, (b) extent of damage, (c) estimate of damage progression with time, and (d) adverse effect of the damage on structural integrity and serviceability (28). HCP is a well-established electrochemical method which is widely used to determine the extent of the area undergoing corrosion in reinforced concrete elements by delineating areas where there is a high probability of active corrosion.

The testing involves measuring the electrical potential (or the voltage difference) between a standard reference electrode, usually copper-copper sulfate, and the reinforcing steel. The Cu-$CuSO_4$ reference electrode (CSE) is a copper rod placed inside a copper sulfate solution or a silver rod in a saturated potassium chloride solution. The electrical potential between the reference electrode and the rebar is measured using a high impedance voltmeter.

A pre-wetted sponge soaked in a liquid detergent solution is used to bridge between the reference electrode and the surface of the concrete. The results serve as an indication of the probability of active corrosion in the surveyed area. The schematic of the HCP testing is illustrated in Figure 2-13 and Figure 2-14.

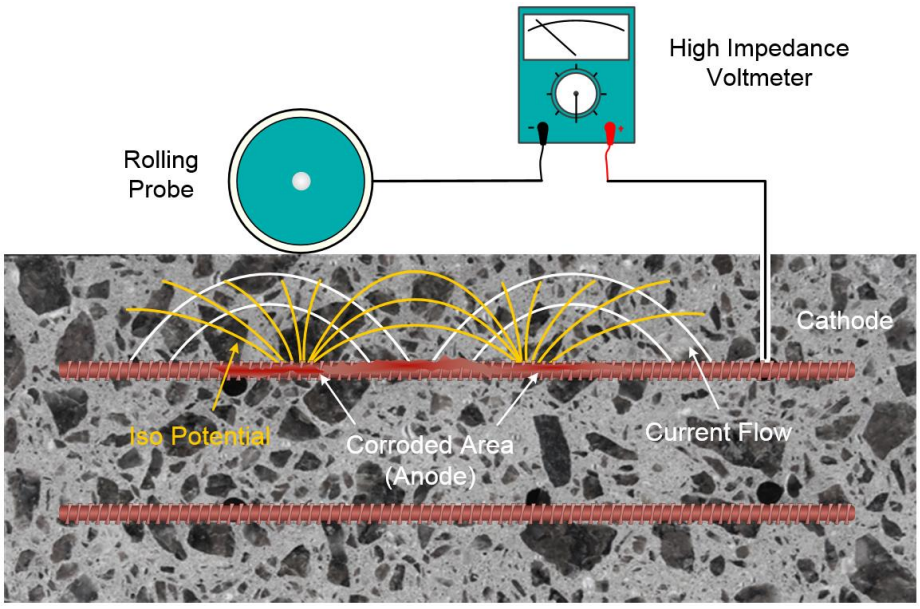

Figure 2-13. Half-cell potential measurement.

HCP testing is performed in accordance with the ASTM C876-15 *"Standard Test Method for Half-Cell Potentials of Uncoated Reinforcing Steel in Concrete"* (29). Per this standard, there are three threshold values, which need to be considered for analyzing the HCP measurements:

- Potentials less than -350 mV (more negative) are indicative of a greater than 90% probability of active corrosion;
- Potentials within the range of -200 mV and -350 mV indicate that corrosion activity in that area is uncertain;
- Potentials greater than -200 mV (more positive) are indicative of a greater than 90% probability of no active corrosion.

RILEM suggests that these limits need to be treated with caution as there are other influencing factors overlooked by the ASTM and therefore, these threshold values may need to be adjusted on a case-by-case basis. A good approach for adjusting ASTM C876 limits is by determining acid soluble chlorides content in concrete per ASTM C1152-04, *"Standard Test Method for Acid-Soluble Chloride in Mortar and Concrete"*. Comparing the content of acid-soluble chlorides in concrete with the threshold values triggering corrosion suggested by ACI 222R-01 is a valuable tool for adjusting the ASTM limits for HCP measurements (19).

HCP contour maps do not provide quantitative information regarding the rate of corrosion. Electrical resistivity maps complement HCP information, and ideally, the two methods should be used in tandem.

HCP testing on a typical bridge deck using a Proceq rolling probe is shown in Figure 2-15.

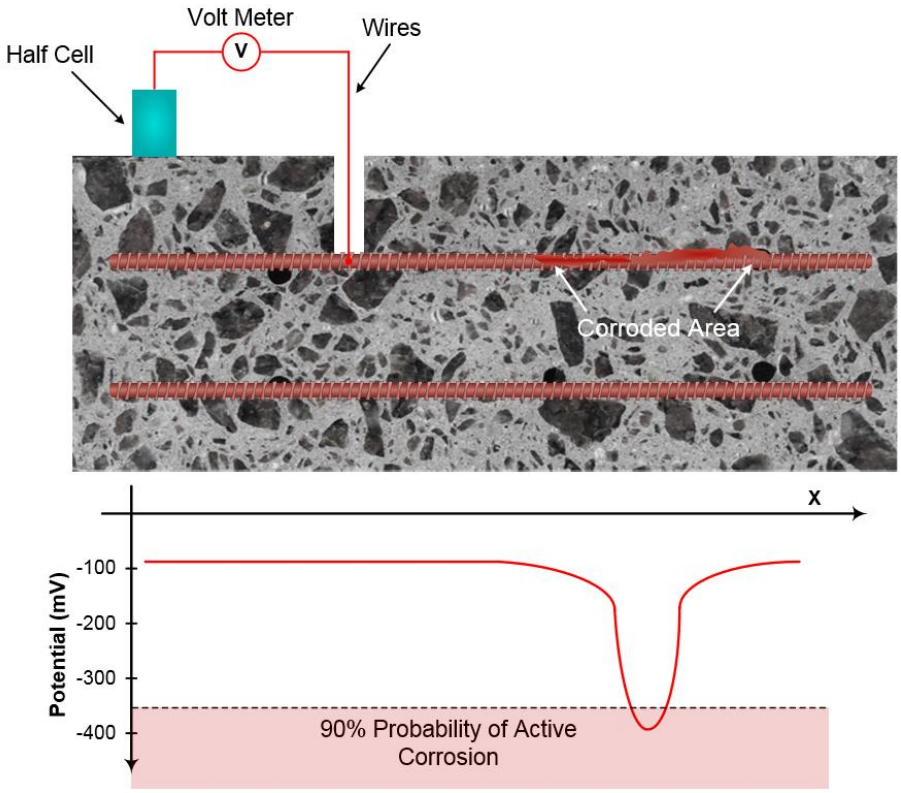

Figure 2-14. Half-cell potential principle (ASTM C876).

Figure 2-15. HCP testing using a Proceq probe.

2.3.5 Ultrasonic Surface Waves (USW)

USW method is used to measure the average elastic modulus of pavements and concrete decks. Unlike impact echo, where the response to an impact generated by an impactor is recorded by a single receiver, for USW testing, two receivers record the response, predominantly to the passing Rayleigh waves. One receiver is closer to the impact source (near receiver), and one farther away from the impact source (far receiver). Figure 2-16 shows a widely used USW system known as PSPA (Portable Seismic Property Analyzer). For USW to detect an anomaly, the scatterer's size needs to be larger than the propagating wavelength. The surface wave phase velocity, V_R, is determined from the phase of the cross-power spectrum of signals at the two receiver locations. The average elastic modulus across the deck thickness is then calculated as follows (30):

$$E = 2(1+\nu)\left[\rho(1.13-.16\nu)V_R{}^2\right] \qquad (2\text{-}3)$$

Where ν is the concrete Poisson's ratio, and ρ is the density. The expression in the bracket on the right side is the shear modulus.

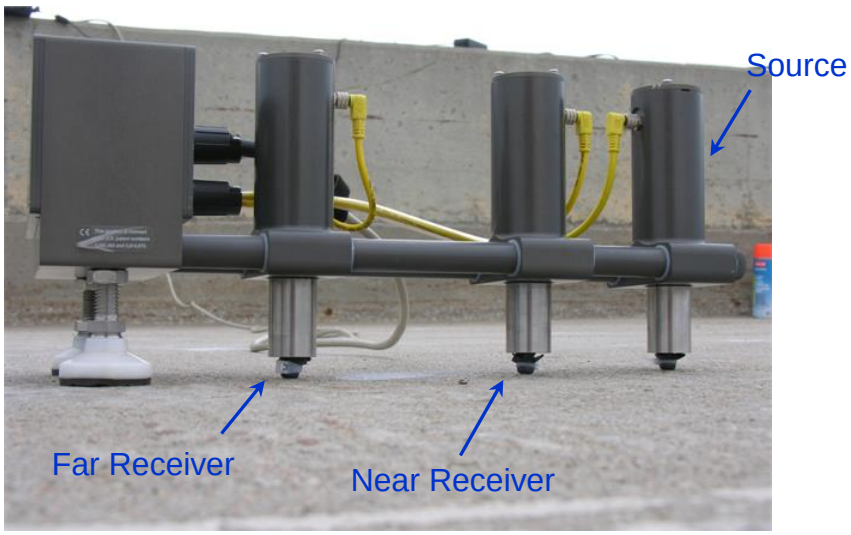

Figure 2-16. Portable seismic pavement analyzer (PSPA).

Since the USW method provides modulus, it is well suited to evaluate potential deterioration and modulus reduction caused by corrosion, delamination, cracks, and other causes.

2.3.6 Chain Dragging / Hammer Sounding

Chain dragging and hammer sounding are the most basic, yet the most commonly used NDE methods for detecting shallow delamination. In chain dragging, a steel chain is dragged along the surface of the deck. In hammer sounding, the surface is struck using a steel rod or hammer. These methods rely on the operator's experience in listening to the sound generated by the chains or a hammer: a good quality concrete generates a clear ringing sound while a delaminated region makes a dull and hollow sound. Despite its popularity, this method is dependent on the operator's skill and hearing ability. It is also incapable of detecting delamination that is not fully developed.

This testing is performed in accordance with procedure C of ASTM D4580M-12 "Standard Practice for Measuring Delamination in Concrete Bridge Decks by Sounding".

2.3.7 Ground Penetrating Radar (GPR)

Ground penetrating radar is a rapid, nondestructive technique used in a wide range of applications including evaluation of transportation infrastructure, geophysical investigations, mine detection, locating utilities, and archaeological investigations among others. The use of GPR for highway investigation dates back to 1985 when FHWA developed the first vehicle-mounted GPR (6).

Today, GPR is considered the most effective technique to detect and characterize the location and extent of corrosion-induced deterioration at the level of the top reinforcement mat in reinforced concrete bridge decks (8).

Traditionally, in order to assess the condition of a reinforced concrete bridge deck, the amplitudes of signals reflected from top reinforcement mat are picked from the B-scans and plotted in a contour map. Certain threshold levels are defined for each contour map indicating the deterioration level. Areas corresponding to high attenuation levels are identified as deteriorated. This practice is explained in more details in Chapter 3.

A typical GPR system consists of five components: an antenna, a data acquisition unit, a graphical user interface (GUI) for example a laptop or a tablet, a survey wheel, and a distance measuring instrument (DMI). The antenna is composed of two types of transducers: a signal transmitter and a receiver. Based on the transmitter/receiver configuration, GPR systems are classified as monostatic, bistatic, or multistatic. In a monostatic system, one antenna works as both transmitter and receiver. A bistatic system is one that transmitting and receiving units are set up at a known distance from one another even though they may be housed together in the same enclosure. This is the conventional type for commercial GPRs. Finally, when a radar system is comprised of at least three transmitter(s)/receiver(s), it is called a multistatic radar. A multistatic GPR has several receivers, and at least one transmitter unit.

From the coupling standpoint or the antennas' location with respect to the ground during deployment, GPR systems are either ground-coupled or air-coupled. Air-coupled systems (usually horn antennas) are suspended several inches above the ground. The recommended height for the GSSI 2 GHz horn antenna, for example, is 18 to 20 inches. These systems

allow for a higher speed of survey and can be used at the normal speed of traffic without any wear and tear that ground-coupled antennas suffer from. Ground-coupled systems, on the other hand, are launched while the antenna (usually bow-tie antenna) is in direct contact with the ground. In ground-coupled setups, the antenna must be within the range of one-tenth of the wavelength from the surface to produce optimal results (10). GPR surveys using ground-coupled systems must be conducted at lower speeds (such as walking speed). Air-coupled antennas are used to measure the thickness of pavement layers while ground-coupled antennas are preferred for condition assessment of bridge decks.

GPR is one of the leading technologies used to assess the deck condition concerning reinforcement corrosion and delamination/discontinuities in concrete induced by corrosion. GPR attenuation maps provide a qualitative assessment of the deck condition identifying potential delamination and corrosive environment. The presence of moisture, chloride ions, iron oxide, cracks, and water-filled delamination increases the attenuation of electromagnetic waves. The attenuation is low for a deck in good condition, whereas high attenuation is indicative of delamination or corrosive environment.

(a) (b)

Figure 2-17. (a) Ground-coupled GPR, (b) Air-coupled GPR.

Similar to other NDE methods, GPR has certain limitations. For example, GPR is not suitable for evaluation of bridges where conductive aggregates, such as slags, have been used. Moreover, GPR surveys cannot directly detect delamination or cracks unless they are filled with water to produce a high dielectric mismatch. It is always advised to validate the results of GPR using other NDE test methods or via ground truth information obtained by coring. For example, the presence of corrosion needs to be confirmed using the half-cell potential survey.

There are two ASTM standards governing GPR application:

- ASTM D6087 - 08 *"Standard Test Method for Evaluating Asphalt-Covered Concrete Bridge Decks Using Ground Penetrating Radar"* provides the general procedures for investigating concrete bridge decks whether they are overlaid with asphalt or not (31).
- ASTM D6432 - 11 *"Standard Guide for Using the Surface Ground Penetrating Radar Method for Subsurface Investigation"* is a broader standard for subsurface investigation using GPR and does not address field procedures or data interpretation (32).

2.3.7.1 Multi-Channel Antenna versus GPR Array: Key Distinctions

The multistatic GPR antennas can be configured into *multi-channel* or *array* systems. Both configurations increase the rate of the survey as they can cover larger swathes in far shorter time periods compared to the conventional bistatic GPR systems. Therefore, the use of arrays or multi-channel antennas in bridge deck evaluation significantly reduces traffic interruption. Because they produce higher density data, these antennas can generate more

accurate condition maps. Array systems provide more versatility in how a person might choose to transmit/receive data depending on the specific application or objective. Multi-channel systems with dual polarity enable the operator to more accurately interpret the linear targets which are not parallel or perpendicular to the survey path. Despite their many advantages, the GPR arrays and multi-channel GPR systems have not been adopted for bridge investigation on a large scale.

Multi-channel GPR antennas are often times mistakenly referred to as GPR arrays. However, there are clear distinctions between the two groups. GPR array systems allow the user to select among various transmitter and receiver combinations, e.g., T1 → R1, R2, R3; T2 → R1, R2, R3; T3 → R1, R2, R3; etc.). Any T element (or a transmitter) can be configured physically or virtually via a graphic user interface (GUI) so that its transmitted signal is picked up by any other R element (or a receiver) within the array (Figure 2-18).

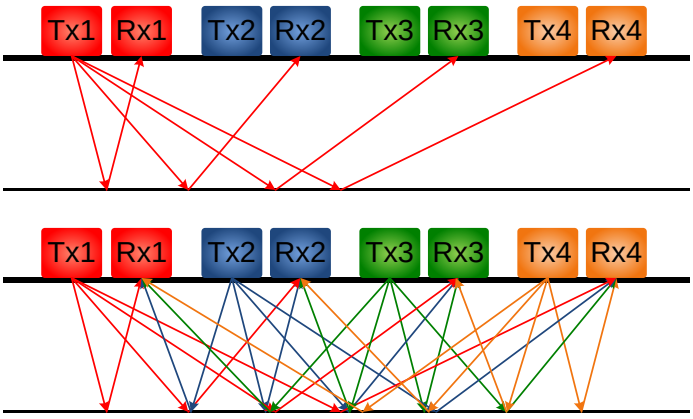

Figure 2-18. GPR array system.

A GPR array system manufactured by MALÅ is shown in Figure 2-19.

Figure 2-19. GPR array manufactured by MALÅ.

On the other hand, *multi-channel systems* house several usually dual-polarized antenna configurations for the purpose of maximizing spatial resolution and the quality of imaging. A multi-channel GPR system consists of a number of single-channel antennas housed together in a single unit (Figure 2-20). In such systems, each individual unit can only communicate as a T/R pair within its designated channel: channel 1 transmitter cannot generate a signal that can be received by any receiver other than that of channel 1, etc.

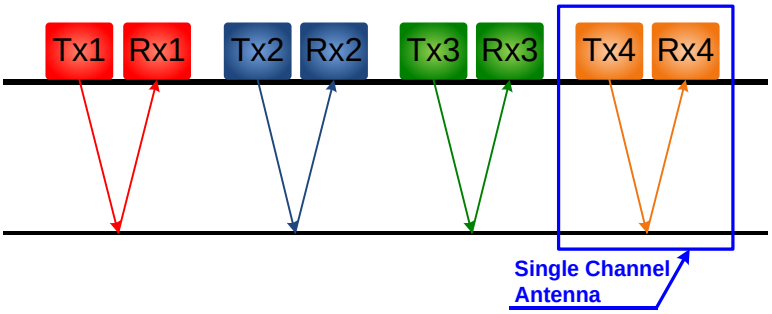

Figure 2-20. Multi-channel GPR system.

Hi-BrigHT manufactured by IDS is a multi-channel antenna.

Figure 2-21. Multi-channel GPR system (HiBrigHT) manufactured by IDS.

2.3.8 Summary of NDE Techniques for Bridge Deck Condition Assessment

Given their impact on service life and safety, four types of deterioration are the most crucial for bridge deck condition assessment: delamination, reinforcement corrosion, vertical cracks, and concrete degradation. As per the SHRP 2 report, there is not a single technology that is capable of detecting and characterizing all deterioration types (14). A summary of SHRP 2 findings regarding the capability of different NDE test methods for detecting the aforementioned deterioration types is presented in Table 2-2.

Table 2-2
NDE Technologies most suited to detect a given deterioration

Deterioration Type	NDE Technology
Delamination	impact echo, chain drag/hammer sounding, infrared thermography, and ground penetrating radar
Corrosion	half-cell potential, electrical resistivity, galvanostatic pulse measurement, and ground penetrating radar
Vertical Cracks	ultrasonic surface waves (USW)
Concrete Degradation	ultrasonic surface waves (USW), impact echo, and ground penetrating radar

Chapter 3. Basic Principles and GPR Practice in Bridge Deck Evaluation

3.1 Introduction

RADAR (RAdio Detection And Ranging) is a piece of electromagnetic-based equipment for detecting location, range, and speed of remote objects. The acronym radar was first used by the United States Navy during the Second World War (WWII) and shortly thereafter was widely accepted by the engineering community worldwide. The history of radar can be traced back to more than half a century earlier when the German physicist Heinrich Hertz discovered that radio waves are transmitted through some materials and reflected by some others.

Before WWII, scientists in several countries including Germany, the United Kingdom, the Soviet Union, France, Japan, and the United States were working on developing radar-related technologies. In 1904, German inventor Christian Hülsmeyer was the first to patent the use of electromagnetic reflections to detect the presence of metallic objects. His telemobiloscope was designed to avoid the collision of ships in foggy situations. The

electromagnetic wave reflections were not used to detect buried objects until Gotthelf Leimbach, and Heinrich Löwy patented the first such application in 1910 (11).

During the WWII, the radar capabilities were embraced by both the Allies and the Axis powers especially by the Royal Air Force (RAF) of the United Kingdom for their anti-aircraft defense systems. Throughout the war and particularly after the exchange of secret technologies between the U.S. and the U.K., the radar technology was further improved and developed closer to what is known as modern radar today. With the advent of computers in the second half of the 20th century, radar technology entered a new phase. Computer programs enabled researchers to perform data analysis and interpretation more efficiently. Today, radars are being used across various fields including military, aviation, marine, geology, geophysics, and construction.

Ground penetrating radar (GPR) is a special form of pulse radar that uses electromagnetic wave reflection to either locate objects or anomalies present in the body surveyed or measure the material properties of the subsurface. The first GPR experiment was conducted in Austria in 1929 by Walter Stern in an attempt to measure the depth of a glacier. The technology was generally ignored for decades until NASA's lunar program in the 1970s. In the last manned mission to the moon in 1972, Apollo 17 was equipped with a GPR system to study the electrical and geological properties of the moon's surface (33). Introduction of the first commercial GPR system by Geophysical Survey Systems, Inc. (GSSI) in 1971 brought the technology into a new phase and led to widespread use of GPR in various disciplines.

Currently, GPR is used as a nondestructive evaluation (NDE) tool for a wide range of purposes. In archeological investigations, GPR is used to locate buried archeological

features prior to excavation. In 2018, GPR was used to definitively determine whether there was a hidden chamber behind King Tut's 3000 years old tomb in Egypt (34). In geophysical sciences, it is used to study soils, bedrocks, groundwater, and glaciers. In forensic investigations, GPR is used by law enforcement authorities to locate buried evidence, weapons, and bodies. GPR is also being used to detect landmines in war zones. In the evaluation of transportation infrastructure which is the subject of the present study, GPR is used for condition assessment of bridge decks, tunnel linings, and pavement profiling.

Ground penetrating radar surveys are based on analysis of electromagnetic signals reflected from subsurface elements within a structure or the boundary elements. GPR antenna transmits electromagnetic pulses through the medium being surveyed. For each transmitted signal, the receiver records the reflected signal and the travel time. The condition maps are prepared based on the analysis of the signal amplitude and travel time. The principle of GPR is illustrated in Figure 3-1.

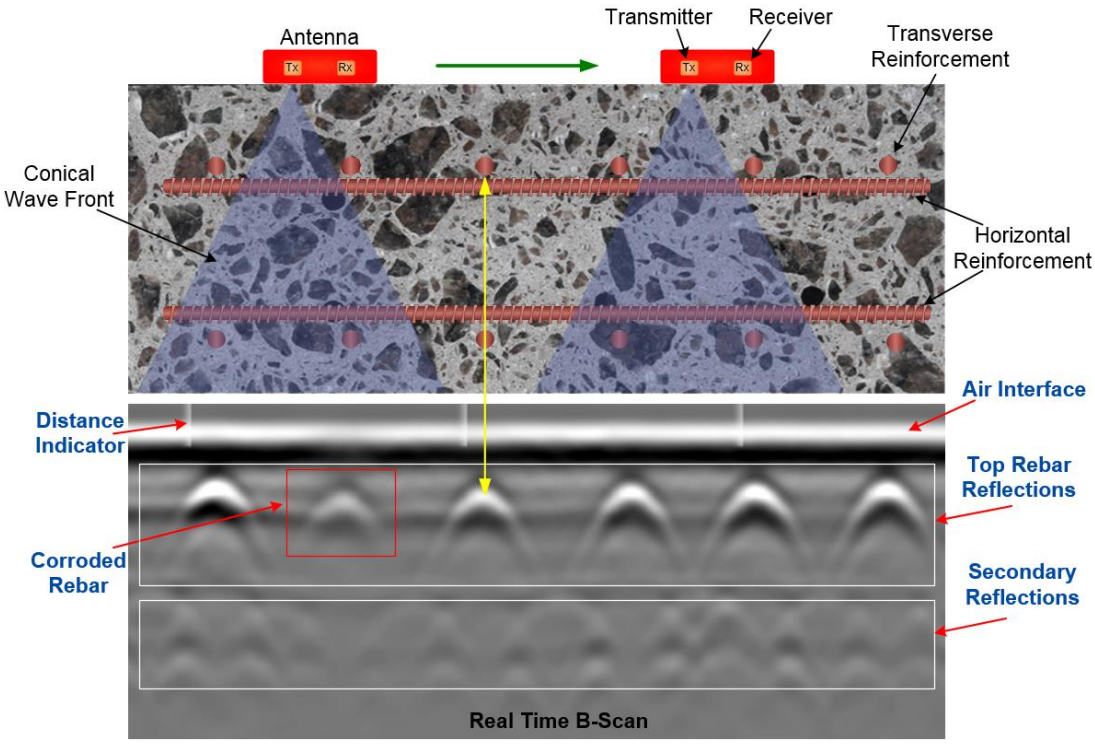

Figure 3-1. Principle of GPR.

In order to effectively analyze and interpret GPR data, it is paramount that one is familiar with the theory of electromagnetic wave propagation. In the following sections, basic terminology, and electromagnetic theory pertinent to GPR application is reviewed. These sections discuss basic principles governing ground penetrating radars and their applications. Maxwell equations are briefly discussed followed by a brief discussion of data analysis and interpretation of GPR surveys in bridge deck condition assessment.

3.2 Parameters influencing GPR Performance

Performance of a GPR system is dependent upon the electromagnetic properties of the evaluated object and the subsurface materials as well as certain antenna characteristics. These are discussed in the following sections.

3.2.1 Material properties influencing GPR performance

The material properties affecting the electromagnetic wave propagation in a medium include permittivity, permeability, and conductivity. Each is briefly discussed here in this section.

Permittivity is a measure of the material resistance against formation of an *electrical* field within the medium in the presence of an external electrical field, while permeability is a measure of the material's ability to support the formation of a *magnetic* field inside the medium. Conductivity, which is the inverse of electrical resistivity, is a measure of the material's ability to conduct electricity.

Both permittivity and permeability are required to characterize the electromagnetic wave propagation in a medium. However, the permeability of nonmagnetic materials is very close to the permeability of free space. Therefore, for nonmagnetic materials, including concrete, the only permittivity needs to be determined to characterize EM wave propagation (35). Permittivity (ε) and permeability (μ) of free space are:

$\varepsilon_0 = 8.854\times10^{-12}$ *F/m*

$\mu_0 = 4\pi\times10^{-7}$ *H/m*

The complex permittivity of a material is a function of both dielectric and conductivity values. The real part describes the storage of energy, while the imaginary part represents the energy loss. For a lossless material, the imaginary part of the permittivity is zero. The complex permittivity as defined as below:

$$\varepsilon_c = \varepsilon' - j\varepsilon''$$
$$\varepsilon' = \varepsilon \qquad \varepsilon'' = \frac{\sigma}{\omega} \tag{3-1}$$

where ε is the dielectric constant, σ is the conductivity (in S/m), ω is the angular velocity of the wave (in rad/s), and $j = \sqrt{-1}$.

The real part of permittivity is an indication of the energy stored in the medium and the imaginary part indicates the energy loss due to dielectric effects. For high-frequency GPR applications, the conductions loss is much higher than the dielectric loss and therefore, concrete permittivity can be considered a real value.

Even though dielectric constant is typically frequency-dependent, the dielectric constant in concrete reaches a plateau at higher frequencies (36). Therefore, at GPR operating frequencies, i.e., hundreds of MHz to several GHz, concrete is a non-dispersive material meaning the dielectric constant does not change with frequency.

Conductivity may also be complex and frequency-dependent, but it is assumed that in the operating frequency range for GPR, σ is real and independent of the frequency and therefore not dispersive (37).

Permittivity and permeability of a medium are usually expressed as their ratio to ε_0 and μ_0 (for the free space) and are called relative permittivity/permeability:

$$\varepsilon_r = \frac{\varepsilon}{\varepsilon_0} \qquad \mu_r = \frac{\mu}{\mu_0} \tag{3-2}$$

The speed of light in the free space is calculated as follows using the permittivity and permeability values:

$$c_0 = \frac{1}{\sqrt{\mu_0 \varepsilon_0}} = 3 \times 10^8 m/s \tag{3-3}$$

The velocity of EM wave propagation in the medium is calculated as follows:

$$V = \frac{1}{\sqrt{\mu\varepsilon}} = \frac{c_0}{\sqrt{\mu_r \varepsilon_r}} \tag{3-4}$$

As mentioned earlier, the permeability of nonmagnetic materials such as concrete is very close to the permeability of free space (μ_r = 1). Therefore, from equation (3-4), it can be concluded that the propagation velocity in a medium only depends on the relative dielectric value.

$$V = \frac{c_0}{\sqrt{\varepsilon_r}} \tag{3-5}$$

Table 3-1 provides the approximate relative dielectric constant, conductivity, and the velocity of electromagnetic wave propagation for various materials. The relative dielectric varies from 1 for air to 81 for fresh water. For earth materials and concrete, the relative dielectric depends on the degree of water saturation. Since water has a very high dielectric, a higher amount of water saturation leads to a higher value of dielectric constant (Table 3-2).

Table 3-1
Approximate Electromagnetic Properties of Various Materials (ASTM D6432)

Material	ε_r	Pulse Velocity (m/Ns)	σ (mS/m)
Air	1	0.3	0
Fresh water	81	0.033	0.10 -30
Sea water	70	0.033	400
Sand (dry)	4 - 6	0.15 - 0.12	0.0001 - 1
Sand (saturated)	25	0.055	0.1 - 1
Silt (saturated)	10	0.095	1 - 10
Clay (saturated)	8 - 12	0.106 - 0.087	100 - 1000
Granite (dry)	5	0.134	0.00001
Limestone (dry)	7 - 9	0.113-0.1	0.000001
Quartz	4	0.15	-
Concrete	5 - 10	0.134-0.095	-
Asphalt	3 - 5	0.173-0.134	-
PVC, epoxy, polyesters	3	0.173	-

3.2.2 GPR center frequency (operating frequency)

In addition to the subsurface material properties, the penetration depth of electromagnetic waves is governed by the antenna's center frequency. Antennas with higher center frequencies have a smaller penetration depth, but produce B-scans with higher resolutions, whereas antennas with lower center frequencies attain a greater penetration depth and lower resolution. This is discussed further in 3.2.5.

The electromagnetic wavelength for an antenna with a center frequency of f and a subsurface material with a relative permittivity of ε_r is calculated as follows:

$$\lambda = \frac{V}{f} = \frac{c_0}{\sqrt{\varepsilon_r} \cdot f} \tag{3-6}$$

The area of the electromagnetic field close to the antenna, where the distance to the antenna is less than 1.5 λ, is called the near field region.

3.2.3 Loss Tangent and Wave Number

The energy dissipation in a lossy material, such as concrete, is quantified by the ratio of imaginary and real parts of the complex permittivity. This frequency-dependent ratio is called loss tangent:

$$\tan\delta = \frac{\varepsilon''}{\varepsilon'} = \frac{\sigma}{\omega\varepsilon} \tag{3-7}$$

As discussed, in a lossless material, such as air, the conductivity is zero.

The wave number is defined as the ratio of the angular frequency ($\omega=2\pi f$) and speed of EM waves in the subsurface:

$$k = \frac{\omega}{V} = \omega\sqrt{\mu\varepsilon} \tag{3-8}$$

The wavenumber is constant for a given subsurface material at a specific operating frequency of the antenna (11).

The complex wave number, k_c, is given by:

$$k_c = \beta - j\alpha = \omega\sqrt{\mu\left(\varepsilon - j\frac{\sigma}{\omega}\right)} \tag{3-9}$$

where β is the phase constant in *rad/m*, and α is the attenuation coefficient in *Np/m* (37).

3.2.4 Attenuation

Attenuation is a gradual loss of wave energy as it propagates through the medium. For electromagnetic waves, there are three different causes for attenuation (32):

(a) Electrical conductivity – which results in converting the EM energy to heat;

(b) Dielectric relaxation – which is caused by the imaginary part of the complex permittivity, and also leads to turning the EM energy to heat;

(c) Geometric scattering or the inverse square law – which causes the signal to be scattered due to inhomogeneity in the medium.

Dinh et al. suggest the following for the total attenuation at a given depth in a bridge deck (9):

$$A_{Total} = A_{Conductive\ Loss} + A_{Dielectric\ Loss} + A_{Geometric\ Loss} \tag{3-10}$$

Closed form equations for attenuation coefficient and phase constant can be determined by squaring both sides of equation (3-9). As can be seen below, α and β, attenuation coefficient and phase constant, are both functions of GPR frequency, dielectric constant, and electrical conductivity.

$$\alpha = \omega\sqrt{\frac{\mu\varepsilon}{2}\left[\sqrt{1+\left(\frac{\sigma}{\omega\varepsilon}\right)^2}-1\right]} \rightarrow \alpha = f(\omega,\varepsilon,\sigma) \tag{3-11}$$

$$\beta = \omega\sqrt{\frac{\mu\varepsilon}{2}\left[\sqrt{1+\left(\frac{\sigma}{\omega\varepsilon}\right)^2}+1\right]} \rightarrow \beta = g(\omega,\varepsilon,\sigma) \tag{3-12}$$

From equation (3-11), it can be seen that the attenuation coefficient increases with the frequency. This is why higher frequency antennas have smaller penetration depths as they have higher attenuation rate.

In low loss materials, such as concrete, conductivity is much smaller than the frequency multiplied by dielectric constant ($\frac{\sigma}{\varepsilon\omega} << 1$) (38). Therefore, using equation (3-12) and the binomial expansion of $\left(1+\left(\frac{\sigma}{\omega\varepsilon}\right)^2\right)^{1/2}$, the attenuation coefficient in concrete reduces to:

$$\alpha = \frac{\sigma}{2}\sqrt{\frac{\mu}{\varepsilon}} \tag{3-13}$$

Hence, signal attenuation in concrete is a function of its electrical properties: dielectric constant and electrical conductivity. As the electrical conductivity increases so does the attenuation, therefore the penetration depth decreases.

The penetration depth is the maximum depth that the signal can travel in a medium. It is defined as the inverse of the attenuation coefficient:

$$\delta = \frac{1}{\alpha} \tag{3-14}$$

Dry concrete and soil have lower electrical conductivity; therefore, the attenuation is lower, and the signal can travel deeper into the material. On the other hand, wet concrete and soil are more conductive and attenuate the signal more. Thus, signal penetration depth is reduced (Table 3-2).

The condition maps based on GPR signal attenuation are used for evaluation of bridge decks by locating deteriorated areas. Cracks and presence of moisture and chloride increase

signal attenuation. Attenuations higher than a certain threshold are then interpreted as an indication of deterioration. This is further discussed in 3.4.3.

3.2.5 Resolution

Another important parameter in GPR surveys especially for choosing the proper antenna frequency for a particular application is the resolution the antenna provides. Resolution is defined as the minimum distance between two reflectors which GPR can resolve. If the distance between the two objects is shorter than the antenna's resolution, the GPR cannot differentiate the two and instead detects them as a single object. The resolution applies to both vertical and horizontal directions.

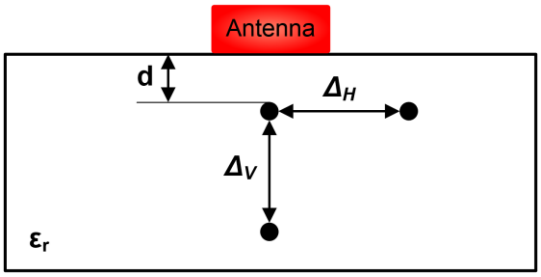

Figure 3-2. Vertical and Horizontal Resolution.

The minimum vertical resolution is approximated between a quarter to half of the central wavelength, where $\lambda/4$ is an optimistic estimation (39; 40). In general, as the antenna's center frequency increases, so does the vertical resolution, which corresponds to a smaller penetration depth. Therefore, in choosing the proper antenna for a given application, one needs to be mindful of the trade-off between the resolution and penetration depth.

Horizontal resolution is the minimum distance that must exist between two reflectors in the same horizontal plane for the GPR to resolve them as two different objects. There are

several formulas proposed in the literature for horizontal resolution. A common approximation is as follows (39):

$$\Delta_H = \frac{\lambda}{2} + \frac{2d}{\sqrt{\varepsilon_r + 1}} \quad (3\text{-}15)$$

Where λ is the center wavelength, ε_r is the relative permittivity of the subsurface, and d is the depth of the reflector (Figure 3-2).

The impacts of water content, dielectric constant and electrical conductivity of concrete, and the center frequency of the antenna on the electromagnetic (EM) wave propagation and the GPR performance are summarized in Table 3-2.

Table 3-2
Effect of different parameters on EM wave propagation and GPR performance (41)

Parameter	Effect
Water content ↗	ε ↗ - σ ↗ - V ↘
Water content ↘	ε ↘ - σ↘ - V ↗
σ ↗	Attenuation ↗ - Penetration depth ↘
σ ↘	Attenuation ↘ - Penetration depth ↗
Center frequency ↗	Penetration depth ↘ - Resolution ↗
Center frequency ↘	Penetration depth ↗ - Resolution ↘
Magnetic permeability	Negligible unless iron-oxide constituents are present.

3.2.6 Bandwidth

Bandwidth is the difference between the upper and the lower range of frequencies transmitted by an antenna. For commercial GPR antennas, the ratio of the center frequency to the bandwidth is approximately 1 (6). For example, a 1.6 GHz antenna transmits signals with the frequencies ranging from 800 MHz to 2.4 GHz, creating a bandwidth of 1.6 GHz.

Because of this wide range of operating frequencies, ground penetrating radars are referred to as ultra-wideband (UWB) radars.

3.3 Maxwell's Equations

Electromagnetic wave propagation through a homogenous medium is described by a set of partial differential equations known as Maxwell's equations, named after the Scottish physicist James Clerk Maxwell. Maxwell's equations, along with constitutive equations, define the electric and magnetic fields at any given location. These equations relate the electromagnetic field at a given point to the electromagnetic source and the electrical properties of the medium.

$$\nabla \times \mathbf{E} = -\frac{\partial \mathbf{B}}{\partial t} \quad \text{(a)}$$
$$\nabla \times \mathbf{H} = \mathbf{J} + \frac{\partial \mathbf{D}}{\partial t} \quad \text{(b)}$$
$$\nabla . \mathbf{D} = \rho \quad \text{(c)} \qquad (3\text{-}16)$$
$$\nabla . \mathbf{B} = 0 \quad \text{(d)}$$

Where

E = electrical field intensity (V/m),

H = magnetic field intensity (A/m),

B = magnetic flux density (Wb/m^2),

D = electrical flux density (C/m^2),

J = electric current density (A/m^2), and

ρ = volume charge density (C/m^3).

The equation (a) is known as *Faraday's law of induction*, equation (b) is known as *Ampère's law*, and equations (c) and (d) are called *Gauss' laws* for electric and magnetic fields, respectively.

For a homogenous isotropic material, the field quantities are related to material properties of the medium via constitutive relations (3-17a) and Ohm's law (3-17b):

$$\begin{aligned} &\mathbf{D} = \varepsilon_c \mathbf{E} && \text{(a)} \\ &\mathbf{B} = \mu_c \mathbf{E} \\ &\mathbf{J} = \sigma . \mathbf{E} && \text{(b)} \end{aligned} \qquad \text{(3-17)}$$

Where ε_c, μ_c, and σ are the complex permittivity (in *F/m*), complex permeability (in *H/m*), and electrical conductivity, respectively. The EM constitutive equations are analogous to Hooke's and the stress-strain constitutive equations in mechanical engineering (37).

For a source-free medium where no current or charges are flowing, the Maxwell's equations reduce to a single field equation called the wave equation. The one-dimensional wave equation for the electric field is as follows (37):

$$\left(\frac{\partial^2}{\partial z^2} - \frac{1}{c^2} \frac{\partial^2}{\partial t^2} \right) \mathbf{E(z, t)} = 0 \qquad \text{(3-18)}$$

Assuming harmonic time variations, $e^{j\omega t}$, the solution to **E(z)** is given by a linear combination of two waves propagating in the positive and negative directions along the z-axis. The $\mathbf{E_{0+}}$ and $\mathbf{E_{0-}}$ are called forward and backward electric fields, respectively.

$$\mathbf{E}(z) = \mathbf{E}_{0+} e^{-jk_c z} + \mathbf{E}_{0-} e^{+jk_c z} \qquad \text{(3-19)}$$

where k_c is the complex wave number explained earlier in Section 3.2.3.

Including the time variation $e^{j\omega t}$, the forward moving electrical field becomes:

$$\mathbf{E}(z,t) = \mathbf{E}_{0+} e^{j(\omega t - k_c z)} \tag{3-20}$$

Further details about the theory of electromagnetic wave propagation can be found in Electromagnetic Waves and Antennas (37) and Ground Penetrating Radar (11).

3.3.1 EM Wave Reflection and Transmission in A Planar Multi-Layer Medium

For planar multi-layer media, such as overlaid bridge decks, the reflection (ρ) and transmission coefficients (τ) are defined using Fresnel equations as follows (37):

$$\rho_i = \frac{\sqrt{\varepsilon_{r,i}} - \sqrt{\varepsilon_{r,i+1}}}{\sqrt{\varepsilon_{r,i}} + \sqrt{\varepsilon_{r,i+1}}} \quad \text{(a)}$$

$$\tau_i = \frac{2\sqrt{\varepsilon_{r,i}}}{\sqrt{\varepsilon_{r,i}} + \sqrt{\varepsilon_{r,i+1}}} = 1 + \rho_i \quad \text{(b)} \tag{3-21}$$

The reflection coefficient is the ratio of amplitudes of reflected and incident waves. The transmission coefficient is the ratio of transmitted and incident wave amplitudes. According to equation (3-21), if the contrast between the dielectric constants of two adjacent layers is relatively small, the reflection from the interface will be negligible. Figure 3-3 illustrates the reflection and transmission in a multilayer system.

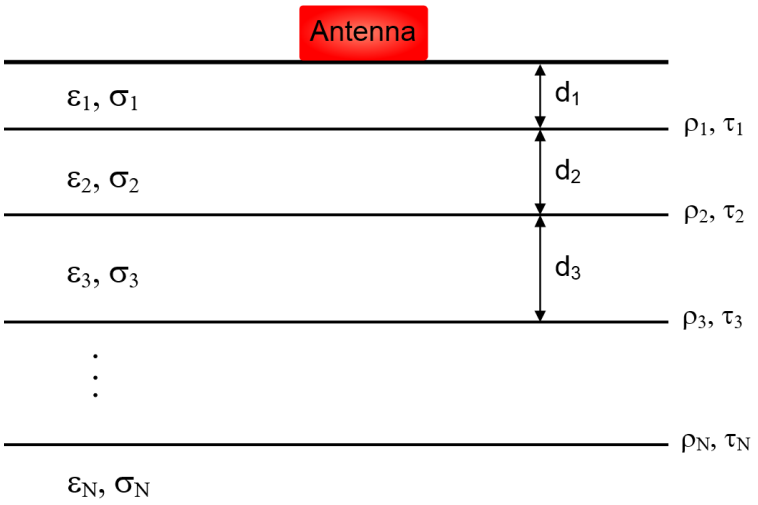

Figure 3-3. Reflection and transmission coefficients in a multilayer system.

The importance of reflection coefficients with regards to the GPR data analysis and interpretation is discussed further in 3.4.2.

3.4 GPR Signal Analysis and Interpretation

GPR survey results have traditionally been analyzed in the time domain. After adjustments and corrections for scattering loss, the reflection amplitudes from the top reinforcing bars are plotted on a contour map. Areas with high attenuation are characterized as deteriorated, or as having a high propensity for supporting corrosion activity.

Much like impact echo, GPR data can also be post-processed in the frequency domain. The dominant frequency can provide information as to the condition of the deck.

Time domain and time-frequency analysis methods for post-processing GPR survey data are discussed in the following sections.

3.4.1 Time Domain Signal Analysis

The traditional approach for post-processing GPR data has been based on the analysis of reflection amplitudes in the time domain. ASTM D6087 discusses two main methods for GPR data processing, both involving evaluating the amplitudes in the time domain:

(a) Deterioration Measurements at Top Reinforcing Steel using the Bottom of the Deck Reflection Attenuation

(b) Deterioration Measurements at or above Top Reinforcing Steel using the Top Reinforcing Reflection Attenuation

In the first approach (data processing using the attenuation at the bottom of the deck), the ratio of the maximum amplitude at the bottom of the deck, $V_{b,max}$, to the reflection amplitude at the surface of the deck, V_s, is calculated.

- If $V_{b,max} / V_s < 0.0264$, this method will not produce reliable results and alternative data processing techniques need to be used.
- If $V_{b,max} / V_s \geq 0.0264$, the individual amplitudes at the bottom of the deck for each GPR trace are measured (V_b). If $V_b / V_{b,max} \leq 0.385$, the area is considered delaminated at the top rebar level.

The constant values of 0.0264 and 0.385 are empirical values. This approach is rarely being used.

The second approach (data processing using the attenuation at the top reinforcement level) is more widely used and is discussed in detail in the next sections.

3.4.2 Formation of Reflection Hyperbolas

When a ground-coupled GPR is dragged on the ground, a number of one-dimensional signals, called A-scans, are recorded. An *A-scan* is the reflected signal versus time. The A-scans in the time domain are stacked up to create the two-dimensional *B-scans* or radargrams. B-scans are the waveforms stacked up versus the survey distance and are representative of the cross-sectional view of the surveyed area. In the B-scan, a point scatterer, such as a reinforcement located perpendicular with respect to the survey direction, appears as a hyperbola. In the B-scan representation of the data, a gray scale is used to depict the positive and negative polarity components of the A-scans. The reflection polarity can be positive (white) or negative (black), depending on the reflection coefficient (3-21). For example, the reflection coefficient for reinforcing steel is calculated as follows:

$$\rho_{bar} = \frac{\sqrt{\varepsilon_{bar}} - \sqrt{\varepsilon_{conc}}}{\sqrt{\varepsilon_{bar}} + \sqrt{\varepsilon_{conc}}} > 0 \qquad (3\text{-}22)$$

Since the dielectric constant for steel is much higher than concrete, the reflection coefficient and, therefore, the polarity becomes positive, and the hyperbolas representing steel reinforcement are white on a B-scan. In general, a positive reflection coefficient is indicative of a decrease in the electromagnetic wave velocity, while a negative reflection means that the EM wave velocity increased.

Figure 3-4 (a) depicts a sample B-scan profile collected on a reinforced concrete (RC) bridge deck along with a sample A-scan. Figure 3-4 (b) shows a B-scan associated with a survey conducted on a slab fabricated in the laboratory. After post-processing and removing the bottom rebar reflections, the B-scan was reconstructed in MATLAB with

five A-scans superimposed on the image. The red circles represent the apex of the hyperbola or the dominant amplitude on the A-scan representing a transverse rebar.

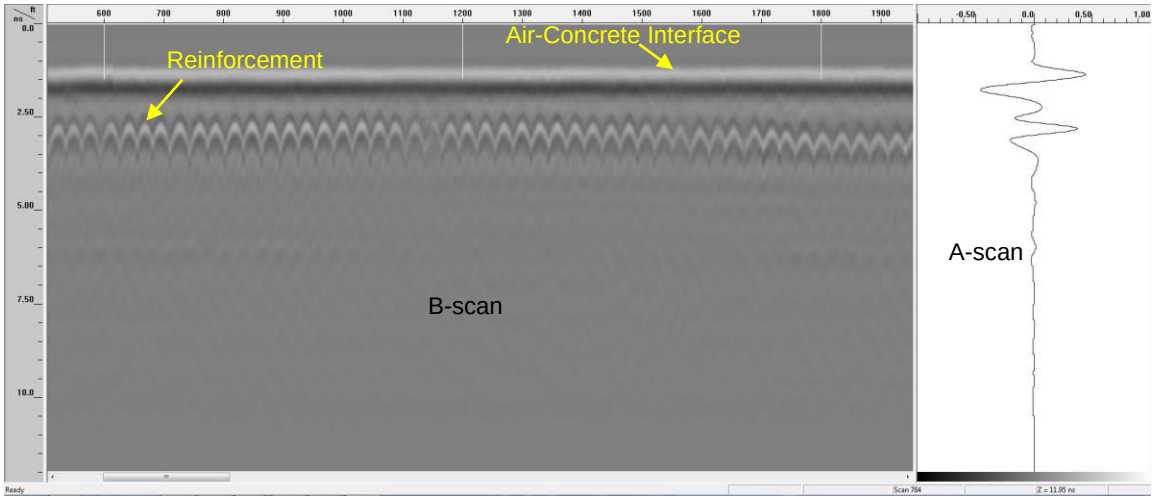

(a)

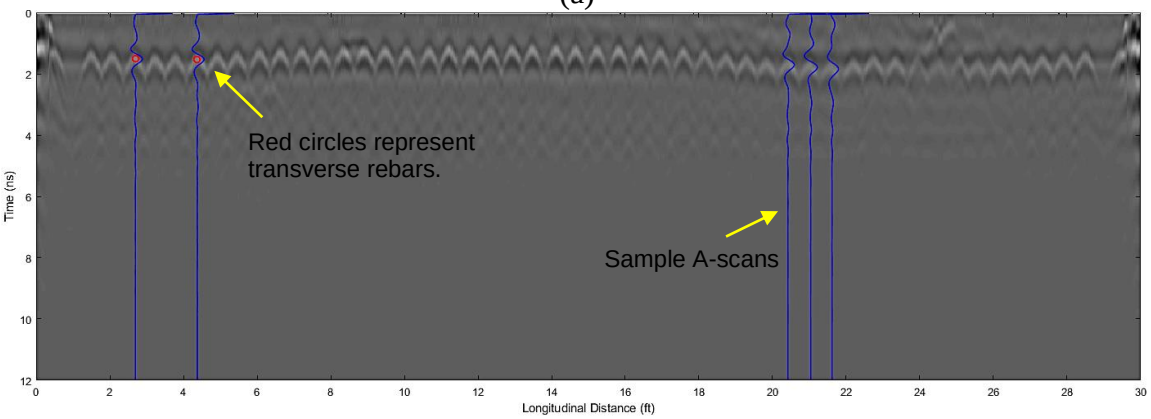

(b)

Figure 3-4. Typical GPR profile of an RC bridge deck.

For simple GPR applications, such as locating rebars, buried utilities, and pipelines, B-scans alone provide satisfactory information. However, for complex applications where the depth of the buried items and the extent and perhaps causation of the defects are of interest, post-processing of the data is required.

When detecting linear metallic objects such as steel reinforcement or pipes, GPR antennas are most sensitive to targets that are oriented perpendicular to the survey direction. This is

due to the antenna's polarization. Polarization is the orientation of the electric field of the radiated wave.

Accordingly, on a bridge deck, the GPR is deployed in a way that the shallowest reinforcement is perpendicular to the survey direction (Figure 3-5). Most often, the top reinforcing bars in a bridge deck are in the transverse direction. In such cases, the data is collected in the longitudinal direction along the traffic flow.

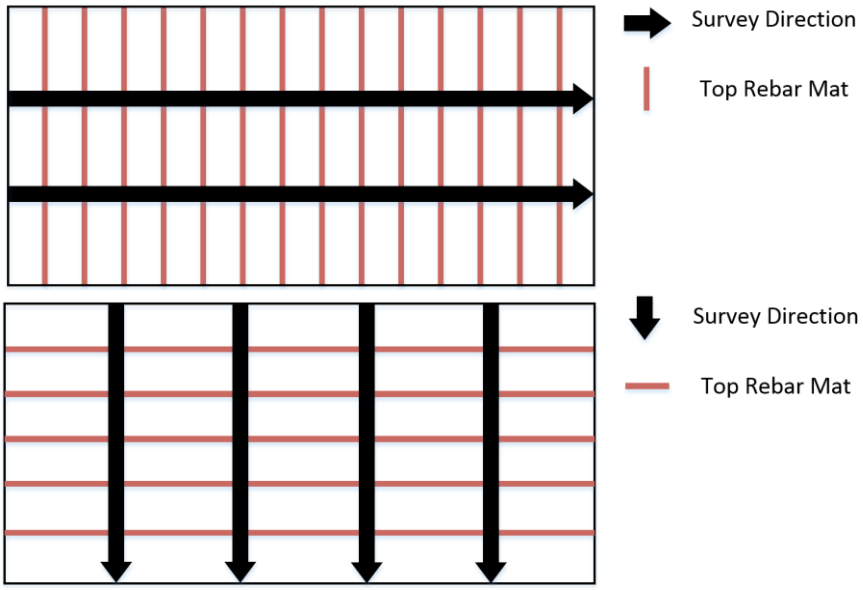

Figure 3-5. Survey direction: perpendicular to the top reinforcing bars.

The GPR signal is not a single pulse radiated directly perpendicular to the surface as a normal incident wave. Instead, the antenna emits a wide beam in the shape of a 60 degrees cone. Therefore, the antenna receives reflection signals as it approaches the target and continues to see the target as it moves away from it. This explains why in the time domain, a single point metallic reflector is represented by a hyperbola. The peak of the hyperbola indicates the location of the reinforcement. The formation of reflection hyperbolas is schematically illustrated in Figure 3-6.

For a given transmitter-receiver pair with a fixed distance, the shape of the hyperbola depends on the scan spacing and the medium dielectric. The smaller the scan spacing (more scans per inch), the wider the hyperbola and vice versa. Similarly, a lower dielectric constant (higher EM wave velocity) produces wider hyperbolas (10).

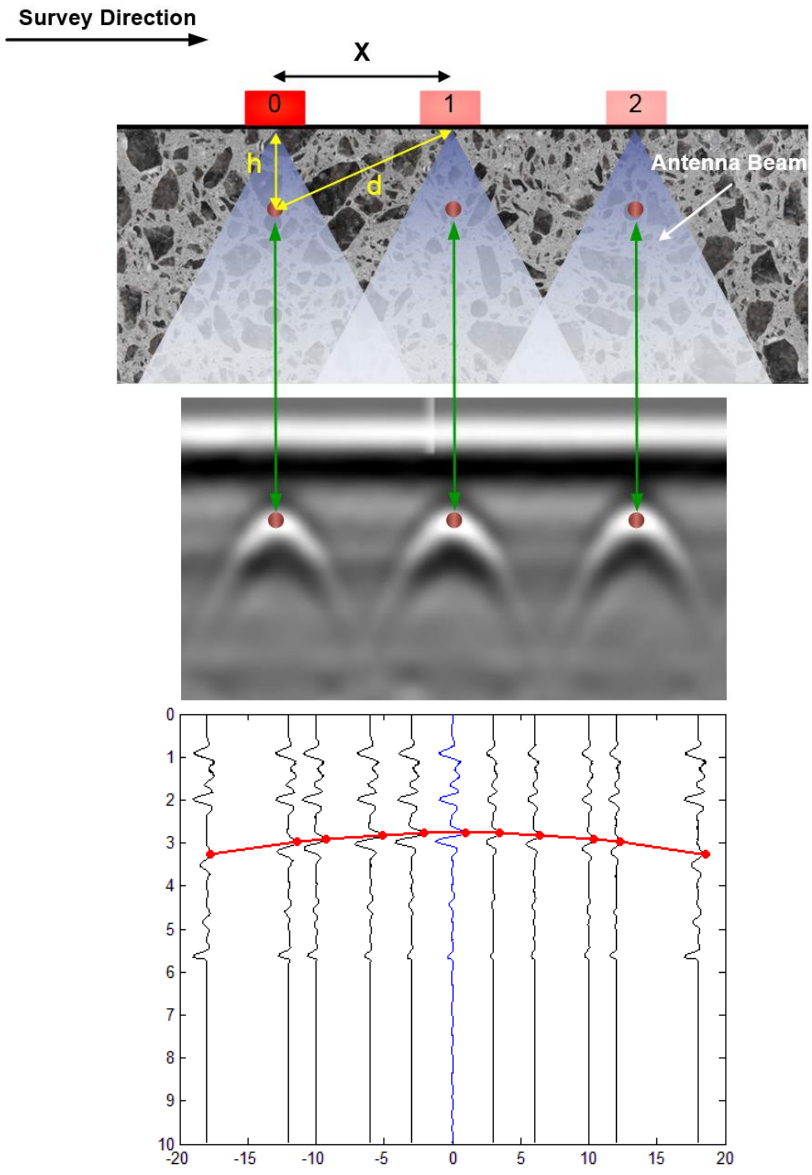

Figure 3-6. Hyperbola formation.

In Figure 3-6, for the antenna in location 1 (middle) the Pythagorean equation can be written as follows:

$$d^2 = h^2 + X^2 \tag{3-23}$$

Where *d* is the distance the EM wave travels from antenna in location 1 to the reinforcement in position 0, *h* is the reinforcement depth, and *X* is the antenna location with respect to the reference location 0.

The distance traveled by the EM wave from the antenna in location 0 to the reinforcement directly below it in position 0, or *h*, and the distance traveled by the EM wave from the antenna in position 1 to the reinforcement in location 0, or *d*, are given by:

$$h = V \times \frac{t_0}{2} \qquad d = V \times \frac{t_1}{2} \tag{3-24}$$

Where *V* is the EM wave propagation velocity, and t_0 and t_1 are two-way travel times in locations 0 and 1, respectively.

Replacing *h* and *d* in equations (3-23) based on equation (3-24) provides the hyperbola equation:

$$\frac{{t_1}^2}{{t_0}^2} - \frac{4X^2}{(Vt_0)^2} = 1 \tag{3-25}$$

In the hyperbola equation, t_1 and *X* are the variables for a fixed reinforcement depth.

3.4.3 Deterioration Detection

A hyperbola in a B-scan image provides enough information to verify the existence of reinforcement steel, pipe, etc. This information is readily available in real time during a GPR survey. However, determining the condition of concrete surrounding the

reinforcement and finding the concrete cover thickness requires post-processing of GPR data.

As discussed, the most common approach for condition assessment of reinforced concrete infrastructure using GPR is based on analyzing the signals reflected from the shallowest reinforcement bars perpendicular to the survey direction. Variations in the concrete electromagnetic properties affect the signal attenuation and reflection. Concrete with high moisture and chloride content, as well as a deck with several delaminated areas and cracks, causes the EM waves to attenuate faster, while a sound deck produces low attenuation levels.

The relative dielectric values can also be representative of the state of concrete. For regular concrete, the relative dielectric constant ranges from 5 to 10 and varies based on the air content, moisture content, and the electrical properties of the aggregates. Dielectric constant increases with (i) degree of concrete saturation with water, and (ii) chloride ion content. Greater dielectric values are typical for concrete with a high content of interconnecting pores and discontinuities, such as delamination and cracks, exposed to an environment containing chloride. It is widely accepted that a higher relative dielectric constant is consistent with reinforced concrete decks having some degree of deterioration (42).

The intrusion of moisture and chloride ions increases the dielectric constant, thereby reducing the velocity / increasing the travel time, which is then manifested as a deeper hyperbola in a B-scan. Zones of high attenuation levels are considered to be most likely deteriorated. It is worth noting that active corrosion of reinforcing steel does not necessarily

point to delamination, as it takes a longer time for the corrosion-induced cracks to develop into delamination (7).

In order to plot a condition map based on GPR surveys, the amplitudes are traditionally normalized with respect to the maximum measurable amplitude by the GPR unit (2^{15} or 32,768 for a typical 16-bit data acquisition system):

$$A_N = 20 \times \log\left(\frac{A}{2^{16}/2}\right) \quad (dB) \tag{3-26}$$

A_N is called the normalized amplitude or normalized dB.

Dinh et al. introduced a new normalization approach in which, instead of the maximum measurable amplitude, all the amplitudes are normalized with respect to the average direct coupling amplitude (9).

$$A_N = 20 \times \log\left(\frac{A}{A_{DirectCoupling}}\right) \quad (dB) \tag{3-27}$$

According to the authors, this new normalization amplitude eliminates the variations in amplitudes caused by using different transmit powers or different gage values during the data collection. Figure 3-7 illustrates A-scans collected on a sound and deteriorated section of the deck. The direct coupling amplitude and the top reinforcement reflections are shown.

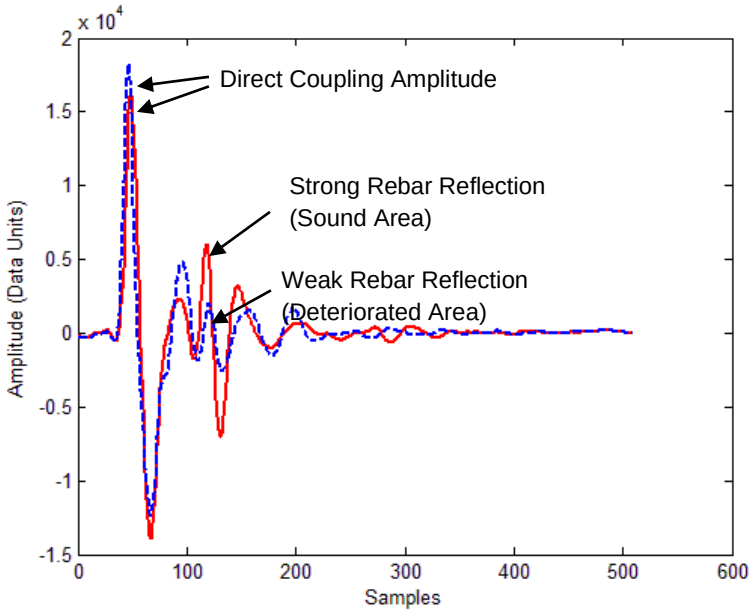

Figure 3-7. Direct coupling amplitude used by Dinh et al. for amplitude normalization.

Figure 3-8 depicts the GPR condition map based on the traditional depth correction method for a bridge in Pequea, Pennsylvania. This bridge was surveyed as part of the Long-Term Bridge Performance (LTBP) Program.

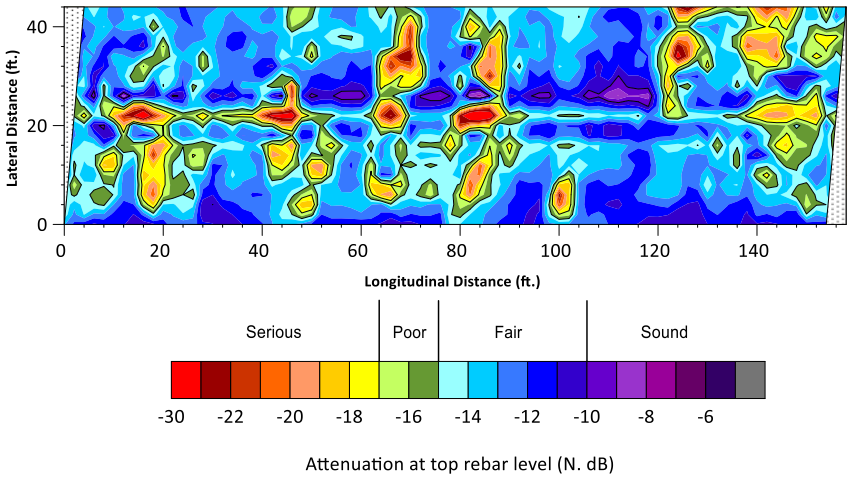

Figure 3-8. GPR attenuation map (Pequea, PA - LTBP).

As per ASTM D6087, “The spatial location of scans containing reflection amplitudes less than 6 to 8 dB below the maximum reflection amplitudes recorded typically correspond to deterioration”.

In Figure 3-1, the second hyperbola from the left is fuzzy compared to the other hyperbolas. That is an indication of stronger attenuation in the vicinity of that particular bar which may be attributed to reinforcement corrosion or higher concentration of chloride ions at that location. Even though B-scans contain useful information, they require post-processing to produce condition maps.

Alternative methods to map bridge deck deterioration have been suggested over time such as calculating the surface dielectric (42), but these alternatives have not gained wide acceptance among other researchers and practitioners.

If the depths of all the reinforcing bars are consistently the same throughout the deck, the strength of the signal reflections or attenuation at the rebar level are indicative of the concrete condition in the vicinity of the reinforcement, or the state of the reinforcement itself. However, there are, realistically, always variations in the concrete cover thickness in a bridge. The reflection amplitudes are therefore corrected for the reinforcement depth and then plotted to provide attenuation contour maps. Depth correction compensates for attenuation due to depth variation (geometric scattering), which has no bearing on the quality of concrete. The depth correction procedure is discussed in detail in the next section.

3.4.4 Depth Correction

In a hypothetical bridge deck that all the steel bars are placed at the same depth, lower amplitudes mean higher attenuation, thereby indicating deterioration. However, there are always variations in the reinforcement depth, even in newly constructed bridges. The EM waves have to travel farther to reach deeper reinforcing bars. Therefore, the signal is naturally weaker by the time it reaches a deeper bar, as opposed to a shallow bar. This

means that the reflection amplitude for a reinforcing steel bar with shallow concrete cover in a deteriorated area may be the same as the reflection amplitude for a deeper bar with thicker concrete cover in a sound area. Consequently, a deeper reinforcing steel bar in perfect condition may be presumed to be a shallower corroded bar. If not taking into account, the signal attenuation due to depth variations can lead to erroneous interpretation of GPR amplitudes.

In an attempt to resolve this issue, the concept of *depth correction* was introduced by Roger Roberts and improved by Barnes et al. (7). Without depth-correction, two reinforcing steel bars of the same quality located in different depths return different amplitudes. The depth correction is intended to isolate the attenuation caused by geometric scattering, hence allowing for the reinforcing bars in similar good condition to have the same amplitude regardless of their concrete cover thickness.

Figure 3-9 depicts the reflected amplitudes measured at the transverse top reinforcement level for a bare concrete bridge deck along Route 1 in Delaware. This survey was performed within the scope of The Long Term Bridge Performance (LTBP) Program. Noticeably, a wide range of amplitudes exists for a given two-way travel time (TWTT). Different amplitudes for the same TWTT can be attributed to changes in the concrete cover thickness or variation in concrete electrical conductivity and, therefore, concrete condition. While a decrease in concrete conductivity is indicative of the presence of discontinuities filled with water and chloride ions or rust, variations in the concrete cover thickness have no bearing on the condition of the concrete.

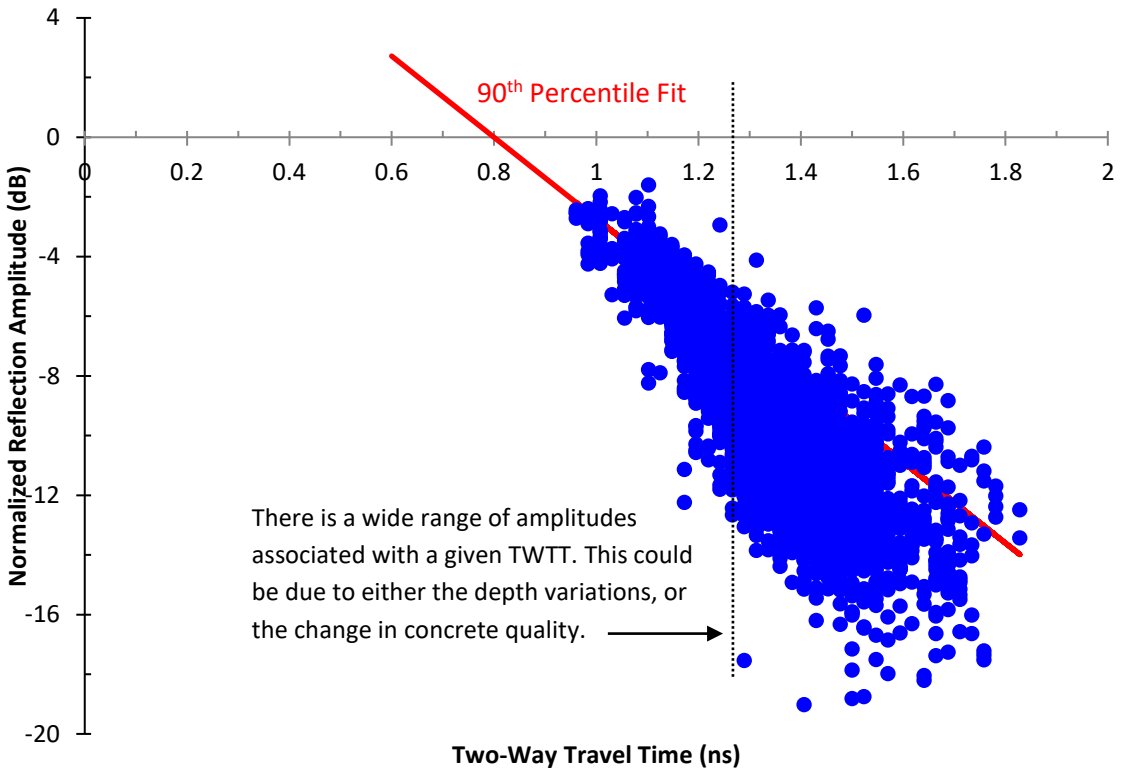

Figure 3-9. Linear Regression trend line: 90th percentile of normalized reflection amplitudes vs. TWTT (A bridge along Route 1 in Delaware).

With a closer look, one can observe a decreasing linear trend in the normalized amplitudes versus TWTT (Figure 3-9). This decreasing trend is not necessarily a sign of concrete deterioration because, as discussed earlier, deeper reinforcements naturally have weaker reflections.

Disregarding the outliers in the normalized dB vs. TWTT plot, a linear trend line can be fit to the 90th percentile of the graph using linear regression (7). This is done by drawing the best fit to the upper 10% edge of the plot. Figure 3-9 illustrates the reflected amplitudes, together with the linear regression line along the 90th percentile normalized amplitudes.

The slope is determined using two points selected along the line. Although any two points can be chosen, typically one point is selected at the amplitude intercept, and the other point

is usually selected at -10 or -20 dB level. After calculating the slope, all the points are rotated using equation (3-28). This procedure is illustrated in Figure 3-10.

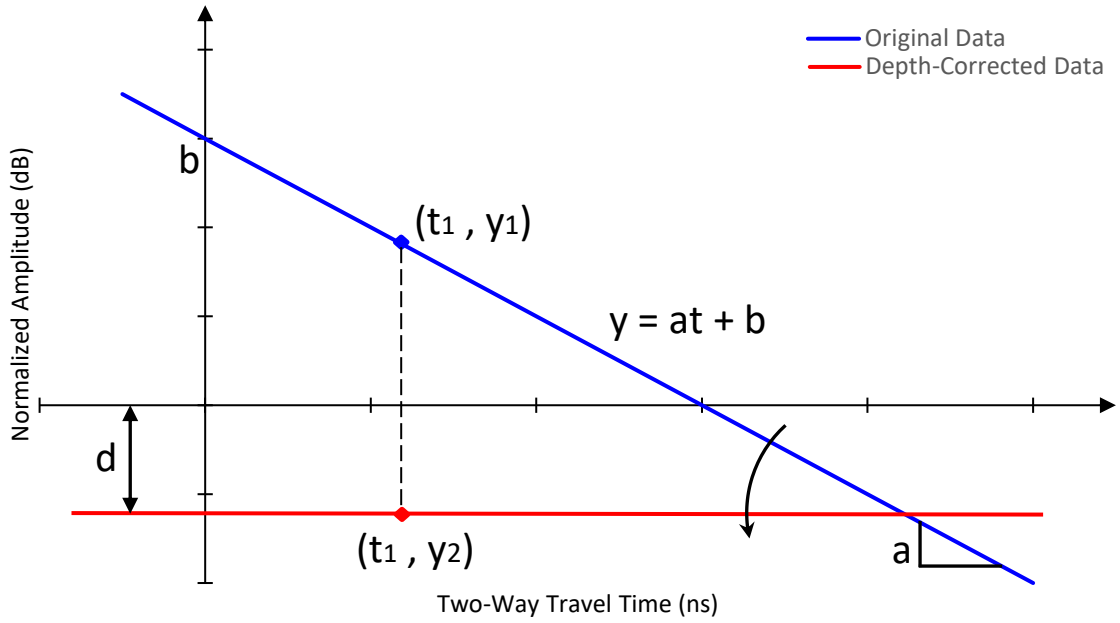

Figure 3-10. Depth-correction procedure.

The working assumption is that at least 10% of every bridge deck consists of sound concrete. The second assumption is that the signal reflected from a given reinforcement consists of two parts: (1) the part that is depth-dependent, and (2) the part that is dependent on EM properties of concrete. It is further assumed that this decreasing linear trend in the normalized amplitude vs. TWTT is due to variations in the cover depth. Depth correction eliminates the depth-dependent variations of reflection signal by subtracting the part proportional to the reinforcement depth so that the amplitudes will be only reflective of the deck condition (7).

$$y_2 = y_1 - (at_1 + b) - d \tag{3-28}$$

It must be noted that the depth-corrected amplitudes provide only a relative scale for comparison, not real amplitude values. The procedure is applied to the amplitudes shown in Figure 3-9, and the depth-corrected amplitudes are presented in Figure 3-11 where the second point is selected at the -10 dB level.

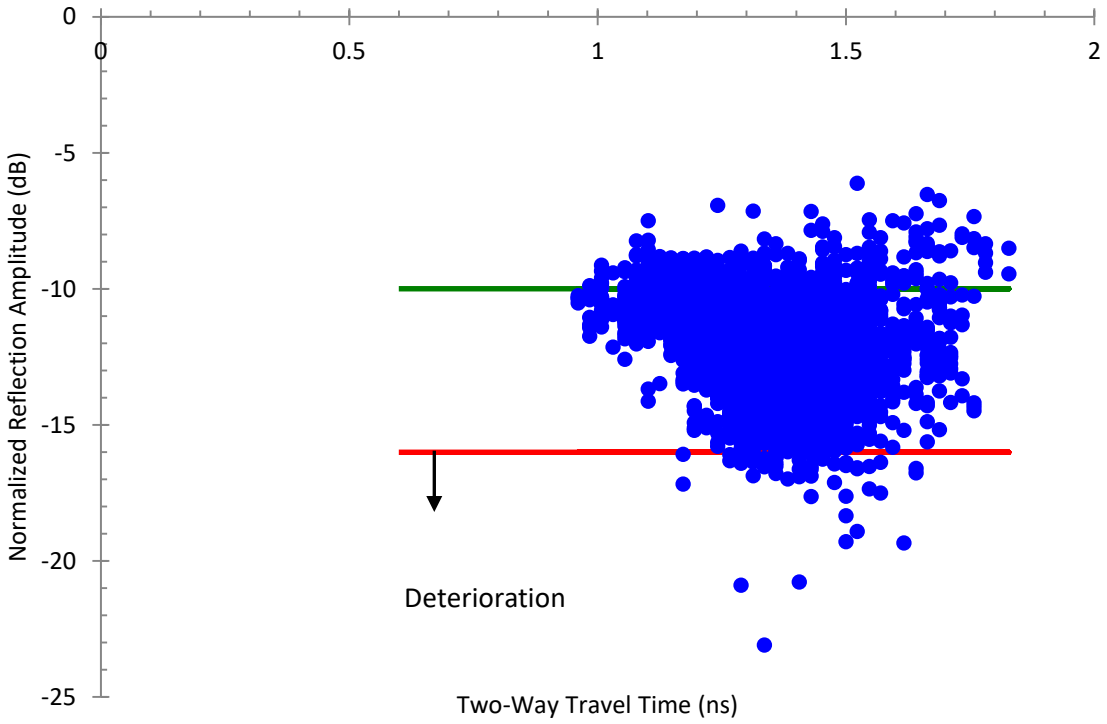

Figure 3-11. Depth-corrected normalized reflection amplitudes (A bridge along Route 1 in Delaware).

After the depth correction, using ASTM D6087, the deteriorated area can be delineated at 6 to 8 dB below *d* (*d* was -10 dB in the example above). The red line in Figure 3-11 is the boundary between sound and deteriorated deck at -16 dB level.

One of the major limitations of the depth correction method explained above is that the threshold values are fairly subjective and different operators may choose different

thresholds for the same bridge and the same data. The selection of the upper bound for the sound deck is also subjective.

It must be noted that, even though a widely accepted tool in bridge deck condition assessment using GPR surveys, *Depth Correction* is yet to be incorporated as a part of the ASTM specifications. It has been proven time and again that the depth corrected deterioration maps have far better accuracy and correlate significantly better with ground truth and condition maps developed using other NDE methods (43; 8; 9; 44; 45).

As mentioned earlier, the working assumption for the depth correction procedure is that at least 10% of a given deck consists of sound concrete. Therefore, using this approach for an entirely deteriorated deck, or an otherwise newly constructed sound deck, could result in an erroneous assessment of the deck condition. To overcome this issue and to enhance the GPR data analysis for bridge deck evaluation, Dinh et al. proposed a new approach for depth correction (9). Instead of using the 90% percentile as a benchmark for sound concrete, they used the LTBP Program database and established a new criterion for sound concrete based on complementary NDE data, specifically by using impact echo, electrical resistivity, and half-cell potential data.

To ensure that the amplitudes from various bridges were comparable, the authors proposed a new normalization method, called *Direct Coupling Normalization*, in which amplitudes were normalized with respect to the average direct coupling amplitude:

$$A_N = 20 \times \log\left(\frac{A}{A_{DirectCoupling}}\right) \quad (dB) \qquad (3\text{-}29)$$

This is in contrast with the typical normalization method, where the peak amplitudes are normalized with respect to $2^{(16-1)}$ or 32,768 for 16-bit data (Section 3.4.3).

Using the complementary data for 24 different bridges, a linear regression of GPR amplitudes was obtained representing a threshold for sound concrete for all the bridges within the network. For a given two-way travel time, the survey amplitudes greater than the reference amplitude from the linear regression were considered sound. Conversely, survey amplitudes less than the reference amplitude for all the bridges were deemed to be indicative of reinforcement in a deteriorated concrete.

3.4.5 Velocity Measurement (Dielectric Measurement)

Apart from using GPR as a complementary tool for condition assessment of bridge decks, it can also be used to measure the subsurface dielectric constant. This is done when dielectric cannot be estimated from the existing tables similar to Table 3-1, or when the accuracy of measurements is critical. This is done using a test method called the Common Midpoint (CMP) Test. Figure 3-12 illustrates the CMP set up for a single layer subsurface.

In this technique, two different antennas are used as a transmitter and receiver, while the spacing between them is gradually increased by moving them in the opposite directions, but with the same distance away from a midpoint. This outward movement of the antennas provides different travel paths for the signals reflected from the same reflection point. The travel time increases with the increase of transmitter-receiver separation distance.

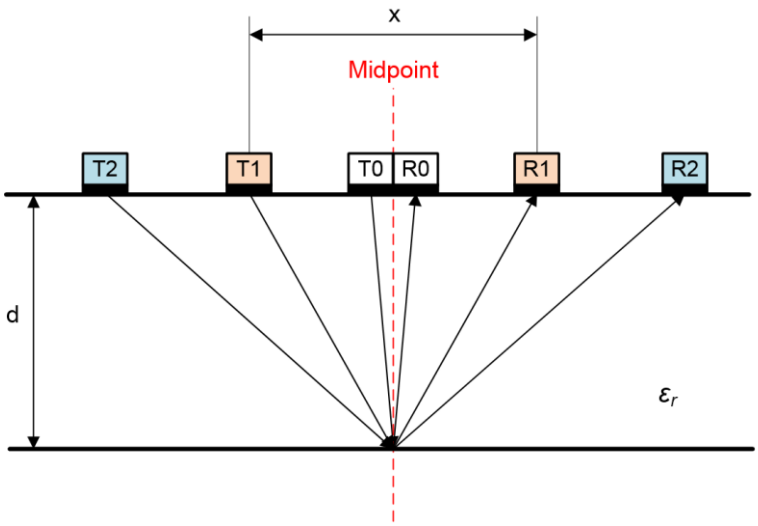

Figure 3-12. Common midpoint configuration for a single layer subsurface.

The layer thickness can be calculated based on the travel time for the Tx-Rx placed at location 0, or the midpoint, in Figure 3-12 as follows:

$$d = \frac{Vt_0}{2} \tag{3-30}$$

where d is the layer thickness, V is the EM wave velocity in that layer, and t_0 is the two-way travel time when the transmitter and receiver are directly above the common midpoint reflector.

For the Tx-Rx separation of x, the travel path is calculated using Pythagorean Theorem as $2\sqrt{d^2 + x^2/4}$. The relationship between the travel path and two-way travel time for the separation x is as follows:

$$2\sqrt{d^2 + \frac{x^2}{4}} = Vt_x \tag{3-31}$$

where t_x is the two-way travel time for the separation x.

The velocity is then calculated by combining equations (3-30) and (3-31), and by eliminating the layer thickness, *d*:

$$V = \frac{x}{\sqrt{t_x{}^2 - t_0{}^2}} \tag{3-32}$$

Using equation (3-5), the relative dielectric can be then calculated as follows:

$$\varepsilon_r = \frac{C^2}{x^2}\left(t_x{}^2 - t_0{}^2\right) \tag{3-33}$$

Where C is the EM wave velocity in the free space.

It must be noted that the relative dielectric measured using the CMP technique is the average of dielectric constants for inhomogeneities across the subsurface under investigation.

3.4.6 Time-Frequency Analysis

The advantages of using time-frequency analysis for post-processing NDE results, particularly for analyzing impact echo signals, has been fully recognized. Most recently, time-frequency analysis has gained more popularity in GPR data analysis (36; 46; 47; 48; 49; 50; 51). Post-processing of GPR surveys results has been mainly done in the time domain. Attention to frequency components has been limited to applying frequency filters, for example, low-pass or band-pass filters, prior to data collection. As discussed earlier, the time domain data analysis does not provide a full-depth assessment of the deck condition. Time-frequency analysis can be potentially used as a complementary tool to extend the GPR evaluation zone beyond the top reinforcing bars. The time-frequency

analysis approach was used to post-process some of the simulation data, but it was later abandoned in the interest of pursuing learning algorithms in the time domain. The basic principles of two time-frequency approaches are discussed next. These two methods include short-time Fourier transform and wavelet transform.

3.4.6.1 Short-Time Fourier Transform (STFT)

Fourier transform has been extensively used for digital signal processing to obtain the frequency content of a given signal. Using Fourier transform, a periodic function of time is decomposed to a discrete set of complex harmonic functions (Fourier spectrum). These functions constitute the spectral distribution of the original time domain signal. For *x(t)*, a continuous function of time, the Fourier transform is defined by:

$$X(f) = \int_{-\infty}^{+\infty} x(t) e^{-j(2\pi f)t} dt \tag{3-34}$$

Where $j = \sqrt{-1}$ and f is the frequency. Given *X(f)*, the original time domain signal can be calculated using the *inverse* Fourier transform:

$$x(t) = \int_{-\infty}^{+\infty} X(f) e^{j(2\pi f)t} df \tag{3-35}$$

Equations (3-34) and (3-35) are called Fourier transform pairs.

For a finite number of samples, the integral is replaced by summation, and the discrete Fourier transform (DFT) is defined by:

$$X(k) = \frac{1}{N} \sum_{0}^{N-1} f(x) e^{-j(2\pi kx)/N} \tag{3-36}$$

Where $k = 0, 1, 2, \ldots, N - 1$

Fast Fourier transform (FFT) is an efficient algorithm for computing the discrete Fourier transform of a signal. FFT returns the averaged signal in the frequency domain or the frequency spectrum. Therefore, if the signal period is long, the spectral content may change making the FFT inaccurate. In addition, it can be difficult to interpret the data when there are multiple reflectors/anomalies in close proximity of one another.

Another major limitation of the Fourier transform is that the time component of the signal is lost as FFT does not specify *when* a certain frequency occurs. That is why FFT is an ideal tool for analyzing stationary signals whose frequency does not change over time. However, GPR signals are non-stationary/transient as the antenna continuously moves and therefore the reflection signal and its frequency content changes over time. Since FFT averages the entire signal, any change in the local frequency is spread to the entire spectrum making it impossible to determine the time/frequency where the perturbation had occurred.

Per equation (3-13), GPR signal attenuation and consequently the wave propagation velocity is frequency-dependent. Moreover, for GPR data analysis, it is imperative to know the exact time-location coordinates of a particular frequency rendering FFT ineffective. Therefore, another complementary data analysis technique is needed to process GPR transient signals.

Short-time Fourier transform (STFT) or windowed Fourier transform is a popular time-frequency analysis technique that has been developed to determine the spectral content, i.e., frequency and phase, at a specific time. In STFT, the signal to be transformed is multiplied by a non-zero short duration window function producing a short segment of the signal. Provided that the window is sufficiently narrow, FFT of this localized signal provides the instantaneous spectral content of the signal. By moving the window along the time axis

and calculating FFT at each segment, the time-varying spectral content of the signal is obtained. The window function can be any continuous smooth function which approaches 1 at the center and approaches 0 away from it. However, the Gaussian function is the most popular choice (52). The STFT of the signal *s* is calculated using the following equation:

$$STFT(t,\Omega) = \int \left[s(t).w(\tau - t) \right] e^{-j\Omega t} d\tau \qquad (3\text{-}37)$$

where

s(t) = time domain signal;

w(t) = window function;

Ω = signal frequency;

τ = time index.

STFT(t,Ω) is a complex function representing the magnitude and phase of the signal in the time-frequency domain.

One of the limitations associated with STFT is that given the fixed width of the windowing function, there is a trade-off between time and frequency resolutions. A wider window gives a finer frequency resolution and poor time/depth resolution. A narrower window, on the other hand, provides a good time/depth resolution at the expense of frequency resolution. This effect is illustrated in Figure 3-13. Figure (a) corresponds to the smallest window amongst all four images, 21 samples, and has the best time resolution (horizontal axis) and the poorest frequency resolution (vertical axis). In figure (b), the window size is 101 samples, and there is a reasonable tradeoff between time and frequency resolutions. Figures (c) and (d) have the window sizes of 301 and 501, respectively, and provide a good

frequency resolution, but a poor time resolution. The maximum frequency obtained from the frequency spectrum is slightly more than 2 GHz. The spectrograms associated with smaller windows show a relatively wide range for the dominant frequency. For example, the dominant frequency in Figure (b) ranges from 2 to about 3 GHz. However, the spectrogram in Figure (c) which is associated with the widest window shows a dominant frequency very close to 2.1 GHz which can also be read from the spectrum.

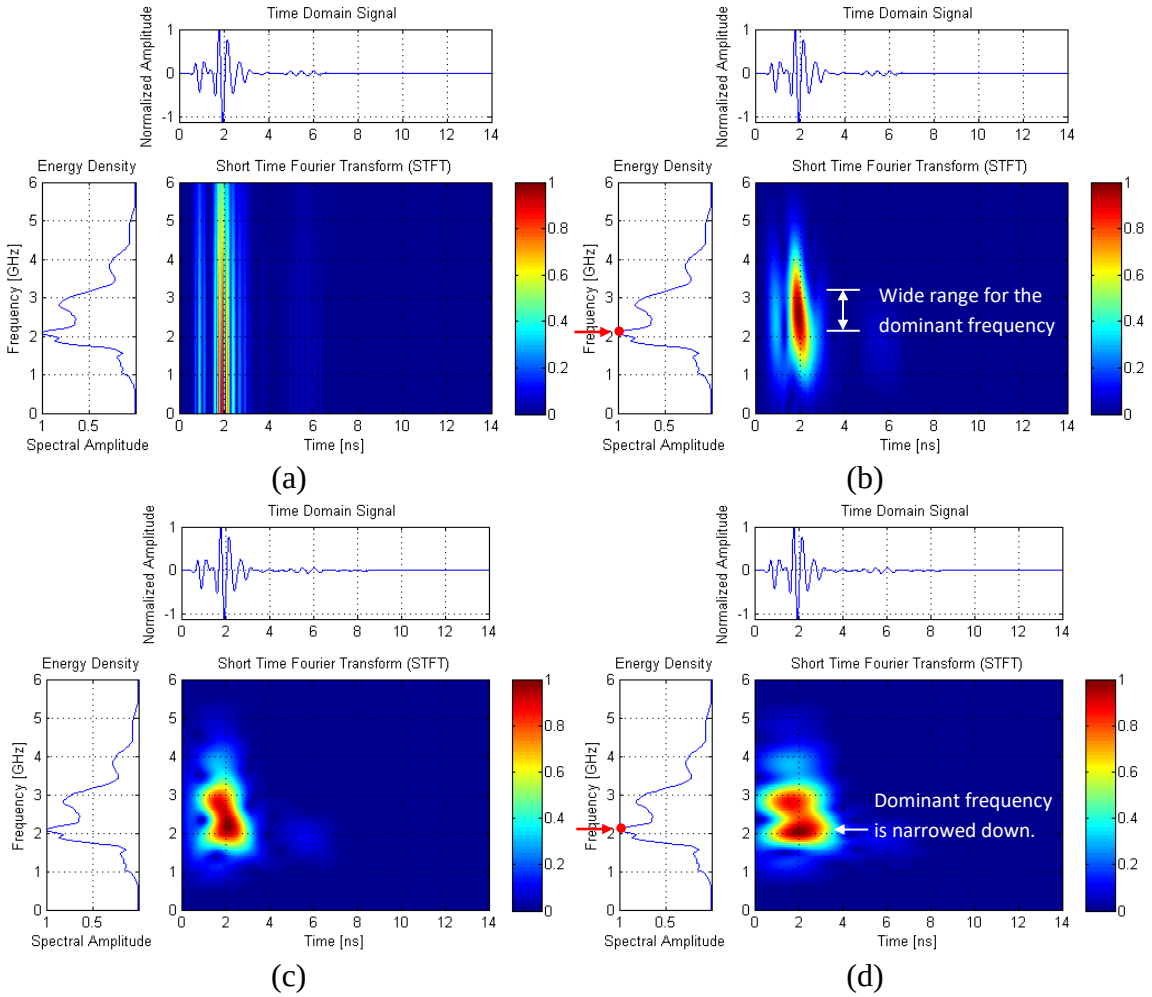

Figure 3-13. The effect of window size on time/ frequency resolution: (a) w = 21, (b) w = 101, (c) w = 301, and (d) w = 501.

Short-time Fourier transform has been used by Leng and Al-Qadi (2009) to measure the dielectric constant of railroad ballast, and by Bradford, (2007) to detect and characterize

nonorganic liquid contamination in a contaminated site. Leucci et al. (2012) used time-frequency analysis to determine the damage and to measure the moisture content of monumental buildings in Italy (38; 50; 53).

Al-Qadi et al. (2010) used STFT to measure the moisture content and thickness of railroad clean ballast. Data collection was performed at 20 km/h using both 1 and 2 GHz GSSI horn antennas. The authors showed that when GPR data is analyzed in the time domain to detect ballast fouling, chances are that the radio frequency (RF) noise is mistaken for clean ballast. This problem was resolved using STFT as the frequency of RF noise, and the dominant GPR frequency are far apart on the spectrum. Additionally, fouled ballast has more fine aggregates and less air void comparing to clean ballast affecting the dielectric value, causing the dominant frequency and the spectrum to change with depth. Their analysis showed that STFT could be effectively used to measure the moisture content and identify the boundary between clean and fouled ballast (46).

Santos et al. (2014) used three spectral features to post-process the GPR profiles in order to differentiate among different target materials: concrete, metal, and plastic. These spectral features included power spectral density (PSD), STFT, and Wigner-Ville distribution (WVD) (54).

3.4.6.1.1 STFT: Laboratory Implementation

To demonstrate the feasibility of adopting STFT analysis to accurately detect deteriorated areas of a bridge deck based on GPR survey results, a slab fabricated with known defects was surveyed using GPR and the results were post-processed using STFT. The validation slab was prepared as a part of the Automated Nondestructive Evaluation and Rehabilitation

System (ANDERS) project funded by the National Institute of Standards and Technology-Technology Innovation Program (NIST-TIP). The validation slab fabricated at Rutgers was 30-ft long, 12-ft wide, and 8-inch thick (Figure 3-14). Artificial defects, including various types of delamination and areas with high salt (sodium chloride) concentrations, were introduced into the slab. The slab was fabricated using normal portland cement concrete with 2.5-in of concrete cover. The transverse bars placed at 6-in on center.

The GPR survey was conducted using a GSSI 1.5 GHz antenna and a SIR-20 control unit. The survey lines were 1-ft apart, with the first line being 1.5-ft away from the edge of the slab and perpendicular to the top reinforcing bars, which were in the transverse direction. Later in Chapter 7, data from this survey will be used for the laboratory implementation of the learning algorithm.

Figure 3-15 depicts the GPR attenuation map plotted based on the 90^{th} percentile depth correction. Concrete in the bottom right corner of the slab had high chloride concentration since during the concrete placement significant amounts of chloride sodium was added to the concrete mix. This explains the higher level of signal attenuation in the bottom left corner of the contour map in Figure 3-15.

Figure 3-16 depicts the B-scan associated with Line B reconstructed in MATLAB after time-zero adjustment and application of a filter to suppress the reflections from the bottom reinforcement and bottom of the deck. Since the time-frequency analysis is time-consuming and computationally demanding, three A-scans were selected for further STFT analysis. The individual A-scans were selected based on the hyperbola appearance on the B-scans and are superimposed on the B-scan in Figure 3-16. Their spectrograms are presented in Figure 3-17.

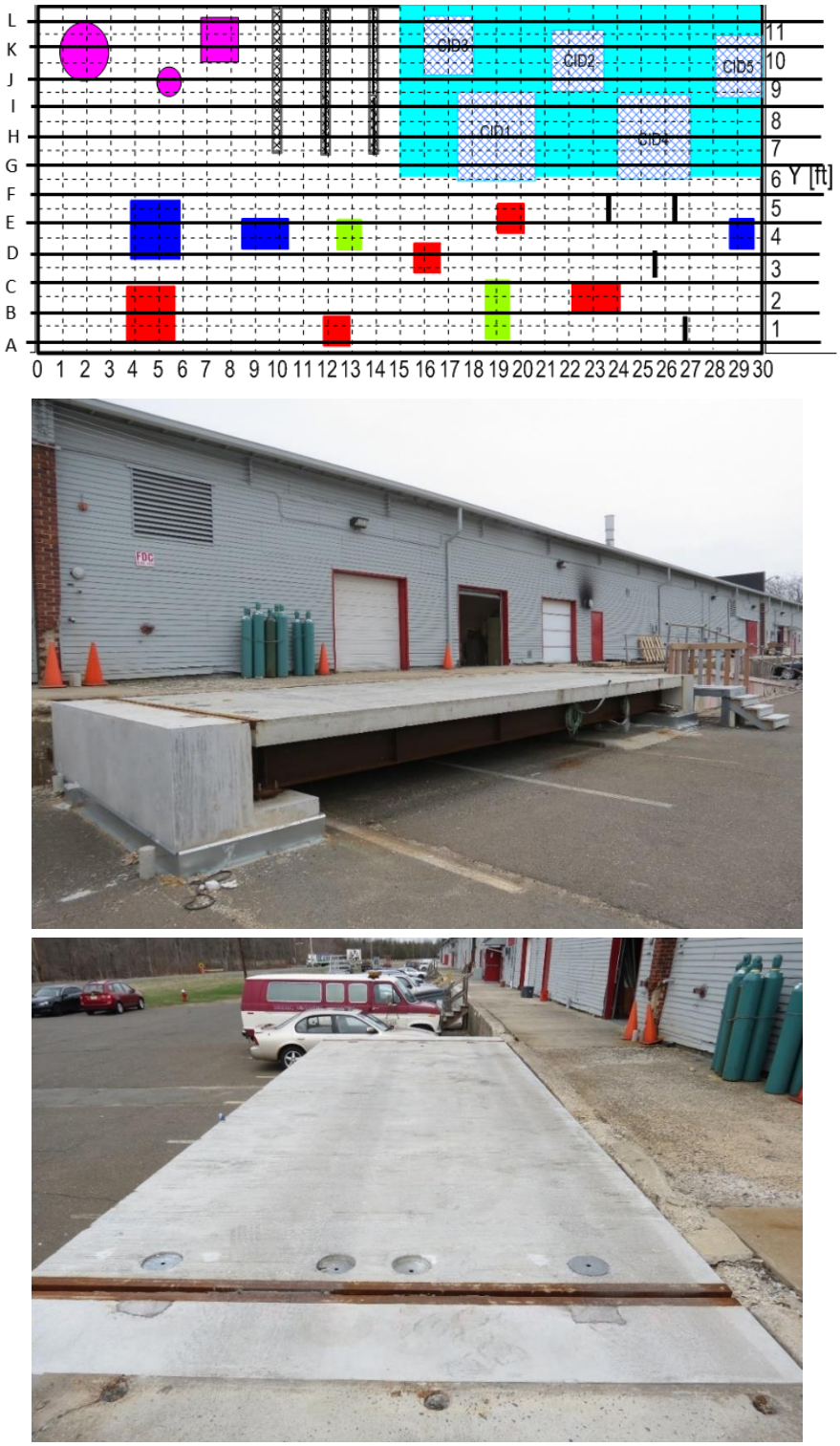

Figure 3-14. Validation slab.

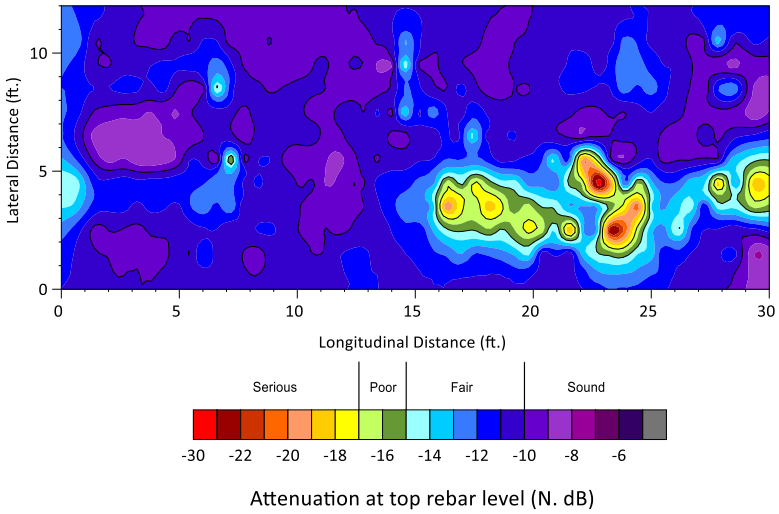

Figure 3-15. ANDERS slab attenuation map.

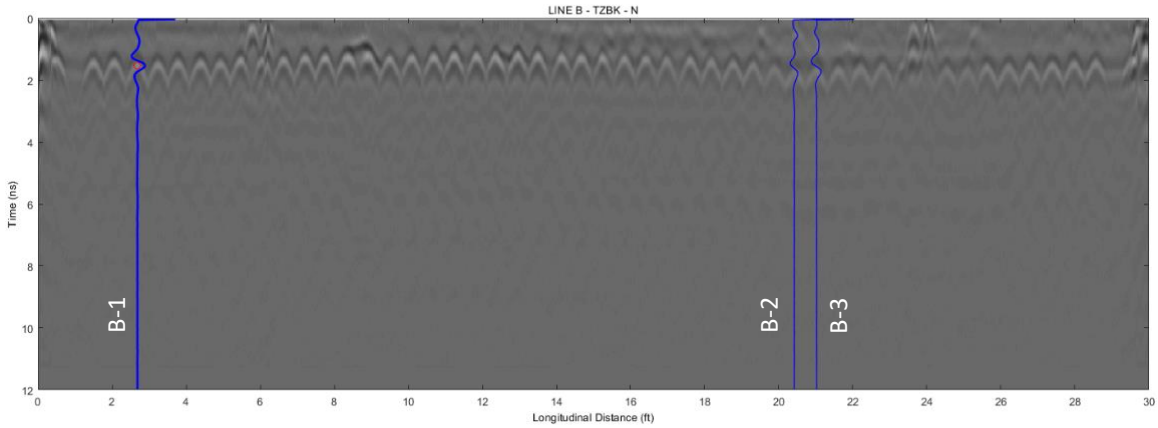

Figure 3-16. B-scan for Line B regenerated in MATLAB.

B-1 was selected from a sound area of the deck, while B-2 and B-3 were chosen from an area with high chloride concentration. Much like the thickness frequency in impact echo, the frequency spectrum associated with a sound area of the deck has a single dominant frequency, 1.25 GHz in this case (Figure 3-17 (a)). The frequency spectrum associated with deteriorated areas has lower dominant frequencies and may have multiple peaks. The same trend is observed for survey lines C and E in Figure 3-18 through Figure 3-21. The results are summarized in Table 3-3. In all cases, the dominant frequency associated with the deteriorated area is lower than the 1.25 GHz for the sound section.

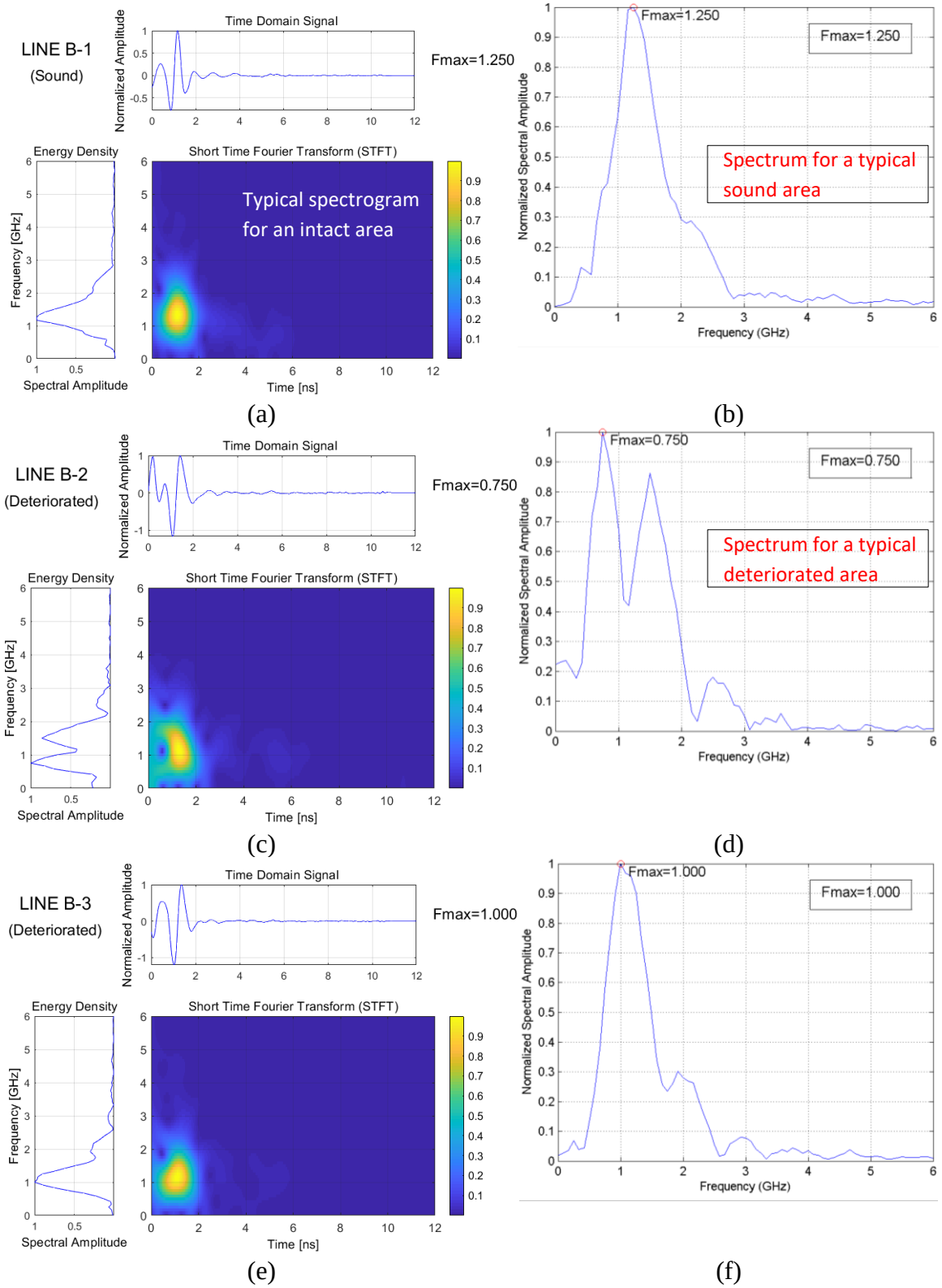

Figure 3-17. Spectrograms for A-scans on Line B – (a) and (b) B-1 representing a sound area, (c) through (d) B-2 and B-3 representing areas with high chloride concentration.

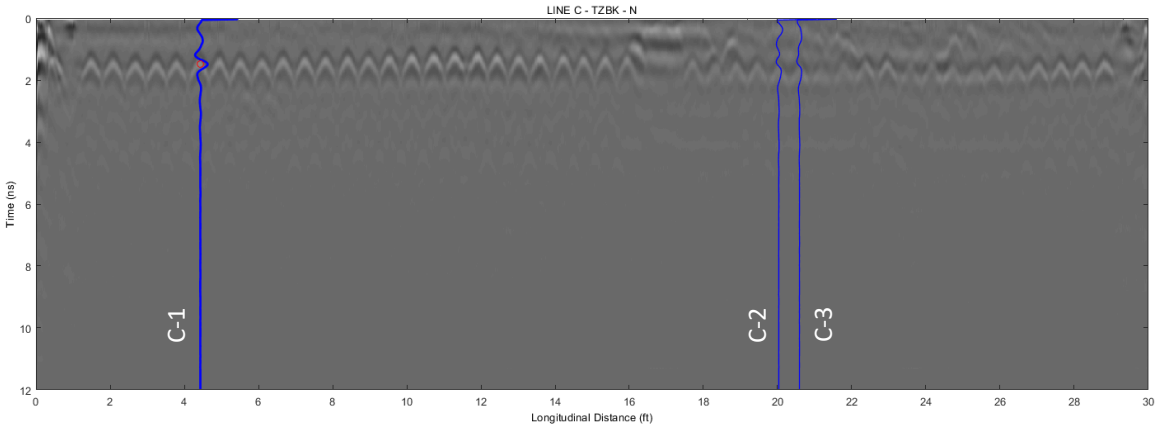

Figure 3-18. B-scan for Line C regenerated in MATLAB.

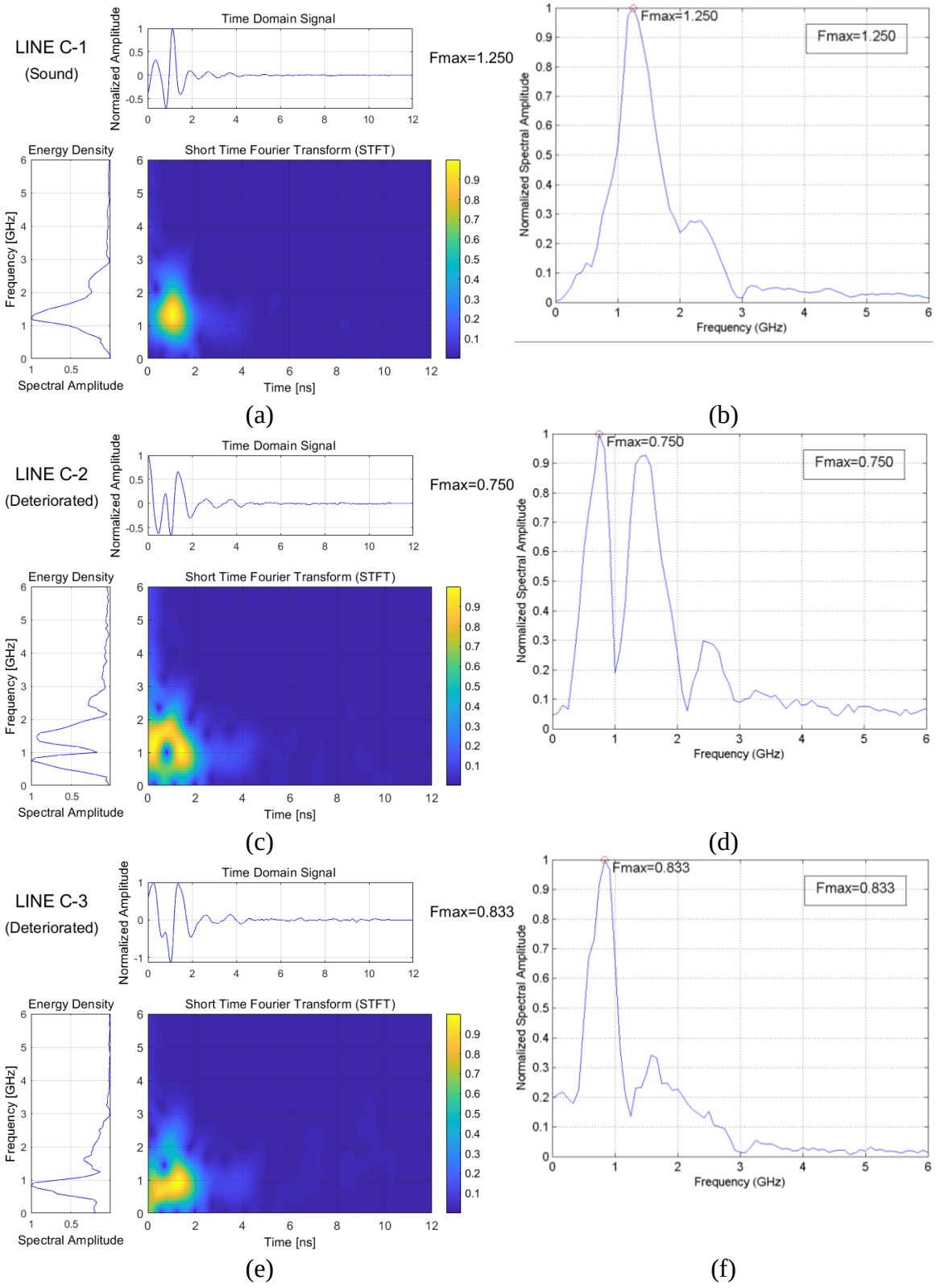

Figure 3-19. Spectrograms for A-scans on Line C – (a) and (b) C-1 representing a sound area, (c) through (d) C-2 and C-3 representing areas with high chloride concentration.

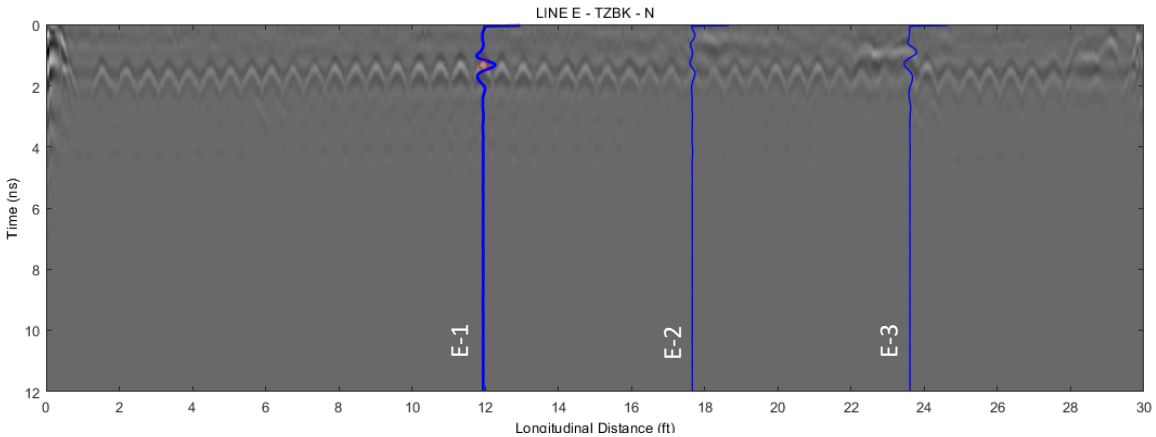

Figure 3-20. B-scan for Line E regenerated in MATLAB.

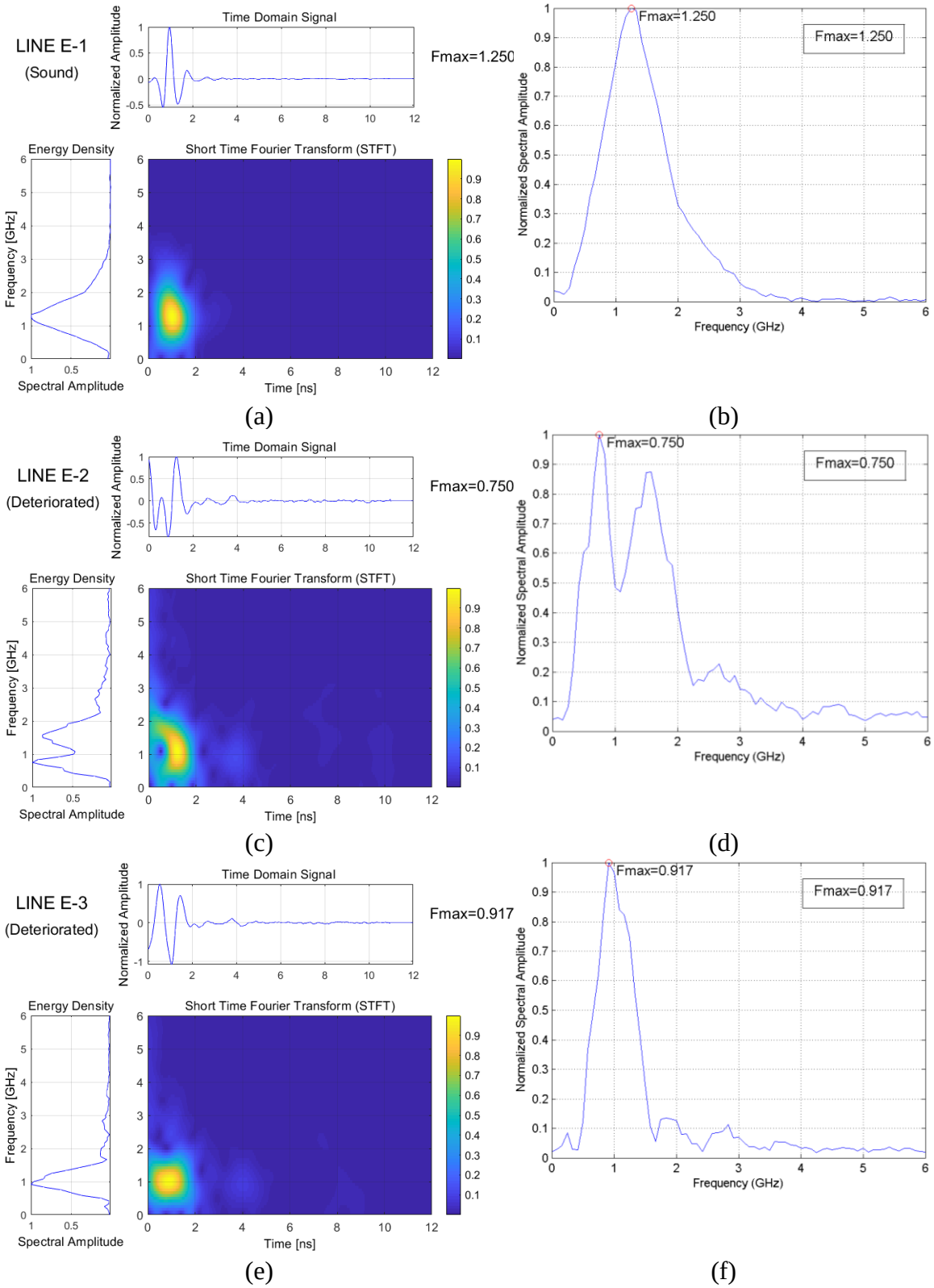

Figure 3-21. Spectrograms for A-scans on Line E – (a) and (b) E-1 representing a sound area, (c) through (d) E-2 and E-3 representing areas with high chloride concentration.

Table 3-3
Material properties

Survey Line	Dominant Frequency (GHz)		
	Line B	Line C	Line E
Location 1 (Sound)	1.25	1.25	1.25
Location 2	0.75	0.75	0.75
Location 3	1.00	0.833	0.917

Given the complexity of STFT analysis and the fact that it is very time-consuming and computationally intensive, it is recommended to use this method only as a complementary tool to spot check when there are doubts regarding the time domain analysis results.

3.4.6.2 Continuous Wavelet Transform

One of the STFT drawbacks is that it cannot provide a good resolution for both time and frequency at the same time. A shorter window provides a higher time resolution which corresponds to a poor frequency resolution. Since the window length is constant, the STFT has constant time and frequency resolutions throughout the spectrogram. Continuous wavelet transforms (CWT) are primarily developed to resolve this issue. The wavelet transform is superior to STFT in the sense that it can use a variable length window function resulting in improved resolutions for both time and frequency.

Compared to STFT, wavelet transforms are more complicated and more computationally demanding. However, their multi-resolution capabilities make them an ideal tool to potentially make an effective full depth assessment of a bridge deck based on GPR survey results, as they provide better time localization of frequency components.

A wavelet is a rapidly decaying wave that has a nonzero value of $\psi(t)$ for a finite time period, and it is zero elsewhere, and has a mean of zero. This is in contrast to Fourier

transforms that are the sum of sine waves that oscillate through infinity. CWT returns coefficients representing time and frequency, which can be used to reconstruct the original signal.

There is a wide range of wavelets of different shapes that can be chosen for any specific application. Once a mother wavelet has been selected, it can be scaled or shifted in sliding windows to cover the entire signal. Figure 3-22 illustrates the Morlet wavelet.

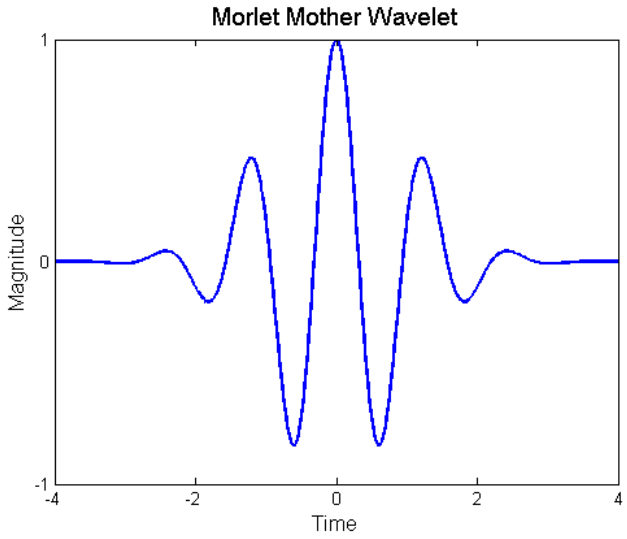

Figure 3-22. Morlet mother wavelet.

A mother wavelet is a function $\psi(t)$ that satisfies the following equation:

$$\int_{-\infty}^{+\infty} \psi(t)dt = 0 \qquad (3\text{-}38)$$

A family of wavelets is generated by scaling and shifting (dilating) the mother wavelet:

$$\psi_{a,b}(t) = \frac{1}{\sqrt{a}}\psi\left(\frac{t-b}{a}\right), \quad a>0 \qquad (3\text{-}39)$$

Where b is the dilation parameter and a is the scale parameter. Scaling compresses or stretches the wavelet in time. By shifting one can change the onset of the wavelet.

The continuous wavelet transformation (CWT) of a function *f(t)* is defined as:

$$w(a,b) = \int_{-\infty}^{+\infty} f(t)\psi^{*}_{a,b}(t)dt, \quad a>0 \tag{3-40}$$

where * denotes complex conjugate.

Theoretically, any kind of wavelet can be selected for wavelet transform analysis; however, since the output is a combination of scaled and translated mother wavelet, it is preferable to choose a mother wavelet as similar as possible to the incident signal. It is also preferred to use differentiable wavelets. For GPR applications, Ricker wavelet, biorthogonal wavelet, and Morlet wavelet seem to be reasonable choices of mother wavelet as they closely represent a GPR incident wave.

Lai et al. (2011) used wavelet transformation to study electromagnetic wave dispersion in reinforced concrete. Their findings confirmed that at higher GPR frequencies, the phase velocity and therefore the real part of dielectric permittivity becomes stable and reach a plateau. This validates the non-dispersive nature of reinforced concrete for GPR applications (36).

Baili et al. (2009) used discrete wavelet transform (DWT) to remove noise from GPR signals which could potentially mask the inhomogeneities in concrete particularly at greater depths. The data collection was performed using a 1 GHz air-coupled antenna on a flexible pavement system. Out of the four mother wavelets used, Daubechies 6 and Symlet 6 performed better.

The time-frequency analysis will be used later in Chapter 5 to post-process the finite element simulation data.

Chapter 4. Computational Electromagnetics

Closed form analytical solutions to Maxwell's equations are only available for very limited ideal geometries. For more complex models, numerical methods must be implemented to acquire approximate solutions (55). Numerical simulations can be used in a wide range of electromagnetic applications, from antenna design to calibration and performance analysis of complex structures. Finite element method (FEM), finite-difference time-domain (FDTD), and method of moments (MoM) are the most commonly used numerical simulation methods in computational electromagnetics. In electromagnetic problems, the partial differential equations (PDEs) are solved using finite element or finite difference methods, while the method of moments is used to solve the integral problems (56).

Maxwell's equations can be solved in both time and frequency domains. Although the two solutions can be converted from one to another using Fourier transforms, the time domain solution is better suited for GPR simulations, since the response has a wide range of frequencies for a single excitation. FEM and FDTD solve the electromagnetic field problems directly in the time domain, while MoM solves them in the frequency domain.

One of the most significant advantages of numerical simulations is their cost effectiveness. They can help gain a better understanding of the problem at hand and shed light on the potential outcomes, as well as assist in quantifying contributions from the parameters involved. Computational methods can help researchers cost-effectively optimize a machine or technique. In GPR simulations, one can see how the electromagnetic waves propagate through the medium at different locations and at various time slices. Consequently, those help researchers design an optimum experiment to obtain the desired outcome or to study the effects of varying parameters in real life. Parametric studies carried out through conducting experimental research can be extremely expensive, labor-intensive, and time-consuming. Moreover, in experimental studies, it is not possible to completely isolate the contribution of a single parameter to the final outcome as there are always unwanted interferences and noises involved. Numerical simulations, on the other hand, enable the researcher to single out the results by varying the parameter of interest in a short period of time and at a considerably lower cost.

In general, mathematical modeling of a physical process such as modeling electromagnetic waves propagation involves the following:

- Constructing a system of partial differential equations (PDEs) and ordinary differential equations (ODEs) and algebraic equations for constitutive equations and setting initial and boundary conditions;
- Discretizing the domain and solving the system of equations on each grid point/cell;
- Evaluating the system for convergence and stability.

Their many advantages and benefits notwithstanding, numerical simulations provide only approximate solutions to Maxwell's equations and not robust closed form solutions. All numerical simulations, in structural, fluid, or electromagnetic fields of study must be evaluated by engineering judgment. Irrespective of whether the simulation tools are powerful enough, the engineers must exercise professional judgment prior to accepting the results. Therefore, a proper understanding of the problem and the governing principles are imperative to procure reliable and meaningful outcomes.

Finite element, finite-difference time-domain, and method of moments are each briefly discussed in this chapter.

4.1 Finite Element Method (FEM)

Finite element method is a numerical method to find approximate solutions to partial differential equations (PDEs). The basic idea was introduced by Courant in 1943 for a cylinder torsion problem. In the next two decades, many researchers worked on further development of the FEM theory and expanding its applications. In the 1950s and '60s, this numerical technique was extensively used under the name of *"Direct Stiffness Method"* in Boeing. In 1960, Ray Clough from UC Berkley, who was working for Boeing as a summer faculty, coined the name *"Finite Element Method"* in a paper on plane stress analysis (57). Although this numerical technique has been around since 1943 for various mechanical, civil, and aeronautical problems, it was not until 1968 that the FEM was implemented to solve electromagnetic problems (56; 58).

Given the complexity of FEM for electromagnetic field problems, it is not yet as popular, and as widely used as FDTD. However, since the FEM formulation is very general, it is

capable of providing approximate solutions for arbitrary geometries and complex materials, where FDTD is not as effective. Moreover, using tetrahedral elements of various sizes, a curved boundary can be accurately simulated. Another important advantage of FEM is that, unlike FDTD, the CFL condition (FDTD stability condition) does not apply to FEM simulations and, therefore, the time step is not bounded by the element size. In other words, regardless of how small the element size may be, the time step does not need to be drastically reduced.

FEM is a numerical method to obtain approximate solutions for differential equations governing physical problems that do not have a closed form solution, even with simplifying assumptions. The problem domain (continuum) is divided into a finite number of discrete parts known as elements. The size of the elements is governed by the wavelength in the medium. It is generally agreed that the edge of an element should be smaller than one-tenth of the wavelength (59).

In HFSS, which is the ANSYS module for electromagnetic simulations, the model is divided into a large number of tetrahedral elements, where a single tetrahedron is a four-sided pyramid (60). This discrete representation of the continuum is known as the finite element model, and the grid formed by the elements is called mesh. The electric / magnetic field components are stored either at the nodes or the midpoints of the edges in the following order:

- Nodes: The field components tangential to the edges are stored at nodal points.
- Midpoint of the edges: The field components normal to the edge but tangential to the face are stored at midpoints of each edge.

Just like any other finite element simulation method, the field components at any given point inside the element are interpolated from the nodal points. A tetrahedral element used in HFSS is depicted in Figure 4-1 (60).

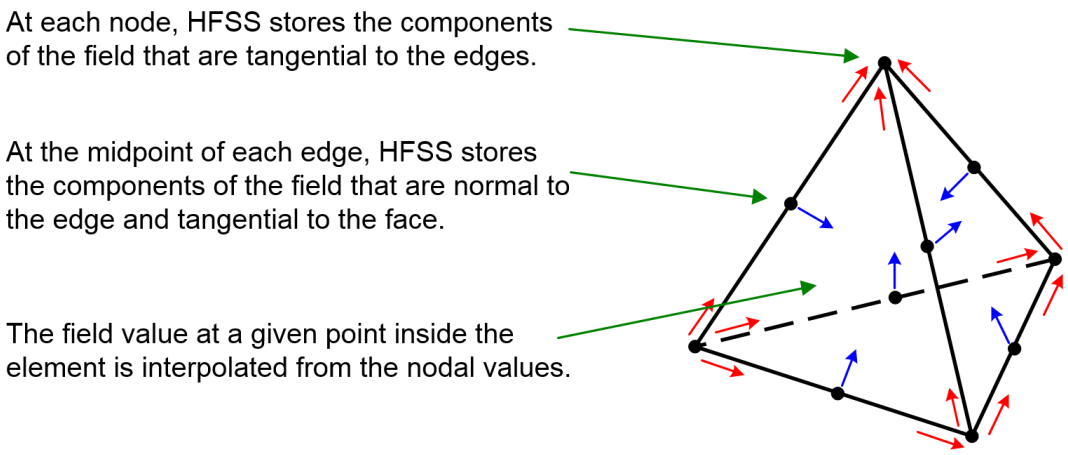

Figure 4-1. A tetrahedron element used in HFSS.

In reality, electromagnetic waves radiate into infinity. Therefore, in order to apply the finite element method, the infinite space needs to be cut off to create a finite space. This can be accomplished by assuming the absorbing boundary condition (ABC) on the outer surface of the domain. The ABC absorbs the waves, virtually allowing the waves to radiate infinitely far into the free space. The ABC must be placed at least a quarter of the wavelength away from the source of radiation (60).

In computational electromagnetics, the variations of the electric field within each element are described by Maxwell equations in the element local coordinate system. Much like FEM for structural analysis, these equations are mapped into the global coordinate system and combined to form the matrix equations that govern the entire region. The final matrix may be massive, but is sparse and often times symmetric (55). Solving this global set of equations gives the electric field, which can then be converted to the magnetic field.

Gamache et al. (61) compared 2D FDFD and FEM simulations using COMSOL Multiphysics for investigating the use of GPR in the detection of low dielectric nonmetallic anti-personnel mines.

4.2 Finite-Difference Time-Domain (FDTD)

Finite-difference time-domain (FDTD) is a popular computational electromagnetic method. It was introduced by Kane S. Yee in 1966. In FDTD, the domain is discretized into a rectangular grid called Yee lattice. Maxwell's equations are applied to each individual cell, and the problem is solved in the time domain. The time-dependent partial derivatives of Maxwell's equations are replaced by a central difference approximation, hence the name finite-difference time-domain. The term was coined by Allen Taflove in 1980 (62). FDTD directly calculates E and H fields iteratively at each grid location using a leapfrog scheme. Figure 4-2 depicts the field distribution on a rectangular unit cell. The E fields are located in the middle of the edges, and the H fields are normal to the cube faces in the middle of E field components.

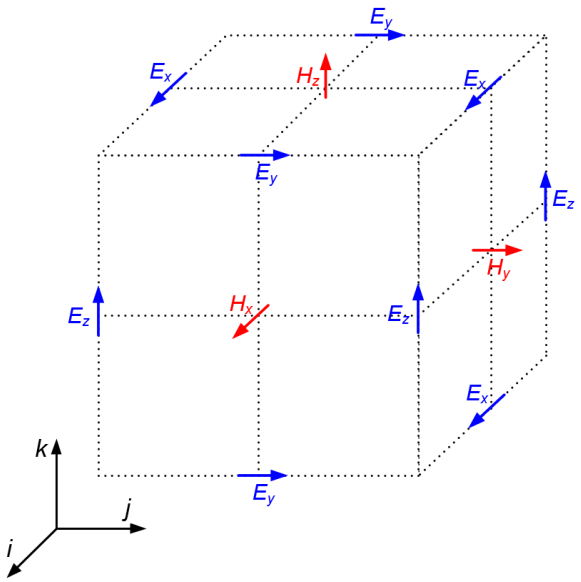

Figure 4-2. Yee lattice.

In FDTD, both space and time are discretized. Given the stability condition, the time increment Δt is *not* independent of spatial increments Δx, Δy, and Δz. FDTD stability condition known as CFL[1] condition is as follows (63):

$$\Delta t \leq \frac{1}{c\sqrt{\frac{1}{(\Delta x)^2}+\frac{1}{(\Delta y)^2}+\frac{1}{(\Delta z)^2}}} \tag{4-1}$$

Where c is the speed of light in the medium.

One of the FDTD's advantages is that inhomogeneity, anisotropy, and nonlinearity of materials can be easily modeled using this technique (55). However, since the entire domain is gridded, this method is computationally-intensive. In particular, simulating small geometrical features or complex structures is difficult and inefficient using FDTD. One of the main issues associated with FDTD is that given the rectangular shape of the unit cells, complex curved boundaries need to be approximated using staircase approximation with very small cells. A fine grid with small spatial increments requires considerably smaller time increments as well to satisfy the CFL stability condition. Therefore, a significant reduction in the spatial and temporal increments to obtain reasonably accurate solutions drastically increases the memory requirements. Also, calculating far field quantities requires considerably bigger domains and therefore the need for more substantial computational resources.

FDTD has been extensively used in civil engineering applications. Ciampoli et al. (64) used the gprMax 2D simulator for modeling the use of a 2GHz horn antenna on a multi-grain railway ballast to investigate the effect of ballast grain sizes in the scattering of EM

[1] CFL condition is named after the initials of Courant, Freidrichs, and Lewy.

waves. The study was accompanied by a series of laboratory tests. The results of FDTD simulations were compared with the results of the experimental program. The laboratory testing results underestimated the grain sizes by approximately 20%.

Gurel et al. (65) used three-dimensional FDTD simulations of a GPR unit in a transmitter-receiver-transmitter (TRT) configuration to detect buried rectangular prisms and circular disks. The authors used perfectly matched layers (PMLs) for boundary conditions. PML is an absorbing boundary condition used to curtail the simulation domain.

Huston et al. (66), in a report for The New England Transportation Consortium, describe the performance of one and two-dimensional FDTD simulations of GPR application on reinforced concrete pavements, along with the results of laboratory and field experiments. The 1D simulations were conducted to study the feasibility of using GPR to detect 1mm thick air-filled delamination.

Two-dimensional FDTD has been the most widely used numerical method for GPR simulation. Fang et al. used FDTD to study electromagnetic wave propagation in pavement structures. In their simulations, they assumed that pavement was a 2-D isotropic material (67).

Feng et al. (68) used a hybrid combination of FDTD and finite element time domain simulations for the detecting defects in tunnel lining using GPR. The hybrid simulations allow for a more accurate simulation of irregularly shaped defects.

Lachowicz and Rucka (69) used the gprMax 3D simulator to detect closely spaced reinforcing bars in complex structures.

Irving and Knight (70) generated an open source MATLAB script for two-dimensional FDTD simulations. They used PML absorbing boundary conditions to truncate the simulation grid.

4.3 Method of Moments (MoM)

The method of moments (MoM) is the oldest computational electromagnetic method (CEM). It was introduced by R. F. Harrington in 1968 to solve the integral form of Maxwell equations using the Green's function (71). MoM solves Maxwell's equations in the frequency domain and is an efficient technique for simple problems involving simple metallic antennas and homogenous materials. However, for more complicated problems, this method becomes computationally expensive (55).

MoM is a boundary element method. In other words, the mesh is generated over the surface, unlike the other methods in which the mesh is created over the model volume. The resulting matrices are often times huge, with many nonzero elements, making this method computationally intense. Despite significant achievements in numerical simulations of GPR, there is still much room for improvement in terms of complexity, accuracy, and efficiency of the model.

In Chapter 5, the results of three-dimensional finite element simulations of GPR surveys on reinforced concrete slabs are presented. The results are first post-processed in the time domain, and then analyzed using STFT.

Chapter 6 includes a two-dimensional parametric study performed using FDTD. The results are later used to develop a database for the purpose of constructing a learning algorithm to evaluate the deck condition.

Chapter 5. Finite Element Study

5.1 Introduction

Given the complexity of the medium and the complex nature of GPR incident waves, the exact solutions for Maxwell's equations are not available for many scenarios, including the case of bridge decks. Therefore, numerical simulations are necessary to obtain a thorough understanding of the electromagnetic wave propagation within an intact or an otherwise deteriorated reinforced concrete bridge deck.

A series of 3D numerical simulations were conducted using FEM to investigate the electromagnetic wave propagation through reinforced concrete bridge decks. The objective was to generate a set of GPR data based on 3D simulations and to compare them with the results of 2D FDTD simulations. The 3D FEM analyses proved to be very time-consuming while producing results comparable to the much faster 2D FTDT simulations. Therefore, in the interest of time, the finite element modeling was abandoned after a series of preliminary simulations.

Finite element method was used to investigate the GPR application on idealized models of reinforced concrete slabs with simple discontinuities describing delamination. The

numerical study described herein was conducted on three-dimensional (3D) finite element models. ANSYS HFSS, formerly known as Ansoft, was employed to perform the numerical simulations. HFSS uses a 3D full-wave electromagnetic field simulation to determine the EM wave propagation, and material behavior when exposed to high frequencies (60). HFSS uses tetrahedron elements to discretize models of arbitrary shapes. The finite element simulations are discussed next.

5.2 Three Dimensional FEM

Identical bow-tie transducers with a 2.6 GHz center frequency were used to simulate both the GPR transmitter and receiver (Figure 5-1).

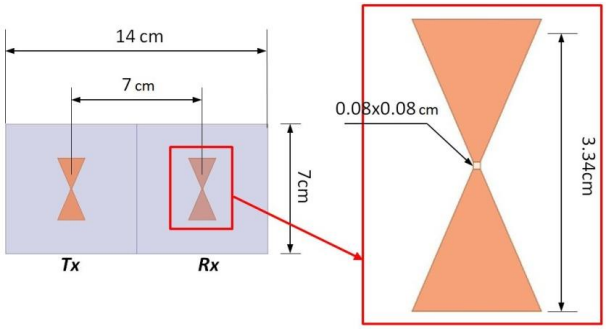

Figure 5-1. Bowtie antenna.

The transient solver was used to solve the problem in the time domain. The short-duration excitation pulse and its energy spectrum used for simulating GPR deployed on a bridge deck are depicted in Figure 5-2. The half bandwidth was set to 1.2 GHz with the minimum frequency of 1.4 and maximum of 3.8 GHz.

For mesh discretization, the automatic adaptive technique was used. Adaptive meshing is an iterative procedure in which the solution begins with an initial coarse mesh. Starting with a coarser mesh is advantageous because it increases the efficiency where fewer elements are needed to produce accurate results. In areas where much smaller elements are

needed for high accuracy, the mesh is refined iteratively at each step. The error in the S-parameters is calculated at the end of each iteration to determine whether the mesh is fine enough to produce an acceptable solution. S-parameters, or scattering parameters, are defined in terms of the incident and reflected signals. For a system with *N* ports, there are N^2 S-parameters, each corresponding to an input-output path. For *Sij*, the subscript *i* refers to the output port and the subscript *j* refers to the input port. For example, S_{12} refers to the response at port 1 due to an incident signal at port 2. Figure 5-3 illustrates the S-parameters for a two-port system (37).

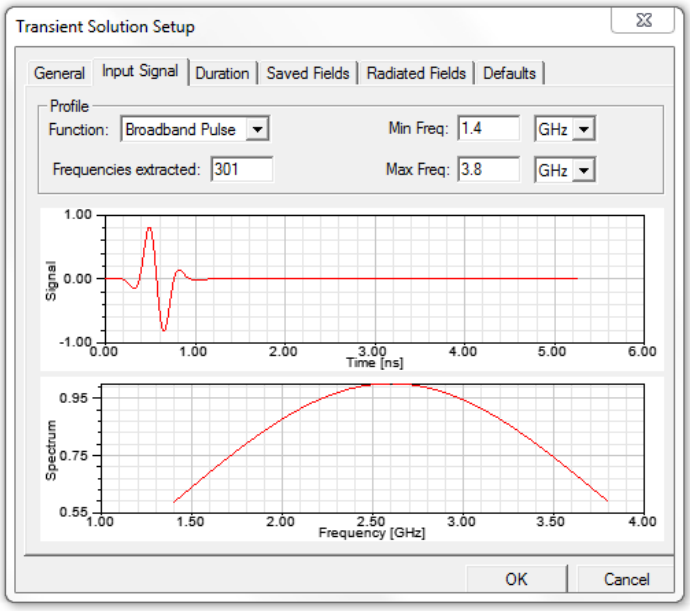

Figure 5-2. Input signal and its energy spectrum (for bridge deck simulations).

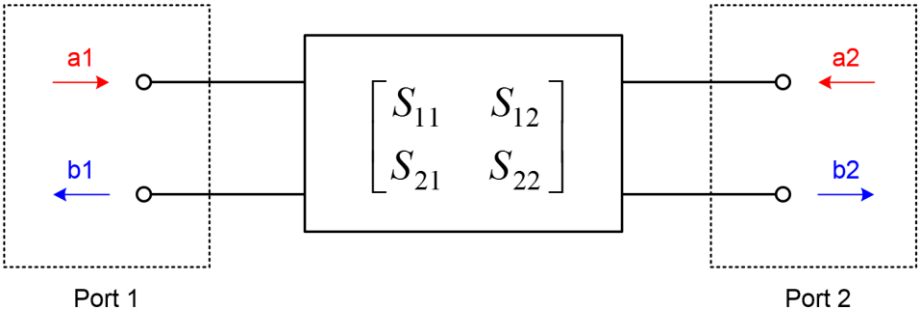

Figure 5-3. S-parameters matrix.

In Figure 5-3, a_js refer to the input/incident signals and b_is refer to the output signals. S_{11} and S_{22} are called the reflection coefficients whereas the off-diagonal elements are called the transmission coefficients.

Assuming all the other incident modes are turned off (or set equal to zero), the S-parameters are defined as the ratio of the signal amplitude at the output port to the signal amplitude at the input port:

$$S_{ij} = \left. \frac{b_i}{a_j} \right|_{a_k=0, k \neq j} \tag{5-1}$$

Therefore, the amplitudes at Port 1 and Port 2 are related as follows:

$$\begin{bmatrix} b_1 \\ b_2 \end{bmatrix} = \begin{bmatrix} S_{11} & S_{12} \\ S_{21} & S_{22} \end{bmatrix} \begin{bmatrix} a_1 \\ a_2 \end{bmatrix} \tag{5-2}$$

The iterative mesh refinement stops when the calculated error (ΔS) is less than a certain user-defined threshold, or after a certain number of iterations are performed. This is the convergence criterion in HFSS. In this study, the convergence criterion was set at ΔS=20% or 10 iterations, whichever is achieved first. The 20% ΔS was reached after eight iterations. The HFSS default ΔS value is 30%. The 20% threshold was chosen by trial and error.

5.2.1 (a) Single Channel GPR on RC Slab

To examine the feasibility of using STFT to analyze GPR survey results, numerical investigations of a single channel GPR antenna deployed on various reinforced concrete slabs with and without damage were conducted. The results were post-processed in both time and frequency domains. The slabs were all 72cm × 24cm × 20cm. The reinforcements

were 1.2 cm in diameter and 20 cm apart horizontally (Figure 5-4 and Figure 5-5). Figure 5-4 illustrates the intact slab with two layers of reinforcement. Figure 5-5 depicts the model with delamination at the level of (a) top reinforcement, and (b) bottom reinforcement. The slab and delamination were each simulated using solid elements with electromagnetic properties of concrete, air, and water.

The slabs were assumed to be in the free space, which was modeled using absorbing boundary condition (ABC) on the outside surface of the air region. The ABC absorbs the waves, virtually allowing the waves to radiate infinitely far into the free space. The distance between each edge of the slab and the ABC, or simply the thickness of the air region, was set to 3cm to comply with the ABC requirement that it must be placed at least a quarter of a wavelength away from the source of radiation. The wavelength for EM waves generated by a 2.6 GHz antenna and traveling through a concrete medium with a dielectric constant of 9 is approximately 3.8 cm.

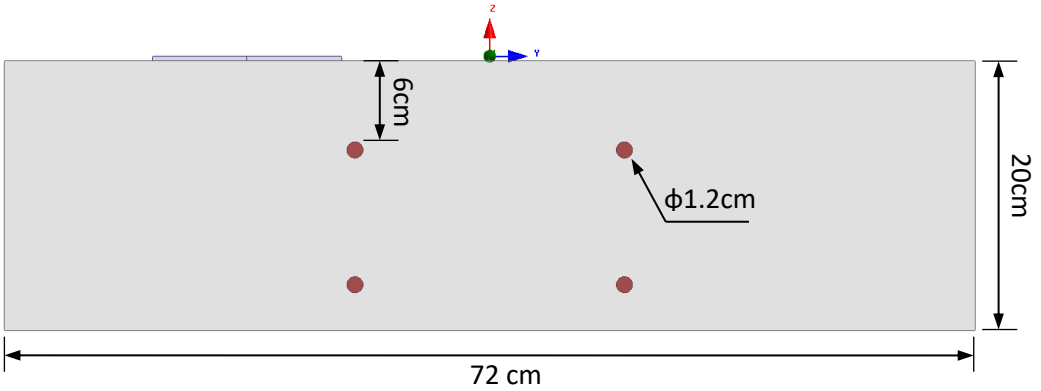

(a)

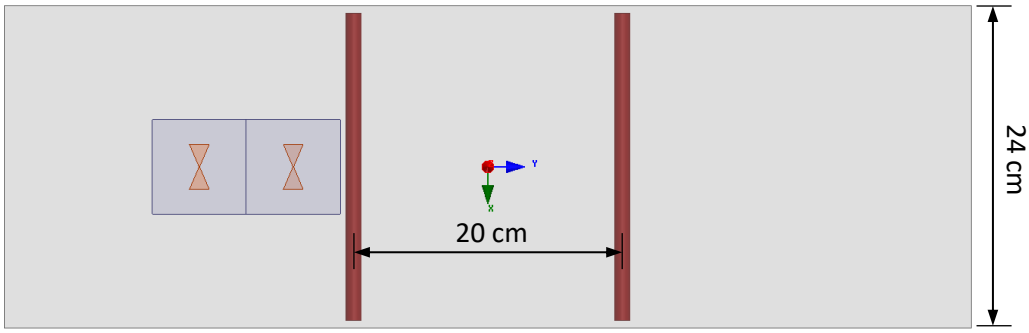

(b)

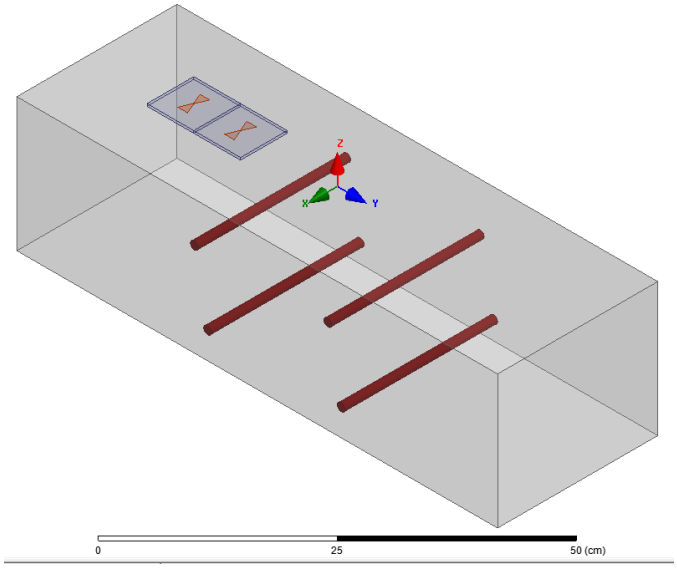

(c)

Figure 5-4. Control Slab: (a) side view, (b) plan view, (c) isometric view.

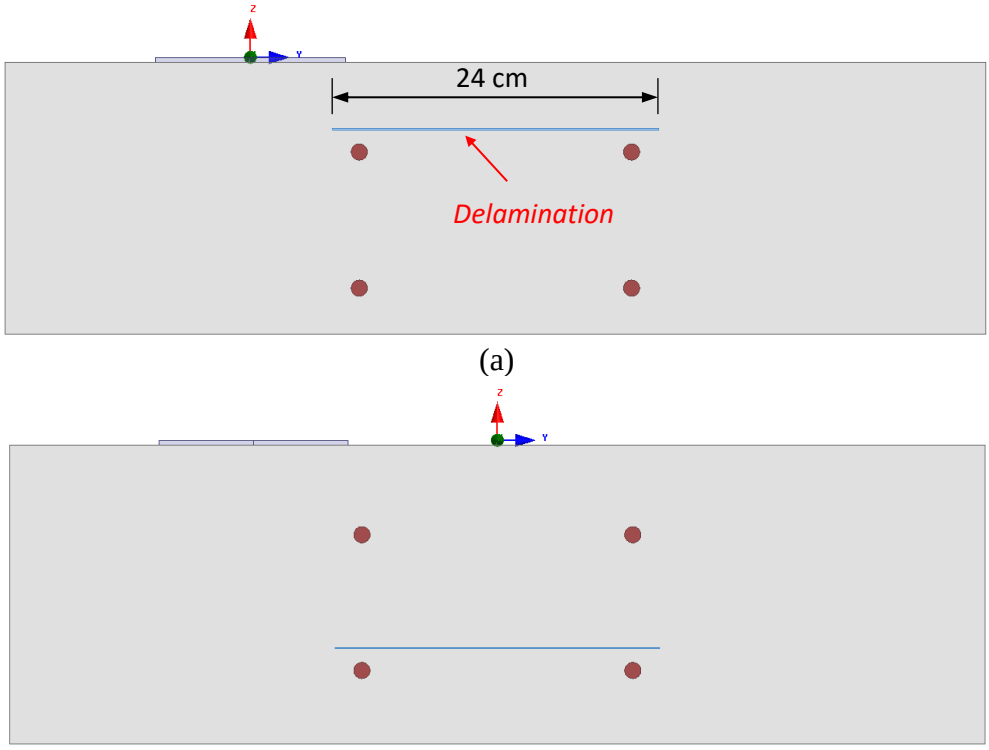

Figure 5-5. Model with delamination at (a) the top reinforcement level, (b) the bottom reinforcement level.

The outer surface of the reinforcements was modeled as a perfect electrical conductor (PEC) boundary condition. PEC forces the E-field perpendicular to the surface and represents a metallic surface (60). A PEC surface is illustrated in Figure 5-6. The tangential component of the E-field is equal to zero at the surface. Each transducer had a lumped port excitation in the model. In HFSS, the feed for a dipole antenna is simulated using a lumped port.

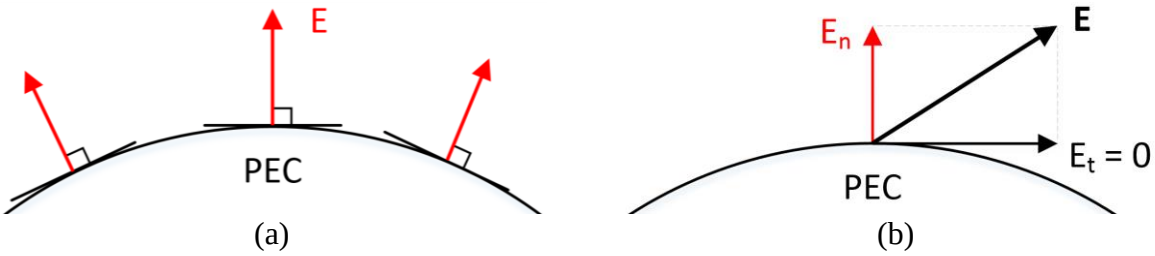

Figure 5-6. Boundary condition at a PEC Surface.

For simulating the antenna movement on the slab, a parametric sweep was performed. The sampling rate of 1 cm was used in the parametric study (Figure 5-7). A smaller sampling rate provides a more realistic and smoother B-scan. However, given the amount of time it takes to run a three dimensional FE model, the 1cm sampling rate was a reasonable compromise. The simulated scenarios are summarized in Table 5-1.

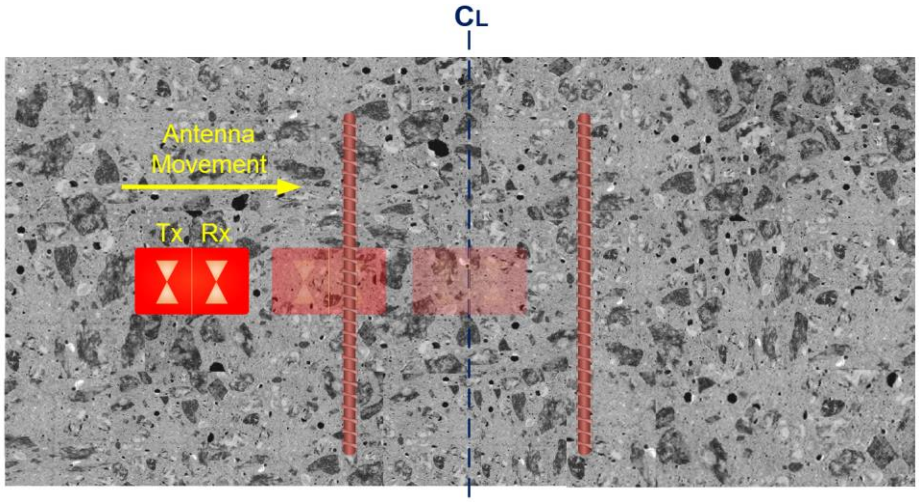

Figure 5-7. The antenna moved towards the center line at 1cm increments.

Table 5-1
3D FEM Case Scenarios

Model Code	Model Description
C	control slab with two layers of reinforcement
B	slab with only bottom layer reinforcement
AD – T1	slab with 1 mm thick air-filled delamination located near the ***top*** reinforcement
AD – B1	slab with 1 mm thick air-filled delamination located near the ***bottom*** reinforcement
WD – T1	slab with 1 mm thick water-filled delamination located near the ***top*** reinforcement
WD – T3	slab with 3 mm thick water-filled delamination located near the ***top*** reinforcement
WD – B1	slab with 1 mm thick water-filled delamination located near the ***bottom*** reinforcement

The material properties used in these simulations are provided in Table 5-2.

Table 5-2
Material properties

Material	Relative Permittivity	Bulk Conductivity (Siemens/m)	Dielectric Loss Tangent
Concrete	9	0.01	0.1
Steel	10000	1e30	0
Plastic	2.2	0	0.0009
Water	81	1	0
Air	1	0	0

The B-scans plotted using the raw simulation data are presented in Figure 5-8. There is not any significant discernable difference between Figure 5-8 (a) and Figure 5-8 (b) (control model and the air-filled delamination near the top reinforcement). Studying the frequency content can help to distinguish among different simulated scenarios.

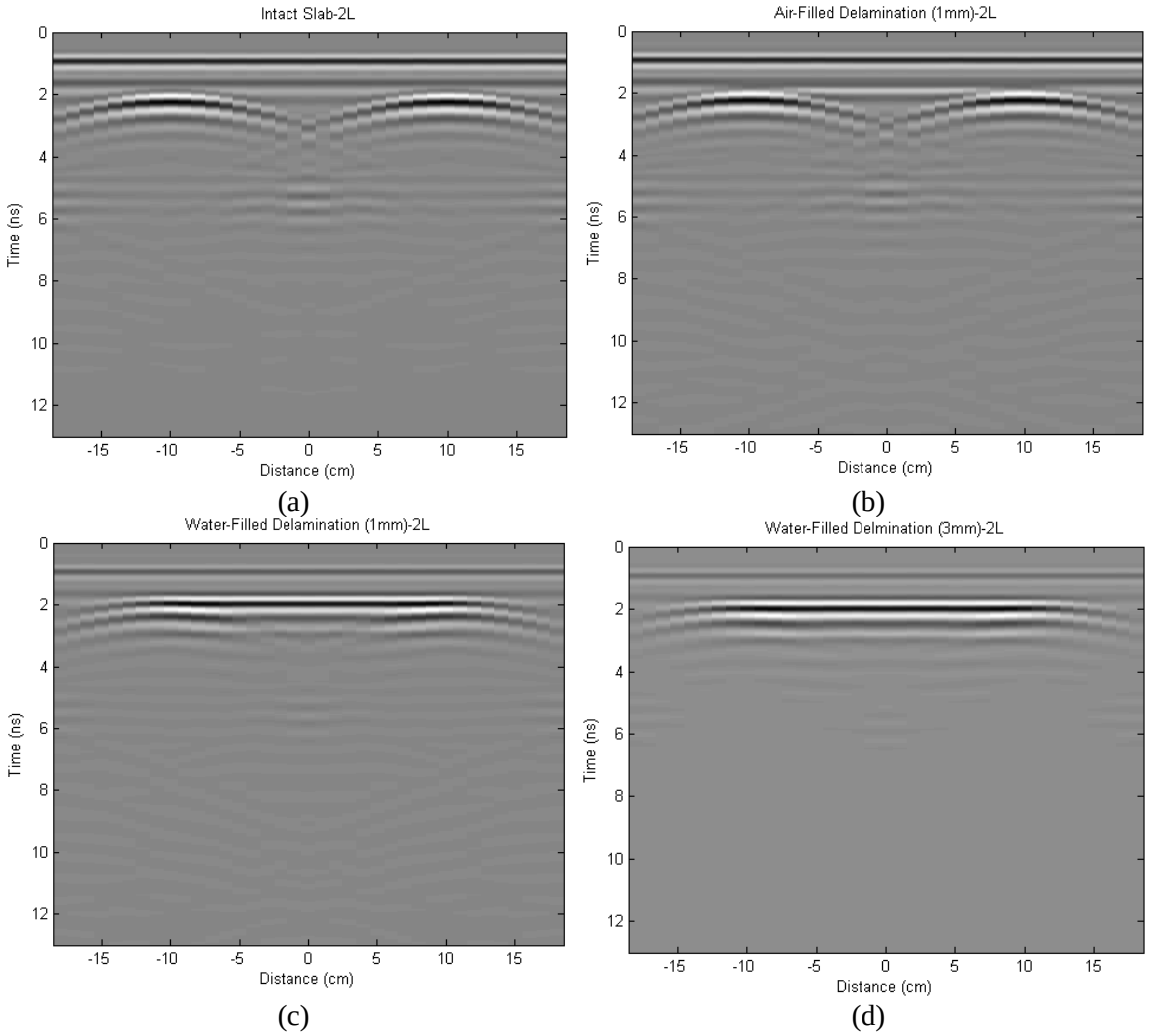

Figure 5-8. B-Scans using FEM raw simulation data. (a) Control slab with no damage, (b) Slab with 1 mm thick air-filled delamination at the top rebar level, (c) Slab with 3 mm thick air-filled delamination at the top rebar level.

To increase the visibility and detectability of low amplitude features, it was deemed necessary to apply a gain function to each individual A-scan. Using a gain function is solely for visualization purposes and does not change the frequency content of a given signal. Since the goal was to suppress some reflections and amplify some others corresponding to the target, the gain function varied with time. Figure 5-12 illustrates a 5-point gain function.

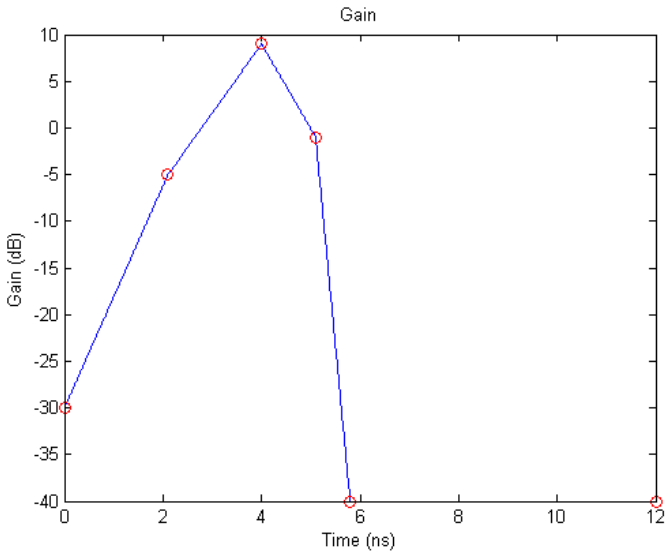

Figure 5-9. Time-varying gain function.

The time-varying gain function in logarithmic scale is given by (38):

$$g(n) = g(1) + \frac{g(N) - g(1)}{N - 1}(n - 1) \tag{5-3}$$

Where n represents the index of the sample along the time axis, and N is the total sample numbers. Therefore, the gain function in dB has a linear relation with time (or the penetrating depth).

The raw amplitudes are then multiplied by $10^{g(i)/20}$:

$$A_g(i) = A_0(i) \times 10^{g(i)/20} \tag{5-4}$$

Where A_g is the signal amplitude after the gain function is applied and A_0 is the amplitude of the raw signal.

Figure 5-10 illustrates a representative A-scan before and after applying the gain function.

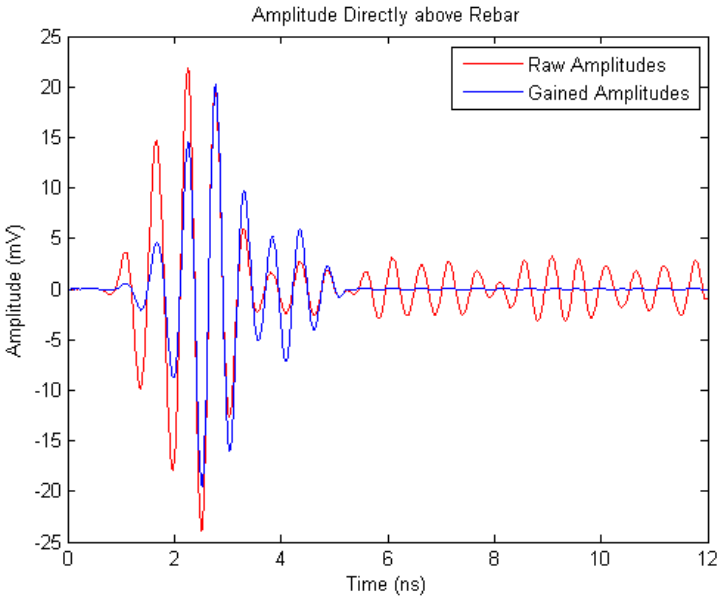

Figure 5-10. A-scan before and after the gain function was applied.

In Figure 5-11, the B-scans for two delaminated models before and after applying the gain function are presented. The gain function was selected in a way to suppress the surface reflection and to promote the reflection from the bottom reinforcement.

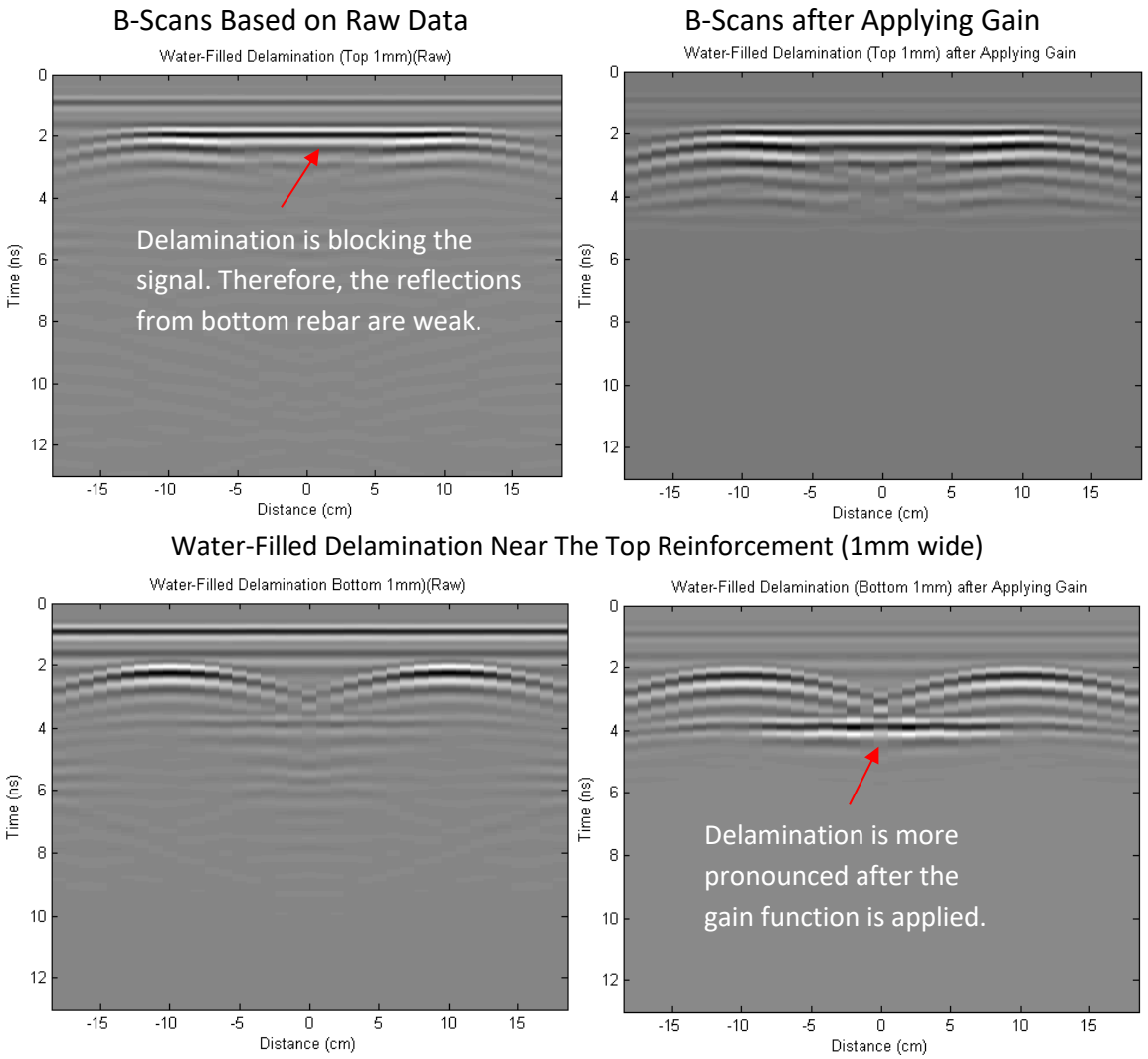

Figure 5-11. B-Scans before and after applying gain function.

Short-time Fourier transform (STFT) was earlier discussed in Section 3.4.6. STFT was applied to raw simulation data (no gain or filter were used). The dominant frequency at the reinforcement location for each case scenario was extracted and plotted in Figure 5-12. The peak frequencies were selected from the spectra, rather than the spectrograms. As shown in Figure 5-13 (b), the dominant frequency in the spectrogram appears to be higher and wider than the peak frequency in the spectrum. If a wider window were to be used, the frequency resolution would have increased, and the peak frequency in the spectrum would

have become closer to the dominant frequency in the spectrograms. However, as discussed earlier, this would have had an adverse effect on the time resolution.

The dominant frequency for the control slab is 1.86 GHz. For the models with delamination located above the top reinforcement, the dominant frequency is higher than that of the control model. On the other hand, when the delamination is close to the bottom reinforcement, the dominant frequency at the reinforcement location is considerably lower (Figure 5-12). These dominant frequencies point out whether the delamination is located near the top or bottom reinforcement, but they do not assist in characterizing the delamination type, i.e., whether it is air- or water-filled. Reviewing the STFT spectrograms can potentially resolve this issue.

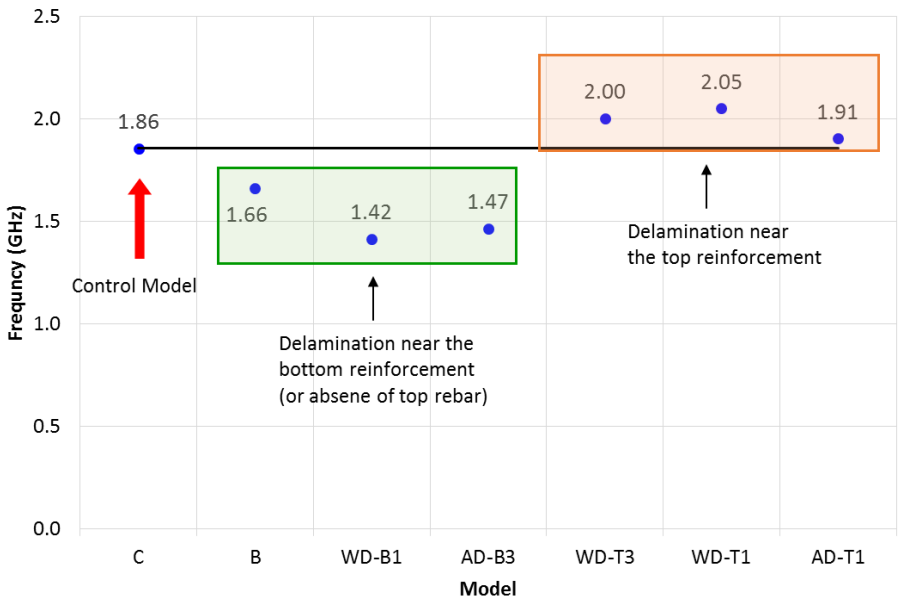

Figure 5-12. Dominant frequency at reinforcement location extracted from STFT.

The STFT spectrograms plotted using the raw simulation results are presented in Figure 5-13. In the case of the control model (Figure a), three distinctive pockets of energy are evident. These energy pockets correspond to the surface reflection, top layer reinforcement, and bottom layer reinforcement/ bottom of the slab.

When the delaminated region is located above the top reinforcement (Figures d, e, and f), the dominant frequency is above the 1.86 GHz associated with the control model. As mentioned earlier, the frequency content alone can narrow down the location of the defect but does not help with characterizing the type of damage. Looking at the spectrograms can provide more insight into the deterioration type: when delamination is water-filled (Figures d and e), there is only a single strong energy pocket between those associated with surface reflection and top reinforcement in the control model. The energy pockets associated with the surface reflection and the bottom of the slab are very weak. On the other hand, when delamination is air-filled (Figure f), all three energy pockets can be seen.

Comparing Figures (d) and (e) provides an insight into the effect of thickness of delamination. When there is a thick delamination, Figure (d), the energy pocket associated with the bottom of the slab/the lower level reinforcement is much weaker than the one in Figure (e) which corresponds to thinner delamination. The reason is the strong masking effect of the thick delamination.

When the delamination is near the bottom reinforcement (Figure (c)) or in the absence of the top reinforcement (Figure (b)), the dominant frequency is significantly lower than 1.86 GHz of the control model. The spectrograms clearly point to the lack of top reinforcement in Figure (b) and the presence of delamination near the bottom reinforcement in Figure c.

STFT provides quantitative information with respect to the dominant frequency as well as limited qualitative information based on the spectrograms which together can assist as a complementary tool in a more comprehensive full depth condition assessment of the bridge deck. However, given the amount of time and level of expertise needed for STFT analyses, it is not yet suited to be used as the only method for post-processing GPR surveys data.

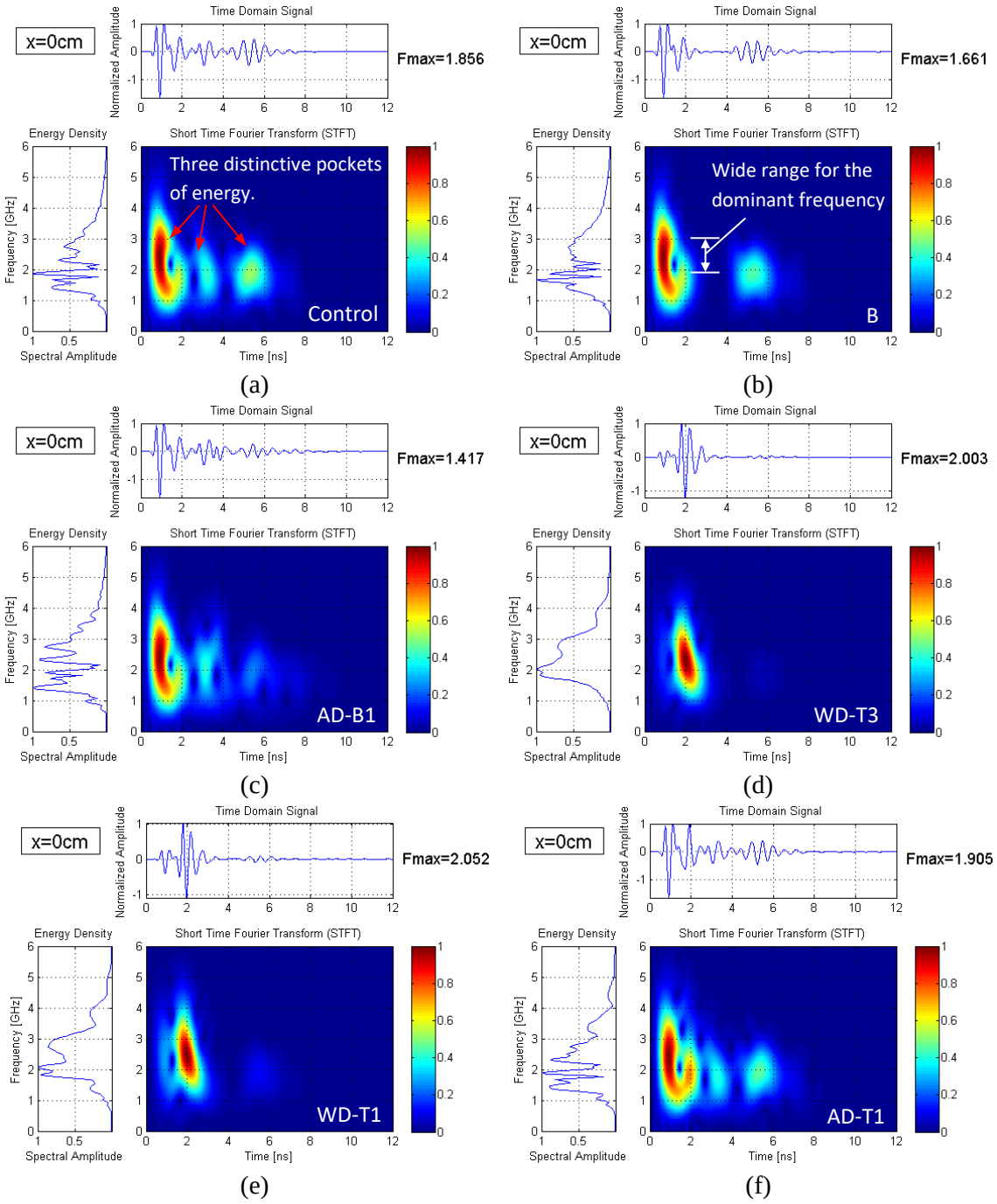

Figure 5-13. Spectrograms of the raw signals at x = 0; (a) control, (b) bottom reinforcement only, (c) AD-B1, (d) WD-T3, (e) WD-T1, (f) AD-T1. (See Table 5-2).

It must be noted that in all these figures, it is difficult to distinguish between the bottom of the slab and the bottom level reinforcement. The reason is that the distance between these two reflectors, i.e., the bottom level reinforcement and the bottom of the deck (1.8 cm) is

smaller than the vertical resolution for this particular antenna. The vertical resolution of a given GPR is about half the central wavelength. Therefore, the vertical resolution, in this case, is about 1.9 cm, which is why the two reflectors can hardly be resolved in either B-scans or spectrograms. Increasing the thickness of the slab in the simulations or changing the center frequency can resolve the resolution issue.

5.2.2 (b) Parametric Study (Dielectric Constant)

To evaluate the effect of dielectric constant on the EM wave propagation in a concrete slab, and its impact on the dominant frequency, a parametric study was conducted. In the new 3D FE models, the electrical conductivity was kept constant at 0.001 S/m. Three simulations were performed with the same geometry (Figure 5-14), but with a changing dielectric constant (6, 7, and 8).

The B-scans, spectrograms, and the normalized spectral amplitudes for each case are presented in Figure 5-15 through Figure 5-17. There is no significant difference observed in the three B-scans; however, the changes in the dominant frequency are noticeable. The dominant frequencies are summarized in Table 5-3. The higher the dielectric, the lower the dominant frequency. Per Equation (3-4), a higher dielectric value corresponds to a lower EM wave velocity. When the velocity of wave propagation is lower, the system's dominant features/natural response shift toward lower frequencies.

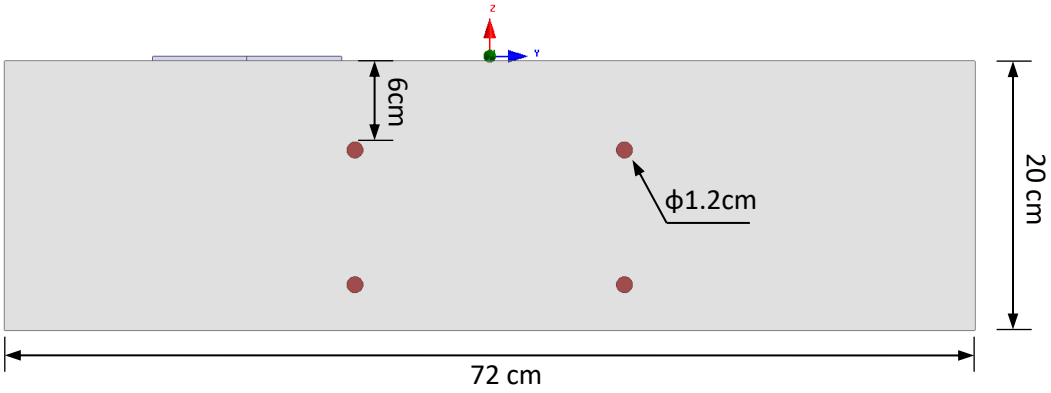

Figure 5-14. Parametric study – keeping the electrical conductivity constant, the dielectric value varied from 6 to 8.

Table 5-3
Dominant frequency for different dielectric values.

Relative Dielectric Constant	Dominant Frequency (GHz)
8	1.710
7	1.808
6	1.954

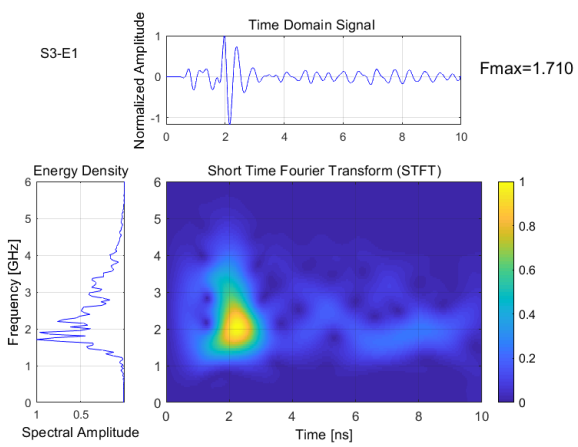

(a)

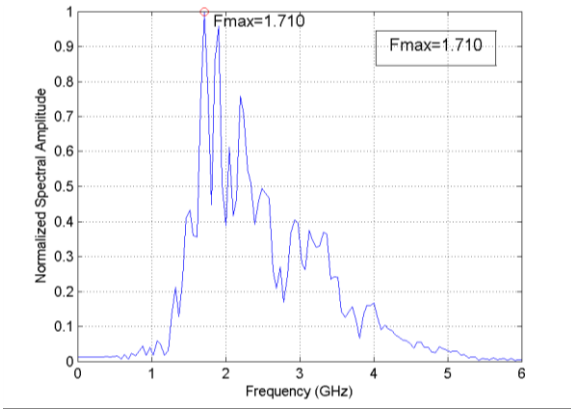

(b)

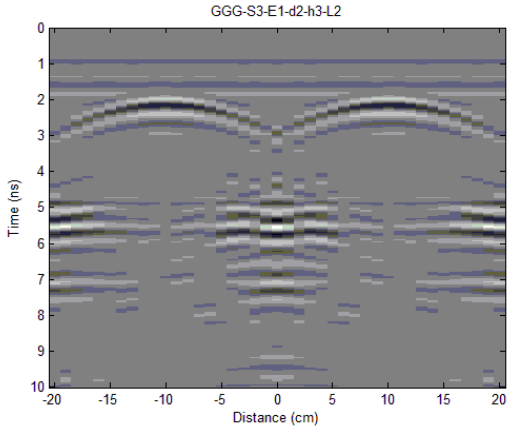

(c)

Figure 5-15. $\varepsilon_r = 8$ (f_{max} = 1.710 GHz); (a) spectrogram, (b) normalized frequency spectrum, (c) B-scan.

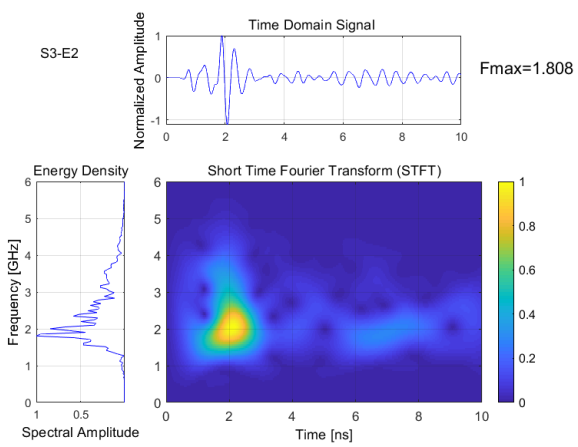

(a)

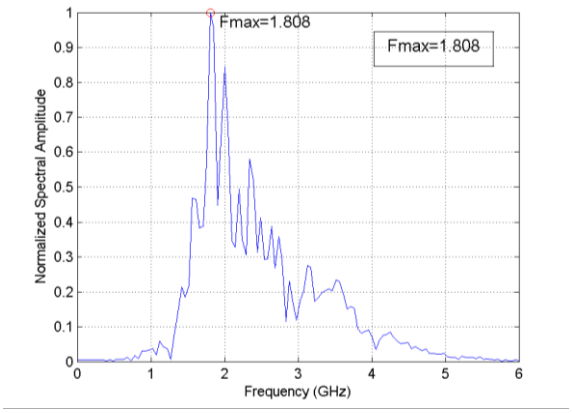

(b)

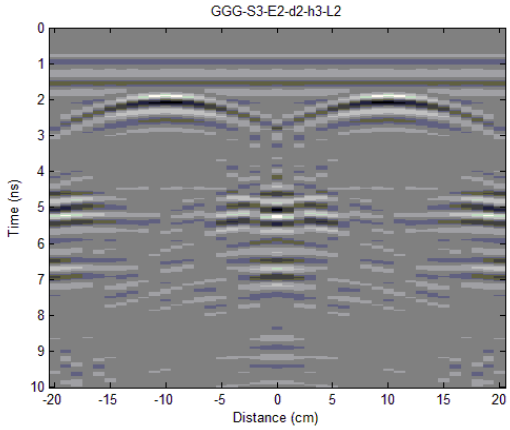

(c)

Figure 5-16. $\varepsilon_r = 7$ (f_{max} = 1.808 GHz); (a) spectrogram, (b) normalized frequency spectrum, (c) B-scan.

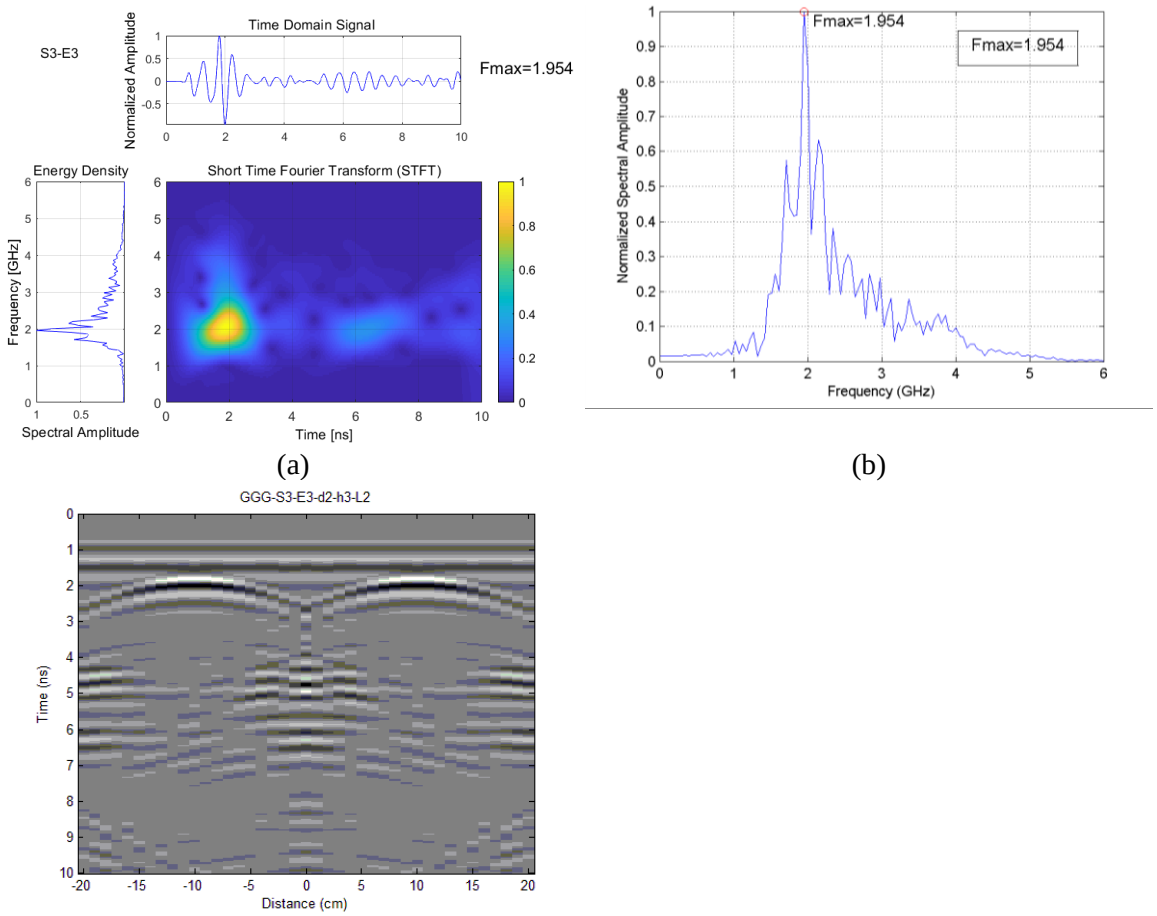

(a) (b)

(c)

Figure 5-17. $\varepsilon_r = 6$ (f_{max} = 1.954 GHz); (a) spectrogram, (b) normalized frequency spectrum, (c) B-scan.

5.2.3 (c) GPR Array on RC Slab

A GPR array was simulated to study the effective transducer pair spacing to obtain meaningful results from a survey. A GPR array can cover larger swathes in a considerably shorter time period compared to single channel antennas, thereby increasing the rate of the survey. However, after a certain Tx-Rx distance, the data from a given transducer pair becomes meaningless. A finite element study was conducted to find the optimal spacing for the purpose of bridge deck surveys.

Five identical transducers similar to the ones used in the single-channel GPR simulations were used to simulate a GPR array. Each transducer could potentially be either active or passive, i.e., transmitter or receiver. The model consisted of a homogenous 110×24×20 cm concrete slab, reinforced with four transverse reinforcing bars (Figure 5-18).

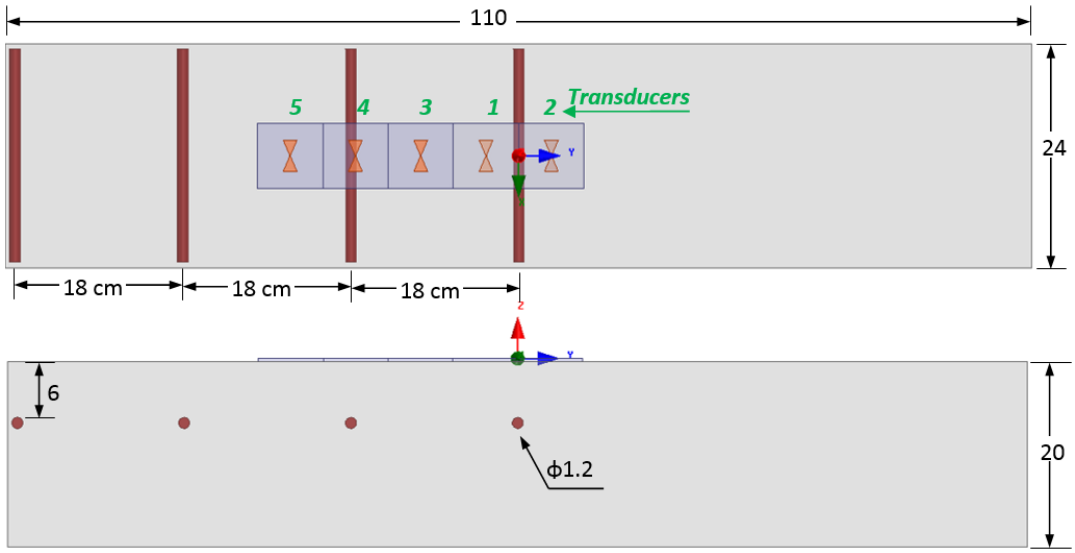

Figure 5-18. GPR array model (dimensions are in cm).

The B-scans based on different transmitter-receiver configurations are presented in Figure 5-19. T_{ij} refers to the transmitter-receiver path, in which i and j represent the transmitter and the receiver, respectively. For example, T25 means unit # 2 is working as a transmitter while unite # 5 is the receiver.

Although the B-scans from T12, T13 (not shown herein), T14, and to some extent T15 are successfully identifying the location of transverse reinforcement, the B-scan from T25 may be misleading in interpreting the GPR data. The center-to-center distance between transmitter # 2 and receiver # 5 is 28 cm (Figure 5-18). In this case, the ratio of the transmitter-receiver spacing to the rebar depth is 2.5 times greater than the wavelength. This suggests that using an array system, the reflections captured by a transmitter-receiver

pair should be disregarded when the ratio of the Tx-Rx spacing to the reflector's depth is greater than $2.5\times \lambda$. It must be noted that this conclusion is valid for a 2.6 GHz antenna and that scaling may be needed for different frequencies. Figure 5-20 illustrates the normalized input signal and a representative output signal. Representative A-scans are shown in Figure 5-21. The amplitudes for T12 are in mV, while the amplitudes for T14 and T25 are in μV.

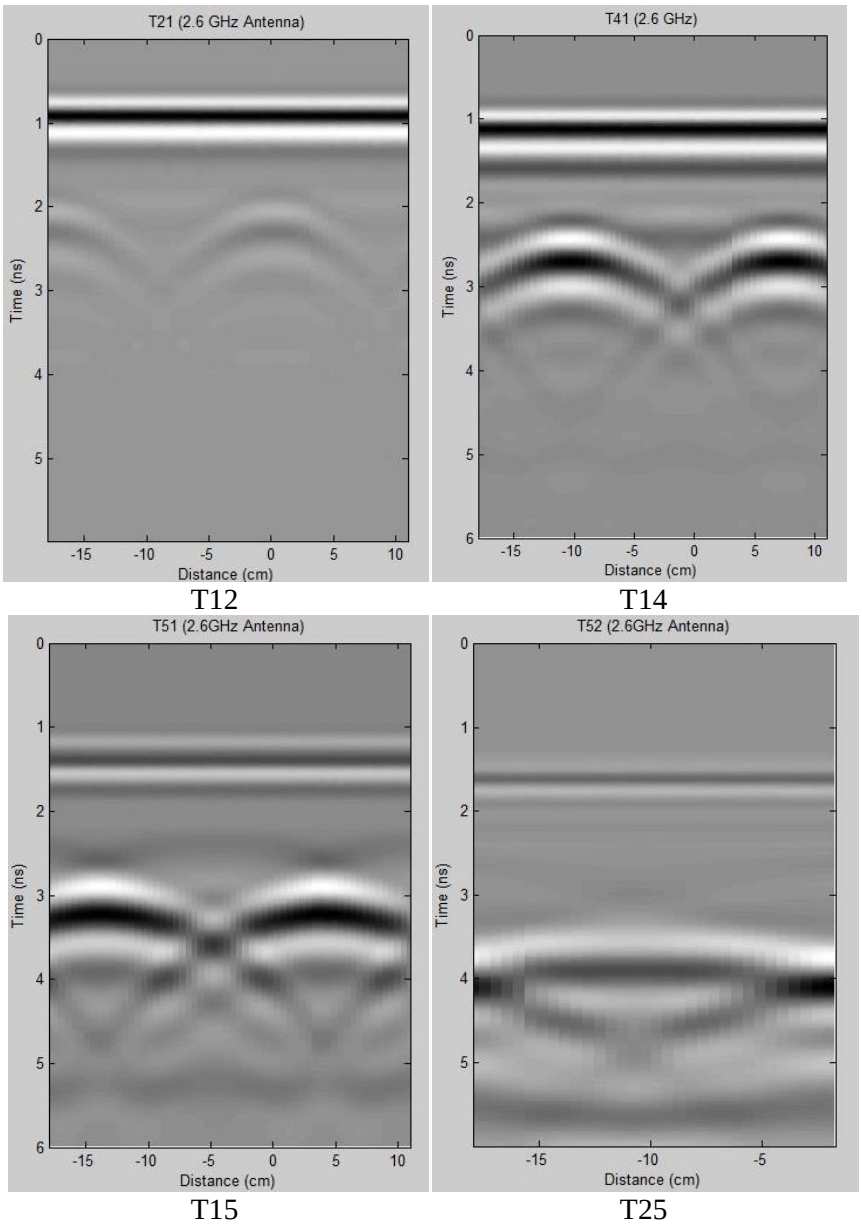

T12 T14

T15 T25

Figure 5-19. B-scans based on different Tx-Rx configurations.

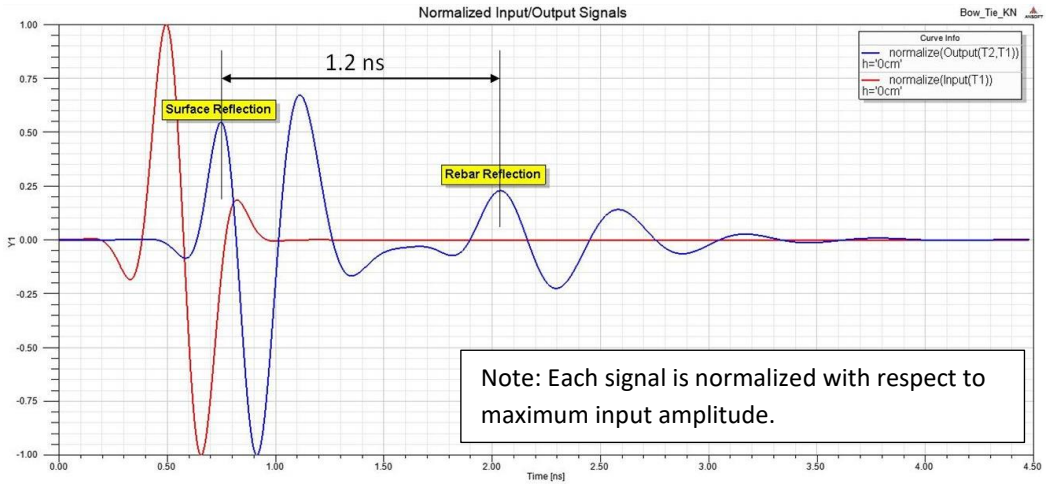

Figure 5-20. Normalized input/output signals (Red = Input, Blue = Output).

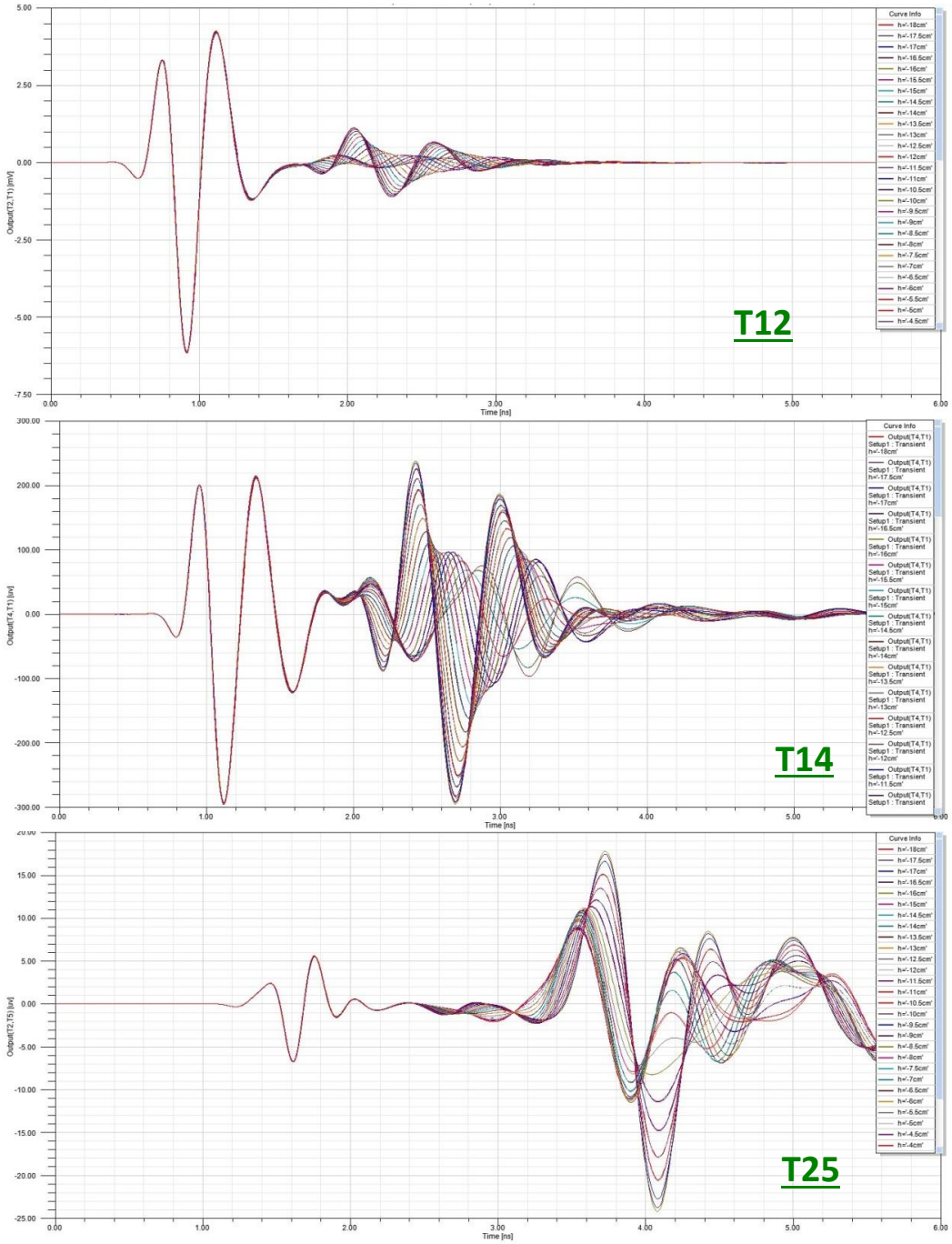

Figure 5-21. Representative A-scans.

The E-field contour maps on vertical and horizontal planes at 2.1 ns time slice are presented in Figure 5-22. The free space is not depicted herein. In this figure, only T1 is active (transmitter), and the other four transducers are receivers. The videos of the contour maps in motion allow for a better understanding of the wave propagation patterns and reflection

or scattering of EM waves in the presence of rebar or delamination. The images below are representative snapshots taken from those videos.

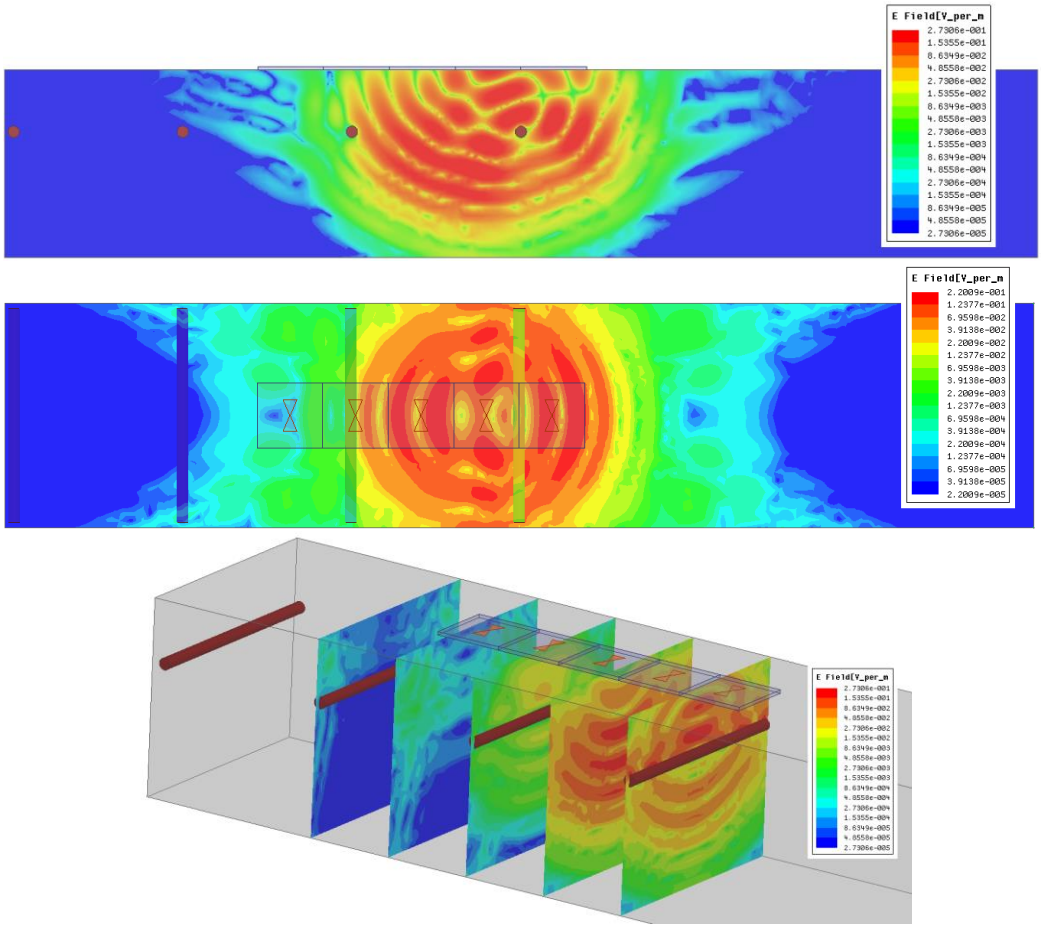

Figure 5-22. E-field at 2.1ns; transducer #1 is the only transmitter.

Figure 5-23 also represents the E-filed contour maps at 2.1 ns; however, in this case, transducers # 1 and # 5 are transmitting simultaneously.

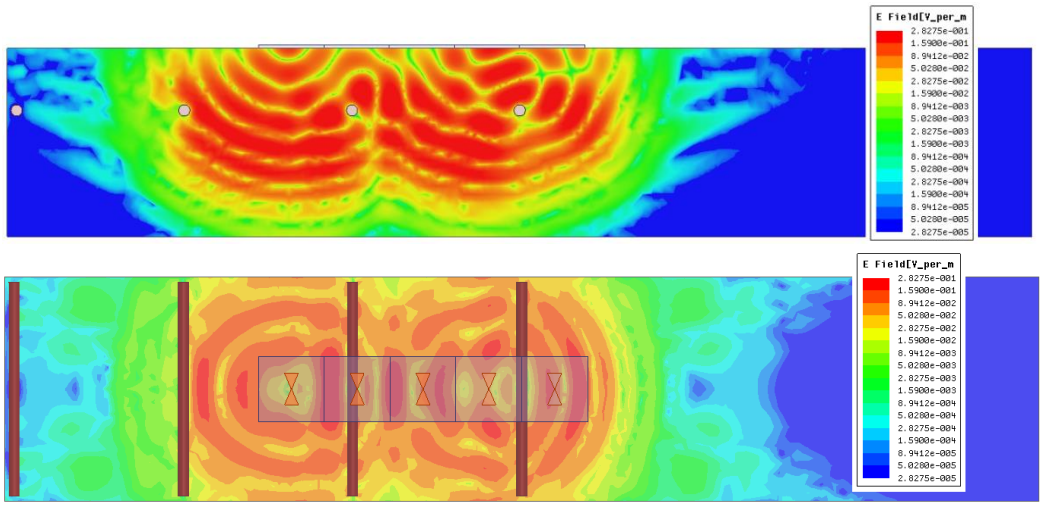

Figure 5-23. E-field at 2.1ns; transducers #1 and #5 are transmitting simultaneously.

Three dimensional FE models can provide a more comprehensive understanding of the EM wave propagation in a reinforced concrete slab. However, the FE simulations are significantly more time-consuming and the minor gain attained in understanding the influence of various parameters does not justify the cost of using FE simulations over simpler two-dimensional FDTD simulations. For the remainder of this study, FDTD simulations will be used.

Chapter 6. Parametric Study: FDTD

6.1 Introduction

A database of GPR data was developed through a parametric study based on a series of two-dimensional numerical simulations. The database was generated for the purpose of assessing the full depth of a bridge deck using machine learning. The simulations focused on studying the impacts of different parameters on the strength of reinforcement reflection, the masking effect of top rebar on the reflection from the bottom reinforcement, and assessment of the deck condition at various depths.

Parameters influencing the reflection from the bottom reinforcement, and the masking effect caused by the top rebars when placed directly above the bottom bars are discussed in Section 6.2. The masking effect when the rebars are not aligned, i.e., when the bottom reinforcement has an offset relative to the top reinforcing bars are explored in Section 6.3. Section 6.4 discussed the effect of variations of electromagnetic properties of concrete on the attenuation levels. Finally, the process of developing a GPR dataset using numerical simulations as the basis of a learning algorithm to assess the full depth of a concrete bridge deck is discussed in Section 6.5.

6.2 Parametric Study – Masking Effect of Top Reinforcement (Rebars Aligned)

A series of 2D FDTD simulations were conducted to investigate the masking effect of the top reinforcement on the signal reflected from the bottom rebar when the top and bottom bars were aligned (Figure 6-1 (a)). A parametric sweep was performed for various transmitter-receiver (Tx-Rx) spacing, as well as the bottom reinforcement depth, to obtain an optimal spacing/depth relationship for evaluating the strength of reflection from the bottom reinforcement. Only a single A-scan was simulated for a symmetrical model (Figure 6-1(a)) for various transmitter-receiver spacing: 6, 7, 10, 12, and 16 cm and for the bottom reinforcement depth varying from 10 to 18cm. The effect of Tx-Rx spacing on the B-scan appearance was shown in Figure 5-19. A series of companion simulations were conducted in which the top reinforcement was removed to study the reflection off the bottom reinforcement alone to quantify the masking effect of the top rebar (Figure 6-1(b)). The antenna center frequency used in all the numerical simulations was 2.6 GHz. The Ricker wavelet was used as the excitation signal.

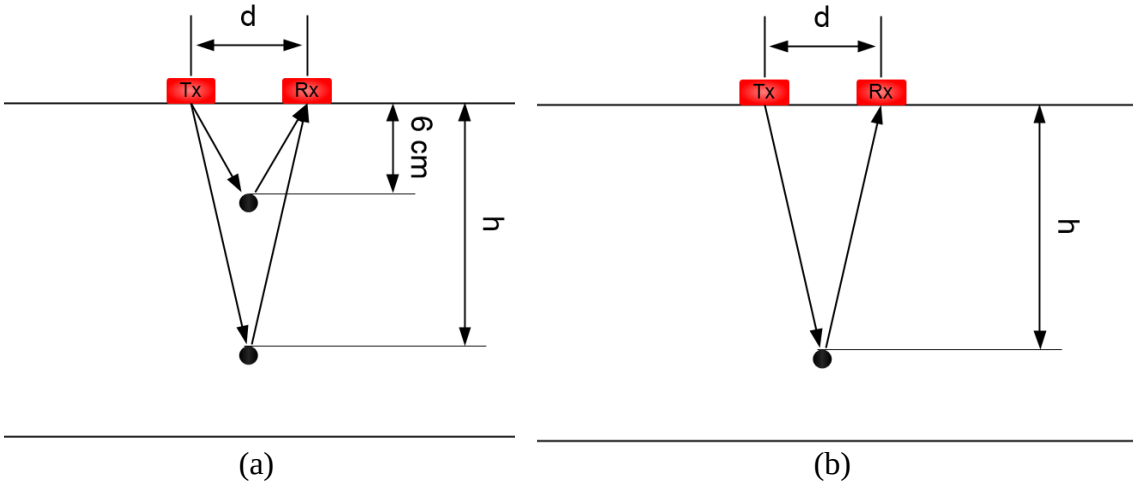

Figure 6-1. (a) Both top and bottom bars present, (b) top bar absent (only one bar toward the bottom of the slab).

Figure 6-2(a) illustrates representative A-scans from this set of simulations. The blue curve is associated with a model when both the top and bottom bars are present, while the black curve represents the model in which only the bottom bar is present (see Figure 6-1). The peaks associated with the direct wave, surface reflection, top bar, bottom bar, and the bottom of the slab are shown. Figure 6-2(b) provides more details of the reflections from the bottom rebar and bottom of the slab. There are several multiples observed in the A-scan, which can be attributed to the high center frequency and, therefore, a high resolution of the simulation. When the simulation was repeated using a 1.5 GHz antenna, there were fewer multiples in the A-scans given the fact that lower frequency antennas provide greater depth of penetration, but lower resolution (Figure 6-3).

Figure 6-4(a) illustrates the masking effect of the top reinforcement on the signal reflected from the bottom reinforcement for various combinations of Tx-Rx spacing and reinforcement depth. The masking effect was calculated as follows:

$$Masking\ Effect\ (\%) = 100 - 100 \times \frac{Amplitude\ at\ the\ Bottom\ bar\ (Top\ bar\ present)}{Amplitude\ at\ the\ Bottom\ bar\ (Top\ bar\ absent)} \qquad (6\text{-}1)$$

The masking effect decreases linearly with increasing depth of the bottom reinforcement and with increasing Tx-Rx spacing. A higher percentage is indicative of a higher masking effect by the top reinforcement. For a typical bottom reinforcement placed 16 cm deep in the slab (green line), the top reinforcement masks over 63% of the amplitude when the Tx-Rx spacing is 6 cm. For a reinforcement at the same depth, the masking effect reduces to under 11% when the Tx-Rx spacing is 16 cm (The green line in Figure 6-4(a)).

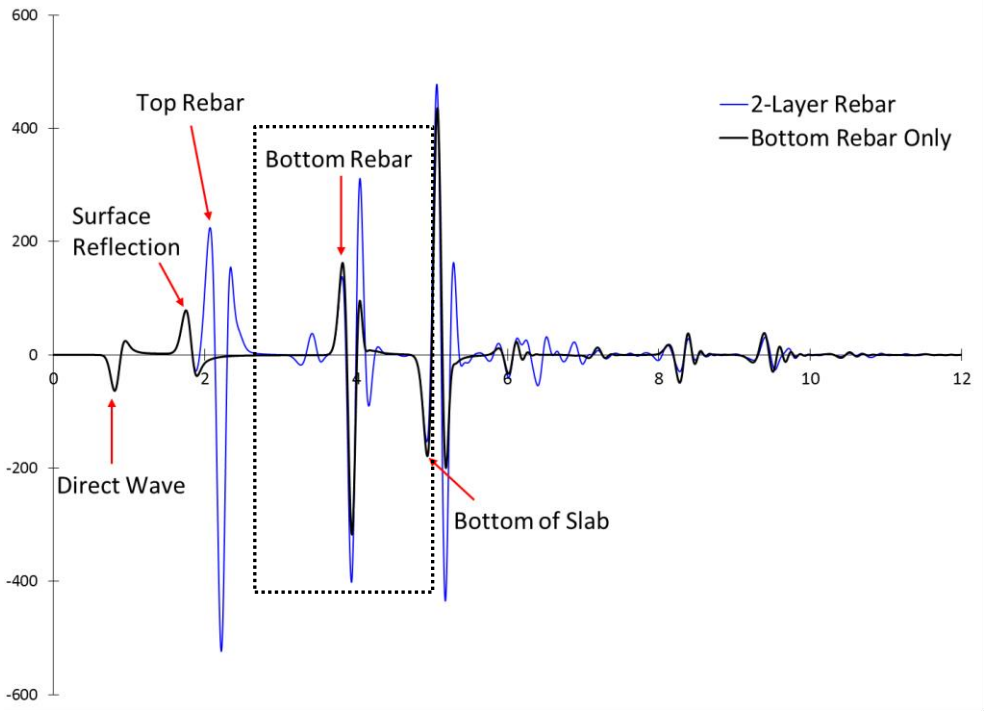

(a)

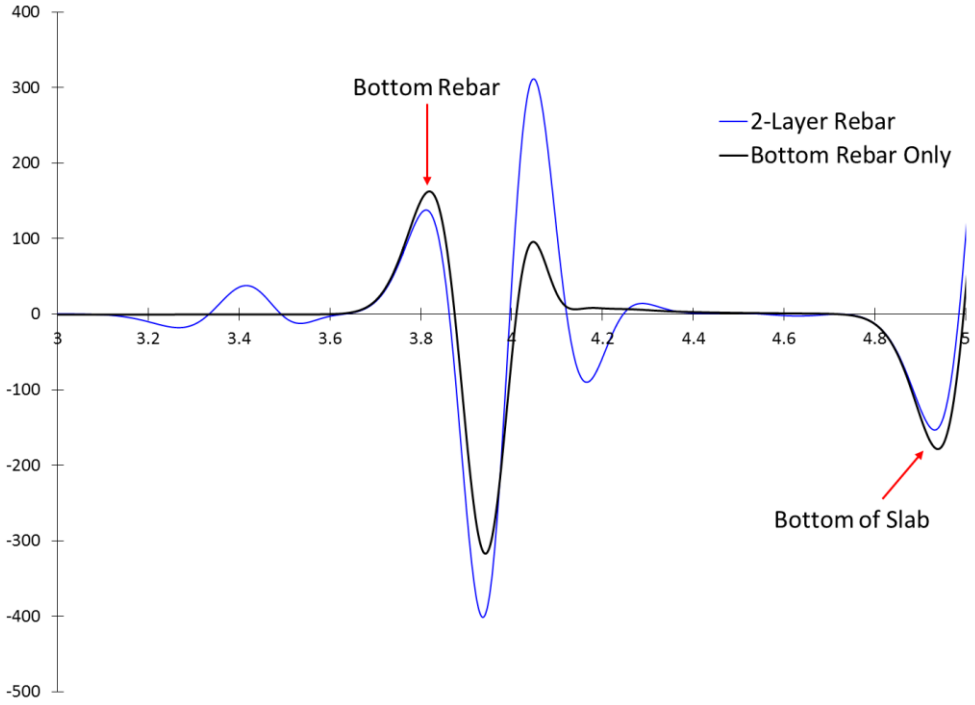

(b)

Figure 6-2. (a) Representative A-scans for Tx-Rx distance of 14 cm, (b) enlarged plot to focus on the bottom rebar reflection.

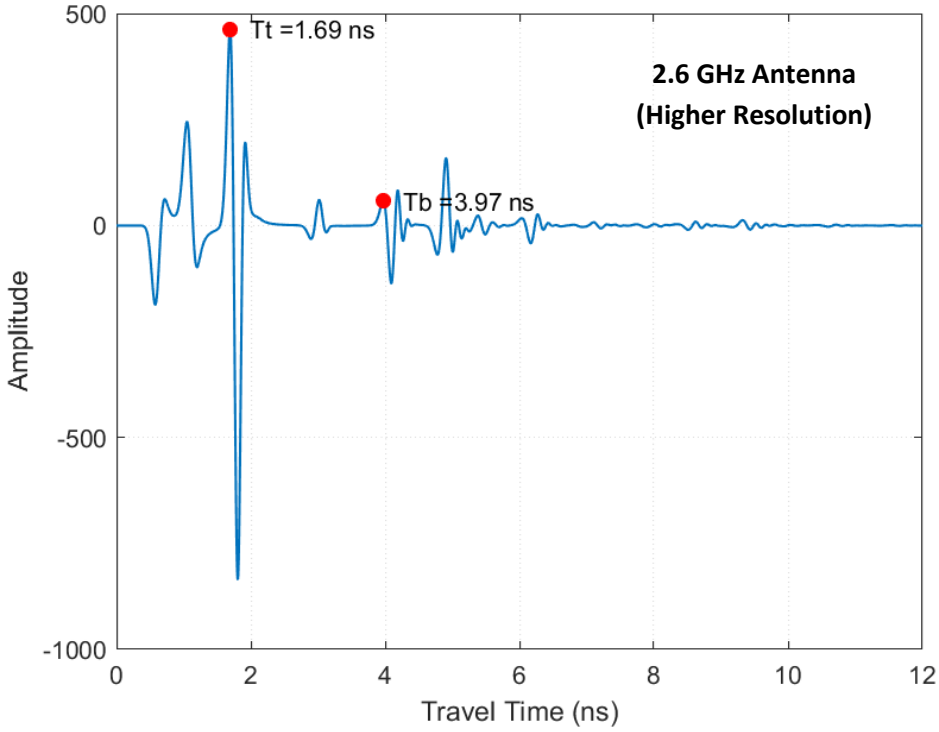

(a)

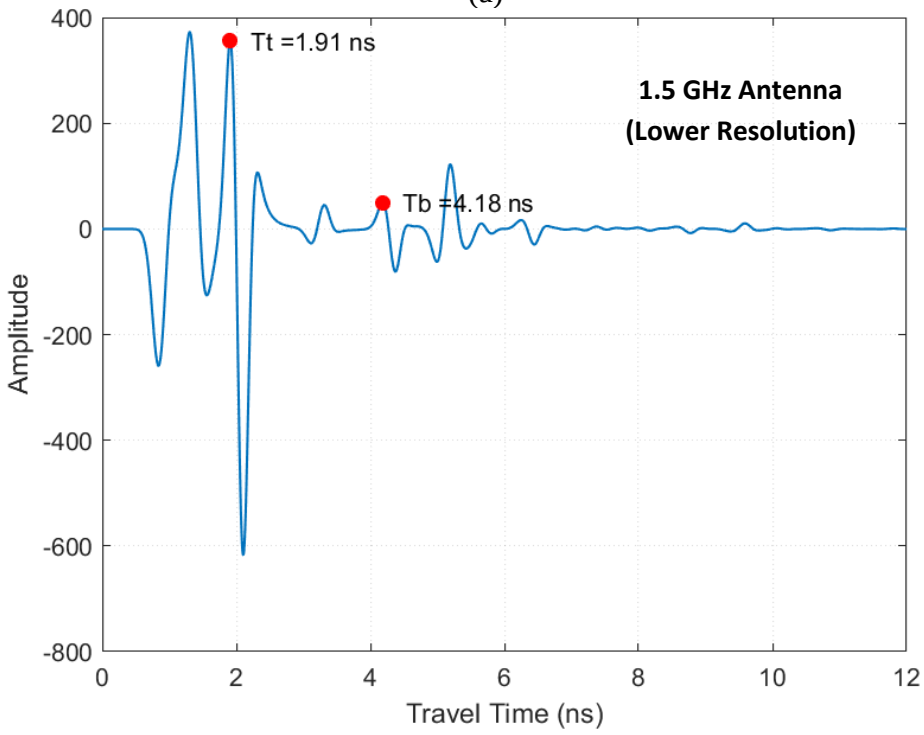

(b)

Figure 6-3. A-scans for Tx-Rx distance of 7 cm and the bottom rebar depth of 18 cm, (a) 2.6 GHz antenna, (b) 1.5 GHz antenna.

In Figure 6-4(b), the masking effect is plotted versus the angle the bottom reinforcement makes with the center line and the transmitter. For deeper bottom rebars, a Tx-Rx spacing greater than 12 cm is better suited for assessing the condition of the bottom section of the deck, as the masking effect is less than 30%. However, since it reduces the reflection received from the top rebar, it is not suitable for assessing the top portion of the deck above the top reinforcement.

Figure 6-5 illustrates how the reflections from the top and bottom reinforcement vary with the transmitter-receiver spacing for a bottom reinforcement placed 16 cm deep in the slab. All the amplitudes were normalized with respect to the maximum measurable amplitude at the top reinforcement. The impact of the Tx-Rx spacing on the measured amplitude indicates that manual control of the spacing between the transmitter and the receiver can assist in studying the reflections from the bottom level reinforcement and thereby providing a full-depth condition assessment of the deck. However, the setup appropriate to evaluate the lower section of the deck is not necessarily useful in the evaluation of the top portion of the slab. Therefore, a GPR array, or GPR a system simultaneously allowing for two sets of Tx-Rx spacing can enable a full depth assessment of the deck.

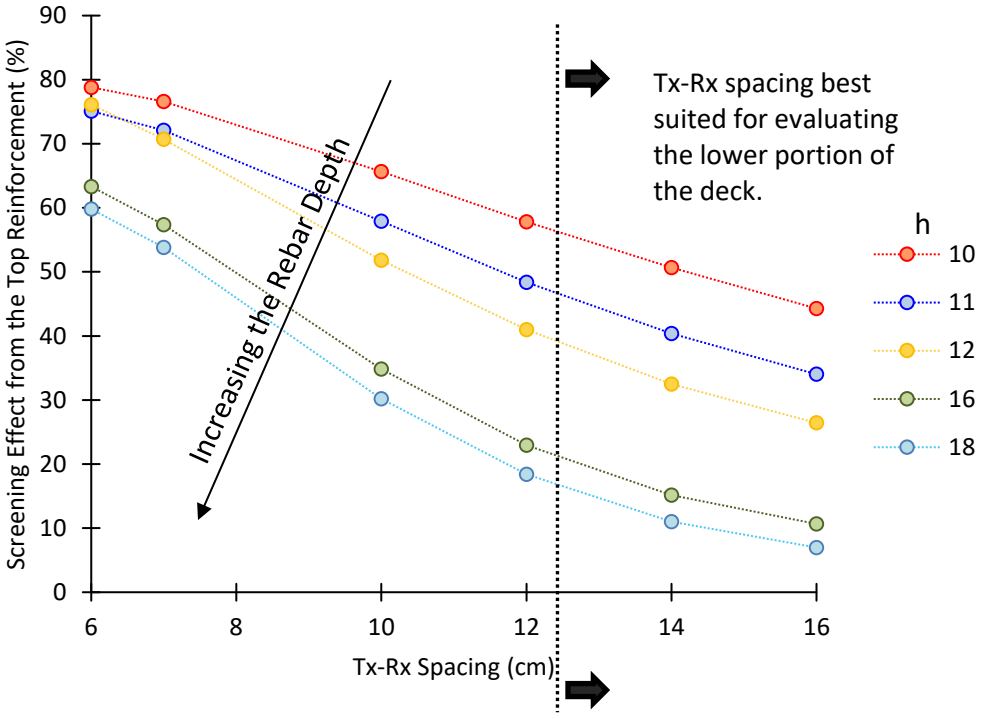

(a)

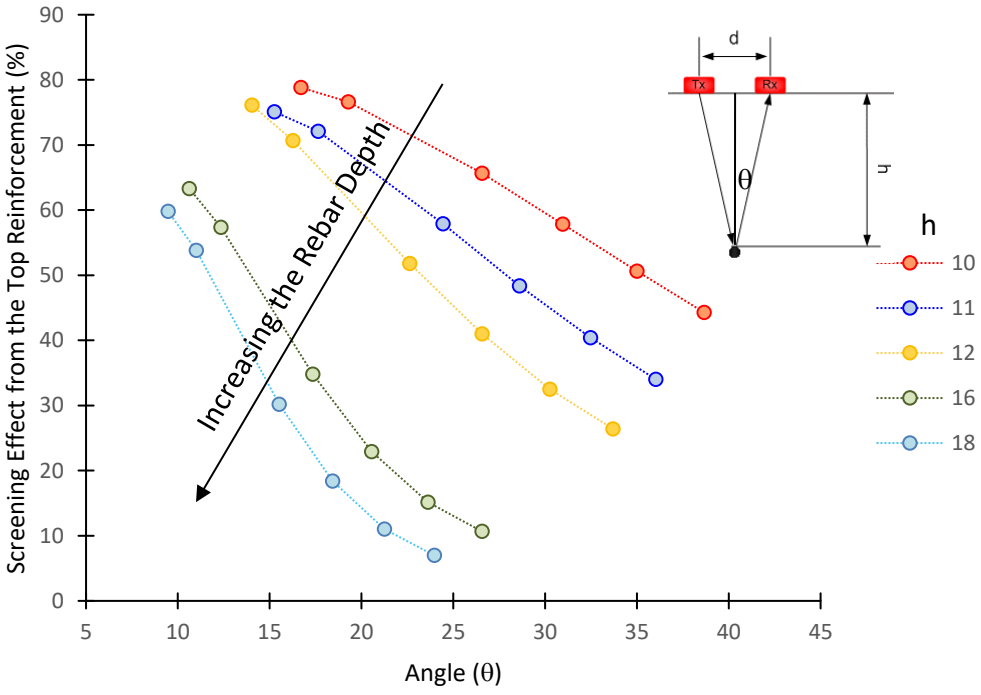

(b)

Figure 6-4. The masking effect of the top reinforcement on the reflection from the bottom rebar when rebars are aligned: (a) masking effect vs. Tx-Rx spacing, (b) masking effect vs. the angle between the bottom reinforcement and the antenna (2.6 GHz antenna).

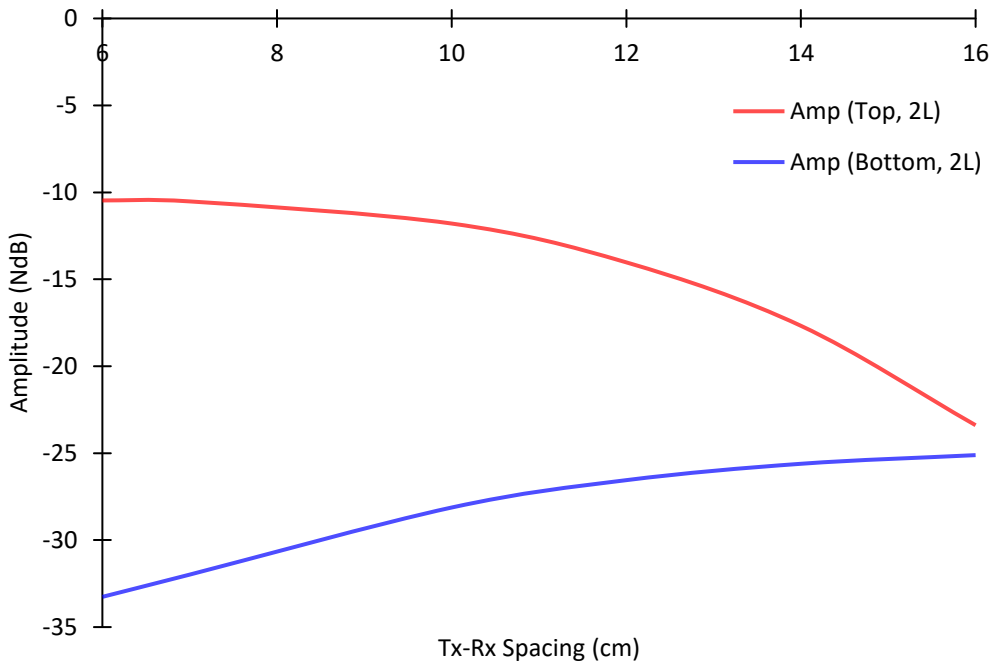

Figure 6-5. Reflection amplitudes in normalized dB from the top and bottom rebars vs. transmitter-receiver spacing (bottom reinforcement depth = 16cm)

The simulations were repeated using an antenna with the center frequency of 1.5 GHz. The masking effect was generally similar to the one for a 2.6 GHz antenna; it decreases linearly with increasing depth of the bottom reinforcement and with increasing transmitter-receiver spacing (Figure 6-6).

Figure 6-7 compares the masking effect for two antennas with different frequencies and two different rebar depths. The broken lines correspond to 1.5 GHz, while the solid lines correspond to the 2.6 GHz antenna. The 1.5 GHz antenna produces a higher masking effect than the 2.6 GHz antenna.

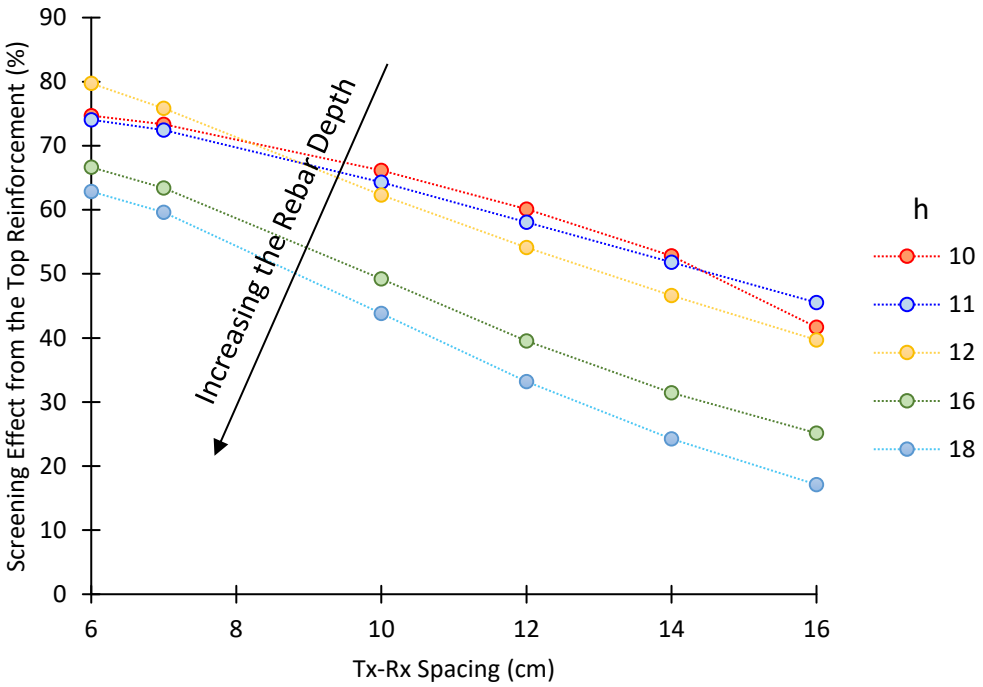

Figure 6-6. The masking effect of the top reinforcement on the reflection from the bottom rebar when rebars are aligned (1.5 GHz antenna).

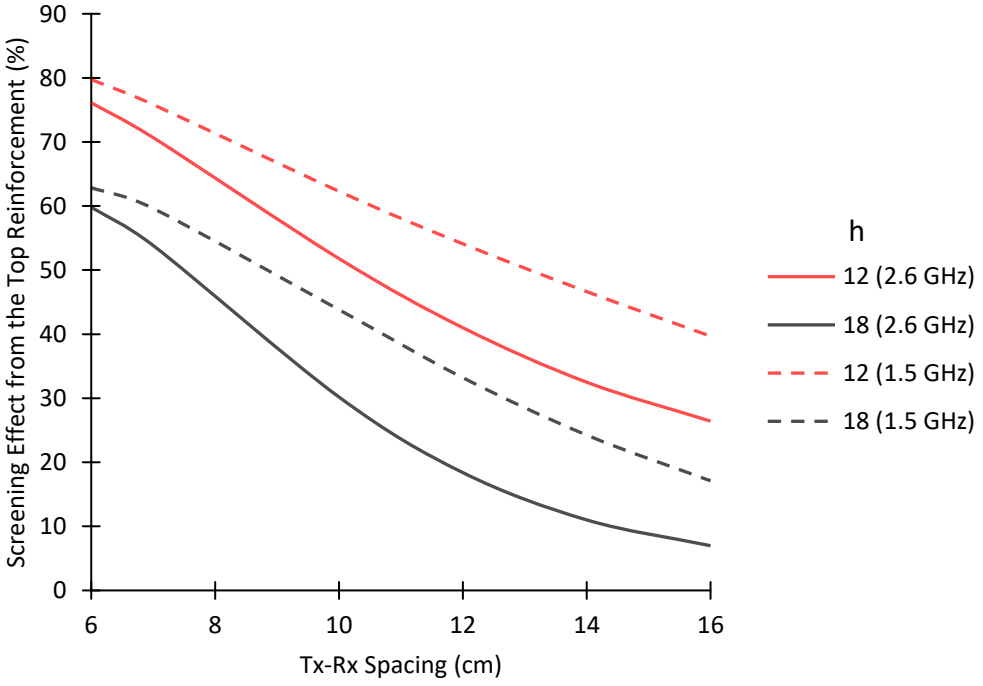

Figure 6-7. Comparison of the masking effect for the 1.5 GHz versus 2.6 antennae. The broken lines are associated with the 1.5 GHz antenna.

The simulations were repeated for different permittivity and conductivity combinations to investigate the effect of EM material properties on the masking effect. Figure 6-8(a) shows the masking effect for electrical conductivities of 0.01 and 0.05 S/m, and Figure 6-8(b) shows the masking effect for dielectric constants of 9 and 13. Increasing the conductivity even fivefold has almost no impact on the masking effect while increasing the dielectric constant from 9 to 13 increases the masking effect by up to 2%. It can be concluded that the masking effect is almost solely governed by the antenna frequency, and rebar and antenna geometry, rather than the electromagnetic properties.

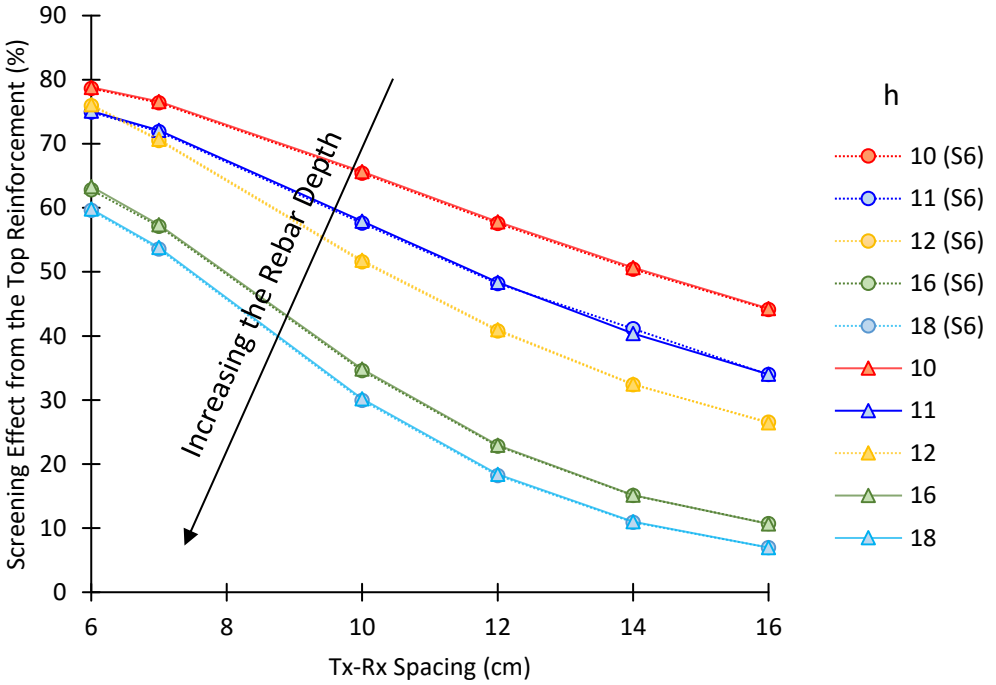

(a)

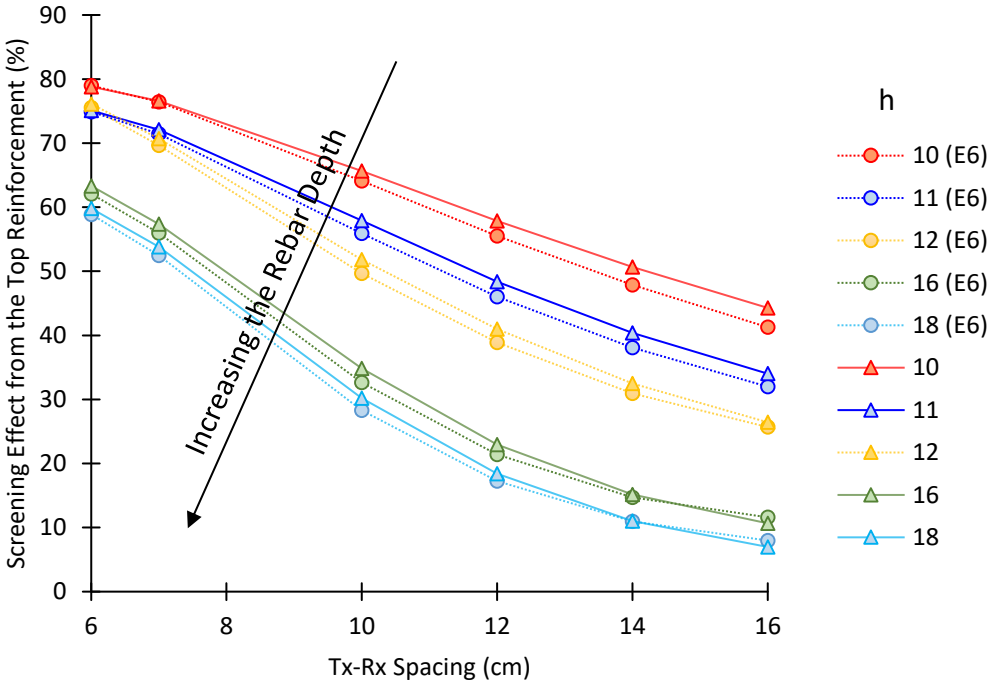

(b)

Figure 6-8. Comparison of the masking effect (2.6 GHz antenna): (a) $\sigma = 0.05$ vs. $\sigma = 0.01$ S/m, (b) $\varepsilon_r = 13$ vs. $\varepsilon_r = 9$.

6.3 Parametric Study – Masking Effect of Top Reinforcement (Rebars Not Aligned)

The masking effect of the top reinforcement on the strength of reflection from the bottom rebar when the top and bottom bars were not aligned was also investigated through 2D FDTD simulations. Similar to Section 6.2, in which the top and bottom bars were aligned, a parametric sweep was performed for various transmitter-receiver spacing, as well as reinforcement depth. Only a single A-scan was simulated for various transmitter-receiver spacing: 6, 7, 10, 12, and 16 cm, and for the bottom reinforcement depth varying from 10 to 18cm. The bottom rebar was placed 2.5 cm away from the center line of the top rebar. In all simulations, the center of the 2.6 GHz antenna was positioned directly above the top rebar (Figure 6-9). Ricker wavelet was used as the excitation signal.

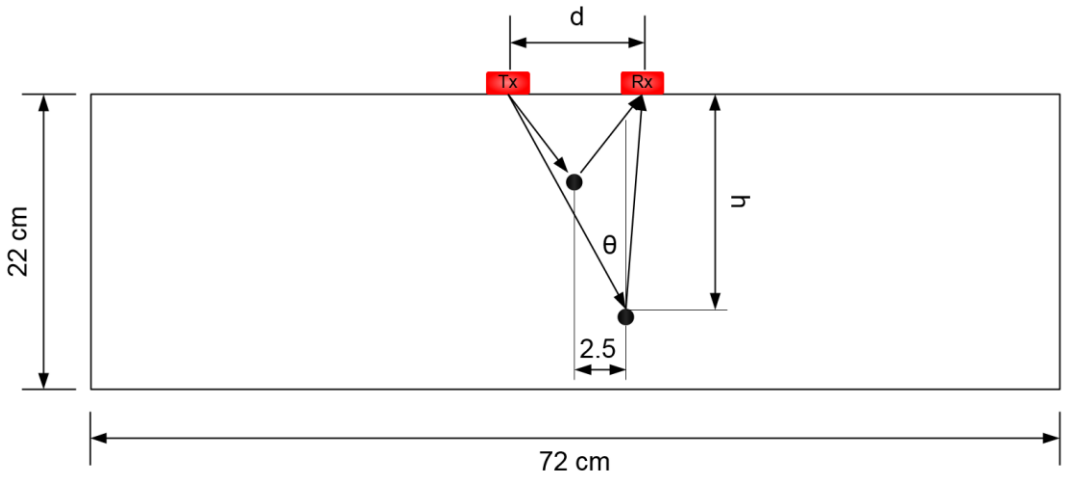

Figure 6-9. Schematic of the model in which the bottom bar is not directly below the top bar.

Figure 6-10 compares the masking effect for two scenarios, in which the bottom bars are placed 10 and 18 cm deep in the slab, while the top rebar is 6 cm deep: (i) when the lower bars are directly below the top bar (solid lines) and (ii) when they have a 2.5 cm offset from the centerline of the top bar (broken lines). As expected, the masking effect for the aligned

bars is higher when the transmitter-receiver spacing is small. As the Tx-Rx spacing increases, however, the masking effect for the bars at an offset surpasses that of the aligned bars. In general, the deeper bars which are at an offset have a smaller masking effect when the Tx-Rx is small. For example, for the bottom bars 18 cm deep (black lines), the two lines meet at Tx-Rx spacing slightly greater than 8 cm. On the other hand, when the bottom rebar is only 10 cm deep (red lines), the two lines meet at Tx-Rx spacing slightly less than 12 cm. Figure 6-11 provides a comparison for all simulated scenarios.

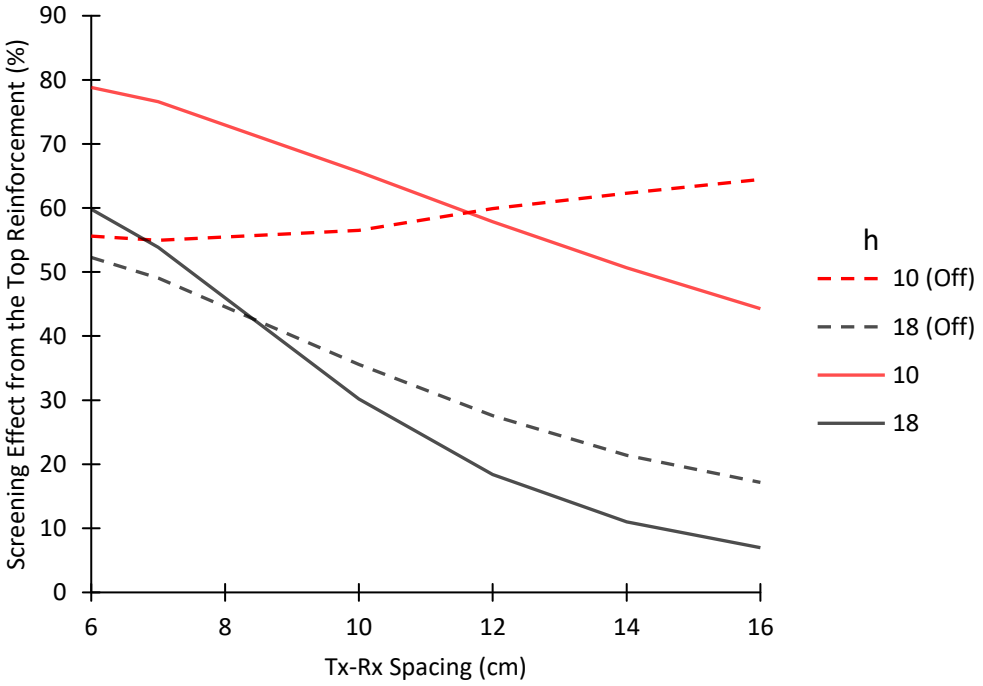

Figure 6-10. The masking effect when the bars are aligned (solid lines) vs. when the bottom bar is not directly below the top bar with a 2.5 cm offset (broken lines) – two scenarios, the bottom bars are 10 and 18 cm deep.

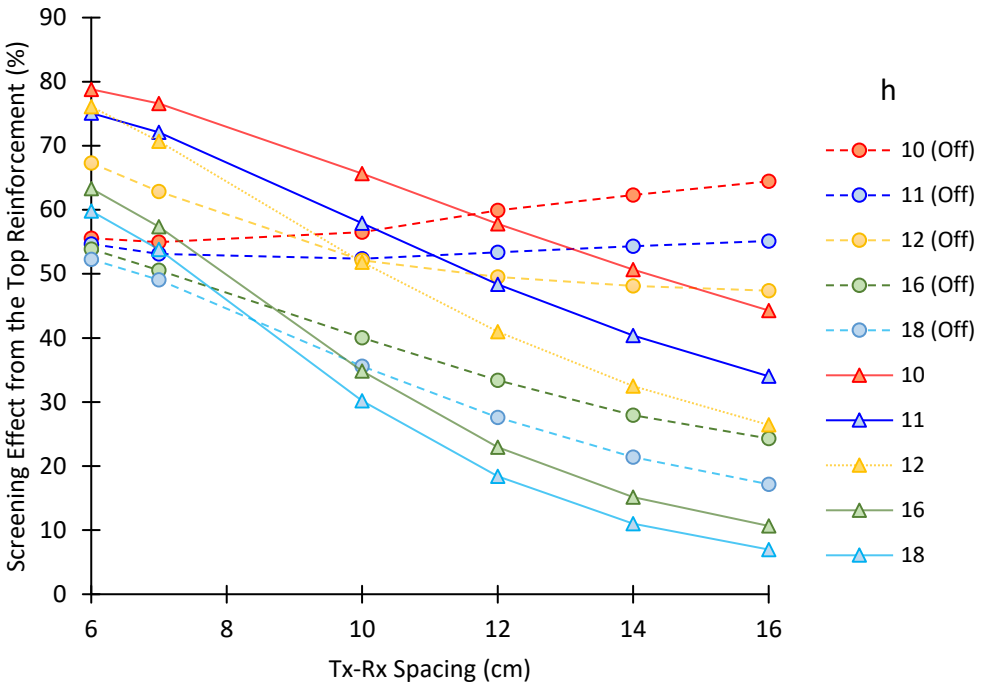

Figure 6-11. The masking effect when the bars are aligned (solid lines) vs. when the bottom bar is not directly below the top bar with a 2.5 cm offset (broken lines) – all scenarios.

6.4 EM Material Properties Effect on Normalized dB Amplitudes

Figure 6-12 shows the variations in the top rebar reflection, in normalized dB, with electrical conductivity for different transmitter-receiver spacing. The attenuation increases with conductivity for all Tx-Rx spacing; however, it is more sensitive for a smaller Tx-Rx. For example, for a spacing of 6 cm, increasing the conductivity from 0.001 to 0.05 increases the attenuation by more than 50%. On the other hand, for a spacing of 16 cm, the same increase in conductivity increases the attenuation by less than 30%. It must be noted that in absolute terms, the attenuation increase is approximately the same at an average of 4.3 NdB for any given transmitter-receiver spacing. To compare with the electrical resistivity values, the red line ($\sigma = 0.001$) corresponds to electrical resistivity of 100 kΩ.cm and the black line ($\sigma = 0.05$) corresponds to electrical resistivity of 2 kΩ.cm.

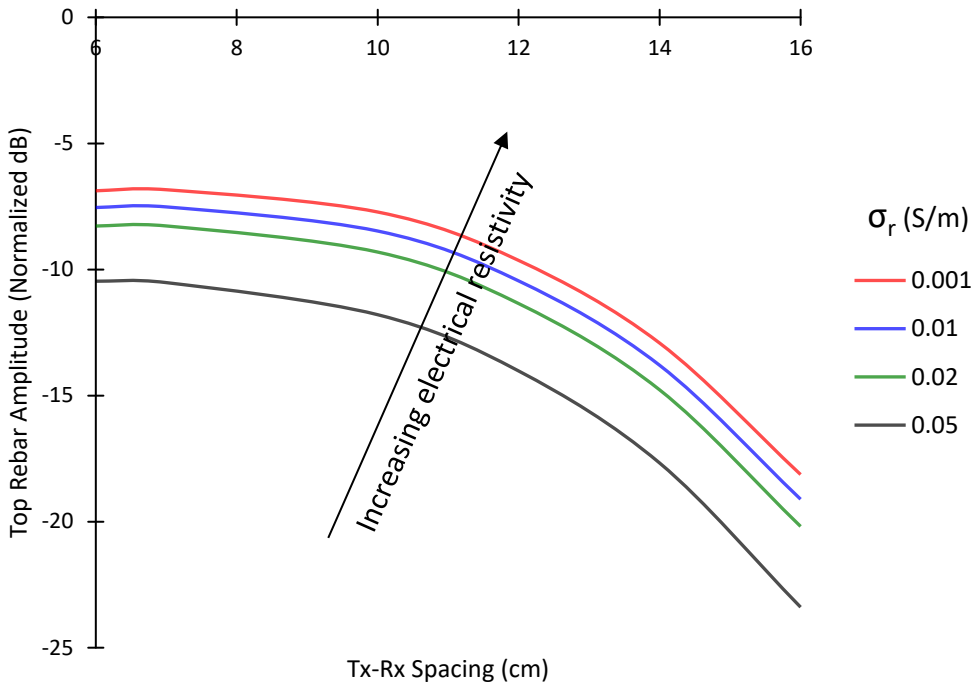

Figure 6-12. Changes in top rebar (6 cm deep) reflection with electrical conductivity.

Figure 6-13 shows the variations in the reflection of the bottom rebar 12 cm deep with electrical conductivity, in normalized dB, for different transmitter-receiver spacing. The attenuation increases with conductivity for all Tx-Rx spacing by roughly the same amount.

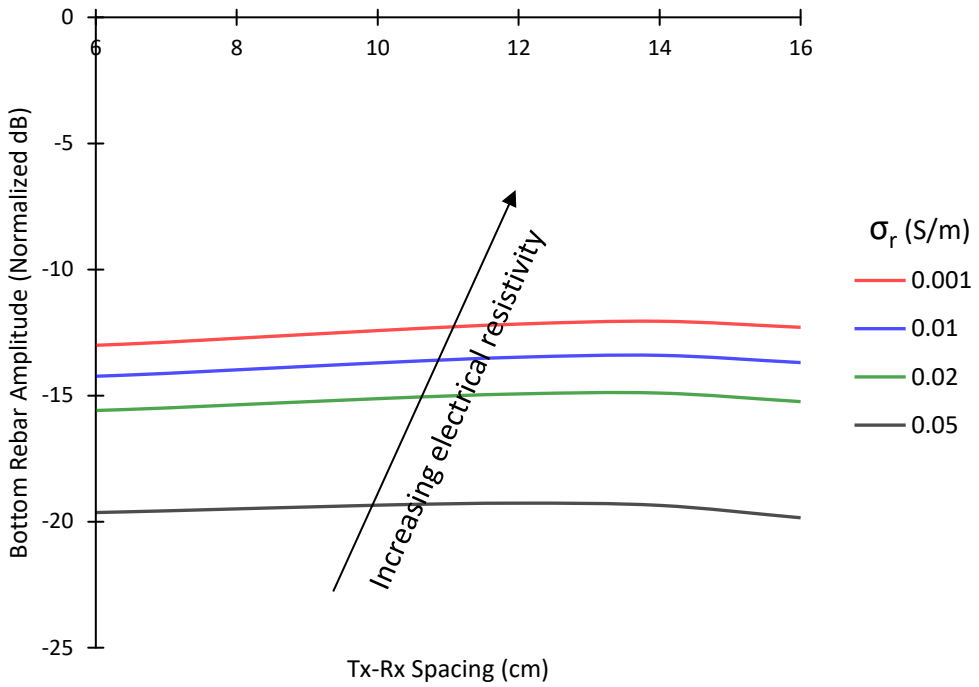

Figure 6-13. Changes in bottom rebar (12 cm deep) reflection with electrical conductivity.

Figure 6-14 shows the variations in the reflection of the top rebar with relative permittivity, in normalized dB, for different transmitter-receiver spacing. The attenuation increases with permittivity for all Tx-Rx spacing. However, it is less sensitive for smaller Tx-Rx. For example, for a spacing of 6 cm, increasing the dielectric constant from 6 to 13 increases the attenuation by approximately 12%.

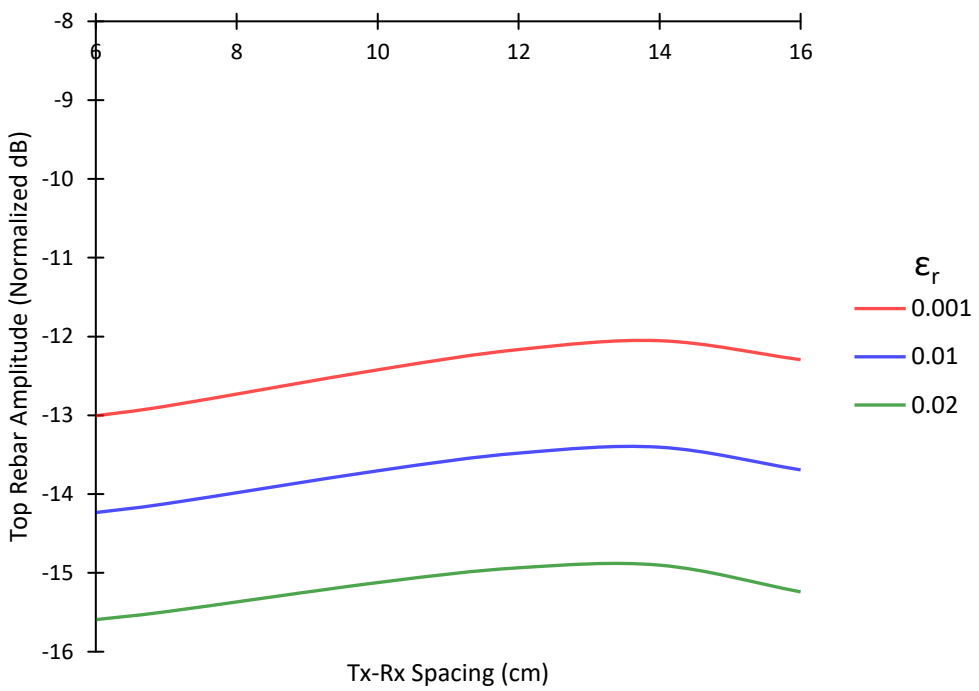

Figure 6-14. Changes in top rebar (6 cm deep) reflection with relative permittivity.

Figure 6-15 shows the variations in the bottom rebar (12 cm deep) reflection in normalized dB with relative permittivity for different transmitter-receiver spacing. The attenuation increases with permittivity for all Tx-Rx spacing. Much like the effect of conductivity, the increase is roughly the same for all Tx-Rx spacing.

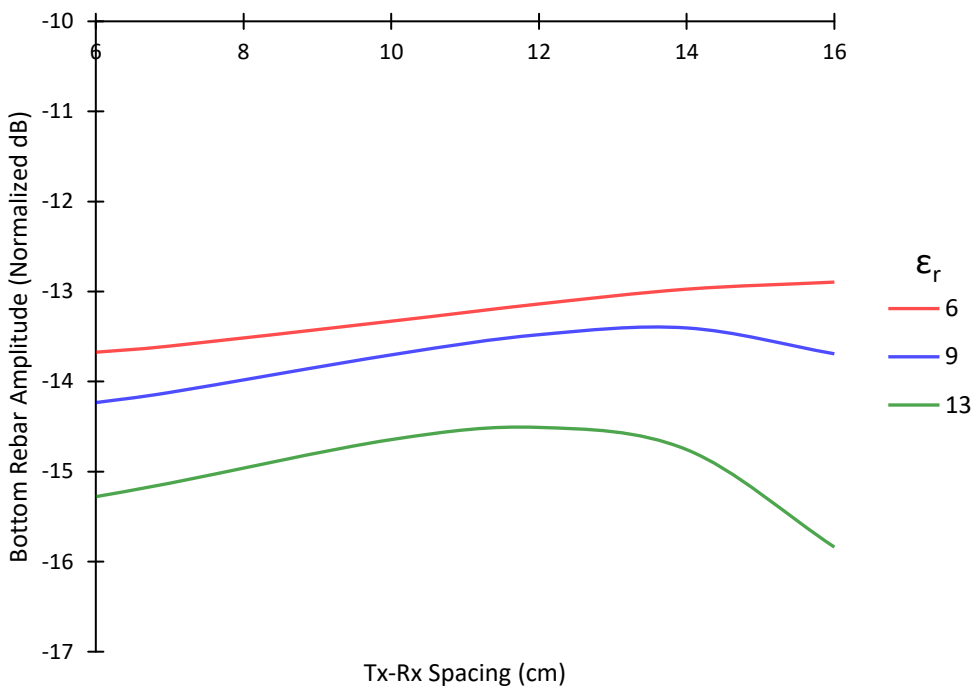

Figure 6-15. Changes in bottom rebar (12 cm deep) reflection with relative permittivity.

Comparing the impact of dielectric constant and conductivity on attenuation at the top rebar level (Figure 6-12 and Figure 6-15) shows that the attenuation is more sensitive to electrical conductivity than it is to relative permittivity. This was an expected result, as the attenuation is directly proportional to electrical conductivity, while it is inversely proportional to the square root of permittivity.

$$\alpha = \frac{\sigma}{2}\sqrt{\frac{\mu}{\varepsilon}} \tag{6-2}$$

6.5 Three-Zone Model

To develop a learning algorithm to assess a concrete deck in its entirety, a complete set of B-scans, representing various concrete conditions and reinforcement depths, was needed.

A total of 864 two-dimensional FDTD simulations were conducted using gprMax (63) to produce the synthetic GPR data.

For the purpose of these simulations, the antenna was moved for a 37 cm distance, symmetrically over the reinforcing bar. The data was recorded at 0.5 cm intervals. The radar configuration used for this study was based on a 2.6 GHz center frequency GSSI antenna, as simulated using ANSYS HFSS (60). A block diagram of the data set generation for later developing of a machine learning (ML) algorithm from numerical simulations is illustrated in Figure 6-16. The process of developing the learning algorithm is explained in detail in Chapter 7.

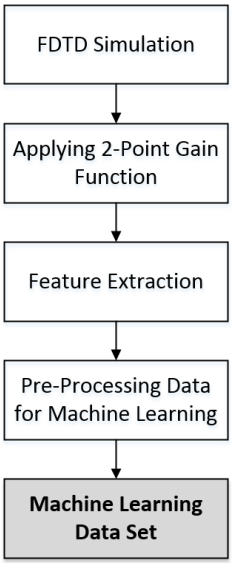

Figure 6-16. Block diagram of data set development for ML through numerical simulations.

The slab was divided into three separate yet interconnected longitudinal layers. A parametric study was performed by changing the concrete properties for each of the concrete layers: (i) the top layer, located directly above the top-level reinforcement, (ii) the middle layer, containing both the top and the bottom reinforcement levels, and (iii) the bottom layer, spanning from beneath the bottom reinforcement mat to the bottom of the

deck. The 2-D model is depicted in Figure 6-17. The location of the bottom rebar was fixed, while the top reinforcing bar was placed at four different depths from the surface of the slab: 5.4, 6.6, 8.6, and 10 cm. For the 5.4 cm case, the thickness of the top concrete layer was decreased from 5 to 3 cm.

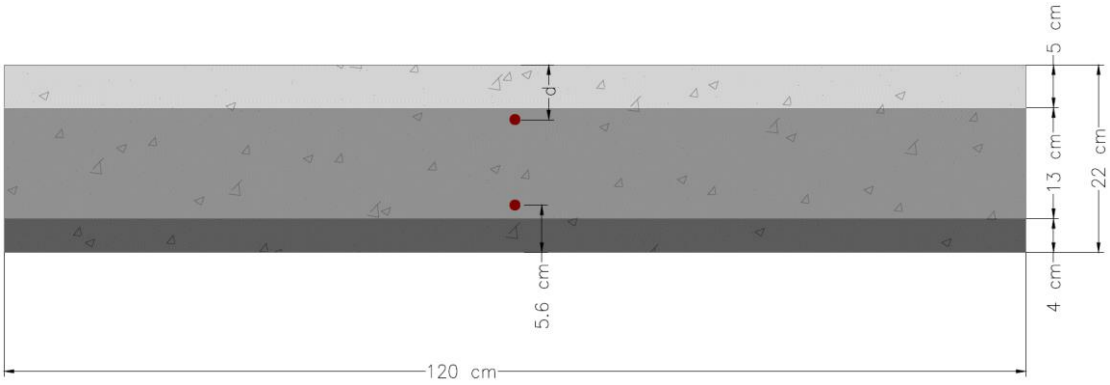

Figure 6-17. Three-layer model.

Concrete was described by two electromagnetic properties – relative permittivity and electrical conductivity. Using the electromagnetic properties as characteristic parameters, six concrete conditions were simulated, ranging from good to critical (72; 73; 74). The electromagnetic properties of simulated concrete are presented in Table 6-1. The concrete quality is decreasing from top to bottom in the table, with S3E3 having the highest quality, with regards to electromagnetic properties, and S6E6 having the lowest quality.

Table 6-1
Concrete condition rating

Material	Bulk Conductivity (σ) (Siemens/m)	Relative Permittivity (ε_r)	Layer Rating	Color
S3E3	0.001	6	100	Yellow
S2E2	0.005	7	80	Light green
S1E1	0.01	8	60	Red
S4E4	0.02	11	40	Green
S5E5	0.03	12	20	Black
S6E6	0.05	13	0	Blue

Each concrete condition was assigned a rating number ranging from 0 to 100. The layer ratings were assigned in equal increments. The ratings should be considered as qualitative indices, not as quantitative indicators. For example, a concrete layer with a rating of 80 does not indicate a 20% lower quality than a layer with a rating of 100. It merely means that the quality of a layer with rating 80 is better than a layer with 60, and worse than a layer with rating 100. It is worth noting that various conditions do not necessarily point to active corrosion. They rather describe the severity of the corrosive environment.

By varying the concrete condition, and the concrete cover over the top reinforcement, 864 FDTD simulations were conducted. In 648 cases of simulations, the top concrete was 5 cm thick (Figure 6-17), while in the remaining 216 simulations, the top layer was 3 cm thick. The slab thickness was 22 cm in all simulations. The goal was to examine whether changing the electromagnetic properties of concrete across the slab has any recognizable and quantifiable effect on the reflections from the bottom reinforcement, and the back-wall alike. If so, those would be used to assess the concrete quality across the slab. In each simulation, the antenna was moved in 0.5 cm increments, symmetrically over the top rebar, to produce 74 A-scans.

Time-zero adjustment was applied to all A-scans to remove the strong surface reflection. This was followed by using a four-point time-varying gain function/filter to all the individual A-scans to amplify the bottom bars reflections, and to reduce the multiple reflections beyond the bottom of the slab. The individual A-scans were used to generate B-scans using a MATLAB code.

Figure 6-18 provides the schematic of the antenna location and a representative A-scan. The A-scan location is shown on the B-scan in Figure 6-19. The corresponding gain function is shown in Figure 6-20.

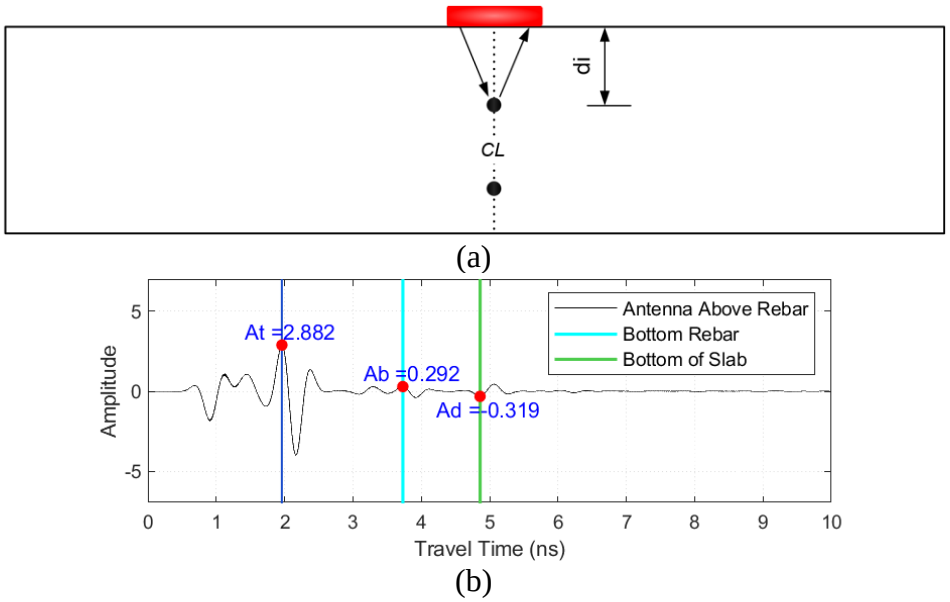

Figure 6-18. (a) Setup schematic, (b) Representative A-scans.

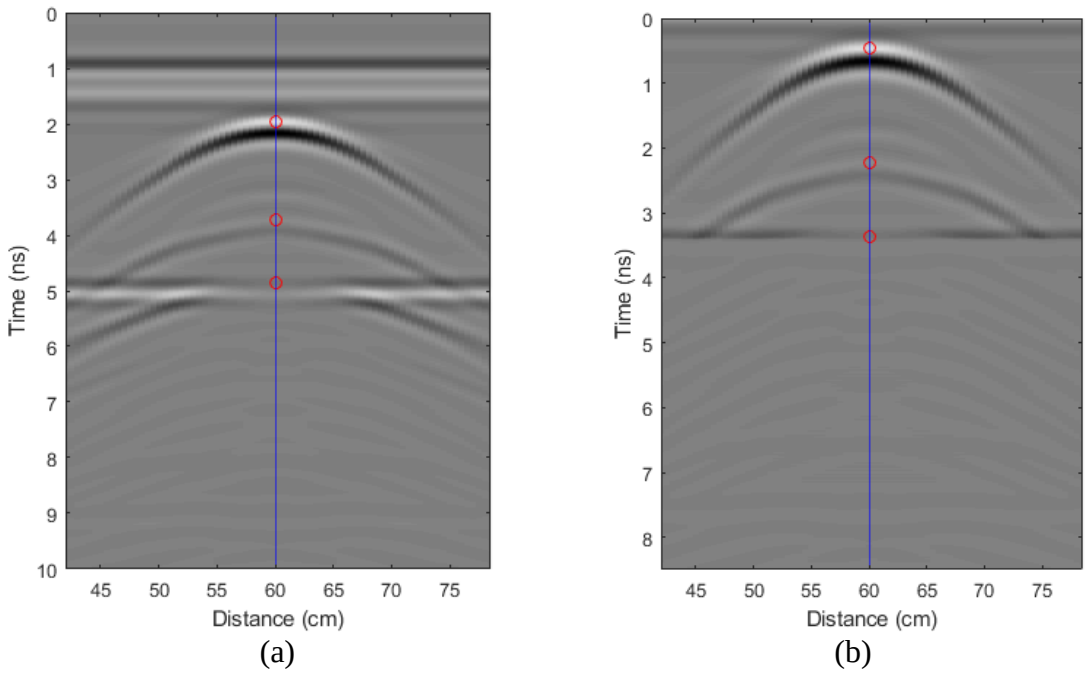

Figure 6-19. Representative B-scans: (a) using raw data, (b) after applying the gain function and time zero adjustment.

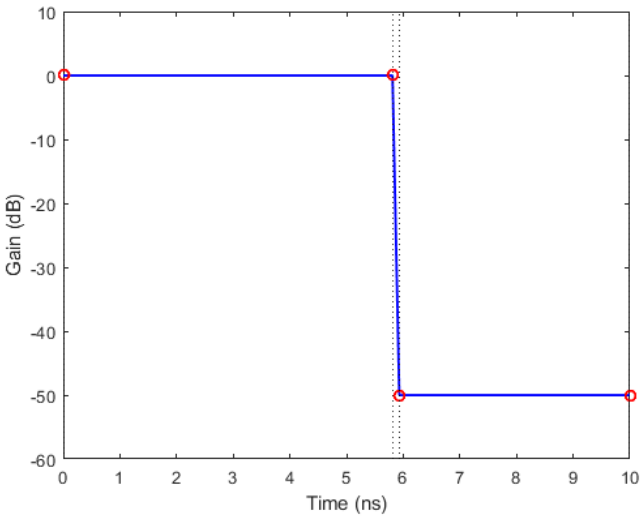

Figure 6-20. Representative gain function.

Figure 6-21 and Figure 6-22 illustrate the B-scans generated using numerical simulations, as well as the A-scans extracted from those to develop the data set for the learning algorithm. Figure 6-21 shows the results for two scenarios – (top): a uniform slab; in other words, all three layers have the same material properties, and (bottom): the first two layers have the same material properties as the first slab; however, the third layer has lower dielectric constant and conductivity. The amplitudes at the top and bottom rebars are the same for both cases, while for the second model a lower reflection is registered for the bottom of the slab.

In Figure 6-22, the two models have the same combination of properties in different orders. In both cases, the bottom layer is S4E4, and the other two layers are a combination of S1E1 and S5E5. While the amplitudes associated with the top and bottom rebars are different, the reflections from the bottom of the deck are approximately the same for both models.

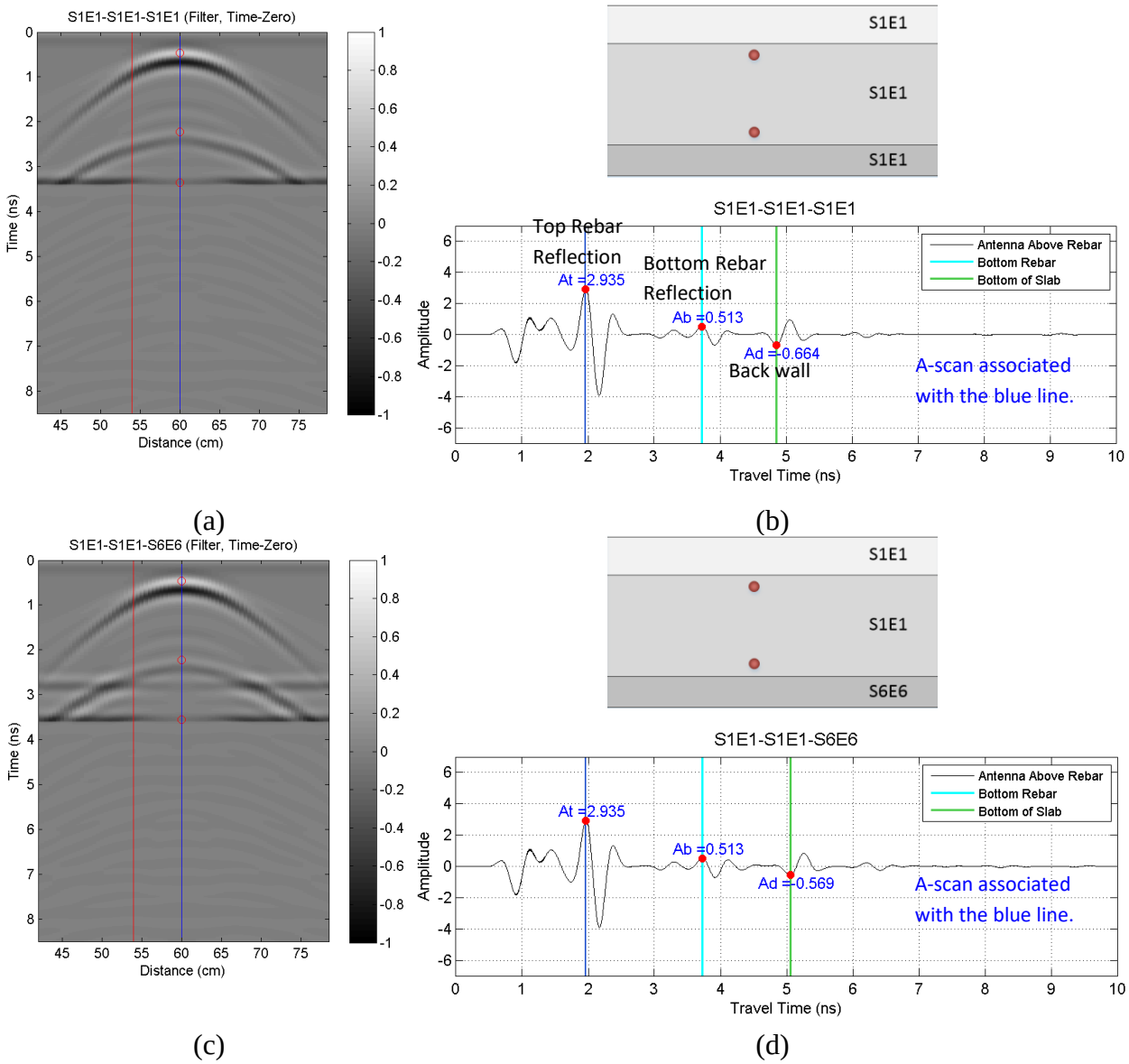

Figure 6-21. B- (a) and A-scans (b) for models with all three layers having the same material properties (S1E1); B- (c) and A-scans (d) for models with the same top and middle layers (S1E1), and the third layer with lower dielectric and conductivity (S6E6).

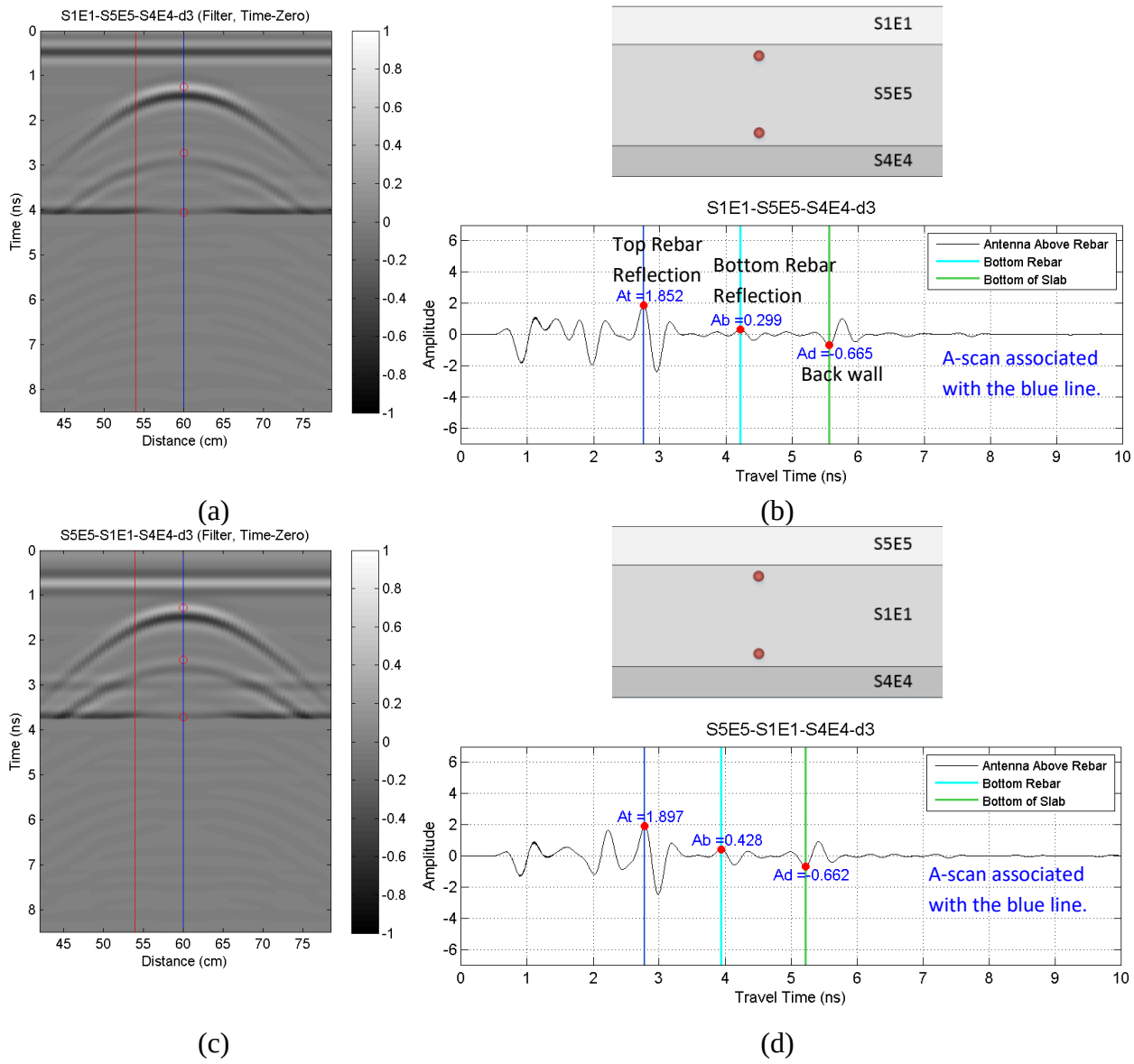

Figure 6-22. B- (a) and A-scans (b) for a model with different material properties in each layer (S1E1-S5E5-S4E4); B- (c) and A-scans (d) for a model with different material properties in each layer (S5E5-S1E1-S4E4).

6.5.1 Signal Reflection at Concrete Layer Interface

The purpose of numerical simulations was to first and foremost demonstrate that machine learning is a feasible approach for condition evaluation of bridge decks using GPR data. One drawback of numerical simulations is that they do not realistically represent actual field conditions. For example, in a real bridge deck, the changes in electromagnetic

material properties are not as drastic and sudden as simulated in the numerical modeling of a three concrete-layer deck.

Since in the first round of simulations, which were discussed in Section 6.5, there were contrasts in dielectric properties of different layers, there were additional reflections registered at the interface between every two concrete layers (cf. Reflection Coefficient in Section 3.3.1). Additional simulations were conducted on models with no reinforcing bars to investigate this phenomenon. The findings are discussed in this section. To rectify this issue, a new set of simulations were conducted in which the permittivity was kept constant for all models, and only the conductivity was changed. This new set of data was used later in Chapter 7 for machine learning purposes.

Figure 6-23 depicts the A-scans for two homogenous models of plain concrete slabs with only one type of concrete. There is no reflection observed at 2 ns. Figure 6-24 shows three A-scans for plain concrete models with different material properties at the top and bottom. The blue line corresponds to a homogenous model with only one concrete type, while the red and black lines correspond to models consisting of two concrete types. There is no reflection at 2 ns for the homogenous model (blue). In contrast, there is a peak for the other two models at the 2 ns time stamp. The reflection is stronger for a higher contrast in EM material properties of the two layers (black line).

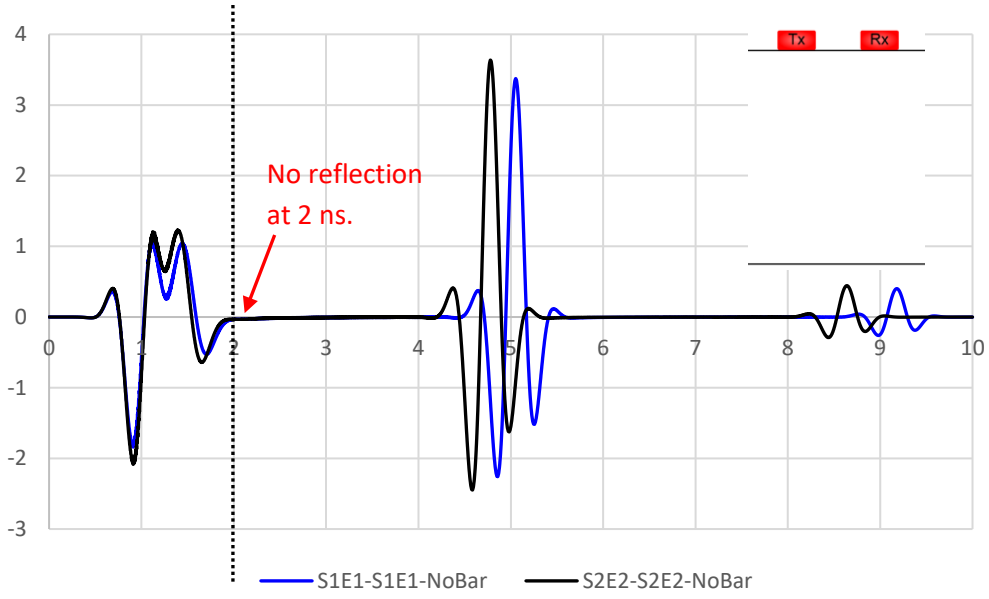

Figure 6-23. A-scans for two homogeneous models with no rebar (S1E1 and S2E2).

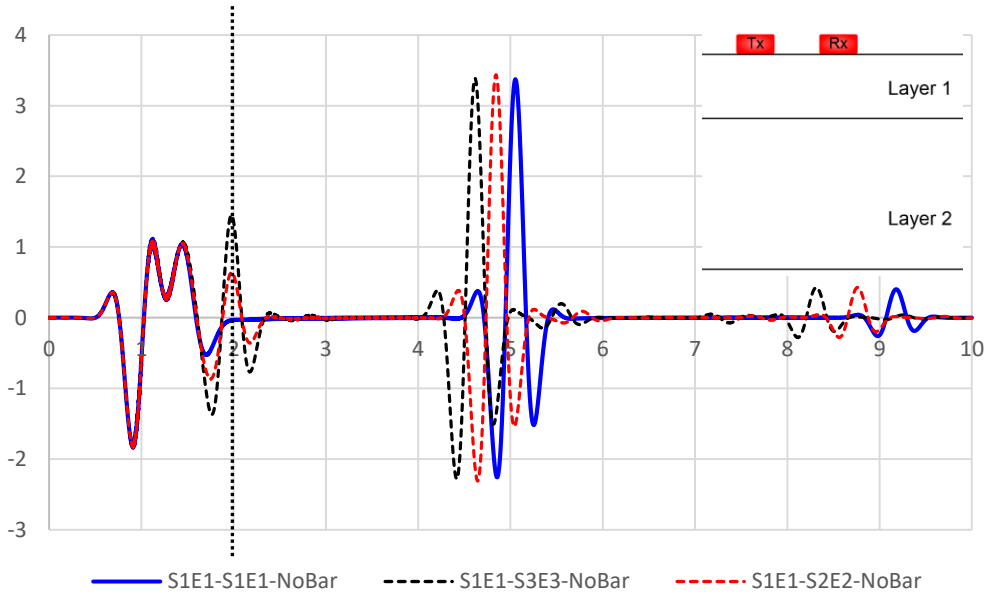

Figure 6-24. A-scans for (i) a homogeneous model with only one type of concrete (blue), and (ii) a concrete slab with two layers of different types of concrete.

Figure 6-25 (a) compares the A-scans for a homogenous model with and without rebar. The A-scan associated with a model with rebar has a peak at around 2 ns corresponding to the reflection from rebar. In the absence of rebar, however, no peak is observed at that time.

On the other hand, Figure 6-25 (b) compares the A-scans for a model consisting of two layers of concrete with different material properties, with and without rebar. Regardless of rebar presence, there is a reflection registered at around 2 ns.

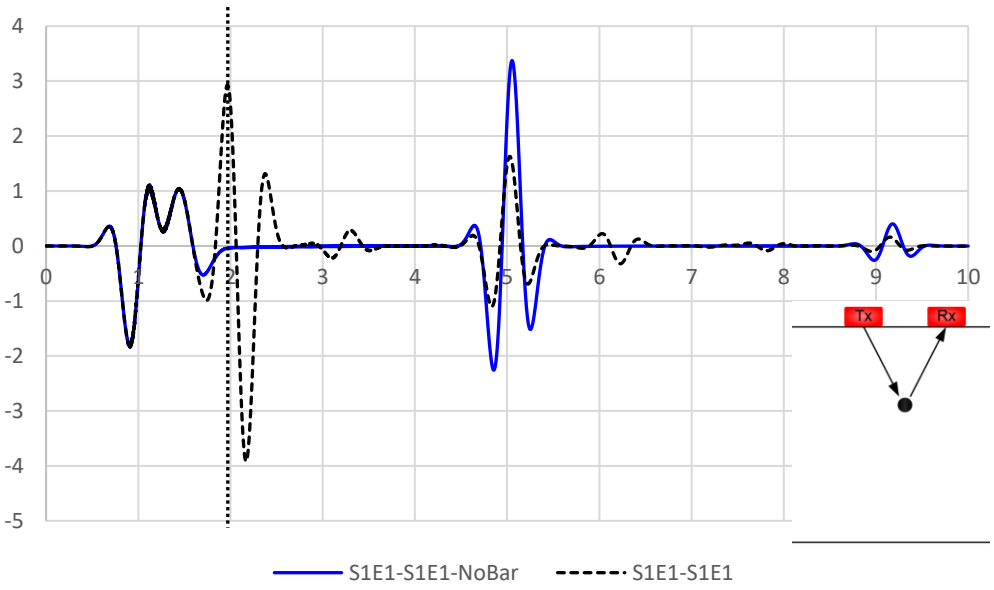

(a)

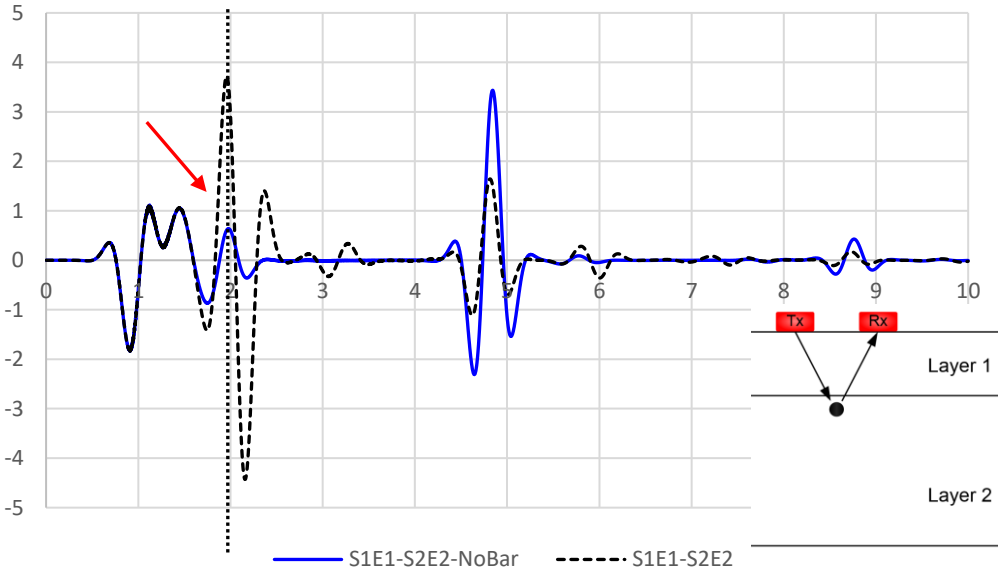

(b)

Figure 6-25. (a) A homogenous model with and without rebar, (b) Two-layer slab with different types of concrete, with and without rebar.

The reflection at the interface in the absence of rebar is approximately 0.6 for the given layer contrast. In a homogeneous slab, the amplitude of the rebar reflection is approximately 3. The recorded amplitude for the broken line in Figure 6-25 (b) is approximately 3.6. This indicates that this amplitude is a combination of rebar reflection and the reflection caused by the sudden change in EM material properties at the interface of the two concrete layers. The likely explanation for this is that in the simulations, the rebar was placed only slightly below the top concrete layer; therefore, the GPR could not correctly resolve the two reflectors. The problem with this superposition affects the recorded top rebar reflections, potentially impacting the predictions of the learning algorithm (Figure 6-26).

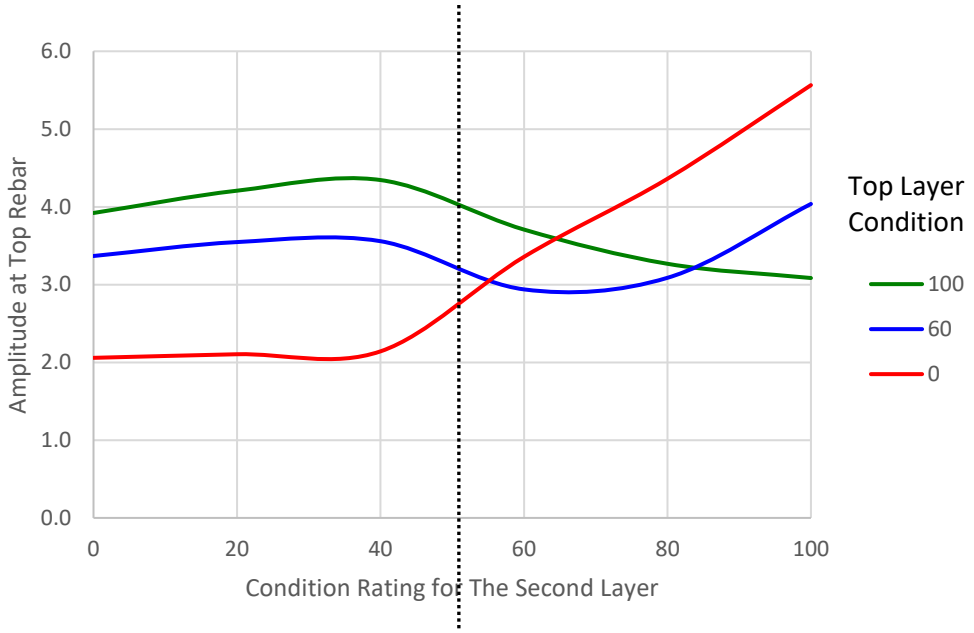

Figure 6-26. Amplitude of the top rebar reflection for different top-second layer contrasts.

Upon recognizing the effect of reflectivity at the interface of different concrete layers, a new set of simulations were conducted by keeping the permittivity constant, thereby eliminating the reflectivity, and only changing the electrical conductivity. The new 3-zone model simulation dataset was used to develop a learning algorithm to expand the GPR

evaluation zone beyond the top reinforcing bars. The learning algorithm and its implementation for the simulation, field, and laboratory data are presented in the next chapter.

Chapter 7. Machine Learning Algorithm

7.1 Introduction

The use of machine learning in analyzing GPR data, particularly of neural networks and pattern recognition for automatic selection of hyperbolas and buried objects, has been gaining momentum in recent years (75; 76; 77; 9). One of the earliest studies on the use of artificial neural network for GPR data interpretation was performed by Molyneaux et al. at University of Liverpool (78). Despite showing a potential for post-processing of GPR data, the algorithm occasionally reported rebars at locations where there were no reinforcement bars. Rodriguez et al. (79) used 2D FDTD simulations combined with a neural network system to develop an algorithm for interpreting GPR survey data. Travassos et al. compiled a review of some of the notable publications in which the use of machine learning or neural networks were used in post-processing GPR data (80).

Machine Learning is the process of enabling a computer algorithm to perform a given task without being specifically instructed to do it. The algorithm learns from its mistakes or errors and builds upon that learned behavior based on statistical information. The term machine learning was coined by Arthur Samuel in 1959 while working at IBM (81). Today,

machine learning is ever present in our daily lives and is extensively used in a wide range of applications for image recognition, speech recognition, internet search, online advertising, credit card fraud detection, medical tests, and any other data-driven prediction.

In the context of machine learning, the input variables are called *features*, often noted as $x^{(i)}$. The output variables are called *targets* and are noted as $y^{(i)}$. The success of a machine learning algorithm is heavily dependent on the proper selection of independent and influential features. Not all features carry the same weight or impact on the prediction. For a problem with n features, there will be a total of 2^n different combinations of features as every single feature can be either included in or excluded from a subset of features (82). In addition to using the original features, it is common also to use some kind of transformation to modify the originals in order to gain a fast-converging or a more accurate algorithm. For example, one may use logarithmic transformations, trigonometric functions, or any polynomial combinations of the raw inputs so they can fit a desired curve such as the Gaussian curve.

Machine learning algorithms are divided into two main categories: supervised learning and unsupervised learning algorithms. This study focuses on supervised learning, which is explained in the next section.

In this chapter, learning algorithms are developed based on (i) a dataset generated through numerical simulations, (ii) a dataset of experimental data generated via GPR surveys of four bridge decks. Given the limited size of the numerical simulations-based dataset, the former algorithm was used only to evaluate the experimental data for a validation slab. The latter algorithm was validated using both the validation slab, and another bridge data set.

7.2 Supervised Learning

Supervised learning is a learning algorithm that uses a set of known data (training set) to build a function for mapping the input values into target variables, which can then be used to make predictions for an unseen dataset. Based on the type of the desired value to predict, supervised learning is divided into two categories (82):

- Regression: when the value we are trying to predict is continuous;
- Classification: when what we are trying to predict consists of a set of discrete values, which can be organized into different classes. In a classification problem, the target values are called labels.

The target variables in the present study are discrete values characterizing the concrete condition. Therefore, the problem at hand is a classification problem. It must be pointed out that despite the discrete nature of target values in this problem, their order was also paramount to this study, lending the problem some characteristics of a regression problem as well. This is explained in more details in the following sections.

The function that maps the features into the target space is called a classifier. A classification problem can be binary or multi-class depending on the number of categories in the target space. For example, medical tests are binary classification problems, where the outcome is either positive (or 1), or negative (or 0). In a multi-class classification problem, there are more than two classes/labels. For example, a problem to determine eye colors in Department of Motor Vehicles (DMV) photos is a multi-class classification problem.

Figure 7-1 (a) represents a binary classification problem in which the outcome is either a circle (or 0) or a square (or 1). Figure 7-1(b), on the other hand, illustrates a multi-class classification problem in which each shape represents a different class. The outcome can be one of the four classes: 1, 2, 3, or 4.

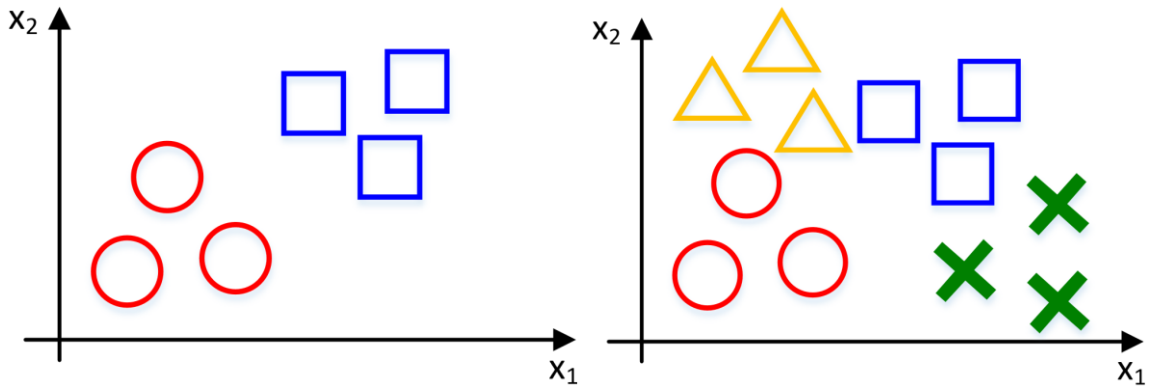

(a) (b)

Figure 7-1. (a) Two-class (binary) classification, (b) multi-class classification.

A data set in general is defined as follows:

$\{(x^{(i)}, y^{(i)}); i = 1, 2, 3, \ldots, n\}$

where $x^{(i)}$s are the inputs for the algorithm, also called features, and $y^{(i)}$s are the values the algorithm is trying to predict, or the outputs also called target variables.

In supervised learning, the data set is randomly split into two sets to (a) train the algorithm and fine-tune the parameters, and (b) validate the learned model. These two data partitions are independent of one another and are called a training set and a test set, respectively. The most common practice is to have a subset of 70% or 80% for the training set, and another subset of 30% or 20% for the test set.

The vector $(x^{(i)}, y^{(i)})$ is called a training sample. A training set is a dataset consisting of all the training samples which together will be used to train the model. Training and test sets are defined as follows:

- Training set = $\{(x^{(i)}, y^{(i)}); i = 1, 2, 3, \ldots, m\}$
- Test set = $\{(x^{(i)}, y^{(i)}); j = 1, 2, 3, \ldots, n - m\}$

A simplified representation of the supervised learning process is presented in Figure 7-2. This is not an all-encompassing representation, and it does not depict a stopping point for the cycle. Acceptable thresholds are defined such that when met, the training stops.

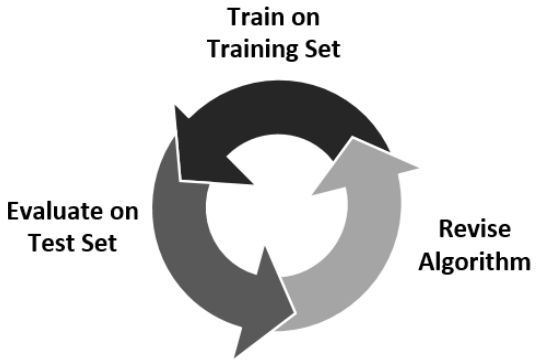

Figure 7-2. Supervised learning process.

In unsupervised learning, the training samples are not labeled. Since different concrete conditions are assigned labels in this study, supervised learning will be used. Specifically, gradient boosting is the learning algorithm used in this study. The basics of gradient boosting are discussed in the following section.

7.2.1 Gradient Boosting (GB)

Gradient Boosting is a machine learning technique which converts a collection of weak learners into a strong learner through a number of iterations. Gradient boosting is a form

of gradient descent algorithm (Figure 7-3). The goal is to minimize the error function. The model starts with an initial guess, θ_0, and keeps changing the value of θ iteratively until the acceptable threshold is reached. At each step, the model learns from the error at the previous step and then assigns different weights to different classifiers. With each iteration, the difference between the actual and the predicted values, also known as the residuals, gets smaller.

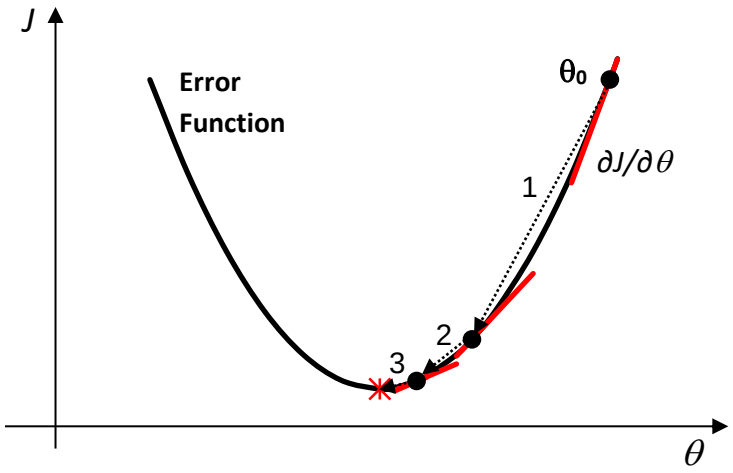

Figure 7-3. Gradient descent process.

The objective of a gradient boosting algorithm, and other machine learning algorithms alike, is to minimize the sum of the residuals, $\Sigma(y^{(i)} - \hat{y}^{(i)})$; where $y^{(i)}$ is the actual value, and $\hat{y}^{(i)}$ is the model prediction for the i^{th} training sample. The sum of the residuals is a simple error function. An error function is a measure of how close the predicted values are to the actual numbers. Another commonly used error function is the mean squared function:

$$J = \frac{1}{n}\sum_{i=1}^{n}\left(y^{(i)} - \hat{y}^{(i)}\right)^2 \qquad (7\text{-}1)$$

The algorithm seeks to minimize this error function. For simplicity, we can assume that a linear function, *h(x)*, is used to obtain the predicted value $\hat{y}^{(i)}$ as follows:

$$h_\theta(x^{(i)}) = \sum_{i=1}^{n} \theta_i x^{(i)} \tag{7-2}$$

Where θ_is are the parameters indicating the importance or weight of a given input (82). For the above prediction function, the mean square error function will be as follows:

$$J(\theta) = \frac{1}{n} \sum_{i=1}^{n} \left(y^{(i)} - h_\theta(x^{(i)}) \right)^2 \tag{7-3}$$

A common approach for minimizing the error function is to use an optimization algorithm called gradient descent. The gradient descent algorithm assumes an initial value for the parameter θ, and iteratively updates it to make the error function, *J(θ)*, smaller and smaller. The parameters in a gradient descent algorithm are updated based on the slope of the error function as follows (82):

$$\theta_{j+1} = \theta_j - \alpha \frac{\partial}{\partial \theta_j} J(\theta), \qquad j = 0 : n \tag{7-4}$$

Where α is the learning rate, which is a hyperparameter. Hyperparameters are parameters that control the actual model parameters, in this case, θ. The value of α is not dictated by the data set and is generally selected through trial and error. On the right side of the above equation, $\frac{\partial}{\partial \theta_j} J(\theta)$ is the derivative or the slope of the error function:

$$\begin{aligned} \frac{\partial}{\partial \theta_j} J(\theta) &= \frac{\partial}{\partial \theta_j} \left(\frac{1}{n} \sum_{i=1}^{n} \left(y^{(i)} - h_\theta(x^{(i)}) \right)^2 \right) \\ &= \frac{2}{n} \sum_{i=1}^{n} \left(\frac{\partial}{\partial \theta_j} \left(h_\theta(x^{(i)}) \right) \left(h_\theta(x^{(i)}) - y^{(i)} \right) \right) \end{aligned} \tag{7-5}$$

$$= \frac{2}{n}\sum_{i=1}^{n}\left(x^{(i)}\left(h_\theta(x^{(i)}) - y^{(i)}\right)\right)$$

Therefore, at every iteration, the parameters are updated for every single training example as follows (82):

$$\theta_{j+1} = \theta_j - \frac{2\alpha}{n}\sum_{i=1}^{n}\left(x^{(i)}\left(h_\theta(x^{(i)}) - y^{(i)}\right)\right) \qquad (7\text{-}6)$$

The algorithm repeatedly scans through the training examples and updates the parameters until the values predicted by the algorithm are sufficiently close to the actual target values, i.e., the error function reaches an acceptable threshold.

In the present study, gradient boosting technique was used to provide a full depth assessment of concrete bridge decks based on numerical simulations, and the experimental data based on field and laboratory GPR surveys. These are discussed in the following sections.

7.3 Application to Numerical Simulations

The results from the two-dimensional finite-difference time-domain simulations in Section 6.5 were used to construct a learning algorithm based on gradient boosting to provide a full depth condition assessment of a reinforced concrete slab. In the initial simulations, six concrete conditions were considered. However, in order to make the resulting algorithm applicable to at least one set of experimental data, the condition ratings were reduced to four by lumping ratings of 20 and 40 together to represent the poor condition (rating 30), and lumping ratings of 60 and 80 together to describe the fair condition (rating 60). That

made the numerical simulations results comparable to the four conditions used in actual GPR bridge surveys: sound (100), fair (60), poor (30), and serious (0).

Figure 7-7 illustrates an overview of the machine learning methodology.

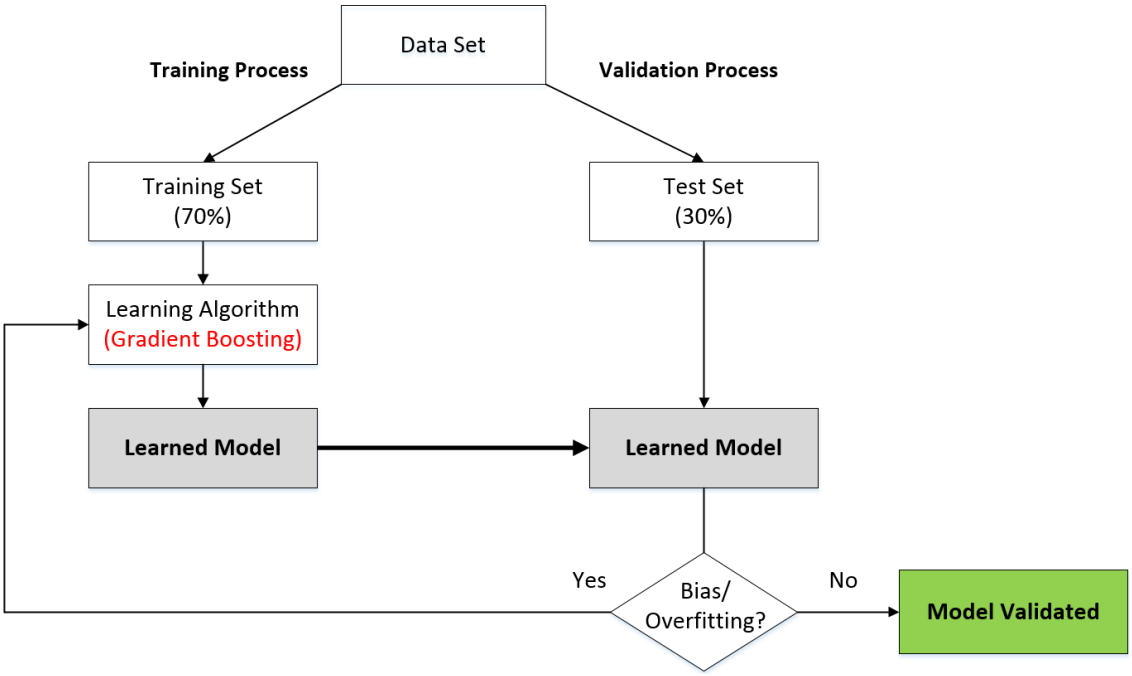

Figure 7-4. Overview of the machine learning methodology.

The learning algorithm uses six input features: two amplitudes, two travel times, the ratio of attenuation levels at the top and bottom rebar, and the reference conductive loss:

- AmpT = Attenuation at the top rebar
- AmpB = Attenuation at the bottom rebar
- Tt = Two-way travel time for top rebar
- Tb = Two-way travel time for bottom rebar
- RTB = Ratio of attenuation levels at the top and bottom rebars

- Lc = Reference conductive loss, which is calculated by subtracting a given amplitude from the one for a sound section, and is and normalized by the TWTT. This was introduced by Dinh et al. (9), and was briefly described at the end of Section 3.4.4. It will be further discussed in Section 7.4.1 for the experimental GPR data.

In other words, the input features in general are:

$$X^{(i)} = \{AmpT, AmpB, Tt, Tb, RTB, Lc\} \quad (7\text{-}7)$$

Initially, the attenuation and corresponding two-way travel time for the bottom of the deck were also used as additional input features. However, since the attributes for the bottom of the deck are not always readily available for the experimental data, they were later excluded as features. Adding those features would assist in predicting the condition of the bottom layer of the deck. Nonetheless, the present algorithm focuses only on the top concrete layer above the top rebar, and the middle concrete layer encompassing the top and bottom rebars.

It must be noted that since most commercial GPR antennas have a fixed transmitter-receiver spacing, Tx-Rx was a constant here as well, which is why it was not included as another input feature.

As discussed, the algorithm was aiming to predict Rt and Rb, the quality of concrete directly above rebar, and the condition of concrete encompassing both rebars, respectively. Hence, the target variables were defined as follows:

$$Y^{(i)} = \{Rt, Rb\} \;\; ; \;\; R_j = \{0, 30, 60, 100\} \quad (7\text{-}8)$$

The target variables in the present study, $Y^{(i)}$, representing the concrete condition, are discrete values. Therefore, the problem at hand is a classification problem. It must be pointed out that despite the discrete nature of target values in this project, their order was also paramount to this study, lending the project some characteristics of a regression problem as well. Table 7-1 presents a randomly selected set of $\{X^{(i)}, Y^{(i)}\}$ pairs. The last two columns are the targets.

Table 7-1
Randomly selected set of representative $\{(X^{(i)}, Y^{(i)})\}$ samples.

AmpT	AmpB	Tt	Tb	TBR	Lc_Top	Lc_Mid	Rt	Rb
-9.97	-26.22	1.97	3.73	2.63	0.73	0.81	100	60
-10.24	-26.45	1.97	3.73	2.58	0.59	0.75	60	60
-13.58	-32.24	1.97	3.73	2.37	-1.11	-0.81	0	30
-13.49	-29.42	2.56	3.74	2.18	0.38	-0.06	30	100
-10.53	-26.21	1.97	3.73	2.49	0.44	0.81	60	100

A total number of 846 $\{(X^{(i)}, Y^{(i)})\}$ data points were used for this algorithm. The data set was then randomly split into two sets: (a) 70% to train the algorithm and fine-tune the hyperparameters, and (b) 30% to validate the learned model. Figure 7-4 illustrates an overview of the machine learning methodology used in this study.

Figure 7-5 and Figure 7-6 depict 3D plots of concrete ratings for the top and middle layers when the top reinforcing bar was located 6.6 cm deep. In both plots, a clear pattern can be ascertained for the top, and the middle concrete layers as the data points are grouped together. One can draw a line to separate a particular group from the others. The three axes represent the reflected signal amplitudes at the top rebar, bottom rebar, and the bottom of the slab. Each color is representative of a specific concrete condition and properties.

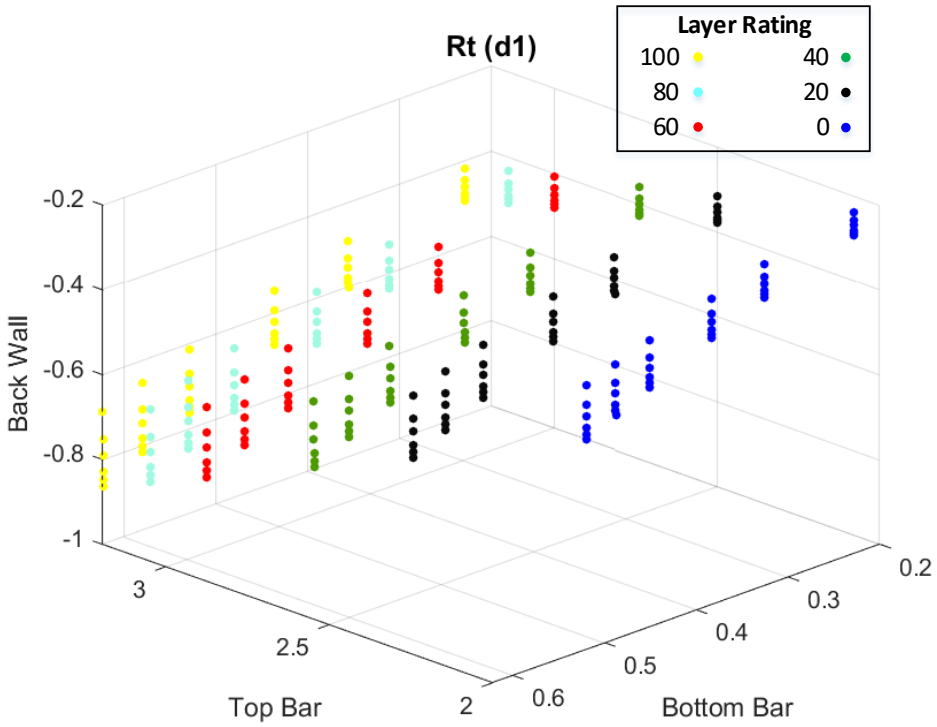

Figure 7-5. 3D plot of the top layer ratings for d = 6.6 cm.

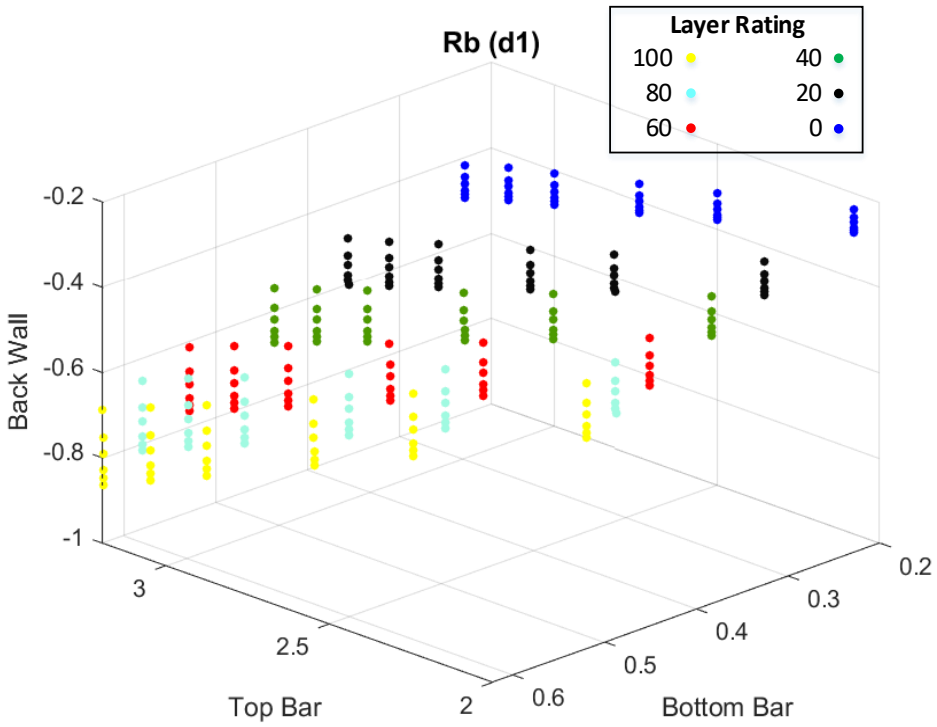

Figure 7-6. 3D plot of the middle layer ratings for d = 6.6 cm.

Since the bottom rebar attributes are not useful features in predicting the condition of the top layer, two different modules (or sub-algorithms) were constructed to predict: (i) Rt (the top concrete layer rating), and (ii) Rb (the middle layer concrete layer rating).

7.3.1 Module 1 (predicting Rt)

To predict the layer ratings for the top layer of the deck, the initial input variables in (7-7), except for the bottom rebar attributes, were used to train the model. The subset of features for Module 1 is as follows:

$$X^{(i)} = \{AmpT, Tt, Lc\} \quad (7\text{-}9)$$

Initially, the algorithm was suffering from overfitting, returning high accuracy on the training set, while performing poorly on the test set. This was resolved by adjusting the hyperparameters. Hyperparameters are the model parameters that are not learned by the machine and are rather specified by the programmer. Hyperparameters are generally selected via trial and error and are not changed through the learning process. The best algorithm returned results with an accuracy of over 94%. The feature importance is provided in Table 7-2. The normalized reference conductive loss has over 10% influence on accurately predicting the condition of the top layer. This is important because Lc neutralizes the effect of depth variations in condition assessment.

Table 7-2
Feature Importance (Module 1)

Feature	Importance (%)
AmpT	69
Tt	19
Lc	12

7.3.2 Module 2 (predicting Rb)

To assess the condition of the middle layer of the slab, all the features in (7-7), except for the TWTT for the top rebar were used in developing the new algorithm. The best algorithm using these features returned an accuracy of 68%. The accuracy could be improved using a bigger dataset. It is also possible to improve it using the commonly used feature transformation to modify the original input variables. Using the latter approach, the accuracy was increased to 80%; however, the resulting algorithm did not perform well on the experimental data. Therefore, 68% was the final achieved accuracy for the current dataset. The feature importance for the top three features is presented in Table 7-3.

Table 7-3
Feature Importance (Module 2)

Feature	Importance (%)
AmpB	51
RTB	23
Lc	21

7.4 Field and Laboratory Implementation

To implement this methodology for assessment of real bridge decks, GPR surveys were performed both on a validation slab in the laboratory, and on four concrete bridge decks. A new dataset was generated, and a new learning algorithm developed building upon the simulations-based algorithm. The results are presented in the next sections.

As mentioned earlier in the numerical simulations section, the condition ratings assigned based on EM material properties were used as targets. To establish these targets for the experimental data, and to demonstrate that the condition ratings are an appropriate replacement for the amplitude and TWTT, the contour maps were plotted based on both

attenuation and condition ratings. It was demonstrated that the two contour maps were very much alike, indicating that it is acceptable to use the condition ratings for machine learning purposes, instead of the amplitudes. After it was established that the two contour maps were quite comparable, the condition ratings could be used as the ML targets. In Sections 7.4.2.1 and 7.4.2.2, the correlation between the condition rating maps and attenuation maps is established. Then, in Section 7.4.1.3, developing the learning algorithm based on experimental data is discussed.

7.4.1 Field Implementation

Given the ideal conditions in numerical simulations, it was possible to extract the reflections from the bottom of the deck and use them as one of the features for full-depth condition assessment of the slab. In the real GPR surveys, however, it is not always possible to isolate the reflections from the bottom of the deck, and sometimes even the reflections from the bottom rebars are difficult to pick in the B-scans. In the three-layer slab simulations, the reflections from the bottom of the slab and the corresponding two-way travel times were important features in assessing the condition of the bottom layer below the bottom reinforcing bars. Given the limitations in obtaining the attributes of the bottom of the deck, the assessment of real bridge decks is limited to the top and middle portions only. The top part is located directly above the top level reinforcement, and the middle portion encompasses both the top and the bottom reinforcing bars.

The GPR data used in this study were collected as part of the Federal Highway Administration's (FHWA's) Long-Term Bridge Performance (LTBP) Program. Within the scope of this program, the condition of a total of more than twenty bridges was periodically

evaluated. The bridges were selected by FHWA in collaboration with the state DOTs and the LTBP research team from Rutgers' Center for Advanced Infrastructure and Transportation (CAIT). The NDE team was responsible for assessing the condition of bridge decks via NDE methods. In the first phase of the program, bare concrete bridge decks were evaluated using six different NDE methods: impact echo, ultrasonic surface waves, ground penetrating radar, half-cell potential, electrical resistivity, and chain dragging/ hammer sounding.

The GPR surveys were primarily conducted using a GSSI 1.5 GHz antenna and a SIR-20 control unit. The data were collected using different gain settings for each bridge. The survey lines were 2-ft apart, with the first line being 1-ft away from the curb and parallel to the traffic as the top reinforcing bars were in the transverse direction.

Four bridges representing different conditions were selected to develop the experimental dataset for this study: Christiana Parkway Bridge in Delaware, Deptford Bridge in New Jersey, Neptune Bridge in New Jersey, and Pequea Bridge in Pennsylvania.

For normalizing the amplitudes and for depth correction, the new approach introduced by Dinh et al. (2016) was used (9). This new approach was briefly discussed in Section 3.4.4 and will be further explained in this section. The top layer of bridges above the top reinforcing bars was evaluated first, followed by the evaluation of the middle portion.

After time-zero adjustment and background removal, the reflection amplitudes and corresponding two-way travel times for the top and bottom rebars were extracted by picking the hyperbolas directly from the B-scans in the 3D profile of each bridge in RADAN 7 (83). A representative B-scan and picked hyperbolas are depicted in Figure 7-7. The amplitudes were extracted in data units and later converted into NdB.

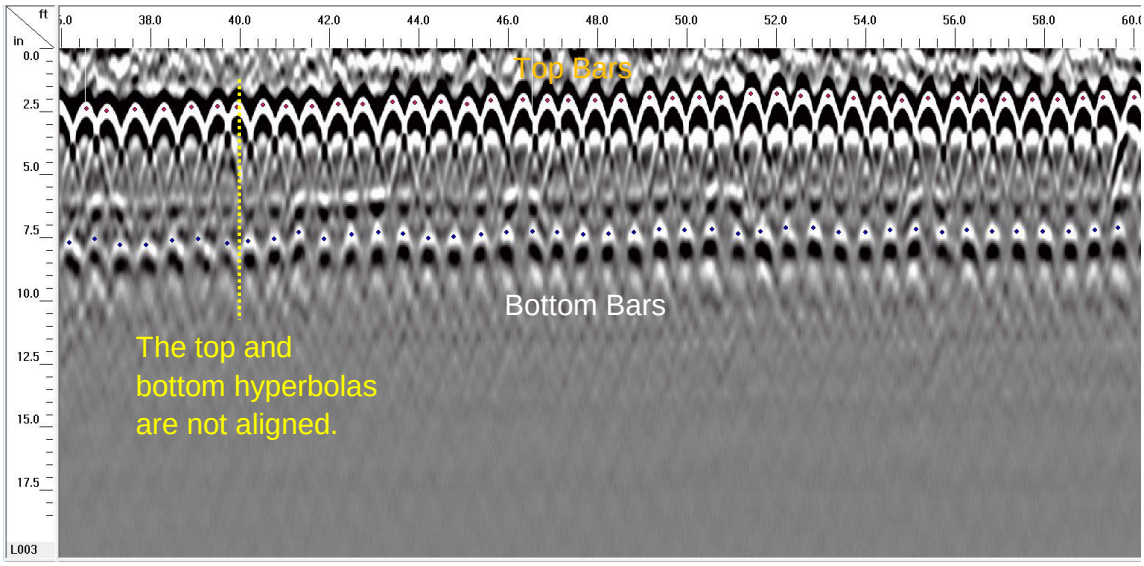

Figure 7-7. Top and bottom bars picked in RADAN 7.

Instead of using the maximum measurable amplitude by the control unit (2^{15} for SIR-20) for normalizing the amplitudes, the average direct-coupling reflection for each bridge was used. Using an average direct-coupling reflection helps eliminate the effect of different power or gain settings at the time of data collection. The direct-coupling reflections may vary throughout the deck depending on the surface condition, for example, due to the presence of patches or pothole. However, those remain fairly stable for a given bridge, regardless of concrete condition (Figure 7-8). To eliminate the effect of surface irregularities, the average of direct-coupling reflections was used. The direct coupling amplitudes were extracted from the 3D *.DZT files using a MATLAB script. The raw amplitudes were then normalized using Equation (3-27).

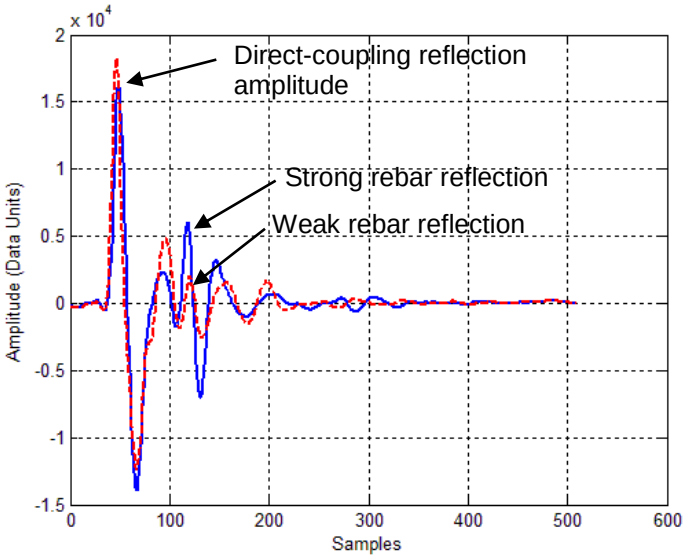

Figure 7-8. Representative A-scans for rebars in different conditions.

7.4.1.1 Evaluation of the Top Layer

Figure 7-9 depicts the 3D representation of the reflection amplitudes for the top reinforcing bars for Pequea Bridge. Reflection amplitudes for each bridge were first analyzed using the traditional 90th percentile depth correction method. Figure 7-10 (a) illustrates the raw top rebar reflection amplitudes. Figure 7-10 (b) shows the depth corrected amplitudes for the same bridge. Green dots represent deck in sound condition, blue dots represent deck in fair condition, yellow dots represent deck in poor condition, and finally, red dots represent deck in serious condition. The thresholds for different conditions are as follows:

$$\begin{aligned} &Amp_c\ (NdB) < -12 && \rightarrow \text{Serious condition} \\ &-12 < Amp_c\ (NdB) < -10 && \rightarrow \text{Poor condition} \\ &-10 < Amp_c\ (NdB) < -5 && \rightarrow \text{Fair condition} \\ &Amp_c\ (NdB) > -5 && \rightarrow \text{Sound condition} \end{aligned} \tag{7-10}$$

Where Amp_c is the depth corrected amplitude in normalized dB.

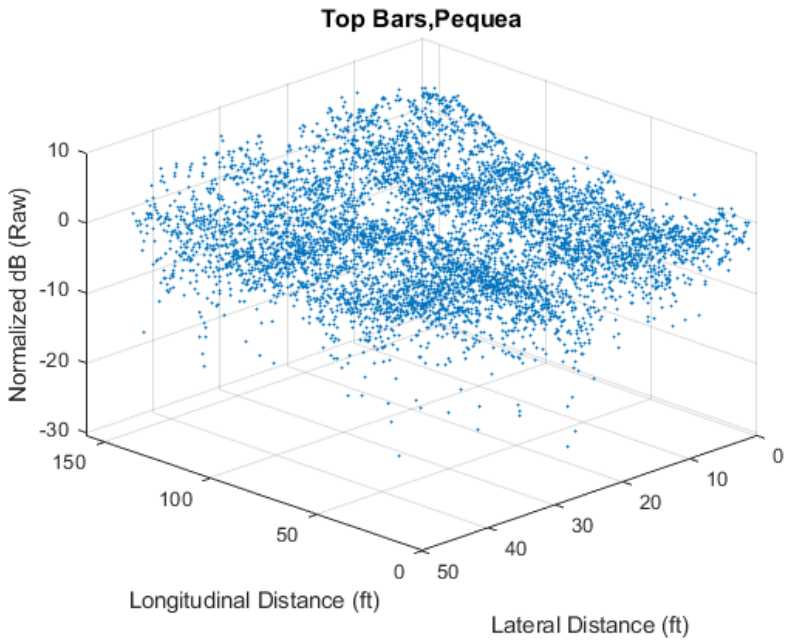

Figure 7-9. 3D representation of normalized top rebar reflection amplitudes (Pequea Bridge).

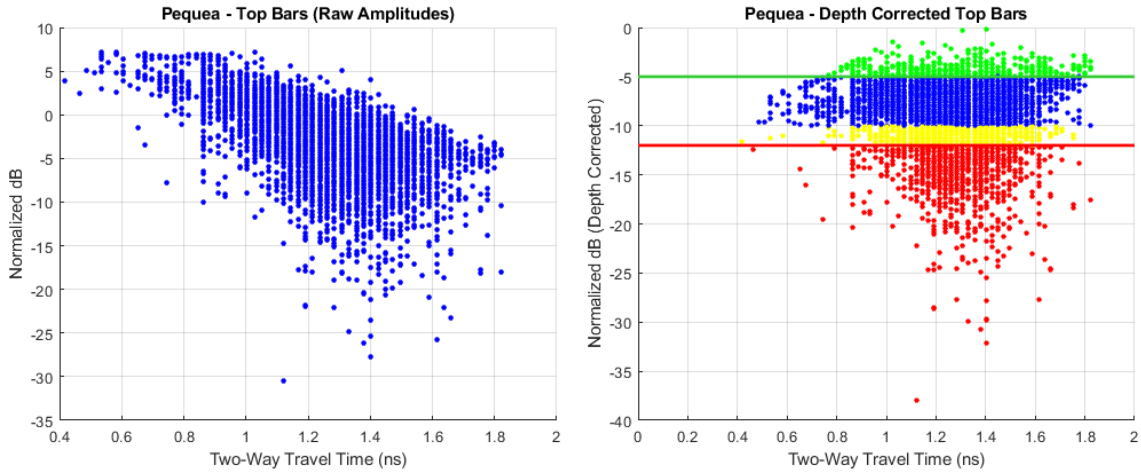

(a) (b)

Figure 7-10. Pequea Bridge top rebars reflection amplitudes (a) raw amplitudes, (b) traditional 90th percentile depth correction.

The condition maps for the four bridges based on the modified depth correction approach are presented later in Figure 7-13 (a) to Figure 7-16 (a).

A combined total of 30,696 data points were extracted for the top reinforcing bars for all four bridges. The reflection amplitudes for the top bars for all four bridges are presented in Figure 7-11.

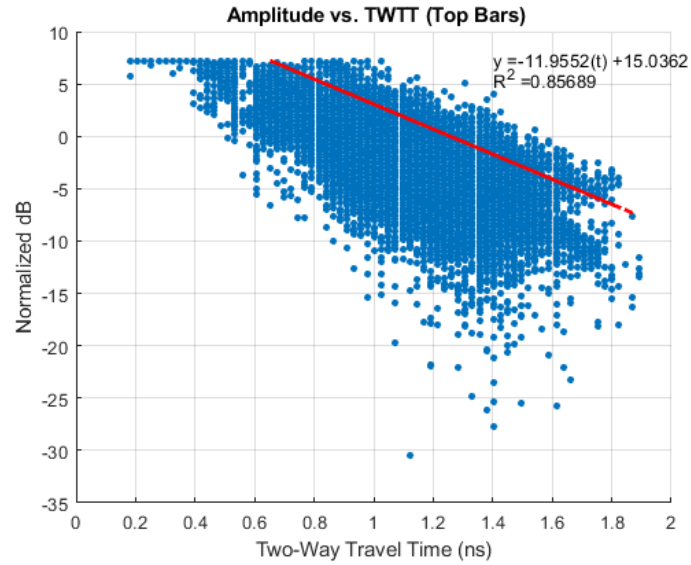

(a)

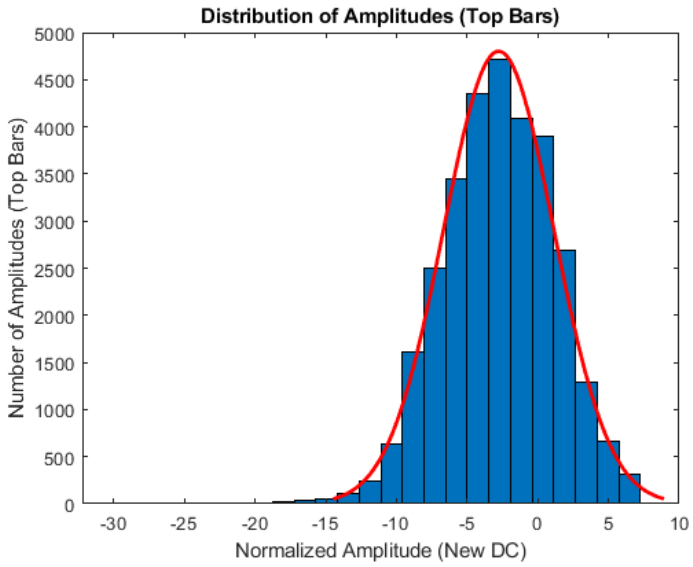

(b)

Figure 7-11. Raw top reflection amplitudes for all bridges: (a) normalized amplitudes vs. TWTT, (b) data distribution.

The reflection amplitudes corresponding to sound areas of all bridges were extracted, and the best fit linear regression line was calculated. The coefficient of determination, r^2, for

this linear regression was 0.86. The regression line serves as the reference to identify the concrete condition. For a given two-way travel time, this line returns the amplitude for a hypothetical rebar in an area of the deck with good condition at the top layer. The top rebar amplitudes and the reference line for the sound deck are shown in Figure 7-11 (a).

Following the new depth correction approach introduced by Dinh at al. (2016), individual amplitudes for each bridge were subtracted from the reference amplitude. For a given two-way travel time, the survey amplitudes greater than the reference amplitude based on the linear regression were considered sound. Conversely, survey amplitudes less than the reference amplitude for a given two-way travel time were deemed to be associated with reinforcement in a deteriorated concrete. This approach was modified to generate a condition rating for each measured amplitude. The subtracted amplitudes for each bridge were assigned a rating number 0, 30, 60, and 100 representing the top layer of the deck in sound, fair, poor, and serious conditions, respectively (Table 7-4). This procedure is summarized in a flowchart in Figure 7-12.

Table 7-4
Concrete condition rating (top layer)

Condition of the Deck	Condition Rating	$y - \hat{y}$
Sound	100	> 0
Fair	60	-5 < < 0
Poor	30	-7 < < -5
Serious	0	< -7

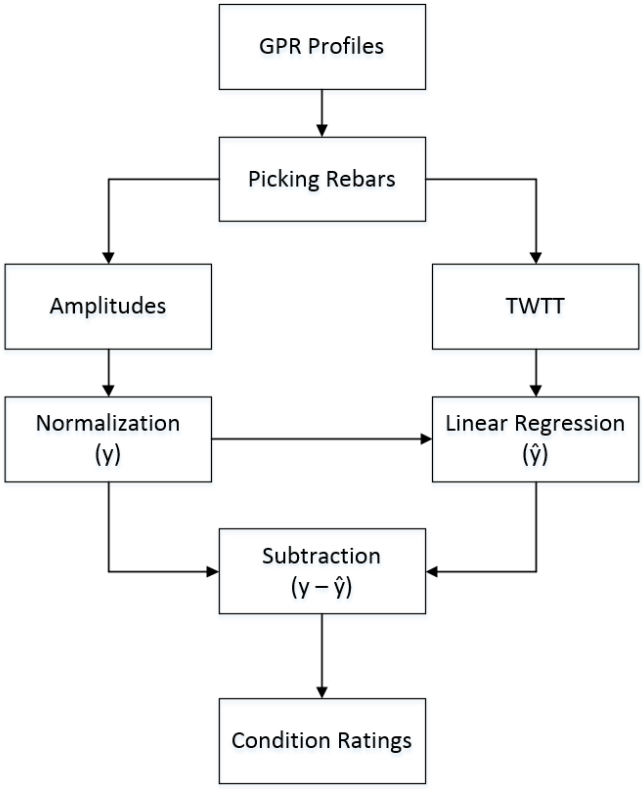

Figure 7-12. New procedure for condition assessment of top deck layer.

The condition maps for the four bridges based on the condition ratings are presented in Figure 7-13 (b) to Figure 7-16 (b). Instead of attenuation, the condition ratings were plotted for the new depth correction. The surface electrical resistivity maps are also presented for comparison.

The condition maps based on the condition ratings appear to provide a more conservative assessment of the top layer, as opposed to the maps based on the traditional method. The deteriorated areas of the latter seem to have a good correlation with the maps generated based on surface resistivity. The deteriorated areas, as detected by GPR attenuation and surface resistivity, are both characterized by the corrosive environment. However, the GPR attenuation is a function of corrosiveness within the bulk of concrete in which the EM

waves travel, while the Wenner probe measures the resistivity of the concrete section, approximately, above the top rebar.

Given the fact that the condition ratings provided a more conservative assessment of the deck, and possibly a better correlation with the surface resistivity map, the condition rating numbers obtained through the new approach were used for the learning algorithm. The TWTT, raw amplitudes, and the condition ratings were the three features used to train the model. This learning algorithm is later used for the condition assessment of a validation slab and a new bridge. The use of this algorithm means that there will be no need to perform the depth correction for a new bridge or slab. The raw amplitudes normalized to the direct coupling amplitude are fed to the learning algorithm, and the condition map is plotted based on the resulting condition ratings.

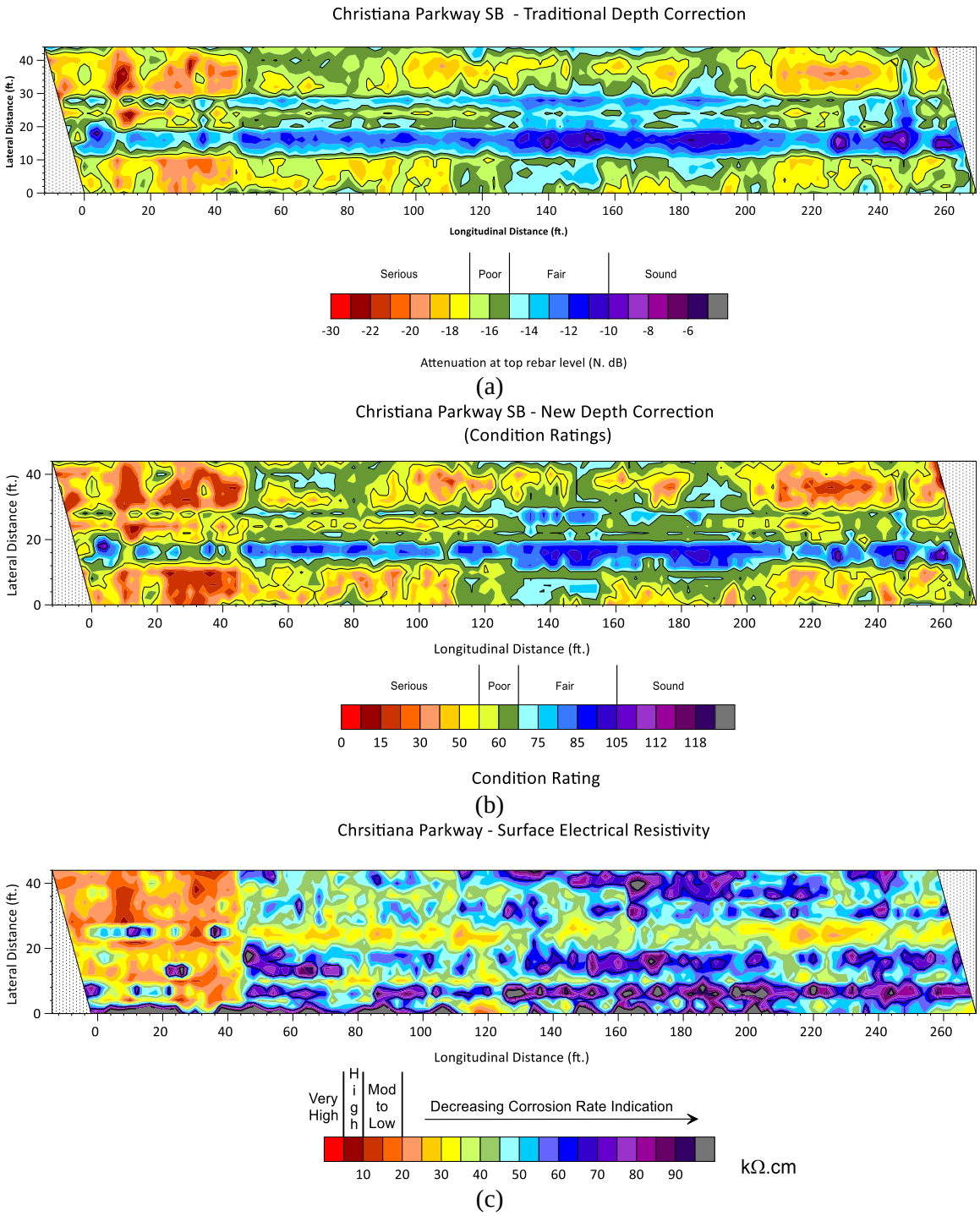

Figure 7-13. Condition maps for Christiana Parkway Bridge: (a) GPR based on traditional depth correction, (b) GPR based on new depth correction and condition rating, (c) electrical resistivity.

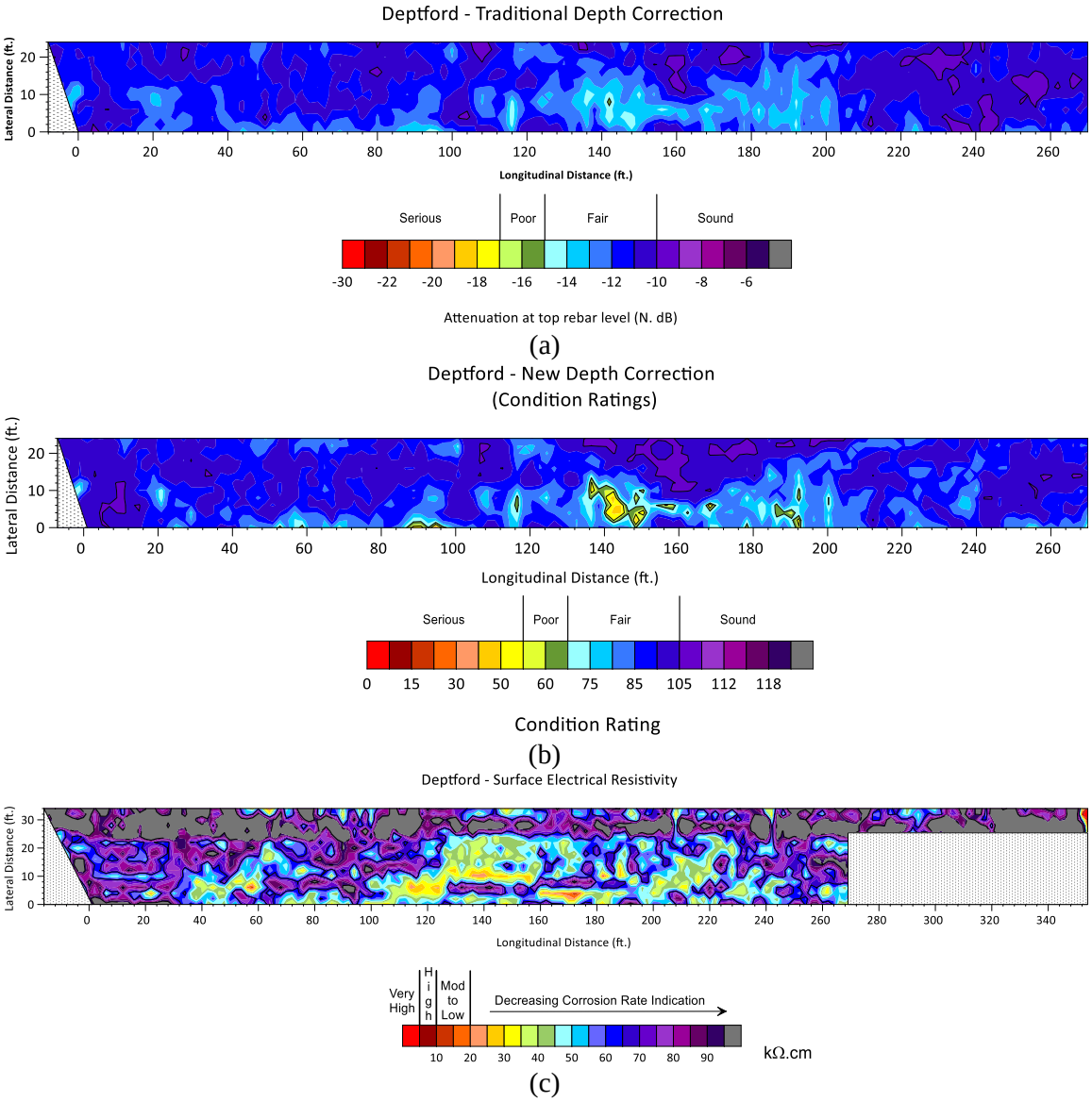

Figure 7-14. Condition maps for Deptford Bridge: (a) GPR based on traditional depth correction, (b) GPR based on new depth correction and condition rating, (c) electrical resistivity.

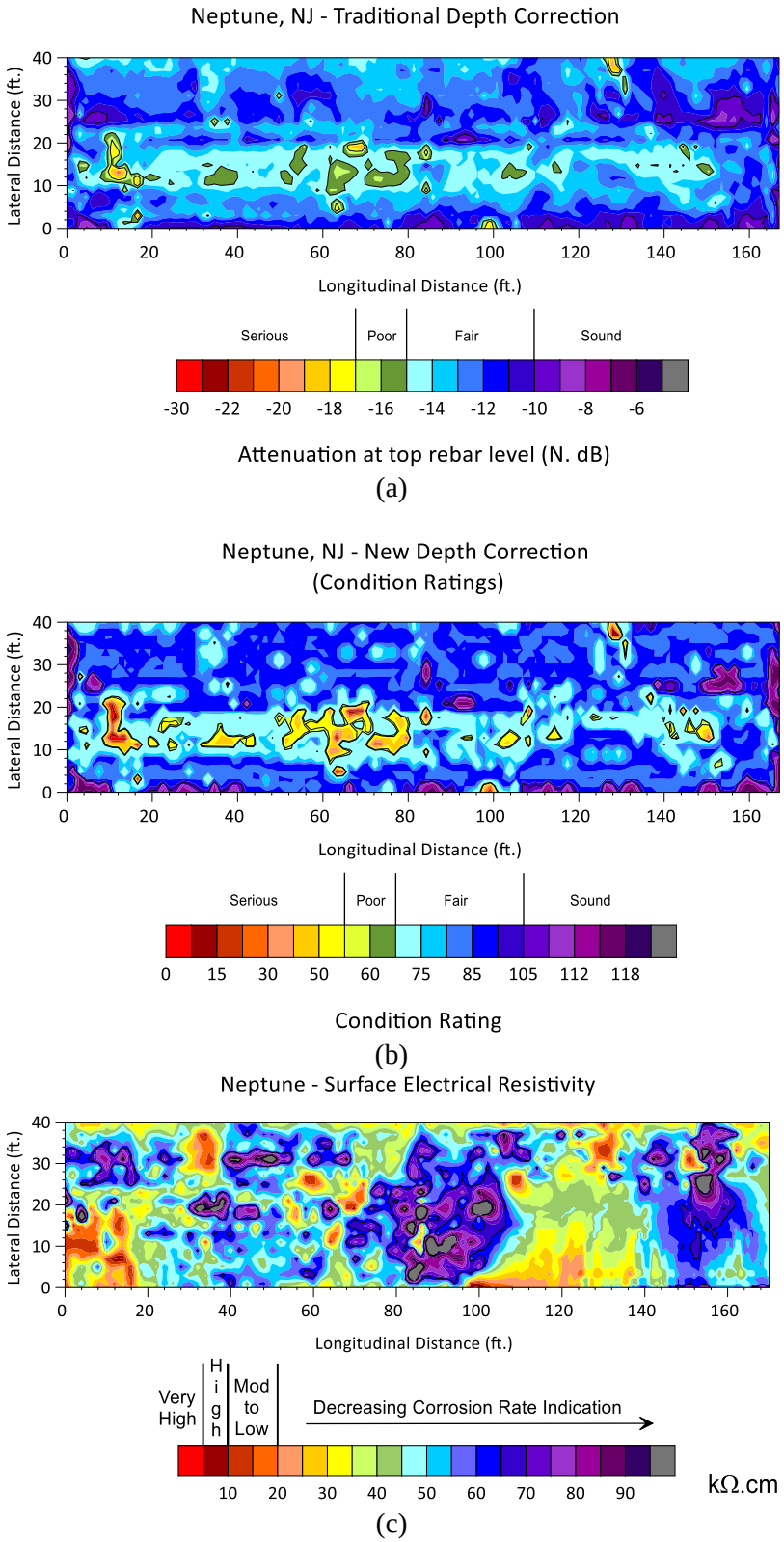

Figure 7-15. Condition maps for Neptune Bridge: (a) GPR based on traditional depth correction, (b) GPR based on new depth correction and condition rating, (c) electrical resistivity.

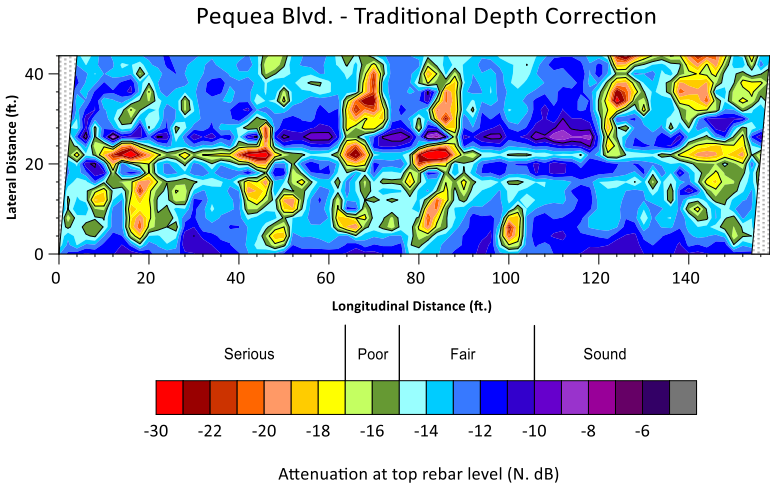

(a)

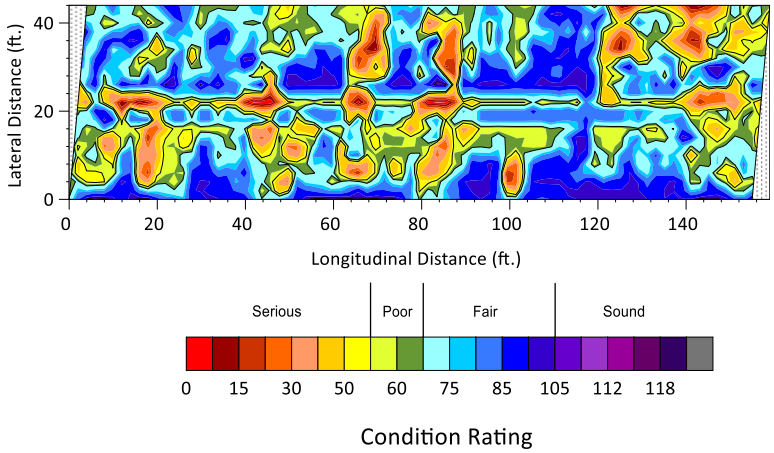

(b)

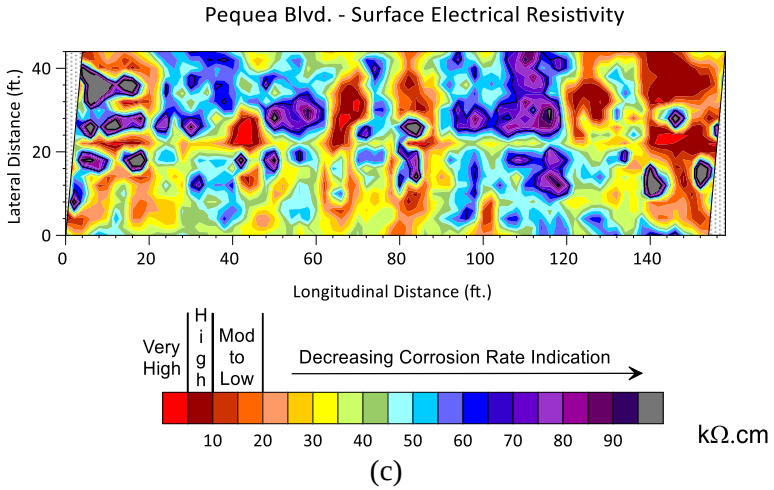

(c)

Figure 7-16. Condition maps for Pequea Bridge: ((a) GPR based on traditional depth correction, (b) GPR based on new depth correction and condition rating, (c) electrical resistivity.

7.4.1.2 Evaluation of the Middle Layer

Two post-processing methods were used to analyze the condition of the middle portion of the deck. In the first method, only the reflection amplitudes from the bottom rebars were used, much like the evaluation of the top layer. In the second method, the minimum reflection amplitude over each foot of the bridge was extracted eliminating the other amplitudes. The reduced data from the second method were used to train the learning algorithm. The results are presented and compared in the next sections.

7.4.1.2.1 Method 1 – Using the Bottom Rebar Reflection Amplitudes

Figure 7-17 depicts the 3D representation of the reflection amplitudes for the top and bottom reinforcing bars for Pequea Bridge. Similar to the analysis of the top layer, bottom rebar reflection amplitudes for each bridge were first analyzed using a modified 80th percentile depth correction method. In this case, it was assumed that approximately 15 to 20% of the middle portion of each bridge deck is in a sound condition.

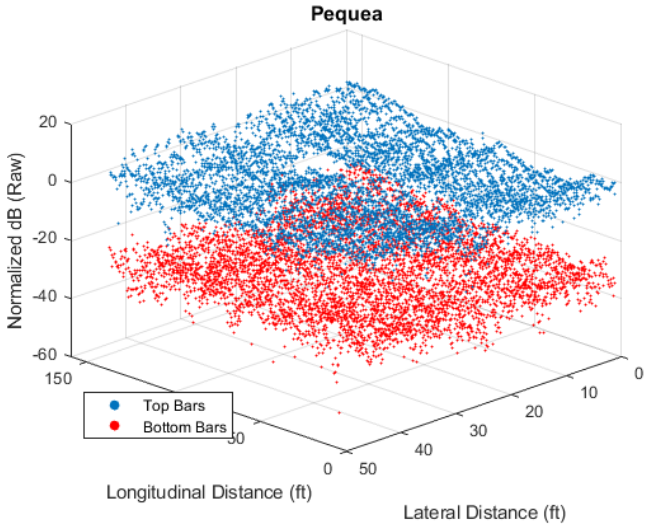

Figure 7-17. 3D representation of normalized top and bottom rebar reflection amplitudes (Pequea Bridge).

A combined total of 25,891 data points were extracted for the bottom reinforcing bars for all four bridges. The reflection amplitudes for the bottom bars for all four bridges are presented in Figure 7-18. The same procedure shown in Figure 7-12 was used for post-processing the reflection amplitudes from the bottom rebars.

Similar to the top rebar analysis, the reflection amplitudes corresponding to sound areas of all bridges were extracted, and the best fit linear regression line was calculated. The coefficient of determination, r^2, for this linear regression was 0.78. Again, the regression line serves as the reference to determine the concrete condition of the middle layer of the deck. For a given two-way travel time, this line returns the amplitude for a theoretical rebar in an area of the deck in good condition. The bottom rebar amplitudes and the reference line for the sound deck are shown in Figure 7-18 (a).

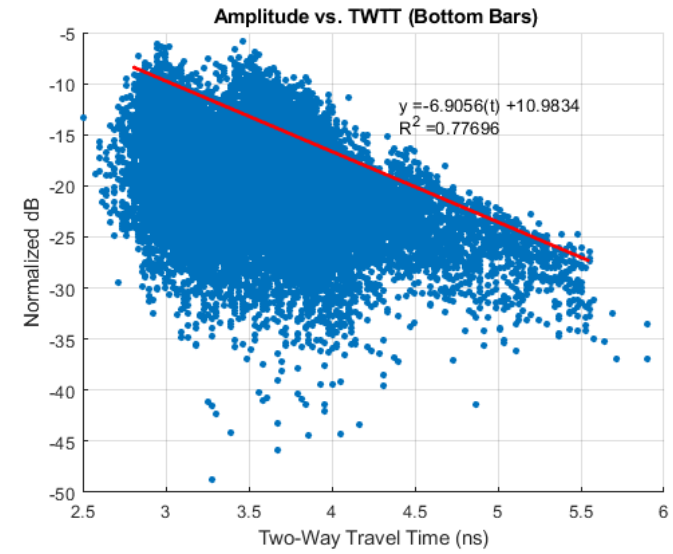

(a)

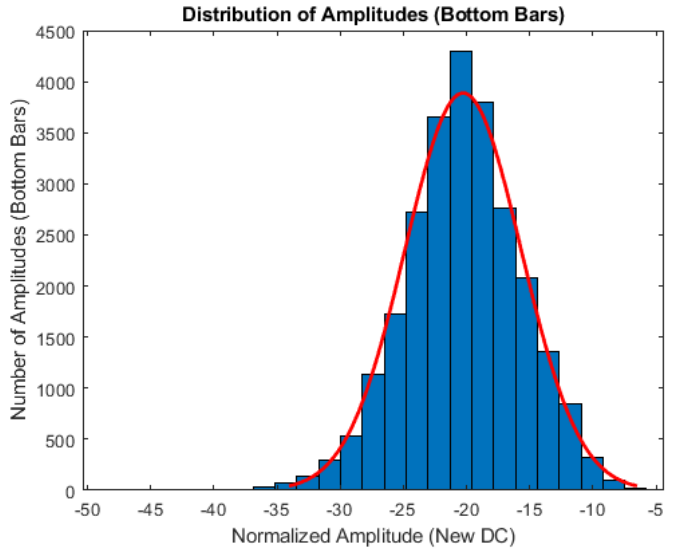

(b)

Figure 7-18. Bottom reflection amplitudes for all bridges: (a) normalized amplitudes vs. TWTT, (b) data distribution.

The same methodology as the top layer was used for further analysis of the reflection from the bottom bars to assess the condition of the middle section. The individual amplitudes for each bridge were subtracted from the reference amplitude. For a given two-way travel time, the survey amplitudes greater than the reference amplitude based on the linear regression were considered sound. Conversely, survey amplitudes less than the reference

amplitude for all the bridges were deemed to be indicative of reinforcement in deteriorated concrete (Table 7-5).

Table 7-5
Concrete condition rating (middle layer)

Condition of the Deck	Condition Rating	$y - \hat{y}$
Sound	100	> 0
Fair	60	-10 < < 0
Poor	30	-15 < < -10
Serious	0	< -15

The corrected amplitudes using the reference amplitude line for each bridge were assigned a rating number ranging from 0 to 100. Concrete in the middle layer of the deck in sound, fair, poor, and serious condition was assigned 100, 60, 30, and 0, respectively.

The condition maps for the middle layer of the four bridges based on the new depth correction approach are presented in Figure 7-19 (a) to Figure 7-22 (a). Instead of attenuation, the condition ratings were plotted for the new depth correction. The condition maps based on the two methods (80^{th} percentile depth correction and condition rating based on the reference amplitude line) exhibit a good correlation, even though the condition rating maps for the middle layer appear to be less conservative than the condition maps based on traditional depth correction. This correlation indicates that instead of analyzing individual bridge data using the arbitrary N^{th} percentile depth correction, it is reasonable to use the raw GPR amplitudes and the reference amplitude line.

The condition rating numbers were used to train a learning algorithm to predict the middle layer condition. The TWTT, raw amplitudes, and the condition ratings were the three features used to train the model. This learning algorithm is later used for condition

assessment of a validation slab and the new bridge. The use of this algorithm means that there will be no need to perform any additional depth correction for a new bridge or slab. The raw amplitudes normalized to the direct coupling amplitude are fed to the learning algorithm, and the condition map is plotted based on the resulting condition ratings.

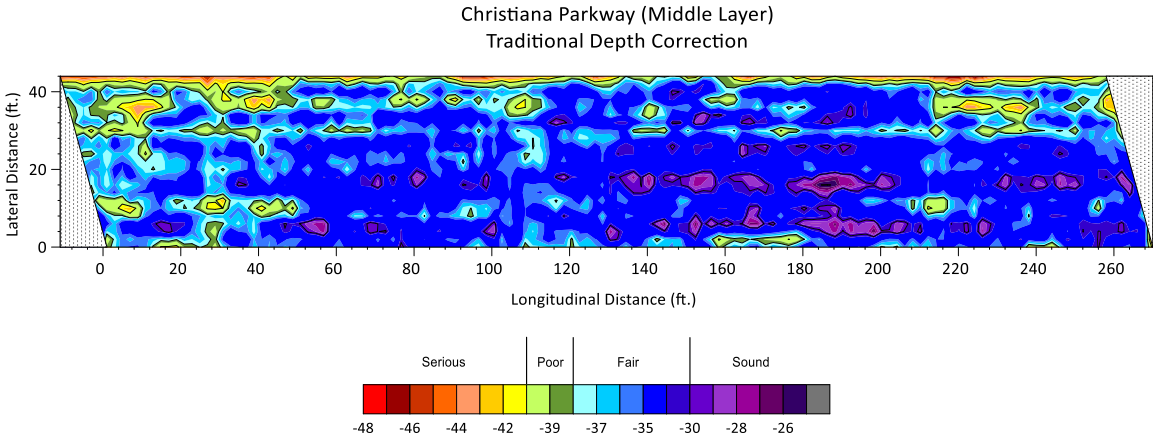

(a)

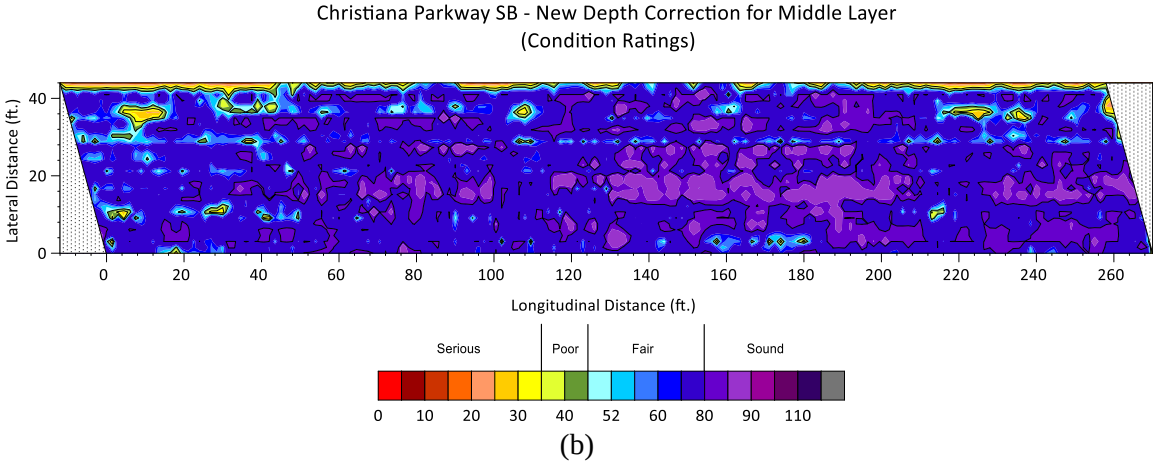

(b)

Figure 7-19. Condition maps for Christiana Parkway Bridge: (a) GPR based on traditional depth correction, (b) GPR based on new depth correction and condition rating.

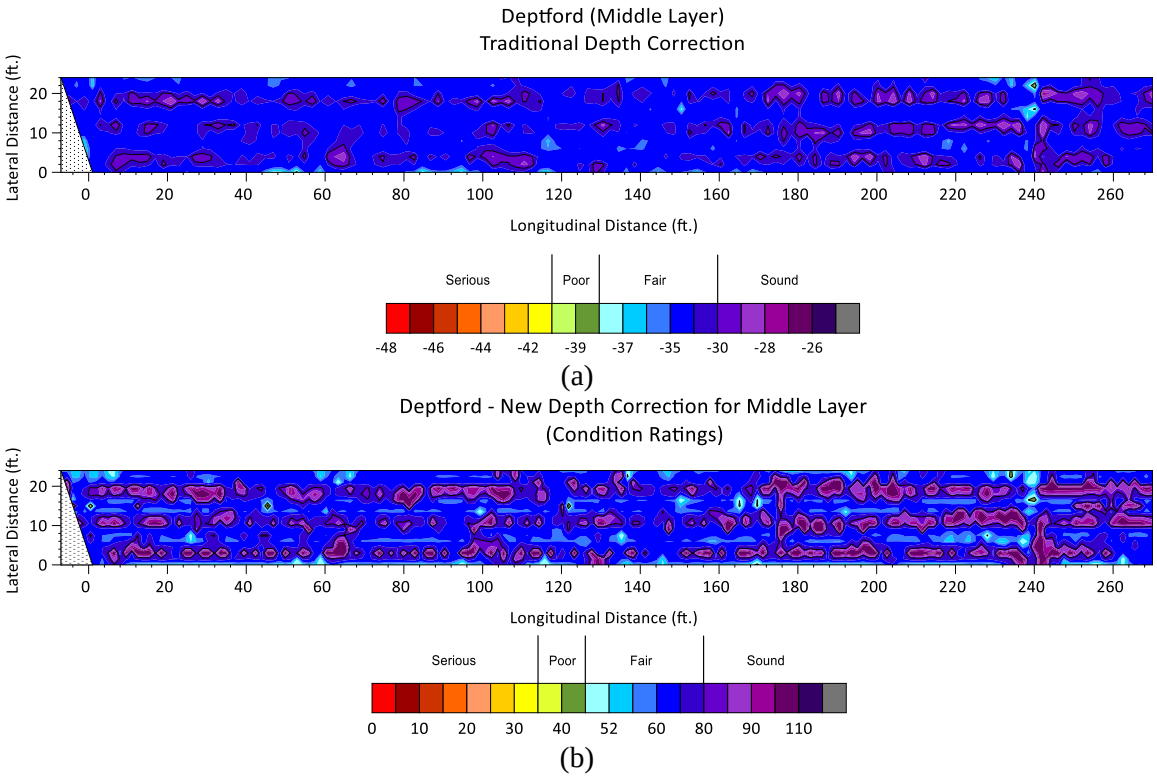

Figure 7-20. Condition maps for Deptford Bridge: (a) GPR based on traditional depth correction, (b) GPR based on new depth correction and condition rating.

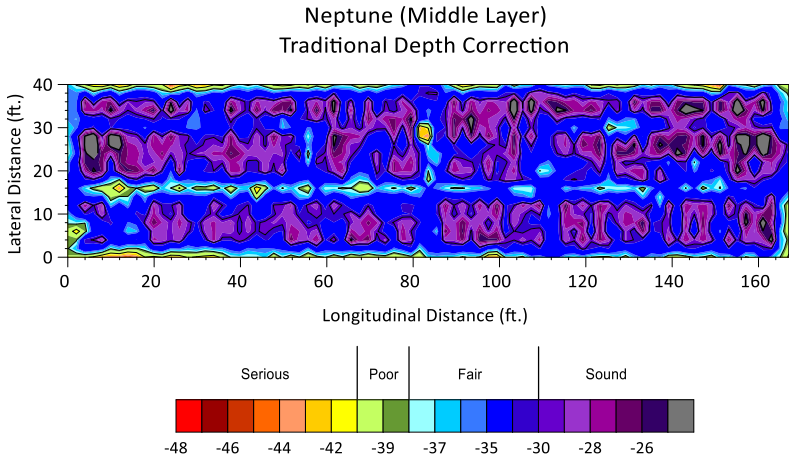

(a)

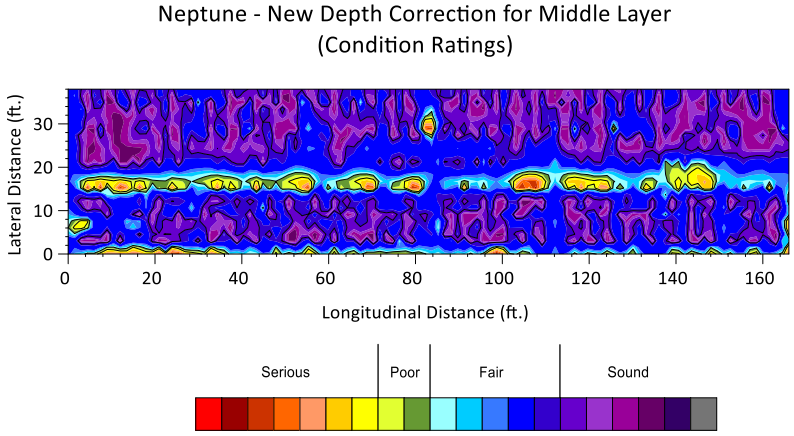

(b)

Figure 7-21. Condition maps for Neptune Bridge: (a) GPR based on traditional depth correction, (b) GPR based on new depth correction and condition rating.

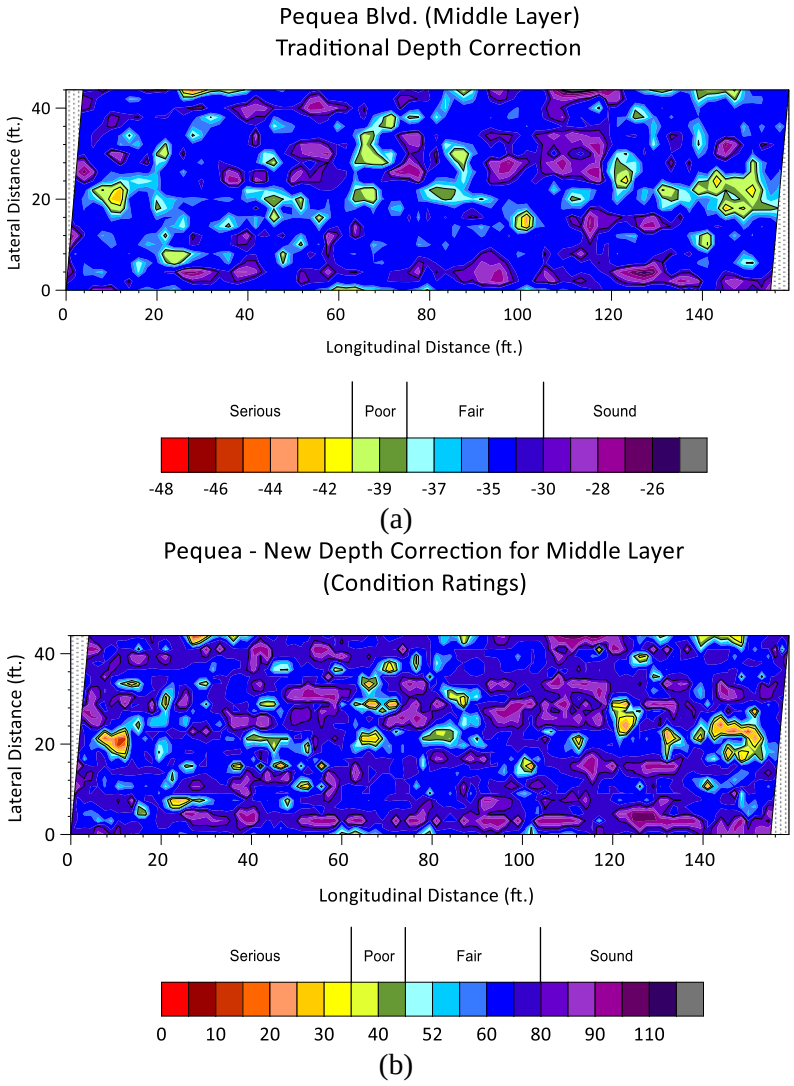

Figure 7-22. Condition maps for Pequea Bridge: ((a) GPR based on traditional depth correction, (b) GPR based on new depth correction and condition rating.

7.4.1.2.2 Method 2 – Data Reduction over Each Foot of a Survey Line

In Figure 7-23 (a), the normalized dB amplitudes for an individual survey line are presented. Figure 7-23 (b) depicts a close-up view of the top and bottom amplitudes as picked on a B-scan. It can be observed that location-wise, there is not a one to one correlation between the top and bottom rebars. The normalized dB amplitudes for the top and bottom bars for all survey lines for each bridge and their corresponding physical locations are presented in Figure 7-24.

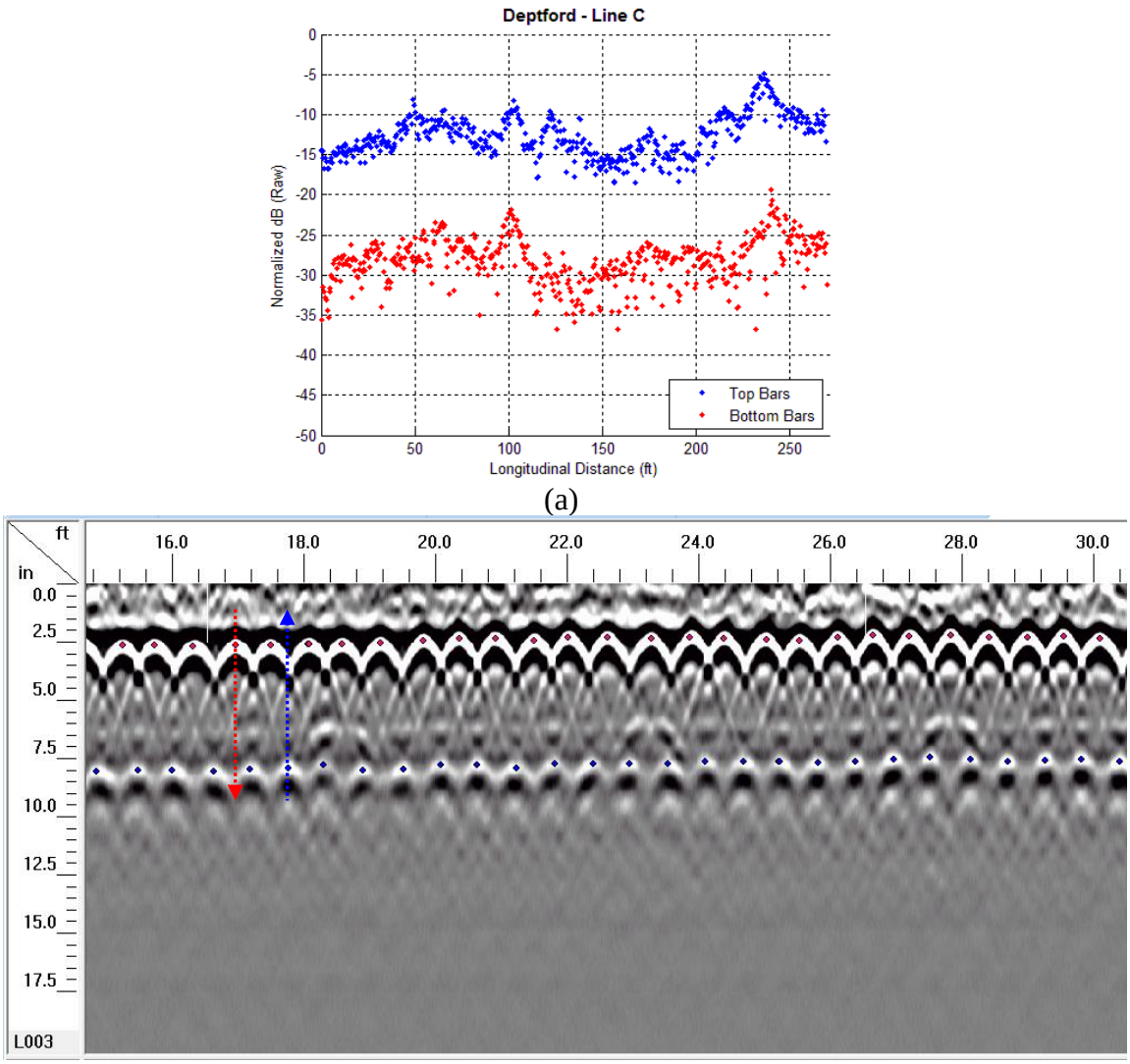

Figure 7-23. Normalized dB for top and bottom amplitudes for a survey line.

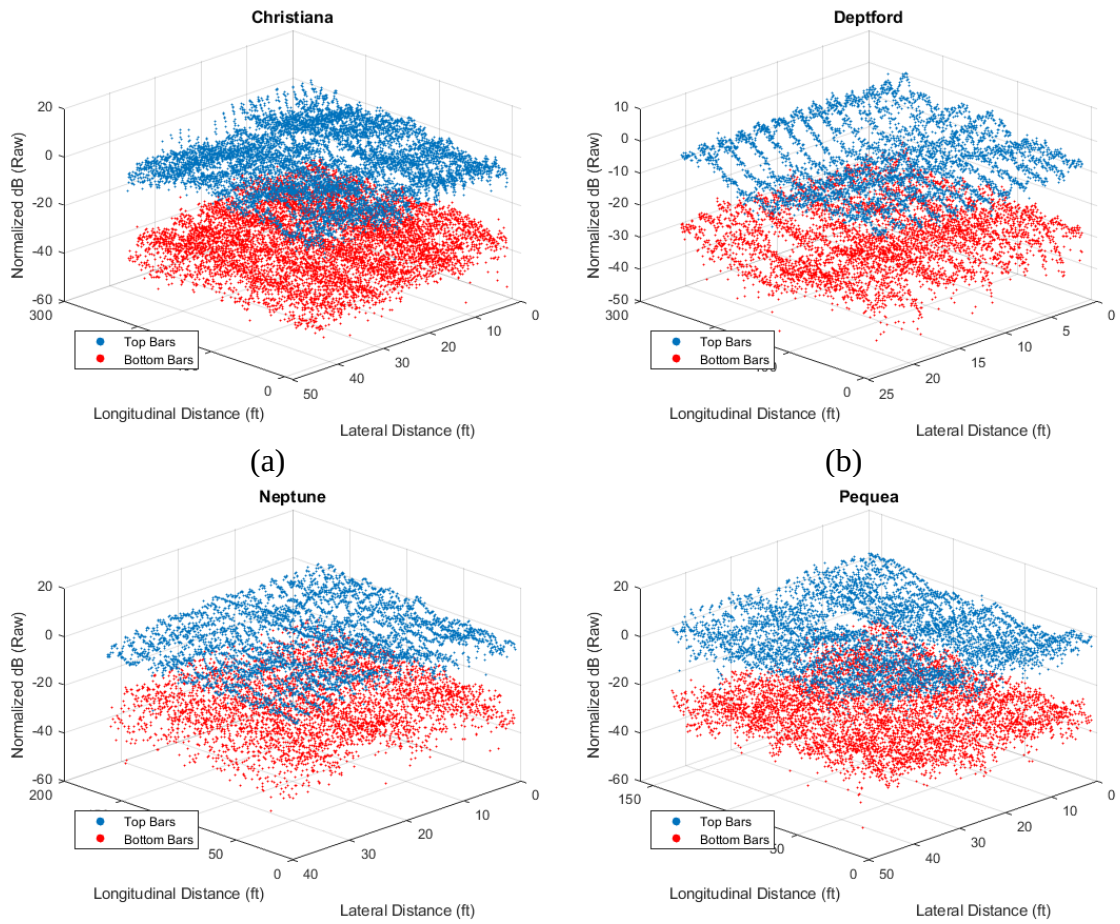

Figure 7-24. Normalized dB for top and bottom amplitudes with respect to physical location on the bridge.

In a learning algorithm, all the features must be of the same length. However, when picking rebars, the number of points picked for the top and bottom levels do not necessarily match. Additionally, the simulation results showed that the attributes for both top and bottom rebars are needed when analyzing the condition of concrete below the top rebar level. One of the input features for the machine learning algorithm used to predict the layer ratings (concrete condition) based on the numerical simulation data was the ratio of the top rebar amplitude to the bottom rebar amplitude collected at the *same location*. In real GPR radargrams, however, the hyperbolas associated with the top and bottom reinforcing bars are not necessarily aligned and collected at the same longitudinal location (Figure 7-23 (b)).

To resolve these two issues, a data reduction procedure was employed in which at every foot of a given survey line, the minimum raw amplitude was selected discarding the other hyperbolas over that foot. This method of data reduction provides a more conservative condition assessment of the deck below the top reinforcing bars. Figure 7-25 (a) depicts all the raw amplitudes for the top and bottom rebars associated with the survey line L on Deptford Bridge. Figure 7-25 (b) demonstrates the same survey line after data reduction. The data-reduced image is sparser, but the two images are not significantly different.

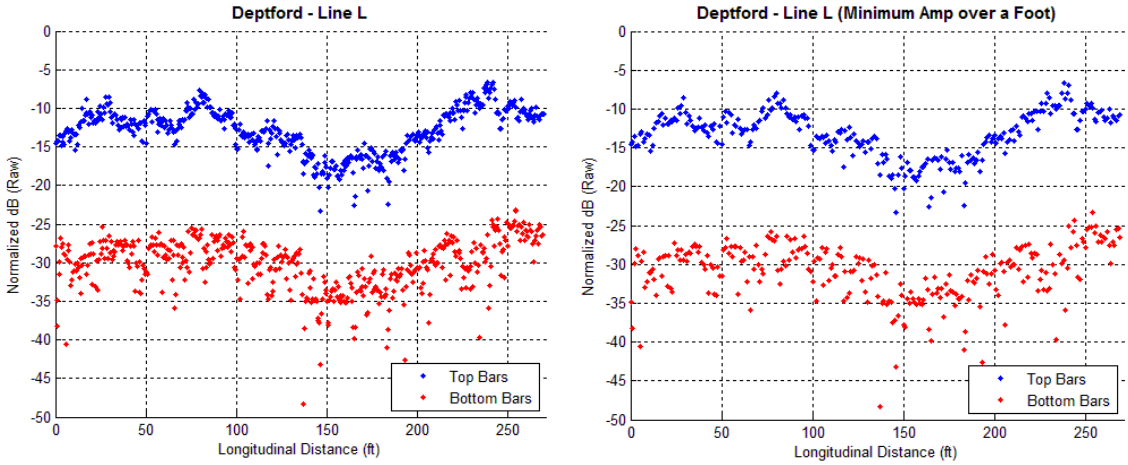

(a) (b)

Figure 7-25. Survey Line L, Deptford Bridge; (a) all the raw amplitudes, (b) minimum amplitudes over every one foot of the survey line.

The data reduction was performed only to assess the middle layer of the deck. For evaluating the top layer, the entire data points for all bridges were used.

7.4.1.2.2.1 Adjustment of layer rating for the bottom bars

One indication of deterioration below the top reinforcing bars is that there is a significant attenuation at the bottom rebar compared to the top rebar at the same location. Therefore, for each bridge and after data reduction, the attenuation difference between the top and bottom bars were calculated. Additionally, the average of attenuation drops and the

standard deviations were calculated. If the attenuation drop at a given location was more than the overall average plus hundred and twenty percent of the standard deviation, the middle layer was assumed to be in serious condition. In other words, an additional criterion for the serious condition was defined as follows:

$$Amp_{Bottom} - Amp_{Top} > \mu + 1.2 \times \sigma \qquad (7\text{-}11)$$

The rationale behind this criterion is that the condition of the middle layer depends on the attenuation between the top and bottom rebars. Therefore, a significant attenuation at the bottom rebar level compared to the top rebar could be indicative of concrete in poor condition.

Figure 7-26 (a) illustrates the amplitudes at the top and bottom rebars for a specific survey line. Figure 7-26 (b) shows how the condition ratings for the middle layer were adjusted based on the attenuation drop; the points above the red line were assigned a serious condition rating.

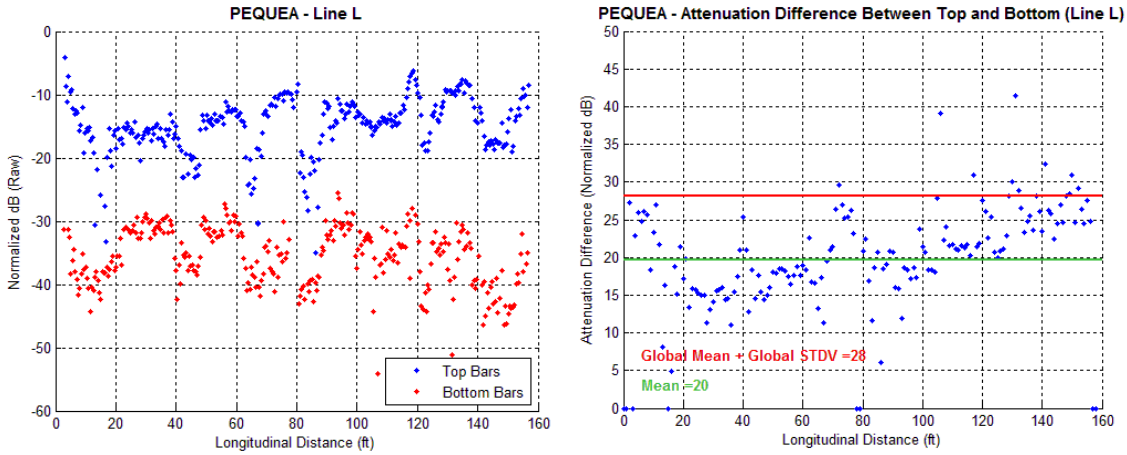

(a) (b)

Figure 7-26. (a) Attenuations at the top and bottom rebars for Line L, Pequea Bridge, (b) Adjusting bottom layer ratings for deteriorated areas based on attenuation difference.

7.4.1.3 Learning Algorithm

Similar to the learning algorithm developed for the FDTD simulation data in 7.3, the GPR data from surveying four bridges were used to develop a learning algorithm to predict the condition of the deck. Two modules were used: *Module 1* to predict the condition at the top layer of the deck, and *Module 2* to predict the condition at the middle layer.

7.4.1.3.1 Module 1: Predicting the condition of the top layer

The learning algorithm for module 1 uses three input features: reflection amplitude from the top rebars, the two-way travel time for the top rebar, and an artificial feature which was the exponential function of the amplitude, or exp(Amp_T). The target value was the condition rating.

$$X^{(i)} = \{AmpT, Tt, \exp(AmpT)\}$$
$$Y^{(i)} = \{Rt\} \;\; ; \;\; Rt = \{0, 30, 60, 100\} \qquad (7\text{-}12)$$

The goal was developing a model for predicting the condition ratings for other bridges and the laboratory slab without the need to do individual depth corrections.

A total number of 30,696 $\{(X^{(i)}, Y^{(i)})\}$ data points were used for this algorithm. The data set was randomly split into two sets: (a) 70% to train the algorithm and fine-tune the parameters, and (b) 30% to validate the learned model. The training set and the test set were independent of one another. The best accuracy for the test set was over 98% for the assumptions that were made in the definition of condition ratings. The main assumption was that the condition ratings for the four bridges used for constructing the model were correct and providing ground truth.

The feature importance was also evaluated. The two-way travel time has the highest impact followed by the amplitude. The feature importance is summarized in Table 7-6.

Table 7-6
Feature Importance (Module 1)

Feature	Importance (%)
Tt	49.77
AmpT	25.90
exp(AmpT)	24.33

It must be noted that when the condition ratings were generated based on the traditional depth correction approach, the accuracy of the model was 71.3%. This is indicative of the validity of the new approach and the need to produce the reference regression line.

This model is later used to predict the condition of a laboratory slab.

The same algorithm was used on the data for the bottom rebars. A total number of 25,891 $\{(X^{(i)}, Y^{(i)})\}$ data points were used. Despite the high accuracy obtained, this approach is flawed as it does not take into account the effect of the top rebars. Such high accuracy could be attributed to potential overfitting given that the data consisted of only four bridges. Similar to the approach for numerical simulations, another algorithm was developed to assess the condition of the middle layer. This is discussed in the next section.

To validate the learning algorithm, the GPR data for a bridge in Wilmington, Delaware was processed. The condition ratings were calculated based on the modified depth correction approach. The raw amplitudes and the TWTT's were fed to the model based on the original four bridges. Out of 12,084 data points, 12,004 of the predicted condition ratings matched those calculated using the modified depth correction. This indicated the potential for avoiding the use of arbitrary depth correction for a new bridge as long as a

learning algorithm can be developed based on several bridges within a network when the same GPR system is used for data collection. Figure 7-27 illustrates the condition maps for the top layer of the deck based on both the traditional analysis, and the new condition rating. Figure 7-28 depicts the Wilmington bridge data superimposed over the original four bridges.

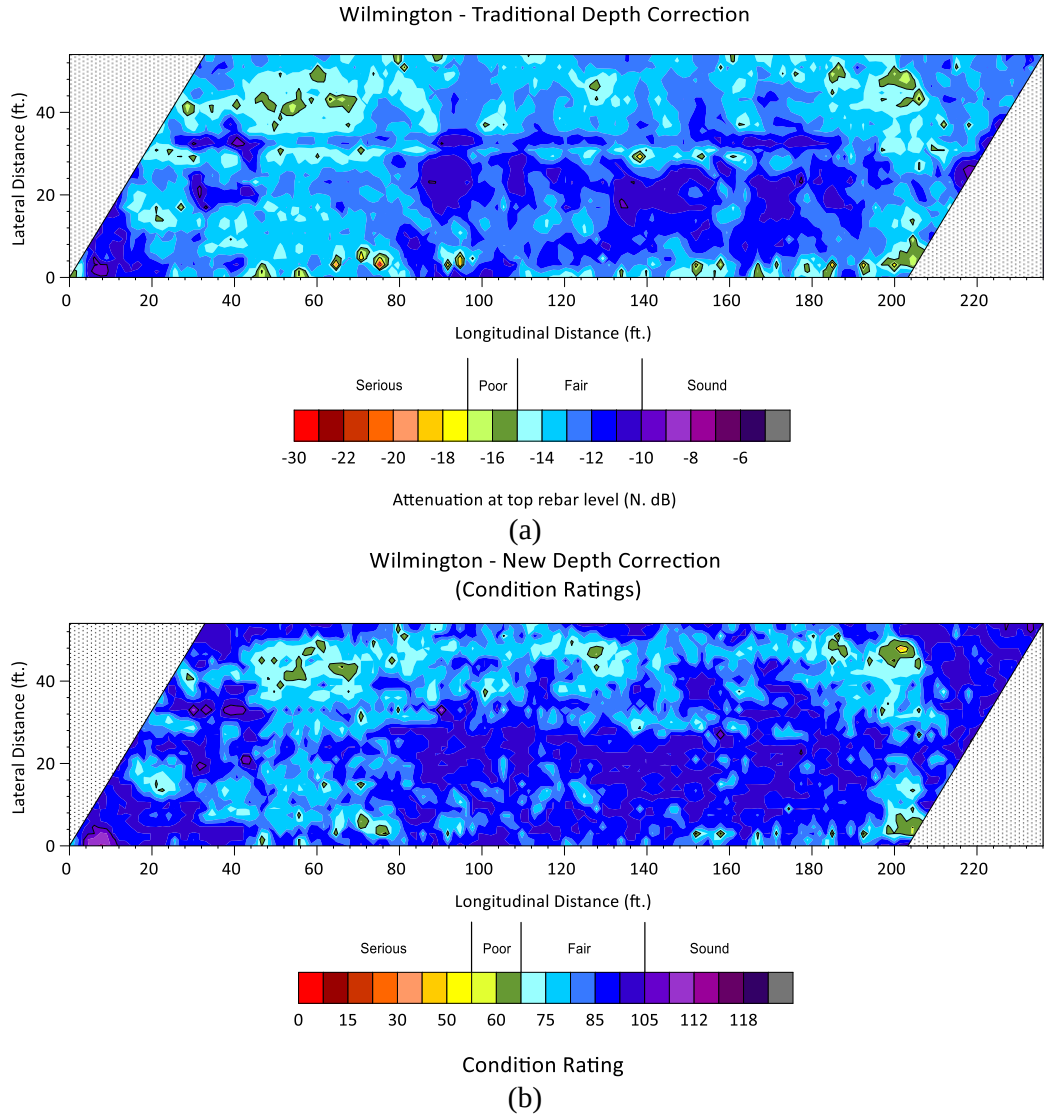

Figure 7-27. Condition maps for the top layer of Wilmington Bridge: (a) GPR based on traditional depth correction, (b) GPR based on new depth correction and condition rating.

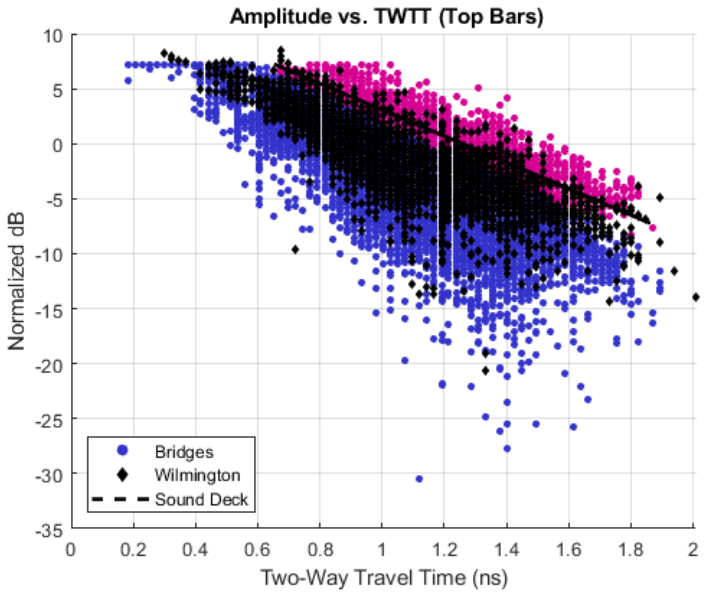

Figure 7-28. Top rebar reflection amplitudes (for the four bridges) normalized with respect to the average direct-coupling amplitude. The Wilmington bridge amplitudes are shown using black dots.

7.4.1.3.2 Module 2: Predicting the condition of the middle layer

The learning algorithm for module 2 uses seven input features after the data reduction explained earlier in Section 7.4.1.2.2: reflection amplitude from the top and bottom rebars, the two-way travel times, and two artificial features, which were the exponential function of the amplitudes, and the ratio of the amplitudes. The target value was the condition rating.

$$X^{(i)} = \{AmpT, AmpB, Tt, Tb, \exp(AmpT), \exp(AmpB), AmpT/AmpB\}$$
$$Y^{(i)} = \{Rt, Rb\} \;;\; R_j = \{0, 30, 60, 100\} \quad (7\text{-}13)$$

A total number of 15,259 $\{(X^{(i)}, Y^{(i)})\}$ data points were used for this algorithm. The data set was randomly split into two sets: (a) 70% to train the algorithm and fine-tune the parameters, and (b) 30% to validate the learned model. The training set and the test set were independent of one another. The best accuracy for the test set was 79.7%.

The feature importance was also evaluated. The reflection amplitude from the bottom rebar has the highest impact followed by the two-way travel time for the bottom rebar. The feature importance is summarized in Table 7-7.

Table 7-7
Feature Importance (Module 2)

Feature	Importance (%)
AmpB	50.17
Tb	37.25
Tt	6.16
AmpB/AmpT	2.94
AmpT	2.32
exp(AmpT)	1.15
exp(AmpB)	0

Figure 7-29 illustrates the condition maps for the middle layer of the deck based on both depth correction method, and the condition rating.

As discussed, the learning algorithm has two modules: one for the top layer of the deck above the top rebar, and one for the middle portion of the deck. Whereas little ground truth information is available about the middle portion of the deck, the predictions for the top layer can be compared against traditional attenuation maps as well as electrical resistivity maps. In both cases, the ML predictions are in good agreement. Since the learning algorithm based on the numerical simulations works well and with high accuracy for both the top and middle layers, and since it was already established that the experimental-based algorithm works well for the top layer, it can be argued that the learning algorithm based on the experimental data works well for the middle layer as well.

This model is later in this chapter used to predict the condition of a laboratory slab.

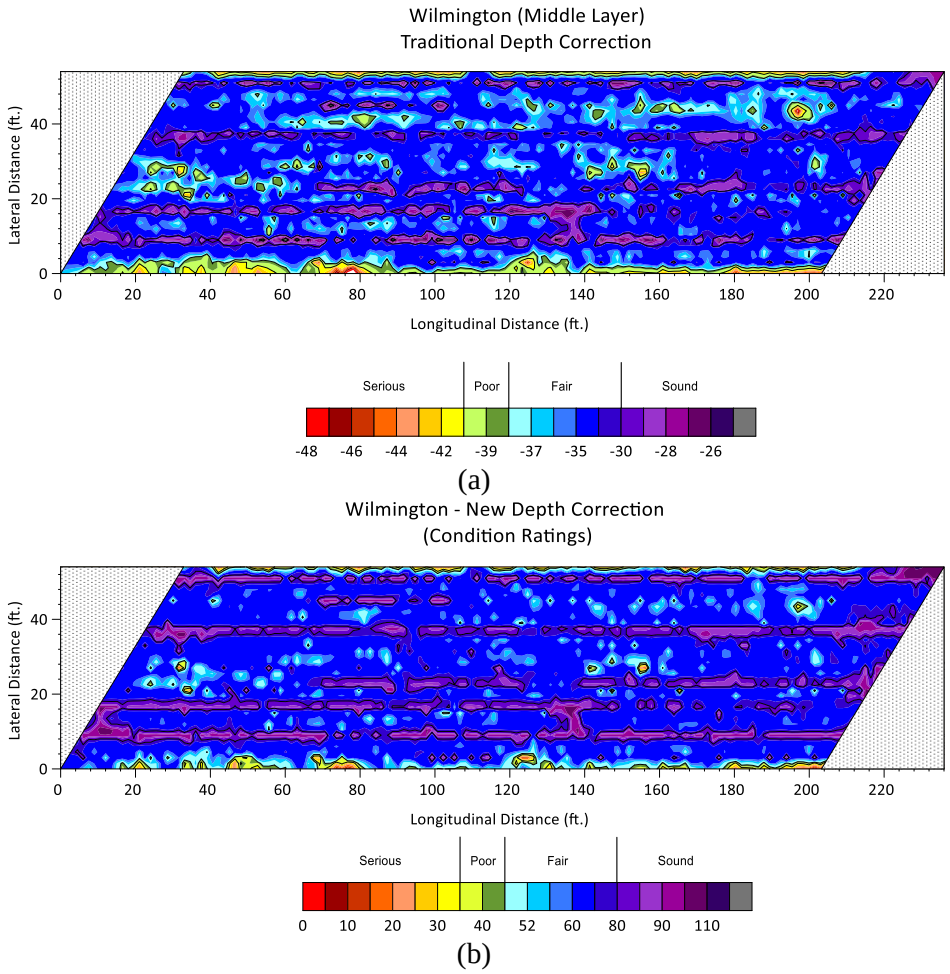

Figure 7-29. Condition maps for the Wilmington Bridge: (a) GPR based on traditional depth correction, (b) GPR based on new depth correction and condition rating.

7.4.2 Laboratory Implementation (A) – Experimental Data-Based Algorithm

The laboratory validation was performed using the same GPR system used in surveying the highway bridge decks. The validation slab was prepared as a part of the Automated Nondestructive Evaluation and Rehabilitation System (ANDERS) project funded by the National Institute of Standard and Technology (NIST). The validation slab at Rutgers is 30-ft long, 12-ft wide, and 8-inch thick (Figure 7-30). Artificial defects, including various types of delamination and areas with high salt (sodium chloride) concentrations, were

introduced into the slab. The slab was fabricated using normal portland cement concrete with 2.5-in of concrete cover. The transverse bars placed at 6-in on center.

Figure 7-30. Validation slab.

The GPR survey was conducted using a GSSI 1.5 GHz antenna and a SIR-20 control unit. The survey lines were 1-ft apart with the first line being 1.5-ft away from the edge of the

slab and perpendicular to the top reinforcing bars which were in the transverse direction. A total of 495 rebars were picked for the top reinforcing level, and a total of 467 for the bottom level.

7.4.2.1 Assessment of the Top Concrete Layer

Figure 7-31 depicts the top rebar amplitudes from the slab superimposed on the top rebar amplitudes for the four bridges. The amplitudes corresponding to sound concrete are shown in pink. The linear regression line is also shown.

The condition maps generated based on the traditional 90^{th} percentile and the new condition rating approach are presented in Figure 7-32. The GPR map based on the condition rating, Figure 7-32 (b), was generated based on the procedure described in Figure 7-12; after normalization, the amplitudes were subtracted from the reference amplitude line (linear regression), and the condition ratings were assigned. The condition rating approach provides a more conservative condition map compared to the traditional depth corrected condition map.

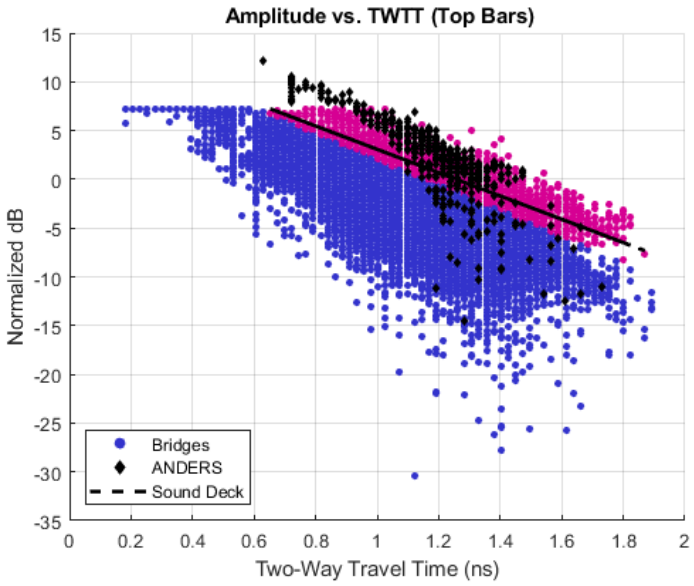

Figure 7-31. Top rebar reflection amplitudes normalized with respect to the average direct-coupling amplitude. The validation slab amplitudes are shown using black dots.

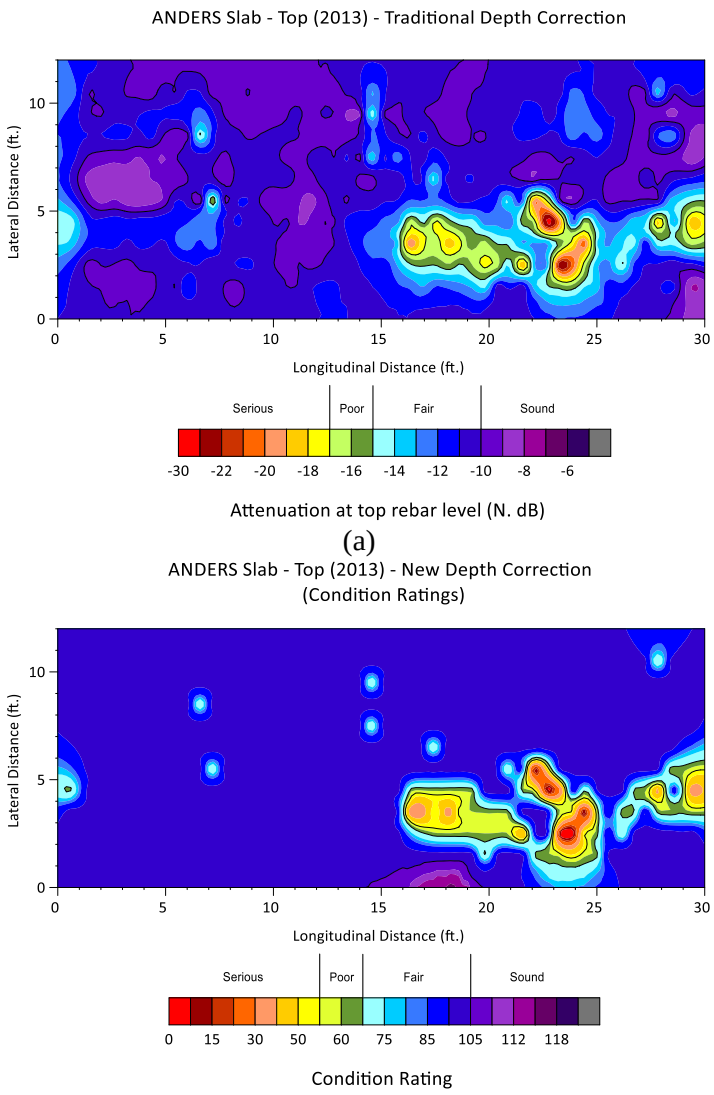

Figure 7-32. Condition maps for the ANDERS slab: (a) GPR based on traditional depth correction, (b) GPR based on new depth correction and condition rating.

7.4.2.1.1 Learning Algorithm (Top Layer)

To validate the learning algorithm developed in Section 7.4.1.2.1, the top rebar amplitudes, the corresponding TWTT's, and exponential functions of the amplitudes for the ANDERS slab were fed to the *Module 1* algorithm. Out of 495 points, the algorithm predicted the condition rating of 491 points correctly. This high level of accuracy indicates that using machine learning and a library of GPR data, it is possible to avoid the arbitrary 90th

percentile depth correction without compromising the ability to assess the deck condition properly.

7.4.2.2 Assessment of the Middle Concrete Layer

Figure 7-33 depicts the top rebar amplitudes from the slab superimposed on the bottom rebar amplitudes for the four bridges. The amplitudes corresponding to sound concrete are shown in pink. The linear regression line is also shown.

The condition maps generated based on the traditional 80th percentile and the new condition rating approach are presented in Figure 7-34. The GPR map based on the condition rating, Figure 7-34 (b), was generated based on the procedure described in Figure 7-12; after normalization, the amplitudes were subtracted from the reference amplitude line (linear regression), and the condition ratings were assigned. The condition rating map for the middle layer is less conservative than the traditional depth corrected condition map.

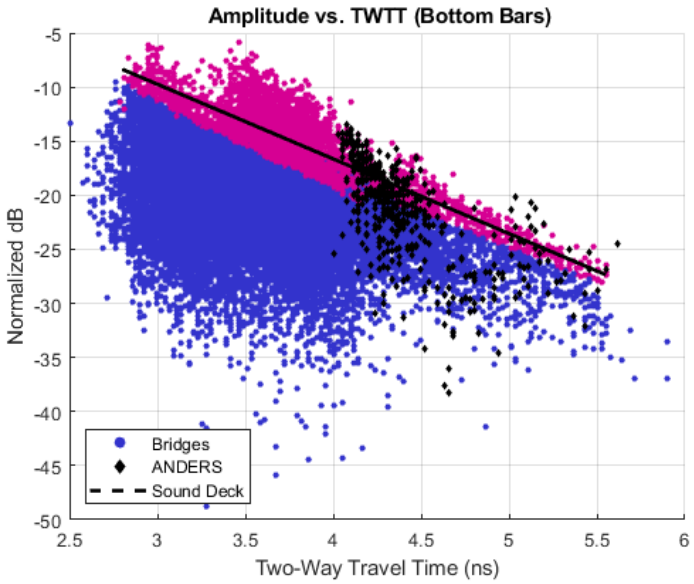

Figure 7-33. Bottom rebar reflection amplitudes normalized with respect to the average direct-coupling amplitude. The validation slab amplitudes are shown using black dots.

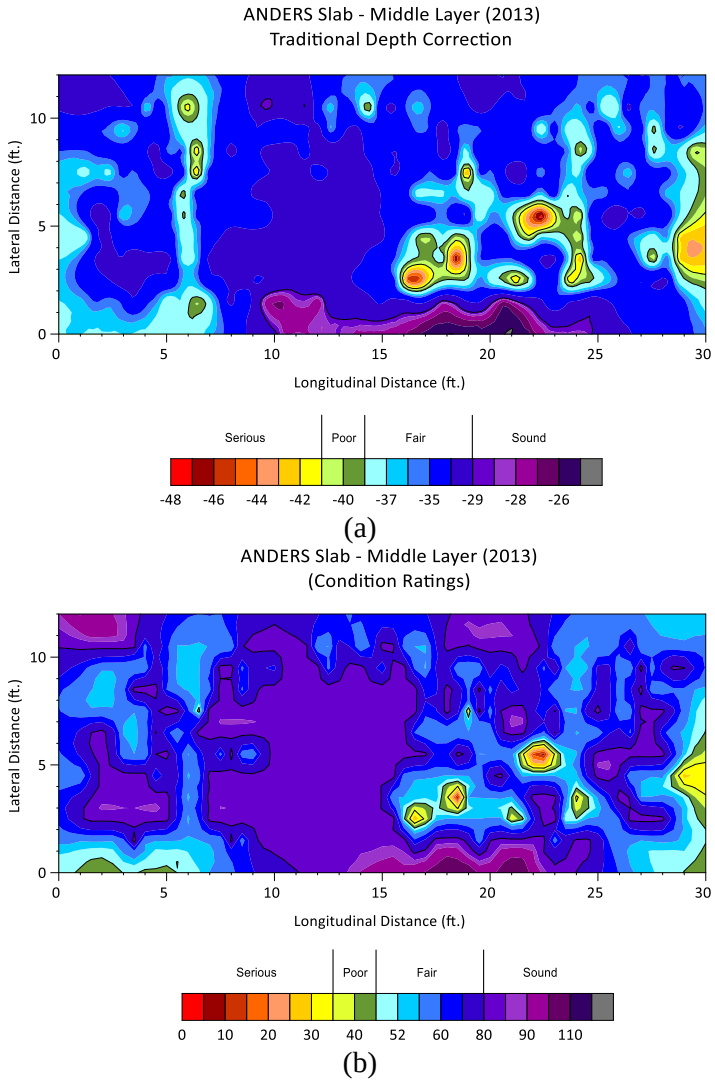

Figure 7-34. Condition maps for the ANDERS slab: (a) GPR based on traditional depth correction, (b) GPR based on new depth correction and condition rating.

7.4.2.2.1 Learning Algorithm (Middle Layer)

To validate the learning algorithm developed in Section 7.4.1.3.2, the ANDERS slab attributes were fed to the *Module 2* algorithm. The accuracy of the model in the middle layer condition prediction was 72.7%. This could potentially be improved should a bigger initial dataset be used to construct the model.

7.4.3 Laboratory Implementation (B) – Numerical Data-Based Algorithm

To examine the possibility of using experimental data in conjunction with the learning algorithm developed using numerical simulations, the validation slab was additionally evaluated using the algorithm developed in Section 7.3. To determine the accuracy, the predicted values were compared against the condition ratings assigned previously based on the modified depth correction approach.

The *Module 1* algorithm (Section 7.3.1) predicts the condition of the top layer of the validation slab with 87% accuracy. This is less than the algorithm accuracy on the test set, which was close to 94%. Table 7-8 provides a randomly selected set of $\{X^{(i)}, Y^{(i)}\}$ pairs. The last column shows the values predicted by the algorithm. The second and third rows are mispredicted; the actual condition is fair, while the algorithm returns a poor condition.

Table 7-8
Randomly selected set of representative $\{(X^{(i)}, Y^{(i)})\}$ samples (Top Layer).

Index	AmpT	Tt	Lc	Assigned Rt	Rt (Predicted)
1	-10.03	1.26	-6.85	100	100
2	-12.73	1.38	-7.11	60	30
3	-12.92	1.40	-6.90	60	30
4	-8.86	1.33	-4.92	100	100
5	-8.10	1.28	-4.99	100	100

The *Module 2* algorithm (Section 7.3.2) predicts the condition of the middle layer of the validation slab with 56% accuracy. This is less than the algorithm accuracy on the test set, which was close to 68%. This is an objectively low accuracy for the middle layer. However, it is worth noting that the optimal accuracy would have been 68%, given the 32% unavoidable bias in the training data. A bigger dataset to train the model could improve both accuracies. Table 7-9 provides a randomly selected set of $\{X^{(i)}, Y^{(i)}\}$ pairs. The last

column shows the values predicted by the algorithm. The first and second rows are mispredicted; the actual condition for the first row is poor, while the algorithm returns a serious condition. Similarly, in the second row, the actual condition is sound, while the algorithm returns a fair condition.

Table 7-9
Randomly selected set of representative $\{(X^{(i)}, Y^{(i)})\}$ samples.

Index	AmpB	Tb	TBR	Lc	Assigned Rt	Rb (Predicted)
1	-31.50	4.40	2.34	-2.74	30	0
2	-28.92	5.50	2.48	-0.35	100	60
3	-23.29	4.24	2.75	-1.18	60	60
4	-15.85	4.05	4.11	0.28	100	100
5	-37.78	4.64	1.88	-3.61	0	0

Whereas the ability to identify EM material properties at various depths of real bridge decks in order to assign the condition ratings would be ideal, this was not possible for the current set of LTBP data. Therefore, the condition ratings were assigned using a modified traditional depth correction method. To develop a more effective learning algorithm based on numerical simulations, it is recommended that a bigger dataset is developed. Additionally, it is imperative to calibrate the numerical data with experimental data through laboratory testing in which the electromagnetic properties of concrete can be controlled at different depths.

Chapter 8. Findings, Conclusions, and Recommendations

The use of nondestructive evaluation methods, particularly the GPR, provides a far more accurate and objective assessment of a reinforced concrete bridge deck condition compared to the traditional methods of deck inspection. The primary goal of the present study was to develop a novel data processing technique to expand the GPR evaluation zone beyond the top reinforcement level, thereby providing the full-depth assessment of the deck. Based on the numerical simulations, machine learning, and the field and laboratory implementation of the learning algorithms, the following main conclusions were made:

- Results of a learning algorithm based on gradient boosting suggest that machine learning is a robust method for expanding the GPR evaluation zone beyond the top reinforcing steel bars.
- By developing a learning algorithm based on numerical simulations, it was demonstrated that machine learning works very well for numerical data. The ways of how to identify features and targets for the bridge deck condition assessment

were also demonstrated. Building upon the numerical simulation experience, the same process was used to train a new algorithm for the experimental data.

- The reflection from the bottom of the deck, based on the numerical simulations, was shown to be one of the input features for the learning algorithm to assess the condition of the bottom layer of the deck. However, in a real GPR survey, it is not always possible to extract the reflection amplitudes from the bottom of the deck. Therefore, the learning algorithm to predict the condition of real bridge decks was limited to assessing the condition of the top layer, above the top rebar, and the middle layer of the deck, encompassing the zone between the top and bottom rebars.

- GPR survey of a bridge deck generates tens of thousands of data points. Combining the GPR data from several bridges creates a good dataset for machine learning purposes. Provided that a pool of data is generated by putting together the survey results from a more significant number of bridges, an algorithm can be trained for condition evaluation of bridge decks, without the need for the arbitrary 90^{th} percentile depth correction for every new bridge.

- It is expected that a more complex learning algorithm, and a more extensive dataset comprised of data from more bridges, will provide more detailed and accurate information about the deck condition. Further improvement can also be achieved by defining a new criterion for picking the hyperbolas and amplitudes corresponding to the bottom reinforcement for post-processing.

- To develop a more effective learning algorithm based on numerical simulations, it is recommended that a more extensive dataset is developed. Additionally, it is

imperative to calibrate the numerical data with experimental data through laboratory testing, in which the electromagnetic properties of concrete can be controlled at different depths.

Based on the results obtained from numerical simulations of GPR surveys, the following secondary conclusions and observations were made:

- The 3D FEM analysis proved to be more time-consuming while producing results comparable to the much faster two-dimensional FDTD simulations.
- Two-dimensional numerical simulations demonstrated that regardless of the concrete condition at various depths of the deck, reflections from the bottom of the deck do not follow any particular trends. This means that despite the ASTM D6087 recommendation to use the amplitudes of reflections from the bottom of a deck as a potential approach to assessing the deck condition, an assessment based on these amplitudes is not reliable.
- Results of a parametric study using numerical simulations for different reinforcement depths and transmitter-receiver spacing showed that a GPR array, or GPR a system with dual Tx-Rx spacing capability, can enable a full depth assessment of a deck.
- A GPR array can cover larger swathes in a considerably shorter time period compared to single channel antennas, thereby increasing the rate of the survey. Additionally, given the advantage of GPR arrays in recording reflections off of multiple Tx-Rx pairs in a single survey path, they make a more comprehensive evaluation of the deck possible. However, beyond a certain Tx-Rx spacing, the data

from a given transducer pair becomes meaningless. It was shown that for an array with the center frequency of 2.6 GHz, the reflections collected by a transmitter-receiver pair does not provide any meaningful information when the ratio of the Tx-Rx spacing to the reflector's depth is greater than $2.5\times \lambda$.

- Results of a parametric study based on numerical simulations for different permittivity and conductivity combinations showed that the EM material properties have almost no influence on the masking effect exerted by the top bar on the strength of reflection from the bottom rebar. The masking effect is almost solely governed by the antenna frequency and the geometry, rather than the electromagnetic properties.

Based on the results obtained from the time-frequency analysis of simulated GPR signals, the following conclusions and observations were made:

- STFT provides quantitative information regarding the dominant frequency of the response, as well as limited qualitative information based on the spectrograms. The two can assist as a complementary tool in a more comprehensive full depth condition assessment of bridge decks. However, given the amount of time and level of expertise needed for STFT analyses, it is not yet suited to be used as the only method for post-processing GPR surveys data.

- A higher dielectric value corresponds to a lower EM wave velocity. When the velocity of wave propagation is lower, the system's dominant features/natural response shift toward lower frequencies. STFT analysis of 3D finite element models showed that an increase in the concrete dielectric leads to a decrease of the

dominant frequency. Higher dielectric values are typical for concrete with a high volume of interconnecting pores and discontinuities, such as delamination and cracks filled with water, especially when it contains chlorides in high concentrations. It is widely accepted that a higher relative dielectric constant is consistent with reinforced concrete decks having some degree of deterioration. Therefore, a lower frequency response is likely associated with some degree of deterioration in the deck.

References

1. Shatz, Howard J, et al. *Highway Infrastructure and the Economy: Implications for Federal Policy.* RAND Corporation. Santa Monica, CA : RAND Corporation, 2011. ISBN: 978-0-8330-5213-1.

2. (ASCE), American Society of Civil Engineers. Report Card for America's Infrastructure, 2017 Grades. [Online] 2017. http://www.infrastructurereportcard.org/.

3. (FHWA), Federal Highway Administration. FHWA Bridge Programs Count, Area, Length of Bridges by Highway System. *National Bridge Inventory (NBI).* [Online] 2017. [Cited: May 18, 2018.] http://www.fhwa.dot.gov/bridge/fc.cfm.

4. US Department of Transportation. *2015 Status of the Nation's Highways, Bridges, and Transit: Conditions and Performance. Report to Congress.* Washington, DC : s.n. pp. 8-8 (364).

5. Biden, Joseph R. *American Recovery and Reinvestment Act Final Report.* s.l. : U.S. Department of Transportation, 2016.

6. Jol, Harry M. *Ground Penetrating Radar Theory and Applications.* s.l. : Elsevier Science, 2009. ISBN-13: 978-0444533487.

7. *Improved concrete bridge deck evaluation using GPR by accounting for signal depth–amplitude effects.* Barnes, Christopher L, Trottier, Jean-Francois and Forgeron, Dean. 2008, NDT&E International, Vol. 41, pp. 427-433.

8. *Validation of Benefits of Automated Depth Correction Method for Improving Accuracy of GPR Deck Deterioration Maps.* Romero, Francisco A, et al. 2015, Transportation Research Record: Journal of the Transportation Research Board, Vol. 2522, pp. 100-109.

9. *Understanding Depth-Amplitude Effects in Assessment of GPR Data from Concrete Bridge Deck Surveys.* Dinh, Kien, et al. s.l. : NDT & E International, 2016.

10. *GSSI Handbook For RADAR Inspection of Concrete.* s.l. : Geophysical Survey Systems, Inc., 2009.

11. Daniels, David J. *Ground Penetrating Radar.* 2nd. London : Institution of Engineering and Technology (IET), 2007. p. 726.

12. Dérobert, X and Berenger, B. Using ground-penetrating radar (GPR) to assess an eight-span post-tensioned viaduct: a case study. *Non-Destructive Evaluation of Reinforced Concrete Structures.* s.l. : CRC Press, 2010, pp. 574-584.

13. *Nondestructive evaluation of grout defects in internal tendons of post-tensioned girders.* Terzioglua, Tevfik, et al. 2018, NDT and E International, Vol. 99, pp. 23-35.

14. Gucunski, Nenad, et al. *Nondestructive Testing to Identify Concrete Bridge Deck Deterioration.* U.S. Department of Transportation, Federal Highway Administration (FHWA). Washington, D.C. : FHWA, 2013.

15. *A Stronger, More Resilient New York.* s.l. : City of New York, 2013.

16. Blake, Eric S and Zelinsky, David A. *National Hurricane Center Troppical Cyclone Report: Hurricane Harvey (AL092017).* s.l. : National Oceanic and Atmospheric Administration (NOAA), 2017.

17. *Durability Evaluation of Concrete Crack Repair Systems.* Tsiatas, George and Robinson, Joseph. Washington, D.C. : Transportation Research Board of the National Academies, 2002, Transportation Research Record, Vol. 1795, pp. 82-87.

18. Weyers, Richard E, et al. *Concrete Bridge Protection, Repair, and Rehabilitation Relative to Reinforcement Corrosion: A Methods Application Manual. SHRP-S-360.* National Academy of Sciences (NAS). Washington, D.C. : Transportation Research Board (TRB), 1993.

19. 222-R, ACI Committee. *Protection of Metals in Concrete Against Corrosion.* s.l. : American Concrete Institute, 2001. ISBN: 9780870310607.

20. 116R-00., ACI Committee. *Cement and Concrete Terminology, Manual of Concrete Practice, Part 1.* Farmington Hills, MI P.O. Box 9094 : American Concrete Institute, 2005.

21. ACI Committee 224. *ACI 224.1R-07: Causes, Evaluation, and Repair of Cracks in Concrete Structures.* s.l. : American Concrete Institute, 2007.

22. Sansalone, Mary J and Streett, William B. *Impact-echo: Nondestructive Evaluation of Concrete and Masonry.* Ithaca : Bullbrier Press, 1997.

23. *Standard Test Method for Measuring the P-Wave Speed and the Thickness of Concrete Plates Using the Impact-Echo Method.* West Conshohocken, PA : ASTM International, 2015.

24. *NDE-Based Assessment of Deterioration Progression in Two Concrete Bridge Decks.* Gucunski, N, et al. Washington DC : National Research Council, 2013. Transportaion Research Board (TRB).

25. *Report on Nondestructive Test Methods for Evaluation of Concrete in Structures.* ACI Committee 228, ACI. s.l. : American Concrete Institute (ACI), 2013. ISBN: 0-87031-820-9.

26. *ASTM G57-06(2012): Standard Test Method for Field Measurement of Soil Resistivity Using the Wenner Four-Electrode Method.* s.l. : ASTM International, 2012.

27. *Test methods for on site measurement of resistivity of concrete - a RILEM TC-154 technical recommendation.* Polder, Rob B. 2001, Construction and Building Materials, Vol. 15, pp. 125-131.

28. *Half-cell potential measurements – Potential mapping on reinforced concrete structures.* Elsener, B, et al. s.l. : RILEM TC 154-EMC: 'Electrochemical Techniques for Measuring Metallic Corrosion', 2003, Materials and Structures, Vol. 36, pp. 461-471.

29. *ASTM C876-15: Standard Test Method for Corrosion Potentials of Uncoated Reinforcing Steel in Concrete.* West Conshohocken, PA : ASTM International, 2015.

30. Nazarian, Soheil, Baker, Mark R and Crain, Kevin. *Development and testing of a seismic pavement analyzer.* Strategic Highway Research Program, National Research Council. Washington, D.C. : s.n., 1993. pp. 42, 138.

31. *ASTM D6087 - 08. Standard Test Method for Evaluating Asphalt-Covered Concrete Bridge Decks Using Ground Penetrating Radar.* West Conshohocken, PA : ASTM International, 2008.

32. *ASTM D6432 - 11. Standard Guide for Using the Surface Ground Penetrating Radar Method for Subsurface Investigation.* West Conshohocken, PA : ASTM International, 2011.

33. Johnson, Jay K, et al. *Remote Sensing in Archaeology: An Explicitly North American Perspective.* s.l. : University Alabama Press, 2006. p. 344.

34. It’s Official: Tut’s Tomb Has No Hidden Chambers After All. *National Geographic.* [Online] May 6, 2018. [Cited: May 21, 2018.] https://news.nationalgeographic.com/2018/05/king-tut-tutankhamun-tomb-radar-results-science/.

35. *Simulation-based microwave imaging of plain and reinforced concrete for nondestructive evaluation.* Gunes, Oguz and Buyukozturk, Oral. 3, s.l. : International Journal of the Physical Sciences, 2012, Vol. 7. DOI: 10.5897/IJPS11.1376.

36. *Frequency-dependent dispersion of high-frequency ground penetrating radar wave in concrete.* Lai, W L, Kind, T and Wiggenhauser, H. 2011, NDT&E International, Vol. 44, pp. 267–273.

37. Orfanidis, Sophocles J. *Electromagnetic Waves and Antennas.* Piscataway : s.n., 2010. p. 37.

38. *Time–frequency analysis of GPR data to investigate the damage of monumental buildings.* Leucci, Giovanni, Masini, Nicola and Persico, Raffaele. 2012, Journal of Geophysics and Engineering, Vol. 9, pp. S81-S91.

39. *Resolution of GPR bowtie antennas: An experimental approach.* Rial, Fernando I., et al. 2009, Journal of Applied Geophysics, Vol. 67, pp. 367–373.

40. *GPR modelling applied to vertical and horizontal resolution of buried objects.* Ziani, T, Teguig, D and Takkouche1, M A. Torino, Italy : s.n., 2011. International Conference on Electromagnetics in Advanced Applications (ICEAA).

41. Lalagüe, Anne. Use of Ground Penetrating Radar for Transportation Infrastructure Maintenance. *Thesis for the degree of Philosophiae Doctor.* Trondheim : Norwegian University of Science and Technology (NTNU), 2015. ISBN 978-82-326-1033-4.

42. *Bridge deck condition surveys using radar: Case studies of 28 New England decks.* Maser, K. 1304, s.l. : TRB National Research, 1991, Transportation Research Record, pp. 94–102.

43. *Phenomena and Conditions in Bridge Decks That Confound Ground-Penetrating Radar Data Analysis.* Barnes, Christopher L and Trottier, Jean-François. s.l. : Transportation Research Board (TRB), 2009, Transportation Research Record, Vol. 1795, pp. 57-61.

44. *Patch Analysis of Reinforced Concrete Bridge Decks Using Ground Penetrating Radar.* Martino, Nicole, et al. Washington, D.C. : s.n., 2013. TRB 2013 Annual Meeting.

45. Gucunski, Nenad, et al. *Comprehensive Bridge Deck Deterioration Mapping of Nine Bridges by Nondestructive Evaluation Technologies.* Iowa Department of Transportation. Ames : Iowa Highway Research Board, 2011.

46. *Development of a time–frequency approach to quantify railroad ballast fouling condition using ultra-wide band ground-penetrating radar data.* Al-Qadi, Imad L, et al. 4, August 2010, International Journal of Pavement Engineering, Vol. 11, pp. 269-279.

47. *Using ground penetrating radar and time-frequency analysis to characterize construction materials.* Lai, W L, Kind, T and Wiggenhauser, H. 2011, NDT&E International, Vol. 44, pp. 111–120.

48. *Performance Enhanced High Speed UWB GPR System for Buried Rebar Detection.* Xia, Tian, et al. Denver : s.n., 2013. Symposium on the Application of Geophysics for Engineering and Environmental Problems (SAGEEP).

49. *Complex Dielectric Permittivity Measurements from Ground-Penetrating Radar Data to Estimate Snow Liquid Water Content in the Pendular Regime.* Bradford, J H, Harper, J H and Brown, J. 2009, Water Resources Reseach, Vol. 45.

50. *Dielectric Constant Measurement of Railroad Ballast and Application of STFT for GPR Data Analysis.* Leng, Zhen and Al-Qadi, Imad. Nantes, France : s.n., 2009. Non-Destructive Testing in Civil Engineering (NDTCE'09).

51. *GPR signal de-noising by discrete wavelet transform.* Baili, Jamel, et al. 2009, NDT&E International, Vol. 42, pp. 696-703.

52. Daubechies, Ingrid. *Ten Lectures on Wavelets.* Philadelphia, PA : CBMS-NSF Regional Conference Series in Applied Mathematics, 1992.

53. *Frequency Dependent Attenuation Analysisof Ground-Penetrating Radar Data.* Bradford, John H. 3, 2007, Geophysics, Vol. 72, pp. J7-J16.

54. *Spectral analysis of ground penetrating radar signals in concrete, metallic and plastic targets.* dos Santos, V R N, et al. 2014, Journal of Applied Geophysics, Vol. 100, pp. 32-43.

55. Jin, Jian-Ming and Riley, Douglas J. *Finite Element Analysis of Antennas and Arrays.* Hoboken : John Wiley & Sons, 2009. p. 452. ISBN 978-0470401286.

56. *A Simple Introduction to Finite Element Analysis of Electromagnetic Problems.* Sadiku, Matthew N O. 2, May 1989, IEEE Transactions on Education, Vol. 32, pp. 85-93.

57. *Speech by Professor R. W. Clough: Early history of the finite element method from the view point of a pioneer.* Clough, Ray William. 2004, International Journal for Numerical Methods in Engineering, Vol. 60, pp. 283–287.

58. *The finite-element method, Part I: R. L. Courant.* Pelosi, Giuseppe. 2, 2007, IEEE Antenna and Propagation Magazin, Vol. 49, pp. 180-182.

59. *ADVANCES IN 3D ELECTROMAGNETIC FINITE ELEMENT MODELING.* Nelson, E M. Vancouver, BC : s.n., 1997. Particle Accelerator Conference. Vol. 2, pp. 1837-1840.

60. ANSYS High Frequency Structure Simulator. *ANSYS HFSS.* [Online] ANSYS. [Cited: July 15, 2012.] http://www.ansys.com/Products/Simulation+Technology/Electromagnetics/High-Performance+Electronic+Design/ANSYS+HFSS.

61. *A Comparison of FDFD and FEM Methods Applied to the Buried Mine Problem.* Gamache, Ronald, Rappaport, C M and Farid, Mtitou. Boston : s.n., 2006. Excerpt from the Proceedings of the COMSOL Users Conference.

62. *Application of the Finite-Difference Time-Domain Method to Sinusoidal Steady-State Electromagnetic-Penetration Problems.* Taflove, Allen. 3, August 1980, IEEE Transactions on Electromagnetic Compatibility, Vol. 22, pp. 191-202. Electronic ISSN: 1558-187X.

63. Giannopoulos, Antonis. *GPRMax2D / 3D User's Manual.* Edinburgh : s.n., 2005.

64. *A spectral analysis of ground-penetrating radar data for the assessment of the railway ballast geometric properties.* Ciampoli, Luca Bianchini, et al. 2017, NDT and E International, Vol. 90, pp. 39-47.

65. *Three-Dimensional FDTD Modeling of a Ground-Penetrating Radar.* Gürel, Levent and Oguz, Ugur. 4, July 2000, IEEE Transactions on Geoscience and Remote Sensing, Vol. 38, pp. 1513-1521.

66. Huston, Dryver, et al. *Nondestructive Testing of Reinforced Concrete Bridges Using Radar Imaging Techniques.* The New England Transportation Consortium. 2002.

67. *The First-Order Symplectic Euler Method Simulation of GPR Wave Propagation Simulation of GPR Wave Propagation.* Fang, Hongyuan, Lin, Gao and Zhang, Ruili. 1, January 2013, IEEE Transactions on Geoscience and Remote Sensing, Vol. 51, pp. 93-98.

68. *Specific evaluation of tunnel lining multi-defects by all-refined GPR simulation method using hybrid algorithm of FETD and FDTD.* Feng, Deshan, Wang, Xun and Zhang, Bin. 2018, Construction and Building Materials, Vol. 185, pp. 220–229.

69. *3-D finite-difference time-domain modelling of ground penetrating radar for identification of rebars in complex reinforced concrete structures.* Lachowicz, Jacek and Rucka, Magdalena. 2018, Archives of Civil and Mechanical Engineering (ACME), Vol. 18, pp. 1228-1240.

70. *Numerical modeling of ground-penetrating radar in 2-D using MATLAB.* Irving, James and Knight, Rosemary. 2006, Computers & Geosciences, Vol. 32, pp. 1247–1258.

71. Gibson, Walton C. *The Method of Moments in Electromagnetics.* s.l. : Chapman & Hall/CRC Press, 2007. p. 288. 978-1-4200-6145-1.

72. *Dielectric permittivity of concrete between 50 Mhz and 1 GHz and GPR measurements for building materials evaluation.* Robert, Antoine. 1998, Journal of Applied Geophysics, Vol. 40, pp. 89–94.

73. *Effect of water and chloride contents and carbonation on the electromagnetic characterization of concretes on the GPR frequency band through designs of experiment.* Derobert, Xavier and Villain, Geraldine. 2017, NDT and E International, Vol. 92, pp. 187–198.

74. *Evaluation of dielectric properties of concrete by a numerical FDTD model of a GPR coupled antenna - Parametric study.* Klysz, G, Balayssac, J P and Ferrieres, X. 2008, NDT&E International, Vol. 41, pp. 621– 631.

75. *Buried Object Detection and Analysis of GPR Images: Using Neural Network and Curve Fitting.* Singh, Navneet P and Nene, Manisha J. Kerala, India : IEEE, 2013. International Conference on Microelectronics, Communication and Renewable Energy (ICMiCR-2013).

76. *Location of Steel Reinforcement in Concrete Using Ground Penetrating Radar and Neural Networks.* Shaw, M R, et al. 3, 2004, NDT & E International, Vol. 38, pp. 203-212.

77. *Automatic detection of buried utilities and solid objects with GPR using neural networks and pattern recognition.* Al-Nuaimy, W, et al. 2000, Journal of Applied Geophysics, Vol. 43, pp. 157-165.

78. *Radar assessment of structural concrete using neural networks.* Molyneaux, T C K, et al. 5, 1995, NDT & E International, Vol. 28, pp. 281-288.

79. *A prediction algorithm for data analysis in GPR-based surveys.* Rodriguez, J B, et al. 2015, Neurocomputing, Vol. 168, pp. 464-474.

80. *Artificial Neural Networks and Machine Learning techniques applied to Ground Penetrating Radar: A review.* Travassos, Xisto L, Avila, Sérgio L and Ida, Nathan. 2018, Applied Computing and Informatics.

81. Awad, Mariette and Khanna, Rahul. *Efficient Learning Machines: Theories, Concepts, and Applications for Engineers and System Designers.* s.l. : Apress, 2015. ISBN-13 (electronic): 978-1-4302-5990-9.

82. Ng, Andrew. CS229: Machine Learning. *Stanford University.* [Online] 2017. cs229.stanford.edu.

83. *RADAN 7 Manual.* Geophysical Survey Systems Inc. Nashua, New Hampshire : Geophysical Survey Systems Inc, 2017.

84. *Processing strategiesforhigh-resolutionGPRconcreteinspections.* Hugenschmidt, Johannes, Kalogeropoulos, Alexis and Soldovieri, Francesco. 2010, NDT&EInternational, Vol. 43, pp. 334–342.

85. *Experimental verification of a linear inverse scattering algorithm for the localization of planar interfaces.* Leone, Giovanni and Barresi, Rafaella. 1, 2009, International Journal of Electronics and Communications (AEU), Vol. 63, pp. 24-30.

86. (ASCE), American Society of Civil Engineers. Report Card for America's Infrastructure, 2009 Grades. [Online] 2009. https://apps.asce.org/reportcard/2009/grades.cfm.

87. *Advanced signal processing method for Ground Penetrating Radar feature detection and enhancement.* Zhang, Yu, et al. San Diego : SPIE, 2014. Nondestructive Characterization for Composite Materials, Aerospace Engineering, Civil Infrastructure, and Homeland Security. Vol. 9063.

88. *Characterization and Detection of Bridge Deck Deterioration.* Maser, K R, et al. Lake Maggiore, Italy : s.n., 2012. Bridge Maintenance, Safety, Management, Resilience and Sustainability: Proceedings of the Sixth International IABMAS Conference.

89. *Application of hybrid FETD-FDTD method in the modeling and analysis of antennas.* Venkatarayalu, N V, et al. 9, September 2008, IEEE Transactions on Antennas and Propagation, Vol. 56, pp. 3068-3072.

90. Ng, Andrew. *Machine Learning Yearning: Technical Strategy for AI Engineers, In the Era of Deep Learning (Draft).* 2018.

91. *Ground Penetrating Radar: The Electromagnetic Signal Attenuation and Maximum Penetration Depth.* Leucci, Giovanni. 2008, Scholarly Research Exchange.

92. *gprMax: Open source software to simulate electromagnetic wave propagation for Ground Penetrating Radar.* Warren, C, Giannopoulos, A and Giannakis, I. 2016, Computer Physics Communications.

93. *Combined Effect of Moving Wheel Loading and Three-Dimensional Contact Stresses on Perpetual Pavement Responses.* Wang, H and Al-Qadi, I L. 2009, Transportation Research Board, Vol. 2095, pp. 53-61.